

**P-REFINEMENT TECHNIQUES  
FOR  
VECTOR FINITE ELEMENTS  
IN  
ELECTROMAGNETICS**

A Dissertation  
Presented to  
The Academic Faculty

By

Gi-Ho Park

In Partial Fulfillment  
Of the Requirements for the Degree  
Doctor of Philosophy in Electrical and Computer Engineering

Georgia Institute of Technology

December, 2005

Copyright © Gi-Ho Park 2005

**P-REFINEMENT TECHNIQUES  
FOR  
VECTOR FINITE ELEMENTS  
IN  
ELECTROMAGNETICS**

Approved by:

Dr. Andrew F. Peterson  
School of Electrical and Computer  
*Georgia Institute of Technology*

Dr. Waymond R. Scott  
School of Electrical and Computer  
*Georgia Institute of Technology*

Dr. Emmanouil M. Tentzeris  
School of Electrical and Computer  
*Georgia Institute of Technology*

Dr. David G. Taylor  
School of Electrical and Computer  
*Georgia Institute of Technology*

Dr. Doron Lubinsky  
School of Mathematics  
*Georgia Institute of Technology*

Date Approved: August 25, 2005

## ACKNOWLEDGEMENTS

During the last five years, I have been through many ups and downs due to both academic burdens and relationship troubles. Looking back on those turbulences, I have come to realize that I have grown through these years. Now, I have learned to be humble as I approach the end of my research. In the midst of solving the last hurdle in my research, I was almost an outsider of a life-thrilling event: my own wedding. Although the degree is only a sheet of paper, those who have been in my life journey now become a most precious treasure to me.

I have had a pleasant time sharing a research laboratory with Joshua, Jet, Chris, and Ryan. Gregory Durgin has also been a good friend with whom I can share my heart. The members of Student for Christ (SFC) have been with me for the last three years of my studies, and I will always have good memories of them. I deeply appreciate Dr. Andrew Peterson for his insightful guidance throughout my thesis research. Without his timely advice and patience during my hardships, this thesis would not have been possible.

I also thank my family members, especially my elderly mother. Her prayer is always a source of wisdom. I remember what she said when I was struggling with simulation code at the Monterey, CA, APS conference; “a day is like thousand years in God. Don’t lose your heart and rely on God’s wisdom.” That night was like thousand years in faith. Her prayer and love have sustained me through many hardships and trials. I also thank my brother Sooho, who has been a faithful friend and supporter through the

short years of my life. A special thank should be given to my brother Juho; he has been the personification of “not giving up, no matter what”. God has guided him throughout his life even though he doesn’t seem to realize that. Juho will be a wonderful tool giving glory to God. It is for this that I dream and pray. I also send my special thanks from the bottom of my heart to my family members in Korea. They have all supported me with prayer and love.

My dear wife Hwajin Yang is worthy of the following acknowledgement: she prepared for the wedding by herself, without saying a word of complaint, while I was absorbed in writing my thesis. She is wise and helps me to see the bright side of my problems when I am disappointed. Most of all, as the Bible says, she is a suitable helper for me. No one can replace her in my life, now or forever.

The most gratitude should be given to my Father in Heaven; he has always stood beside me and carried me on his back when I was in despair. The only reason I can step into an unknown and insecure world is that He is security, wisdom, and honor for me. Apart from Him, I cannot find any meaning in life. The only source of meaning in my life is Jehovah, “I am Who I am.”

I wish my humble knowledge only be used to exalt the name of Jesus Christ. My new wife and I humbly promise to serve God with all our hearts, with all our minds, with all our souls, with all our strength, and with our bodies. I dedicate not only this thesis, but myself to You, Lord.

## 감사의 글

5년의 시간이 순식간에 지나간 듯 합니다. 별로 어렵지 않았다고 말한다면 솔직한 표현은 아닐테지만, 즐거운 시간이었습니다. 한 과정을 끝내면서 이 과정이나 혼자만의 결과물이 아니라 많은 분들의 도움이 곁들어진 합작품이란 사실을 더욱 깨닫게 됩니다. 그리고, 학위보다 그간에 내 삶속에 함께 해 주셨던 분들, 아니 자신들의 삶을 열어서 나를 받아주셨던 분들에게 진심어린 감사의 말을 전합니다.

연구실을 같이 나뉘셨던 Joshia, Jet, Chris, 그리고 Ryan 로 인해 지루할 수 있던 연구실 생활이 즐거움으로 가득찼던 것을 기억합니다. 그들의 지도 교수인 Greg 은 교수로 임용되어 오면서 부터 마음을 함께 나눌 있었던 좋은 친구였습니다. 그의 재치있는 입담과 따뜻한 마음은 오랫동안 좋은 기억으로 남을 것입니다. 그리고, 3년을 함께 해 온 SFC 친구들도 빼놓을 수 없습니다. 영적으로 홀로 되어서 외로울 때 섬길 수 있도록 하나님이 특별히 허락하신 나의 어린 형제, 자매들입니다. 아니 그들이 제가 하나님앞에 가까이 갈 수 있는 가교 역할을 해 주었습니다. 나의 논문을 지도해 주신 Andrew F. Peterson 교수님께 감사를 드립니다. 5년 동안 딱 두번 만나자고 말을 했던 좋은 교수님입니다. 큰 스트레스 없이 신앙생활과 연구를 해 나갈 수 있었던 것도 교수님의 조급하지 않은 성품 덕분이었습니다. 교수님의 지도 동안에 스스로 모든 것을 해야 한다는 것과 미래는 하나님이 친히 인도하신다는 것을 배우게 되었습니다.

사랑하는 가족들에게 감사를 드립니다. 특별히 어머니의 기도와 격려는 이 학위과정뿐만 아니라 내 인생 전체를 통해서 언제나 지치지않을 수 있는 원동력이었습니다. 하나님의 지혜를 삶으로 나누시고 기도로 격려하는 어머니가 계시지않았다면 이 학위과정까지 오는데 있었던 많은 시련에 벌써 넘어져버렸을 것입니다. 2003년 캘리포니아 몬트레이에서 있었던 학회에서 발표 하루전에 발표 결과물에 문제가 있다는 것을 발견했습니다. 36시간을 꼬박 깨어서 디버깅을 하는 중에 어머니의 격려의 말씀은 아직도 기억에 남습니다; “하나님안에서는 하루가

천년같다. 낙심말고 끝까지 주님을 의지해라.” 그날밤을 천년으로 사용했고 하나님의 지혜는 실패가 없었습니다. 수호형에게도 감사합니다. 언제나 하나님의 말씀을 향한 갈급함을 심어주는 영적인 친구이자 든든한 나의 기도 후원자입니다. 주호형은 끝까지 포기함이 없는 것이 어떤 것인가를 삶으로 나에게 가르쳐줍니다. 하나님의 손길이 형과 함께 한다는 것을 하루속히 깨닫기를 원합니다. 형의 인생 전체를 통해서 살아계신 주님을 만나고 그분께 영광돌리는 형이 되기를 믿고 또한 기도하고 있습니다. 한국에 계신 두분의 형과 두분의 누나 그리고 그 가족에게도 진심으로 감사를 드립니다. 가까이 있어 함께 하진 못하지만, 동생을 위해서 기도하고 보내준 사랑은 하나도 잊을 수 없습니다.

사랑하는 나의 새 신부 양화진에게도 감사를 드립니다. 논문 마무리로 결혼준비는 몸만 준비했던 신랑이었지만, 한번도 불평의 말없이 잘 견뎌준 당신께 정말 감사합니다. 그리스도 안에서 나에게 돕는 배필이 되고 싶다는 당신의 따뜻한 고백, 낙심한 때에 그리스도를 다시 보도록 나의 시선을 인도해주는 당신은 어느 누구도 대신할 수 없는 내 뼈중에 뼈요 살중에 살이랍니다.

가장 큰 감사를 하늘에 계신 나의 아버지께 올려드립니다. 언제나 곁에서 떠나지 않으셨고 심연중에서 나를 등에 업어서 인도해 주신 나의 하나님 바로 그분이 나의 주님이시요 나의 아버지이십니다. 분명한 것이 하나도 없는 미지의 길을 향할 수 있는 오직 한가지 이유는 그 아버지가 내게 삶의 보장이시고 지혜시며 나의 영광이기때문입니다. 그분만의 내 삶에 의미를 부여하는 분이십니다. 그리고, 영원한 나의 분깃입니다.

나의 사랑하는신부와 나는 오직 그 하나님 한분만을 영화롭게하는 데 우리의 마음,뜻,정성, 그리고 몸을 사용하겠습니다. 이 학위 논문과 더불어 나 자신을 주님께 올려드립니다.

# TABLE OF CONTENTS

ACKNOWLEDGEMENT.....	iii
LIST OF TABLES.....	ix
LIST OF FIGURES.....	xi
LIST OF ABBREVIATIONS.....	xv
SUMMARY.....	xvi
CHAPTER 1: INTRODUCTION.....	1
CHAPTER 2: BACKGROUND.....	6
2.1. Mathematical Foundation.....	6
2.2. Helmholtz Equations.....	9
2.3. Rectangular Cavity Problem.....	12
2.4. Parallel-Plate Waveguide Problem.....	16
2.5 Summary.....	23
CHAPTER 3: SCALAR AND VECTOR FINITE ELEMENTS.....	24
3.1. Scalar Basis Functions.....	25
3.2. Vector Basis Functions.....	29
3.3. Summary.....	44
CHAPTER 4: VERIFICATION OF HIERARCHICAL VECTOR FINITE ELEMENTS.....	45
4.1. Analytical Solution.....	46
4.2. Numerical Solutions.....	51

4.3. Summary.....	63
CHAPTER 5: ERROR ESTIMATORS.....	66
5.1. Exact Solutions for T-PPWG and S-PPWG Structures.....	68
5.2 Normal Field Discontinuity (NFD) Error Estimator.....	80
5.3 Discontinuity of Curl Field (DCF) Error Estimator.....	87
5.4 Weak Form Residual (WFR) Error Estimator.....	93
5.5 The Coefficient Sensitivity of the Highest-Order Polynomial (CSH) Error Estimator.....	104
5.6 Evaluation of Error Estimators by Comparing Global Errors and Local Errors with Actual Errors.....	115
5.7 Error Estimators Applied to Structures with a Cell Corrupted with a Known Error.....	120
5.8 Summary.....	145
CHAPTER 6: ADAPTIVE P-REFINEMENT FEM.....	148
6.1. Simulation Results.....	150
6.2. Summary.....	177
CHAPTER 7: CONCLUSIONS.....	183
REFERENCES.....	185



## LIST OF TABLES

Table 3.1 Hierarchical vector basis functions.....	41
Table 5.1 Percentage error in the global error estimates for T-PPWG.....	116
Table 5.2 Percentage error in the global error estimates for S-PPWG.....	117
Table 5.3 Percentage error in the local error estimates along the x-axis for T-PPWG...	117
Table 5.4 Percentage error in the local error estimates along the x-axis for S-PPWG...	118
Table 5.5 Percentage error in the local error estimates along the z-axis for T-PPWG...	118
Table 5.6 Percentage error in the local error estimates along the z-axis for S-PPWG...	119
Table 5.7 Percentage errors in the local error estimates for points along the z-axis for T-PPWG.....	139
Table 5.8 Percentage errors in the local error estimates for points along x-axis for T-PPWG.....	140
Table 5.9 Percentage errors in the local error estimates for points along z-axis for S-PPWG.....	140
Table 5.10 Percentage errors in the local error estimates for points along x-axis for S-PPWG.....	141
Table 5.11 Percentage error of the error at point 3 to sum of errors at all points.....	141
Table 5.12 Ratio of edge-based actual local error to local error estimates at point 3....	142
Table 5.13 Ratio of cell-based actual local error to local error estimates at point 3.....	143
Table 6.1 Uniform p-refinement with Interpolatory vector basis for one-septum structure.....	172
Table 6.2 Adaptive p-refinement with single-step of 25% using NFD estimator for one-septum structure .....	172
Table 6.3 Adaptive p-refinement with multi-steps of 25%+10% using NFD estimator for one-septum structure .....	173

Table 6.4 Adaptive p-refinement with single-step of 25% using WFR estimator for one-septum structure .....	173
Table 6.5 Adaptive p-refinement with multi-steps of 25%+10% using WFR estimator for one-septum structure .....	174
Table 6.6 Uniform p-refinement with interpolatory vector basis for two-septum structure .....	174
Table 6.7 Adaptive p-refinement with single-step of 25% using NFD estimator for two-septum structure .....	175
Table 6.8 Adaptive p-refinement with multi-steps of 25%+10% using NFD estimator for two-septum structure .....	175
Table 6.9 Adaptive p-refinement with single-step of 25% using WFR estimator for two-septum structure .....	176
Table 6.10 Adaptive p-refinement with multi-steps of 25%+10% using WFR estimator for two-septum structure .....	176
Table 6.11 Comparison of two iteration techniques for one-septum and two-septum T- PPWG structures .....	181

## LIST OF FIGURES

Figure 2.1 Discretization of a rectangular cavity.....	15
Figure 2.2 Discretization of parallel-plate waveguide.....	17
Figure 3.1 Simplex coordinate of a triangular element.....	25
Figure 3.2 Interpolation points of $B_{ijk}$ , $M=3$ .....	27
Figure 3.3 Triangular edge element.....	30
Figure 3.4 Zeroth-order curl conforming function of $\overline{\Omega}_0^1 = L_2 \nabla L_3 - L_3 \nabla L_2$ .....	33
Figure 3.5 An illustration of basis functions for piecewise-constant and piecewise-linear approximations of a scalar quantity .....	37
Figure 3.6 Non-hierarchical vector basis functions [17].....	39
Figure 3.7 Hierarchical vector basis functions.....	42
Figure 4.1 Unterminated parallel plate waveguide.....	45
Figure 4.2 Parallel plate waveguide with short-circuited end.....	46
Figure 4.3 Unterminated parallel plate waveguide.....	48
Figure 4.4 Parallel plate waveguide with short-circuited end.....	48
Figure 4.5: Magnetic field for the open-ended parallel plate waveguide.....	54
Figure 4.6 Magnetic field for the short-circuited parallel plate waveguide.....	54
Figure 4.7 Scattering parameter error for the short-circuited parallel plate waveguide...	64
Figure 4.8 Scattering parameter error for the unterminated parallel plate waveguide.....	65
Figure 5.1 Coarse mesh for the parallel plate waveguide.....	71
Figure 5.2 Global error computed as a function of the number of quadrature points used for three orders of vector basis functions.....	72
Figure 5.3 Global error defined from (5.7) as a function of the basis function order.....	73

Figure 5.4 Global error defined from (5.9) as a function of the basis function order.....	74
Figure 5.5 Local edge-based actual error along the z-axis where $x = 0.3$ .....	76
Figure 5.6 Local edge-based actual error along the x-axis where $z = -0.226$ .....	77
Figure 5.7 Local cell-based actual error along the z-axis where $x = 0.3$ .....	78
Figure 5.8 Local cell-based actual error along the x-axis where $z = -0.226$ .....	79
Figure 5.9 Gauss' law.....	81
Figure 5.10 Boundary conditions.....	82
Figure 5.11 Global error comparison of NFD error estimator with the actual error.....	84
Figure 5.12 Local NFD error along the z-axis where $x = 0.3$ .....	85
Figure 5.13 Local NFD error along the x-axis where $z = -0.226$ .....	86
Figure 5.14 Global error comparison of the DCF error estimator and the actual error in the FEM solution.....	90
Figure 5.15 Local DCF error along the z-axis where $x = 0.3$ .....	91
Figure 5.16 Local DCF error along the x-axis where $z = -0.226$ .....	92
Figure 5.17 Global error comparison of WFR error estimator.....	101
Figure 5.18 Local WFR error along the z-axis where $x = 0.3$ .....	102
Figure 5.19 Local WFR error along the x-axis where $z = -0.226$ .....	103
Figure 5.20 Global error comparison of the edge-based CSH error estimator.....	109
Figure 5.21 Global error comparison of the cell-based CSH error estimator.....	110
Figure 5.22 Local edge-based CSH error along the z-axis where $x = 0.3$ .....	111
Figure 5.23 Local edge-based CSH error along the x-axis where $z = -0.226$ .....	112
Figure 5.24 Local cell-based CSH error along the z-axis where $x = 0.3$ .....	113
Figure 5.25 Local cell-based CSH error along the x-axis where $z = -0.226$ .....	114

Figure 5.26 Mesh with a cell corrupted with a known error.....	120
Figure 5.27 The actual local error with and without the additional corruption, as plotted along the z-axis at $x = 0.24$ for the T-PPWG structure.....	123
Figure 5.28 The error functions produced by the estimators for the corrupted and un- corrupted results. The error is plotted along the z-axis at $x = 0.24$ for the T- PPWG structure.....	124
Figure 5.29 The actual local error with and without the additional corruption, as plotted along the x-axis at $z = -0.18$ for the T-PPWG structure.....	127
Figure 5.30 The error functions produced by the estimators for the corrupted and un- corrupted results. The error is plotted along the x-axis at $z = -0.18$ for the T- PPWG structure.....	128
Figure 5.31 The actual local error with and without the additional corruption, as plotted along the z-axis at $x = 0.24$ for the S-PPWG structure.....	131
Figure 5.32 The error functions produced by the estimators for the corrupted and un- corrupted results. The error is plotted along the z-axis at $x = 0.24$ for the S- PPWG structure.....	132
Figure 5.33 The actual local error with and without the additional corruption, as plotted along the x-axis at $z = -0.18$ for the S-PPWG structure.....	135
Figure 5.34 The error functions produced by the estimators for the corrupted and un- corrupted results. The error is plotted along the x-axis at $z = -0.18$ for the S- PPWG structure.....	136
Figure 5.35 Comparison of error estimators for T-PPWG (un-corrupted).....	146
Figure 5.36 Comparison of error estimators for S-PPWG (un-corrupted).....	146
Figure 6.1 (a) One-septum T-PPWG structure (b) Two-septum T-PPWG structure .....	150
Figure 6.2 The NFD estimator with 25% single-step iteration technique for the structure in (a) of Figure 6.1.....	152
Figure 6.3 The NFD estimator with 25%+10% multi-step iteration technique for the structure in (a) of Figure 6.1.....	154
Figure 6.4 The WFR estimator with 25% single-step iteration technique for the structure in (a) of Figure 6.1.....	157

Figure 6.5 The WFR estimator with 25%+10% multi-step iteration technique for the structure in (a) of Figure 6.1.....	159
Figure 6.6 The NFD estimator with 25% single step iteration technique for the structure in (b) of Figure 6.1.....	161
Figure 6.7 The NFD estimator with 25% +10% multi-step iteration technique for the structure in (b) of Figure 6.1.....	163
Figure 6.8 The WFR estimator with 25% single step iteration technique for the structure in (b) of Figure 6.1.....	166
Figure 6.9 The WFR estimator with 25% +10% multi-step iteration technique for the structure in (b) of Figure 6.1.....	168
Figure 6.10 DoF distribution of the NFD error estimator.....	178
Figure 6.11 DoF distribution of the WFR error estimator for one-septum structure.....	179
Figure 6.12 DoF distribution of the WFR error estimator for two-septum structure.....	180

## LIST OF ABBREVIATIONS

FEM	Finite Element Method
MoM	Method of Moment
FDTD	Finite Difference Time Domain
DOF	Degree of Freedom
PPWG	Parallel Plate Waveguide
PEC	Perfect Electric Conductor
S-PPWG	Short-ended Parallel Plate Waveguide
T-PPWG	Open-ended Parallel Plate Waveguide
CT/LN	Constant Tangential/Linear Normal
LT/QN	Linear Tangential/ Quadratic Normal
QT/CuN	Quadratic Tangential/ Cubic Normal
NFD	Normal Field Discontinuity
DCF	Discontinuity of the Curl of Field
WFR	Weak Form Residual
CSH	Coefficient Sensitivity of the Highest-Order Polynomial
GEI	General Error Indicator
TEI	Targeted Error Indicator
IT	Iteration Technique

## SUMMARY

The vector finite element method has gained great attention since overcoming the deficiencies incurred by the scalar basis functions for the vector Helmholtz equation. Most implementations of vector FEM have been non-adaptive, where a mesh of the domain is generated entirely in advance and used with a constant degree polynomial basis to assign the degrees of freedom. To reduce the dependency on the users' expertise in analyzing problems with complicated boundary structures and material characteristics, and to speed up the FEM tool, the demand for adaptive FEM grows high.

For efficient adaptive FEM, error estimators play an important role in assigning additional degrees of freedom. In this proposal study, hierarchical vector basis functions and four error estimators for p-refinement are investigated for electromagnetic applications.



## **CHAPTER 1: INTRODUCTION**

There are many practical applications that require electromagnetic analysis as an aid to the design of electrical systems. Often, due to the complexity of the geometric structures typically encountered, the analysis must be carried out by numerical techniques. For example, in the area of microelectronic systems, technological advances result in a greater density of circuits integrated into a small area, the use of multilevel structures, and a variety of materials. Closed form solutions to Maxwell's equations are limited to structures with simple geometries. Consequently, in electromagnetics, attention has been directed toward numerical analysis methods such as the finite element method (FEM), the finite difference time domain (FDTD) method, and the method of moments (MoM) [1-3].

The finite element method is widely used for analyzing electromagnetic field problems, because it offers several advantages. The global matrix within the FEM formulation is sparse since each degree of freedom (DOF) is interlinked only to nearest neighbors [1-3]. Procedures have been developed for solving sparse matrices to reduce fill-in and minimize memory resources [4,5]. The FEM can easily deal with complex geometric cell shapes, various materials, and curved boundaries [1-3]. Furthermore, one major difficulty associated with the FEM in the past, the treatment of unbounded domains associated with scattering and radiation problems, has been solved by a number of mesh truncation techniques [1,3,6-8].

More importantly, the recent introduction of vector finite elements solved several problems that occurred from attempts to solve the vector Helmholtz equation with scalar elements [9]. Vector finite elements enforce the continuity of the tangential component of the vector quantities but not the normal component. They confine spurious eigenvalues to the zero eigenvalue subspace. They also appear to model singularities more accurately.

In recent years, a number of interpolatory and hierarchical vector elements have been proposed in the literature [1,3,10-25]. These two types of elements offer a trade-off in their relative efficiency and ease of interpretation. The coefficients of interpolatory functions are the sampled values of the appropriate field at various locations, and thus provide a straightforward interpretation of the result. Hierarchical functions, on the other hand, build on basis functions of lower-order in a systematic way, and permit a more efficient computational procedure that minimizes the number of equations that must be recomputed as the basis function order is gradually increased.

In common with all numerical solution procedures, FEM results contain discretization error caused by expanding a continuous function with a finite number of elements. This error can be reduced by diminishing the size of the elements, h-refinement, or increasing the polynomial order, p-refinement, so that the basis functions may better capture the variation of the unknown function over the patched local domain of the calculation [2]. H-refinement techniques have been used in conjunction with low-order vector basis functions for a number of years [2]. However, p-refinement techniques have

not been thoroughly studied to date, probably because of the relatively recent development of higher-order hierarchical vector basis functions.

P-refinement has the advantage that it avoids the time-consuming mesh regeneration process associated with h-refinement. However, to take full advantage of either type of refinement technique, the process must be adaptive. In adaptive refinement, the error estimated from a numerical solution at one level of refinement is employed to predict which regions within the computational domain most need additional degrees of freedom. The procedure then assigns additional degrees within those regions and resolves the problem. Hierarchical vector basis functions are almost always utilized for p-adaptive refinement since they allow most of the equations within the FEM system to remain the same from one level of refinement to the next. On the contrary, interpolatory vector basis functions would require all the equations in the regions undergoing refinement to be replaced. In addition, an interpolatory expansion requires special transition elements to connect between regions of different polynomial degree.

Industrial applications demand more efficient and robust computational tools, since users' expertise often fails for very complicated structures and the high initial fabrication cost of modern systems motivates a high certainty of success before fabrication. For a software tool to be able to analyze a specific problem from the given geometric and material information alone, some form of refinement must be incorporated in an adaptive and intelligent way.

Adaptive finite element methods rely on a local error estimator to decide which elements within the computational domain contain the largest error levels and would benefit from additional degrees of freedom. Although error estimators have been developed for scalar equations [26], little research has been directed to date toward error estimators for the vector electromagnetic field problems of interest. The development, implementation, and evaluation of error estimators for vector electromagnetic field problems forms the principal subject matter of this dissertation.

Chapters 2 and 3 review the FEM formulation. The Helmholtz equation is obtained from Maxwell's equations, and specialized to the rectangular cavity and parallel plate waveguide (PPWG) structures that will be used for illustration. The vector FEM procedure is described, and higher-order hierarchical vector basis functions are reviewed. Chapter 4 provides a validation study to ensure that the vector FEM computer code is correctly implemented.

Chapter 5 presents several error estimators, including one based on the normal-field discontinuity between cells, one related to the tangential-field discontinuity, one based on the residual error associated with the Helmholtz equation, and one based on the relative magnitudes of coefficients of higher-order hierarchical bases. The implementation of these error estimators is described. The performance of these error estimators is reported in Chapter 5, for several canonical problems associated with the PPWG geometry. Results suggest that the normal-field discontinuity (NFD) and weak form residual (WFR) estimators are the most accurate in terms of correctly estimating the

field error. These estimators are implemented within an adaptive p-refinement algorithm and used to analyze several problems (Chapter 6). The performance of the adaptive p-refinement algorithm is reported.

## CHAPTER 2: BACKGROUND

### 2.1 Mathematical Foundation

The solution of an electromagnetic field problem must satisfy Maxwell's equations and the associated boundary conditions. In general, this boundary-value problem can be defined by a governing differential equation in a domain  $\Gamma$  with the general form

$$\mathcal{L}u - f = 0 \quad (2.1)$$

accompanied by boundary or transition conditions

$$B(u) = 0 \quad (2.2)$$

on the boundary  $\partial\Gamma$ .

In electromagnetics, the differential operator  $\mathcal{L}$  usually represents the scalar or vector Helmholtz equations. The function  $f$  is a known excitation function and  $u$  is the unknown quantity, such as the electric or magnetic field. The function  $u$  may be a scalar quantity or a vector quantity;  $u$  can be replaced by the vector quantity  $\vec{u}$  when the governing equation is the vector Helmholtz equation.

An analytical solution is possible for relatively few cases, such as:

- The static potential between infinite parallel plates
- Wave propagation in rectangular, circular, and elliptic waveguides
- Cavity resonance within rectangular, cylindrical, and spherical cavities
- Wave scattering by infinite planes, cylinders, or spheres

For most problems of practical interest in electromagnetics, therefore, an approximate solution is obtained by a numerical method. Typical numerical methods for electromagnetic problems have their origins in the classical Ritz-variational method and Galerkin's method [1,23]. Galerkin's Method is explained here briefly for further study. (For the Helmholtz equation the Ritz-variational method leads to the same matrix equation.)

Galerkin's method is one of the weighted residual methods and, as that name suggests, the solution is found by weighting the residual of the differential equation. Assume  $\tilde{u}$  is an approximation of the exact solution  $u$  expanded as

$$\tilde{u} = \sum_{j=1}^N c_j w_j = \{c\}^T \{w\} = \{w\}^T \{c\} \quad (2.3)$$

where  $w_j$  are the chosen expansion functions and  $c_j$  are coefficients to be determined. Also,  $\{\cdot\}$  denotes a column vector and the superscript T denotes the transpose of the vector. Then the residual is given by

$$r = \mathcal{L}\tilde{u} - f \neq 0 \quad (2.4)$$

A system of equations is obtained by weighing the residual with a set of test functions  $\{t_j\}$  and equating the weighted residual to zero over the domain:

$$R_j = \int_{\Gamma} t_j r d\Gamma = 0 \quad (2.5)$$

The approximate solution to equation (2.1) is obtained by solving this system of equations. In Galerkin's method, the testing or weighting functions are taken to be the same as the expansion functions. Therefore, the weighting functions are chosen as

$$t_j = w_j, j=1,2,\dots, N \quad (2.6)$$

and equation (2.5) is written as

$$R_j = \int_{\Gamma} (w_j L\{w\}^T \{c\} - w_j f) d\Gamma = 0 \quad j=1,2,\dots, N. \quad (2.7)$$

This equation can be written in the form of a matrix equation

$$[S]\{c\} = \{b\} \quad (2.8)$$

where

$$S_{ij} = \int_{\Gamma} (w_i L w_j) d\Gamma \quad (2.9)$$

and

$$b_i = \int_{\Gamma} (w_i f) d\Gamma. \quad (2.10)$$

To avoid the need to use expansion functions that can accurately capture or approximate the exact solution over the entire domain, the domain is divided into smaller subdivisions and functions are defined over each subdomain. If a subdomain is sufficiently small, and the variation of the exact solution over that subdomain is small, expansion and testing functions may have a much simpler form than they would require over the entire domain. The subdivisions are *finite elements*.

This method, the so-called Galerkin FEM, allows subdomain basis and testing functions to be capable of approximating the exact solution of more complicated structures. There is always some error incurred in representing the domain and the solution by this process but, in general, it will be reduced as the element size decreases.



The generation and solution of the Galerkin FEM system requires the following steps:

- Define the problem's computational domain
- Choose discrete elements and expansion functions
- Generate a mesh
- Enforce the residual equation over each element to generate the element matrices
- Apply boundary conditions and assemble element matrices to obtain the overall sparse system
- Solve the overall system equation
- Postprocess field data to extract parameters of interest.

In the following sections, the scalar and vector Helmholtz equations are derived from Maxwell's equations. These equations are specialized to a two-dimensional cavity problem and a two-dimensional parallel-plate waveguide problem. The associated FEM equations are developed.

## **2.2 Helmholtz Equations**

Electromagnetic field problems are described by Maxwell's equations in differential form. Consider a closed region  $\Gamma$ , contained within the surface  $\partial\Gamma$ , which might be truncated by an absorbing boundary condition or closed by perfect electric conductor (PEC) surfaces. This region might contain inhomogeneous materials with

complex geometrical shapes. Assume that the region is source-free and the field is time-harmonic with frequency  $\omega$ . Maxwell's equations are given by

$$\nabla \times \bar{\mathbf{E}} = -j\omega\mu\bar{\mathbf{H}} \quad (2.11)$$

$$\nabla \times \bar{\mathbf{H}} = j\omega\varepsilon\bar{\mathbf{E}} \quad (2.12)$$

$$\nabla \cdot \varepsilon\bar{\mathbf{E}} = 0 \quad (2.13)$$

$$\nabla \cdot \mu\bar{\mathbf{H}} = 0 \quad (2.14)$$

where  $\bar{\mathbf{E}}$  and  $\bar{\mathbf{H}}$  are the electric and magnetic field intensities, respectively. The constitutive parameters,  $\varepsilon$  and  $\mu$ , are the permittivity and permeability of the region, respectively, each of which may vary with position according to the material filling that region. These parameters can be described in proportion to the free space parameters,  $\varepsilon_0$  and  $\mu_0$ :

$$\varepsilon = \varepsilon_r \varepsilon_0 \quad (2.15)$$

$$\mu = \mu_r \mu_0 \quad (2.16)$$

where  $\varepsilon_r$  and  $\mu_r$  are the relative permittivity and permeability, which vary with position.

Two vector Helmholtz equations are derived by combining (2.11) and (2.12). The first is

$$\nabla \times \left( \frac{1}{\varepsilon_r} \nabla \times \bar{\mathbf{H}} \right) = k_0^2 \mu_r \bar{\mathbf{H}} \quad (2.17)$$

involving the magnetic field as the primary unknown and the second is

$$\nabla \times \left( \frac{1}{\mu_r} \nabla \times \bar{\mathbf{E}} \right) = k_0^2 \varepsilon_r \bar{\mathbf{E}} \quad (2.18)$$

where the primary unknown is the electric field. In equations (2.17) and (2.18),  $k_0 = \omega\sqrt{\varepsilon_0\mu_0}$  is the wave number. These are often called the curl-curl equations.

When these equations are specialized to two dimensions, there are two polarizations that arise. The TE-to-z or  $\mathbf{H}_z$  polarization is obtained after employing the vector identity

$$\nabla_t \times \left[ \frac{1}{\varepsilon_r} \nabla_t \times (\hat{z} \mathbf{H}_z) \right] = -\hat{z} \nabla_t \cdot \frac{1}{\varepsilon_r} \nabla_t \mathbf{H}_z$$

to reduce the vector equation (2.17) into the scalar equation

$$\nabla_t \cdot \frac{1}{\varepsilon_r} \nabla_t \mathbf{H}_z = -k_0^2 \mu_r \mathbf{H}_z. \quad (2.19)$$

In a similar manner, an equation for the TM-to-z or  $\mathbf{E}_z$  polarization is obtained as

$$\nabla_t \cdot \frac{1}{\mu_r} \nabla_t \mathbf{E}_z = -k_0^2 \varepsilon_r \mathbf{E}_z. \quad (2.20)$$

In the preceding equations,

$$\nabla_t = \frac{\partial}{\partial x} \hat{x} + \frac{\partial}{\partial y} \hat{y}. \quad (2.21)$$

Equations (2.19) and (2.20) are scalar Helmholtz equations.

Proper boundary conditions must be specified in conjunction with these differential equations. References [1,23] provide a complete and detailed discussion. In this study, an absorbing boundary condition will be used for open regions; it will be derived in Section 2.4. For a PEC surface, the tangential component of the electric field must vanish at the boundary of the PEC:

$$\overline{\mathbf{E}}_{\text{tan}} \big|_{\text{PECsurface}} = 0 . \quad (2.22)$$

At the interface between two homogeneous dielectrics, tangential continuity is expressed:

$$\overline{\mathbf{E}}_{\text{tan}} \big|_{\text{surface}}^+ = \overline{\mathbf{E}}_{\text{tan}} \big|_{\text{surface}}^- . \quad (2.23)$$

The expansion functions should maintain tangential continuity at material interfaces.

Solving Maxwell's equations with their boundary conditions is equivalent to solving the curl-curl equations with their boundary conditions. The curl-curl equation is converted into a variational functional or a weak form equation before it is discretized. The FEM converts the functional or weak form equation into a linear system of equations by discretizing the over-all computational region into many smaller elements. The approximate solution is obtained by solving the linear algebraic equations using standard matrix techniques. These steps are described in the following sections.

### 2.3 Rectangular Cavity Problem

In this section, the vector Helmholtz equations are used to develop scalar and vector finite element formulations for a 2D rectangular cavity problem. Although two-dimensional problems can usually be posed in terms of scalar equations, this dissertation focuses on vector equations in the hope that the results have more applicability to the general three-dimensional case. Additional details of these derivations may be found in fundamental books on finite element methods [1-3,23].

In most cases, an analytical solution to (2.17) and (2.18) is not possible. To obtain a numerical solution, the first step of the FEM procedure is to convert the vector

Helmholtz equation into a weak form equation. The equations can be reduced to a weak form by taking the dot product of either curl-curl equation with a known vector test function,  $\bar{\mathbf{T}}$ . For example, (2.17) is tested to yield

$$\bar{\mathbf{T}} \cdot \nabla \times \left( \frac{1}{\varepsilon_r} \nabla \times \bar{\mathbf{H}} \right) = k_0^2 \mu_r \bar{\mathbf{T}} \cdot \bar{\mathbf{H}} \quad (2.24)$$

By using a standard vector identity, we obtain

$$\bar{\mathbf{T}} \cdot \nabla \times \left( \frac{1}{\varepsilon_r} \nabla \times \bar{\mathbf{H}} \right) = \frac{1}{\varepsilon_r} \nabla \times \bar{\mathbf{H}} \cdot \nabla \times \bar{\mathbf{T}} - \nabla \cdot \left[ \frac{1}{\varepsilon_r} (\nabla \times \bar{\mathbf{H}}) \times \bar{\mathbf{T}} \right] = k_0^2 \mu_r \bar{\mathbf{T}} \cdot \bar{\mathbf{H}} \quad (2.25)$$

By rearranging terms, (2.25) can be written as

$$\frac{1}{\varepsilon_r} \nabla \times \bar{\mathbf{H}} \cdot \nabla \times \bar{\mathbf{T}} - k_0^2 \mu_r \bar{\mathbf{T}} \cdot \bar{\mathbf{H}} = \nabla \cdot \left[ \frac{1}{\varepsilon_r} (\nabla \times \bar{\mathbf{H}}) \times \bar{\mathbf{T}} \right] \quad (2.26)$$

By integrating (2.26) over the computation domain  $\Gamma$ , the right hand term is modified by Gauss' law as follows

$$\iint_{\Gamma} \nabla \cdot \left[ \frac{1}{\varepsilon_r} (\nabla \times \bar{\mathbf{H}}) \times \bar{\mathbf{T}} \right] ds = \int_{\partial\Gamma} \left[ \bar{\mathbf{T}} \times \frac{1}{\varepsilon_r} (\nabla \times \bar{\mathbf{H}}) \right] \cdot \hat{n} dl \quad (2.27)$$

Finally, (2.26) is rearranged to yield

$$\iint_{\Gamma} \left( \frac{1}{\varepsilon_r} \nabla \times \bar{\mathbf{H}} \cdot \nabla \times \bar{\mathbf{T}} - k_0^2 \mu_r \bar{\mathbf{T}} \cdot \bar{\mathbf{H}} \right) ds = \int_{\partial\Gamma} \left[ \bar{\mathbf{T}} \times \frac{1}{\varepsilon_r} (\nabla \times \bar{\mathbf{H}}) \right] \cdot \hat{n} dl \quad (2.28)$$

where the boundary  $\partial\Gamma$  is the contour surrounding the interior region  $\Gamma$  and its outward normal vector is  $\hat{n}$ . Equation (2.28) is the weak form of (2.17).

By similar steps, we can obtain a weak form equation for the electric field  $\bar{\mathbf{E}}$  as

$$\iint_{\Gamma} \left( \frac{1}{\mu_r} \nabla \times \bar{\mathbf{E}} \cdot \nabla \times \bar{\mathbf{T}} - k_0^2 \varepsilon_r \bar{\mathbf{T}} \cdot \bar{\mathbf{E}} \right) ds = \int_{\partial\Gamma} \left[ \bar{\mathbf{T}} \times \frac{1}{\mu_r} (\nabla \times \bar{\mathbf{E}}) \right] \cdot \hat{n} dl \quad (2.29)$$

Equations (2.28) and (2.29) are called the weak forms of the vector Helmholtz equations. The left-hand side terms in these equations are common to a wide range of electromagnetics problems. The right-hand side, which usually provides a means for incorporating boundary conditions, must be manipulated properly depending on whether the system of interest is a deterministic or an eigenvalue problem. The weak equation yields a deterministic system when it models scattering, radiation, and other deterministic problems associated with a source or excitation. It yields an eigenvalue system when it models source-free wave propagation in waveguides and source-free resonances in cavities. The deterministic system will be discussed in Section 2.4. Here, the eigenvalue system is considered as one example that will be used to verify the FEM implementation.

Consider a region surrounded by a PEC surface. The right hand boundary integration in (2.28) is nullified since the curl of magnetic field vanishes on the PEC surface. Equation (2.28) reduces to

$$\iint_{\Gamma} \left( \frac{1}{\epsilon_r} \nabla \times \bar{\mathbf{H}} \cdot \nabla \times \bar{\mathbf{T}} \right) ds = \iint_{\Gamma} (k_0^2 \mu_r \bar{\mathbf{T}} \cdot \bar{\mathbf{H}}) ds \quad (2.30)$$

In order to obtain a numerical solution, the equation must be discretized. Suppose that the computational domain is the rectangular cavity  $\Gamma$ . This domain must be divided into M subsections or elements  $\Gamma_k$ , where  $k=1, 2, 3, \dots, M$ , as illustrated in Figure 2.1 .

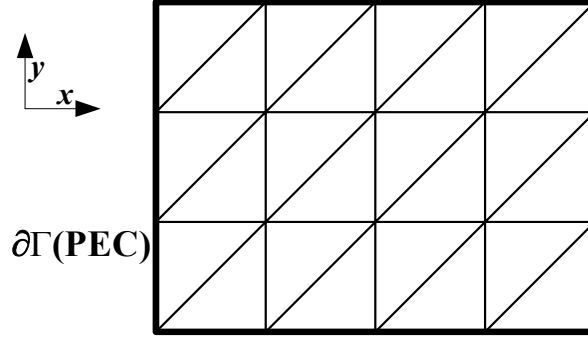


Figure 2.1 Discretization of a rectangular cavity

Within each element the field may be approximated by a finite linear combination of basis functions. These basis functions are known, but are weighted by the corresponding unknown coefficients. Thus, the total field of interest within  $\Gamma$  can be written as a weighted sum of all basis functions:

$$\bar{H}(x, z) \cong \sum_{n=1}^N f_n \bar{B}_n(x, z) \quad (2.31)$$

where  $\bar{B}_n(x, z)$  is a vector basis function that shall be explained in detail in the next section. These basis functions must provide tangential continuity for any set of coefficients. Equation (2.31) is substituted into equation (2.30), and the testing functions are chosen to be the same as the basis functions. The result is a system of equations that can be expressed in matrix form as

$$[A]\{f\} = k^2[B]\{f\} . \quad (2.32)$$

where  $[A]$  and  $[B]$  are  $N$  by  $N$  matrices. These matrices involve entries that may require integrals over several elements; they are normally computed in an element-by-element manner. If expressed over a single element  $\Gamma_k$  these entries have the form

$$\mathbf{A}_{mn}^k = \iint_{\Gamma_k} \left( \frac{1}{\varepsilon_r} \nabla \times \bar{T}_m \cdot \nabla \times \bar{B}_n \right) dx dz \quad (2.33)$$

$$\mathbf{B}_{mn}^k = \iint_{\Gamma_k} (\mu_r \bar{T}_m \cdot \bar{B}_n) dx dz \quad (2.34)$$

where the superscript denotes an element  $k$ .

Equation (2.32) is a generalized matrix eigenvalue equation that can be solved by standard matrix procedures for the eigenvalues and eigenvectors. These quantities are related to the resonant frequencies and resonant modes of the physical cavity structure.

For the scalar Helmholtz equations in (2.19) and (2.20), similar FEM matrix equations can be derived with corresponding matrix entries of the form

$$\mathbf{A}_{mn}^k = \iint_{\Gamma_k} \left( \frac{1}{\varepsilon_r} \nabla T_m \cdot \nabla B_n \right) dx dz \quad (2.35)$$

and

$$\mathbf{B}_{mn}^k = \iint_{\Gamma_k} (\mu_r T_m B_n) dx dz . \quad (2.36)$$

While these will not be used in the present work, we include them here for completeness.

## 2.4. Parallel-Plate Waveguide Problem

A section of source-free two-dimensional parallel plate waveguide (PPWG) is shown in Figure 2.2. The infinity long PPWG structure must be truncated at the input and output ports, denoted  $\partial\Gamma_1$  and  $\partial\Gamma_2$ , respectively, surrounding the region of interest. This section focuses on the boundary term in equation (2.28) since the other parts of the weak



equation are exactly the same as previously discussed for the rectangular cavity problem.

The weak form of the vector equation in terms of the magnetic field is rewritten for convenience:

$$\iint_{\Gamma} [(\nabla \times \bar{T}) \cdot (\frac{1}{\epsilon_r} \nabla \times \bar{H}) - \bar{T} \cdot k^2 \mu_r \bar{H}] dx dz = \int_{\partial\Gamma} (\bar{T} \times \frac{1}{\epsilon_r} \nabla \times \bar{H}) \cdot \hat{n} dt \quad (2.37)$$

The boundary  $\partial\Gamma$  is the contour surrounding the interior region  $\Gamma$  and its outward normal vector is  $\hat{n}$ .

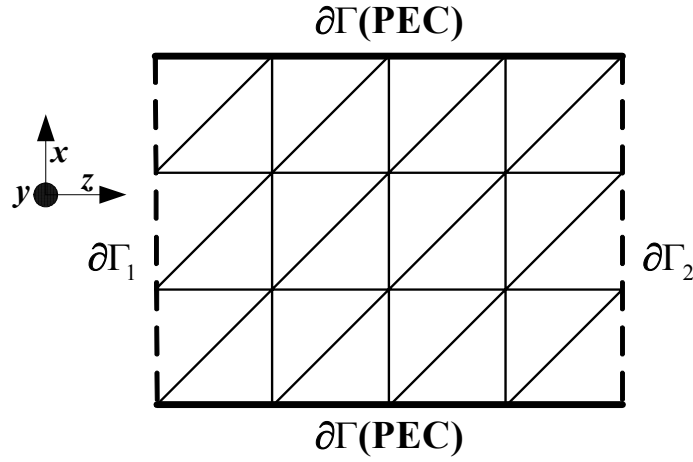


Figure 2.2 Discretization of parallel-plate waveguide

The boundary consists of three parts, the input port  $\partial\Gamma_1$ , the output port  $\partial\Gamma_2$ , and the PEC walls that will be denoted by  $\partial\Gamma$ . After imposing boundary conditions, the equation simplifies to

$$\begin{aligned} & \iint_{\Gamma} [(\nabla \times \bar{T}) \cdot (\frac{1}{\epsilon_r} \nabla \times \bar{H}) - \bar{T} \cdot k^2 \mu_r \bar{H}] dx dz \\ &= - \int_{\partial\Gamma_1} (\bar{T} \cdot \hat{n} \times \frac{1}{\epsilon_r} \nabla \times \bar{H}) dt - \int_{\partial\Gamma_2} (\bar{T} \cdot \hat{n} \times \frac{1}{\epsilon_r} \nabla \times \bar{H}) dt \end{aligned} \quad (2.38)$$

where we have used  $\bar{T} \times \nabla \times \bar{H} \cdot \hat{n} = -\bar{T} \cdot \hat{n} \times \nabla \times \bar{H}$ , and  $\hat{n} \times \nabla \times \bar{H} = j\omega\epsilon\hat{n} \times \bar{E} = 0$  on PEC walls. To define the boundary-value problem uniquely for the area  $\Gamma$  bounded by  $\partial\Gamma_1, \partial\Gamma_2$  and the waveguide walls, it is necessary to prescribe a boundary condition for each of  $\partial\Gamma_1$  and  $\partial\Gamma_2$ .

#### 2.4.1. Absorbing boundary condition along Output Port $\partial\Gamma_2$

First, consider the output port, which must support a transmitted wave passing through in the  $+\hat{z}$  direction. This wave has the general form

$$E_y^t(x, z) = \sum_{n=1}^{\infty} e_n^t \sin\left(\frac{n\pi x}{d}\right) e^{-j\beta_n z} \quad (2.39)$$

where  $e_n^t$  denotes a field amplitude of the  $n$ -th mode and

$$\beta_n = \sqrt{k^2 - \left(\frac{n\pi}{d}\right)^2}. \quad (2.40)$$

The magnetic field associated with (2.39) is obtained from

$$\begin{aligned} \bar{H} &= H_x \hat{x} + H_z \hat{z} = \frac{1}{j\omega\mu} \left[ \hat{x} \left( \frac{\partial E_y}{\partial z} \right) - \hat{z} \left( \frac{\partial E_y}{\partial x} \right) \right] \\ &= \frac{1}{j\omega\mu} \left[ \sum_{n=1}^{\infty} (-j\beta_n) e_n^t \sin\left(\frac{n\pi x}{d}\right) e^{-j\beta_n z} \right] \hat{x} - \frac{1}{j\omega\mu} \left[ \sum_{n=1}^{\infty} \left(\frac{n\pi}{d}\right) e_n^t \cos\left(\frac{n\pi x}{d}\right) e^{-j\beta_n z} \right] \hat{z} \end{aligned} \quad (2.41)$$

where use has been made of  $\bar{H} = \frac{-\nabla \times \bar{E}}{j\omega\mu}$ . In addition, the boundary term can be

simplified according to

$$\hat{n} \times \frac{1}{\epsilon_r} \nabla \times \bar{H} \Big|_{z=z_2} = \hat{z} \times \frac{1}{\epsilon_r} (-\hat{y}) \left[ \frac{\partial H_z}{\partial x} - \frac{\partial H_x}{\partial z} \right] = \hat{x} \frac{1}{\epsilon_r} \left[ \frac{\partial H_z}{\partial x} - \frac{\partial H_x}{\partial z} \right]$$

$$= \hat{x} \frac{1}{\epsilon_r} \frac{1}{j\omega\mu} \sum_{n=1}^{\infty} [(\frac{n\pi}{d})^2 + \beta_n^2] e_n^t \sin(\frac{n\pi x}{d}) e^{-j\beta_n z_2} . \quad (2.42)$$

where the unit normal to the output port,  $\hat{n}$ , is  $+\hat{z}$  in Cartesian coordinates. The coefficients can be expressed in terms of the field as

$$e_n^t = (\frac{-2\omega\mu}{\beta_n d}) e^{j\beta_n z_2} \int_0^d H_x(x, z_2) \sin(\frac{n\pi x}{d}) dx \quad (2.43)$$

Substituting (2.43) into (2.42) yields

$$\begin{aligned} \hat{z} \times \frac{1}{\epsilon_r} \nabla \times \bar{H} \Big|_{z=z_2} &= \hat{x} \frac{2}{\epsilon_r d} \int_0^d \{ H_x(x', z_2) \sum_{n=1}^{\infty} \frac{j}{\beta_n} [(\frac{n\pi}{d})^2 + \beta_n^2] \sin(\frac{n\pi x'}{d}) \sin(\frac{n\pi x}{d}) \} dx' \\ &= \hat{x} \frac{2}{\epsilon_r d} \int_0^d H_x(x', z_2) G(x, x') dx' \end{aligned} \quad (2.44)$$

where

$$\begin{aligned} G(x, x') &= \sum_{n=1}^{\infty} \frac{j}{\beta_n} [(\frac{n\pi}{d})^2 + \beta_n^2] \sin(\frac{n\pi x'}{d}) \sin(\frac{n\pi x}{d}) \\ &= \sum_{n=1}^{\infty} \frac{jk^2}{\beta_n} \sin(\frac{n\pi x'}{d}) \sin(\frac{n\pi x}{d}) \end{aligned} \quad (2.45)$$

Equation (2.44) can be used as an absorbing boundary condition on  $\partial\Gamma_2$ .

#### 2.4.2. Absorbing boundary condition along Input Port $\partial\Gamma_1$

Since it is assumed that the excitation of the waveguide is left-to-right in Figure 2.2, the field on  $\partial\Gamma_1$  will generally consist of an incident field and a reflected field. First, consider the reflected field. The reflected wave propagates in the  $-\hat{z}$  direction and is denoted by

$$E_y^{ref}(x, z) = \sum_{n=1}^{\infty} e_n^{ref} \sin\left(\frac{n\pi x}{d}\right) e^{+j\beta_n z} \quad (2.46)$$

Following the same procedure leading to equation (2.44),

$$\begin{aligned} & -\hat{z} \times \frac{1}{\varepsilon_r} \nabla \times \bar{H}^{ref} \Big|_{z=z_1} \\ &= \hat{x} \frac{2}{\varepsilon_r d} \int_0^d \{ H_x^{ref}(x', z_1) \sum_{n=1}^{\infty} \frac{j}{\beta_n} [(\frac{n\pi}{d})^2 + \beta_n^2] \sin(\frac{n\pi x'}{d}) \sin(\frac{n\pi x}{d}) \} dx' \\ &= \hat{x} \frac{2}{\varepsilon_r d} \int_0^d H_x^{ref}(x', z_1) G(x, x') dx' \end{aligned} \quad (2.47)$$

where  $G(x, x')$  is given in (2.45).

Now, consider the incident field on  $\partial\Gamma_1$ , which has the form

$$E_y^{inc}(x, z) = \sum_{n=1}^{\infty} e_n^{inc} \sin\left(\frac{n\pi x}{d}\right) e^{-j\beta_n z} \quad (2.48)$$

Through the same procedure described above, we obtain

$$\begin{aligned} & -\hat{z} \times \frac{1}{\varepsilon_r} \nabla \times \bar{H}^{inc} \Big|_{z=z_1} \\ &= \hat{x} \frac{-2}{\varepsilon_r d} \int_0^d \{ H_x^{inc}(x', z_1) \sum_{n=1}^{\infty} \frac{j}{\beta_n} [(\frac{n\pi}{d})^2 + \beta_n^2] \sin(\frac{n\pi x'}{d}) \sin(\frac{n\pi x}{d}) \} dx' \\ &= \hat{x} \frac{-2}{\varepsilon_r d} \int_0^d H_x^{inc}(x', z_1) G(x, x') dx' \end{aligned} \quad (2.49)$$

where  $G(x, x')$  is given in (2.45).

An ABC in terms of the total field on  $\partial\Gamma_1$  is obtained by combining equations (2.47) and (2.49). The first term on the right hand side of equation (2.38) can be written as

$$\begin{aligned}\hat{n} \times \frac{1}{\varepsilon_r} \nabla \times \bar{H} &= \hat{n} \times \frac{1}{\varepsilon_r} \nabla \times (\bar{H}^{inc} + \bar{H}^{ref}) \\ &= (-\hat{z}) \times \frac{1}{\varepsilon_r} \nabla \times (\bar{H}^{inc} + \bar{H}^{ref}) \text{ on } \partial\Gamma_1\end{aligned}\quad (2.50)$$

After substituting equations (2.47) and (2.49) into equation (2.50), we obtain

$$\begin{aligned}\hat{n} \times \frac{1}{\varepsilon_r} \nabla \times \bar{H} &= \hat{x} \frac{2}{d\varepsilon_r} \int_0^d (H_x^{ref} - H_x^{inc}) G(x, x') dx' \\ &= \hat{x} \frac{2}{d\varepsilon_r} \int_0^d (H_x - 2H_x^{inc}) G(x, x') dx' \\ &= \hat{x} \frac{2}{d\varepsilon_r} \int_0^d H_x^{tot}(x, z) G(x, x') dx' - \hat{x} \frac{4}{d\varepsilon_r} \int_0^d H_x^{inc}(x, z) G(x, x') dx'\end{aligned}\quad (2.51)$$

where  $G(x, x')$  is given in (2.45). Equation (2.51) is the ABC we will use along  $\partial\Gamma_1$ .

#### 2.4.3. Derivation of the matrix equation

The weak equation for a parallel plate waveguide with TM-to-y excitation and ABCs at the input and output ports is given by

$$\begin{aligned}&\iint_{\Gamma} \left( \frac{1}{\varepsilon_r} \nabla \times \bar{T} \cdot \nabla \times \bar{H} - k^2 \mu_r \bar{T} \cdot \bar{H} \right) dx dz + \frac{2}{d} \int_{\partial\Gamma_1} \left( \frac{1}{\varepsilon_r} \bar{T} \cdot \hat{x} \int_0^d H_x(x', z_1) G(x, x') dx' \right) dt \\ &+ \frac{2}{d} \int_{\partial\Gamma_2} \left( \frac{1}{\varepsilon_r} \bar{T} \cdot \hat{x} \int_0^d H_x(x', z_2) G(x, x') dx' \right) dt\end{aligned}$$

$$= \frac{4}{d} \int_{\partial\Gamma_1} \left( \frac{1}{\varepsilon_r} \bar{T} \cdot \hat{x} \int_0^d H_x^{inc}(x', z_1) G(x, x') dx' \right) dt \quad (2.52)$$

Equation (2.52) is derived by replacing the boundary terms in equation (2.38) with the new expressions from equations (2.44) and (2.51).

Suppose that the computation domain is discretized into many small triangular cells. The vector expansion functions are defined in conjunction with the cellular model of the domain. Consider the use of curl conforming vector basis functions  $\{\bar{B}_n\}$ , which have a constant tangential and linear normal (CT/LN) vector behavior, and impose tangential-vector continuity between cells. Each basis function straddles two cells, except for those that reside along boundaries  $\partial\Gamma_1$  and  $\partial\Gamma_2$ , which only occupy one cell and have a large tangential component along the boundary. The magnetic field is approximated as follows

$$\bar{H}(x, z) \cong \sum_{n=1}^N h_n \bar{B}_n(x, z).$$

We use the same vector functions as test functions.

The resulting system equation is a deterministic linear matrix equation of the form  $[\mathbf{A}]\{\mathbf{h}\} = \{\mathbf{g}\}$ . The entries of  $\mathbf{A}$  have the form

$$A_{mn} = I_{mn} + B_{mn}^{(1)} + B_{mn}^{(2)}$$

where

$$I_{mn} = \iint_{\Gamma} \left\{ \frac{1}{\varepsilon_r} \nabla \times \bar{T}_m \cdot \nabla \times \bar{B}_n - k^2 \mu_r \bar{T}_m \cdot \bar{B}_n \right\} dx dz \quad (2.53)$$

$$B_{mn}^{(1)} = \frac{2}{d} \int_{\partial\Gamma_1} \left\{ \frac{1}{\varepsilon_r} \bar{T}_m \cdot \hat{x} \int_0^d \bar{B}_{n,x}(x', z_1) G(x, x') dx' \right\} dt \quad (2.54)$$

$$B_{mn}^{(2)} = \frac{2}{d} \int_{\partial\Gamma_2} \left\{ \frac{1}{\varepsilon_r} \bar{T}_m \cdot \hat{x} \int_0^d \bar{B}_{n,x}(x', z_2) G(x, x') dx' \right\} dt \quad (2.55)$$

The entries of the excitation vector have the form

$$g_m = \frac{4}{d} \int_{\partial\Gamma_1} \left\{ \frac{1}{\varepsilon_r} \bar{T}_m \cdot \hat{x} \int_0^d H_x^{inc}(x', z_1) G(x, x') dx' \right\} dt. \quad (2.56)$$

The boundary integrals in (2.54) and (2.55) are only nonzero when both  $\bar{T}_m(x)$  and  $\bar{B}_n(x)$  are functions located on the same boundary. For the waveguide geometry, they are functions of  $x$ .

## 2.5 Summary

This chapter reviewed the derivation of the two-dimensional vector Helmholtz equations and specialized them to the problems of a resonant cavity and a parallel-plate waveguide. Expressions for the vector FEM matrix entries, in terms of vector basis and test functions, were developed. These basis functions will be described in Chapter 3.

### **CHAPTER 3: SCALAR AND VECTOR FINITE ELEMENTS**

In the FEM approach, the computational domain is divided into a mesh of electrically small elements. Basis functions are defined in conjunction with the FEM mesh to approximate the unknown function. Each basis function usually straddles several elements and vanishes outside of a small group of contiguous elements. The procedure results in a sparse system of equations that facilitates an efficient matrix solution and minimizes memory resources. In general, two general types of basis functions exist for electromagnetics. One is the classical scalar or node-based basis family that has been used with finite elements since the 1950s. The other is the vector or edge-based type of basis function, introduced in the 1980s.

Node-based elements have been widely used for numerical solutions of the Laplace's equation and the scalar wave equation. However, these traditional basis functions do not work well when used with the three-dimensional vector Helmholtz equation. Edge-based vector basis functions were proposed to overcome some of the difficulties that arose in connection with the vector Helmholtz equation [1,3,10-25]. This chapter discusses both scalar basis functions and vector basis functions for triangular cells, which reasonably model the irregular geometries in two-dimensional problems.



### 3.1. Scalar Basis Functions

In a node-based finite element analysis, the unknown function is approximated by a combination of interpolatory scalar Lagrangian basis functions [1,3,23]. The global representation for the function can be obtained in the form

$$u(x, y) = \sum_{i=1}^N u_i B_i(x, y) \quad (3.1)$$

where the coefficients  $\{u_i\}$  represent the function values at the nodes and each basis function  $B_i(x, y)$  must be unity at node  $i$  and zero at all other nodes within the mesh. If a single triangular element (Figure 3.1) is considered, a number of basis functions are nonzero within that element depending on the polynomial degree of the expansion.

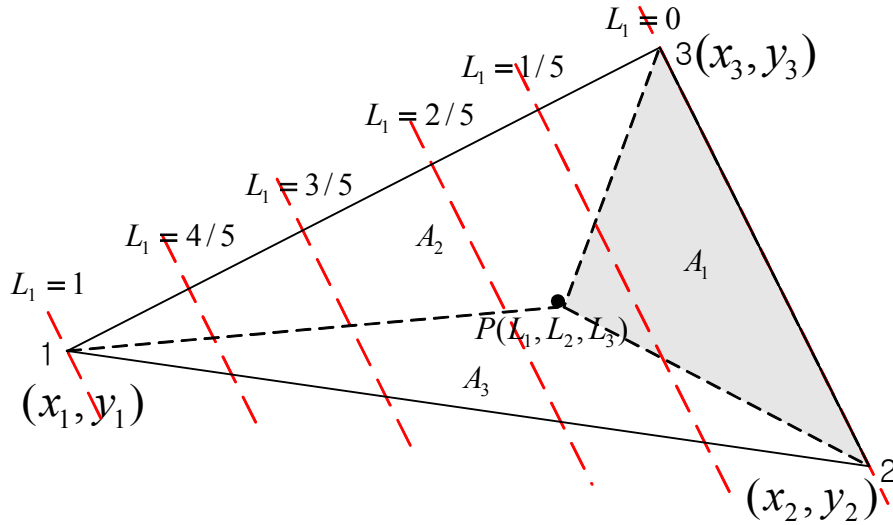


Figure 3.1 Simplex coordinate of a triangular element

For a general way of constructing basis functions of any order, a point  $P(x, y)$  within a triangular element can be expressed in terms of simplex coordinates  $(L_1, L_2, L_3)$  that are defined by

$$x = L_1x_1 + L_2x_2 + L_3x_3 \quad (3.2)$$

$$y = L_1y_1 + L_2y_2 + L_3y_3 \quad (3.3)$$

where

$$L_1 + L_2 + L_3 = 1 \quad (3.4)$$

$$L_1, L_2, L_3 \geq 0 \quad (3.5)$$

As illustrated in Figure 3.1, the simplex coordinate  $L_i$  is zero on the side opposite to the vertex  $i$ .

Basis functions can be defined in terms of polynomial functions of the simplex coordinates, using the polynomial functions

$$R_s(\mathbf{M}, L) = \frac{1}{s!} \prod_{k=0}^{s-1} (\mathbf{M}L - k) \quad (3.6)$$

$$R_0(\mathbf{M}, L) = 1. \quad (3.7)$$

The  $M$ -th order Lagrangian scalar basis functions are defined in terms of simplex coordinates as

$$B_{ijk}(L_1, L_2, L_3) = R_i(\mathbf{M}, L_1)R_j(\mathbf{M}, L_2)R_k(\mathbf{M}, L_3) \quad (3.8)$$

where a triple index  $ijk$  is employed to denote the interpolation point of a specific basis function, and where  $k = \mathbf{M} - i - j$ . The basis function  $B_{ijk}$  interpolates to 1 at point

$(L_1, L_2, L_3) = \left( \frac{i}{M}, \frac{j}{M}, \frac{k}{M} \right)$  and is exactly zero at the other interpolation points. Figure 3.2

shows the interpolation points for  $M = 3$ . Within an element, the representation of the unknown function is written in terms of these basis functions as

$$u_M(x, y) = \sum_{i=0}^M \sum_{j=0}^{M-i} \alpha_{ijk} B_{ijk}(L_1, L_2, L_3) \quad (3.9)$$

where the  $\{\alpha_{ijk}\}$  are the coefficients to be determined by the FEM procedure.

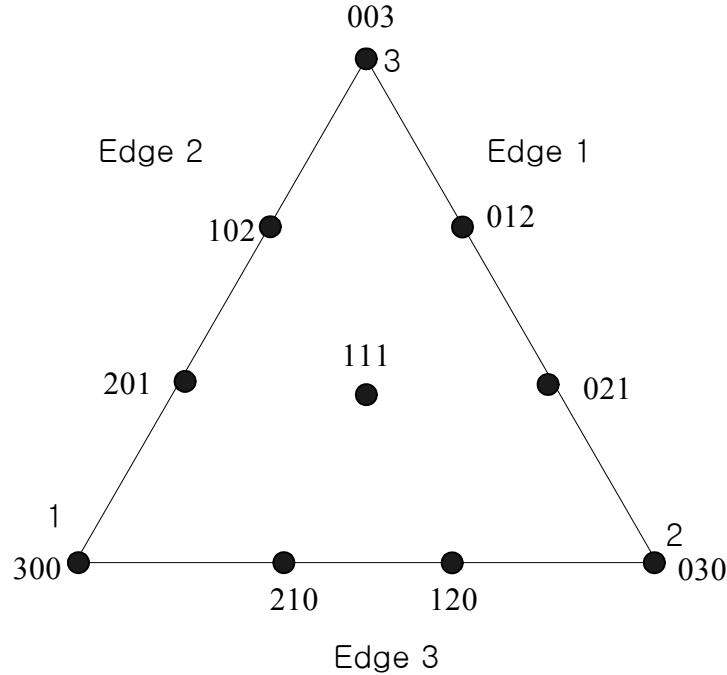


Figure 3.2 Interpolation points of  $B_{ijk}$ ,  $M=3$

While node-based Lagrangian basis functions work well for representing scalar quantities in electromagnetics, serious problems sometimes occur when they are employed to represent vector electric or magnetic fields [27]. Usually, when this has been attempted,

each Cartesian component of the vector quantity of interest is represented by an independent expansion of the form of (3.1) or (3.9). The Lagrangian functions are continuous across cell boundaries, meaning that the tangential and the normal vector components are also forced to be continuous across the cell boundaries. Unfortunately, this behavior fails to represent the proper field discontinuity at the interface of two different materials. The second difficulty lies in the fact that the Cartesian components of the vector quantity are seldom aligned with the tangential or normal directions at a physical boundary, such as the surface of a conductor. In general, vector Dirichlet or Neumann boundary conditions are imposed on either tangential or normal components of electromagnetic fields along a boundary. It becomes more difficult to impose boundary conditions when Cartesian components are in use, since the boundary conditions act as a constraint between several coefficients in (3.1) instead of an independent constraint on one coefficient. Third, grossly inaccurate solutions (spurious modes) are sometimes obtained from node-based discretizations of the vector Helmholtz equation. Spurious modes are believed to be associated with inaccurate representations of eigenfunctions within the null space of the vector Helmholtz operator.

Edge-based vector basis functions have been developed to address the above concerns when analyzing the vector Helmholtz equation with the FEM [15,27]. The following section reviews these edge-based elements.

### 3.2. Vector Basis Functions

Several of the difficulties associated with the use of node-based scalar basis functions to represent a vector quantity stem from the use of the Cartesian components of the vector function. Vector basis functions provide a representation that is independent of Cartesian components, but is tied locally to tangential and normal vector components at cell boundaries. Vector expansions of this type therefore make it easier to impose appropriate boundary and continuity conditions at cell interfaces.

Vector basis functions associate their degrees of freedom with the edges and the faces of the cells within the finite element mesh. The type of function that maintains tangential continuity along the common edges between abutting elements is known as a curl-conforming, edge, or tangential vector basis function. Functions of this type were first proposed for triangular cells by Whitney [10]. Nedgelec generalized the concept and provided a methodology for constructing higher-order vector basis functions of this type [11,12].

#### 3.2.1 Zeroth-Order Vector Basis Functions for Triangles

The simplest edge elements were described by Whitney [10]. On the boundaries of a triangular cell, these elements have polynomial degree zero (constant) in the tangential direction but degree one (linear) in the normal direction. For a triangular element it is difficult to visualize the form of the vector basis by intuition since the edges of an arbitrary

triangular element are not in alignment with the  $x$ - or  $y$ -axis. Therefore, let us consider the use of simplex coordinates,  $(L_1, L_2, L_3)$ , described in Section 3.1.

Within a triangular cell (Figure 3.3), the general form of a Whitney element is

$$\overline{\Omega}_0^n = L_{n+1} \nabla L_{n-1} - L_{n-1} \nabla L_{n+1} \quad (3.10)$$

where  $n = 1, 2$ , or  $3$  indicates the edge number and the index is assumed to be modulo three (in other words, when  $n = 3$  the subscript  $n+1$  is taken to be 1); the subscript 0 indicates the order of that basis function.

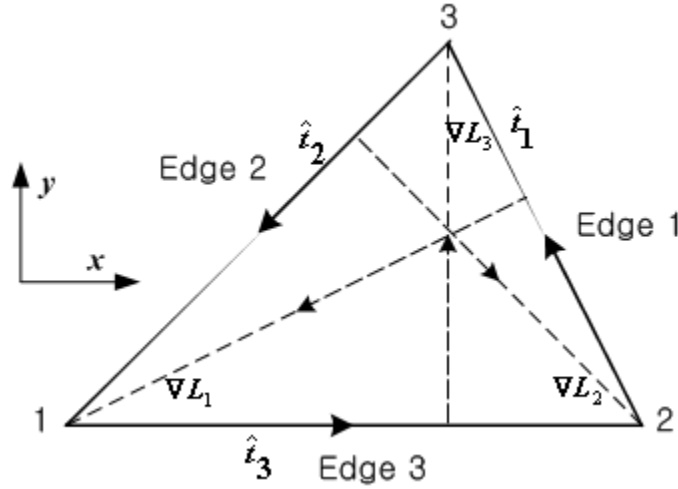


Figure 3.3 Triangular edge element

The zeroth-order edge basis functions defined in Equation (3.10) have the following divergence within the element:

$$\begin{aligned} \nabla \cdot \overline{\Omega}_0^n &= \nabla \cdot (L_{n+1} \nabla L_{n-1} - L_{n-1} \nabla L_{n+1}) \\ &= L_{n+1} \nabla \cdot \nabla L_{n-1} - L_{n-1} \nabla \cdot \nabla L_{n+1} = 0 \end{aligned} \quad (3.11)$$

They appear ideal for representing vector electromagnetic fields in a source-free region, since those fields exhibit zero divergence. However, the divergence is actually nonzero at cell boundaries, where it assumes the form of a Dirac delta function. The curl of the basis functions is given by

$$\begin{aligned}\nabla \times \overline{\Omega}_0^n &= \nabla \times (L_{n+1} \nabla L_{n-1} - L_{n-1} \nabla L_{n+1}) \\ &= \nabla \times (L_{n+1} \nabla L_{n-1}) - \nabla \times (L_{n-1} \nabla L_{n+1}) = 2 \nabla L_{n+1} \times \nabla L_{n-1}\end{aligned}\quad (3.12)$$

Thus, the curl of these edge basis functions is constant. It is noteworthy that the basis functions defined in equation (3.10) and their curls are complete to the same polynomial degree: zero or constant.

Suppose  $\hat{t}_n$  is a unit-tangential vector along edge  $n$  as defined in Figure 3.3. The unit tangential vectors and the simplex coordinates are related as follows:

$$\hat{t}_n \cdot \nabla L_{n+1} = -\frac{1}{\ell_n} \quad (3.13)$$

$$\hat{t}_n \cdot \nabla L_{n-1} = \frac{1}{\ell_n} \quad (3.14)$$

since  $L_{n+1}$  is a linear function that varies from 0 at node  $(n-1)$  to 1 at node  $(n+1)$ , and  $\hat{t}_n$  is directed from node  $(n-1)$  to node  $(n+1)$  with unit amplitude. Therefore,

$$\overline{\Omega}_0^n \cdot \hat{t}_n = \frac{(L_{n+1} + L_{n-1})}{\ell_n} = \frac{1}{\ell_n} \quad (3.15)$$

which means  $\overline{\Omega}_0^n$  has a constant tangential component along edge  $n$ . It also follows that

$$\overline{\Omega}_0^n \cdot \hat{t}_{n+1} = 0 \quad (3.16)$$

since  $L_{n+1}$  vanishes at edge  $(n+1)$  and  $\nabla L_{n+1}$  is normal to edge  $(n+1)$ , and

$$\overline{\Omega}_0^n \cdot \hat{t}_{n-1} = 0 \quad (3.17)$$

since  $L_{n-1}$  vanishes at edge  $(n-1)$  and  $\nabla L_{n-1}$  is normal to edge  $(n-1)$ . From equations (3.15), (3.16), and (3.17), we conclude that  $\overline{\Omega}_0^n$  has no tangential component along edges  $(n-1)$  and  $(n+1)$  but has a constant tangential component along edge  $n$ . In a sense, this basis function interpolates to the tangential component along edge  $n$  of the cell. This feature of edge basis functions can be used to guarantee the tangential continuity of the global representation across inter-element boundaries as long as expansion coefficients in the two adjacent elements are equal. However, these basis functions do not have enough degrees of freedom to guarantee normal continuity. Figure 3.4 shows the actual variation of  $\overline{\Omega}_0^1$  within the cell.

Within a cell, the vector field can be expanded as

$$\overline{E} = \sum_{n=1}^3 E_n \overline{N}_n^0 \quad (3.18)$$

where  $\{E_n\}$  are the coefficients of the basis functions,

$$\overline{N}_n^0 = \ell_n \overline{\Omega}_n^0 \quad (3.19)$$

and where  $\ell_n$  is the length of edge  $n$  of the element. The global form of the expansion is similar, with the tangential continuity imposed between cells and most of the basis functions effectively straddling the two cells adjacent to the interpolatory edge.



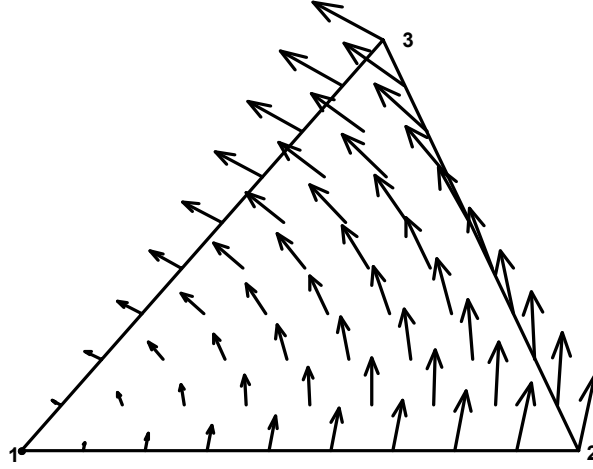


Figure 3.4 Zeroth-order curl conforming function of  $\overline{\Omega}_0^1 = L_2 \nabla L_3 - L_3 \nabla L_2$

Observe that the Whitney type of basis function is mixed-order, with one lower polynomial degree along the primary vector direction of the function than in the perpendicular direction. It is also possible to define vector basis functions that are complete to a consistent polynomial degree. (Such functions involve six degrees of freedom within a triangle instead of three.) However, when using basis functions within an FEM analysis of the vector Helmholtz equation, the extra degrees of freedom within a consistently linear representation appear to be wasted (at least in source-free regions). It appears that, because of the curl operator within the vector Helmholtz equation, it is most efficient to employ basis functions that are complete to the same degree as their curl. Additional degrees of freedom that do not contribute to the curl of the basis functions are not balanced within the FEM system of equations and do not contribute to a more accurate

solution. Furthermore, when analyzing vector cavity problems, the use of polynomial-complete basis functions results in additional nullspace eigensolutions and no new physical eigensolutions, compared to a mixed-order representation [3]. Consequently, for the remainder of this study, only the mixed-order vector basis functions of the spaces proposed by Nedelec [11] are considered.

Even though Whitney edge elements remove the difficulties caused by nodal elements, they are low-order polynomials and therefore the FEM solutions exhibit relatively large errors unless the cells within the mesh are very small. The rate at which the solution accuracy improves as the average cell size is reduced is often referred to as the *convergence rate*. The slow convergence rate associated with the zeroth-order elements can be improved by making use of higher-order vector elements. Two different types of higher-order edge elements, interpolatory and hierarchical vector basis functions, can be constructed based upon the Whitney zeroth-order vector basis functions and span the same vector spaces. The major difference between these higher-order vector elements lies in their construction.

The interpolatory vector basis functions are defined on a set of points within the element. Since each vector basis has its primary value at an interpolation point, the set usually exhibits good linear independence. Their coefficients have a physical meaning as the tangential components of the field at the interpolation points. Their definition also makes it easy to impose boundary conditions. The systematic construction of interpolatory

vector basis functions is described in [19]. Despite these advantages, interpolatory basis functions of a given order are all different from those of the lower-order. Hence, different order basis functions can't be employed together within the same element, which hinders their use within a p-adaptive algorithm.

For hierarchical basis functions, the higher-order functions are superimposed upon the lower-order functions. Since computations that have been performed for lower-order basis functions do not need to be repeated, they permit a more efficient p-adaptive algorithm. In this study, hierarchical vector basis functions are considered.

### ***3.2.2 Higher-Order Hierarchical Vector Basis Functions***

A set of edge-based basis functions is referred to as hierarchical if the vector basis functions of order  $n$  are a subset of the vector basis functions of order  $n+1$ . Unlike zeroth-order edge elements, higher-order vector basis functions are not uniquely specified [13,14,16,18,20]. In this section, a set of non-hierarchical vector basis functions and another set of hierarchical vector basis functions are compared to clarify the concept of hierarchical basis functions. The hierarchical concept is explained using easily understandable scalar one-dimensional functions. Two sets of basis function that represent a linear tangential/quadratic normal (LT/QN) field along element edges and a quadratic field inside the element are compared to clarify the concept of hierarchical vector basis functions.

### **Illustration of one-dimensional scalar hierarchical basis functions**

Figure 3.5 depicts the hierarchical principle for one-dimensional scalar basis functions. Piecewise-constant and piecewise-linear approximations of a scalar quantity, over a straight segment, are considered. The representation of a constant function is unique, and is easily obtained by multiplying a constant basis function of unit amplitude by the appropriate coefficient, as shown in Figure 3.5 (a). However, there are two different ways to express a piecewise-linear function, as illustrated in Figure 3.5 (b) and Figure 3.5 (c). A superposition of two linear basis functions, one with linear variation from 0 to 1 and the second with linear variation from 1 to 0, can be used to obtain a general linear function over the interval. Those functions are actually interpolatory and use the values of the target function at the endpoints of the interval as their coefficients. An equivalent hierarchical representation can be obtained by a superposition of the constant basis function and a second basis function varying linearly from 1 to  $-1$ . The coefficient of the constant basis function is the average value of the linear function on the left side of Figure 3.5 (c),  $(A+B)/2$ . (If the constant basis function is used alone to approximate the target function, this would also be its coefficient.) The linear basis function has an average value of zero and does not interfere with the approximation already provided by the constant function. If the linear function is assigned a coefficient of  $(A-B)/2$ , the representation is exact. From this illustration, the physical meaning of the coefficients should be clear. For the interpolatory case, the coefficients are the values at both ends of the interval, whereas in the hierarchical basis case, they represent the average value and the first derivative over the interval.

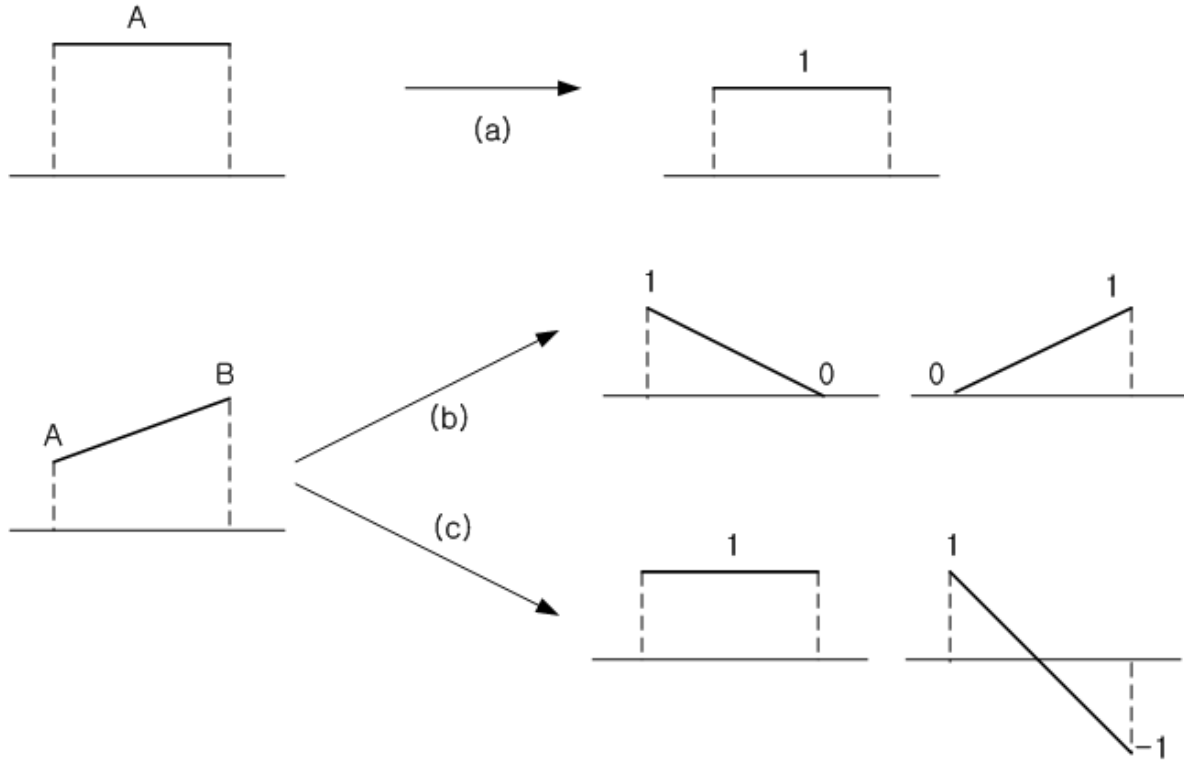


Figure 3.5 An illustration of basis functions for piecewise-constant and piecewise-linear approximations of a scalar quantity over a one-dimensional segment

### **Mixed-order non-hierarchical vector basis functions**

A set of non-hierarchical LT/QN vector basis functions proposed by Peterson consists of the following functions:

$$L_n \nabla L_{n+1} \quad (3.20)$$

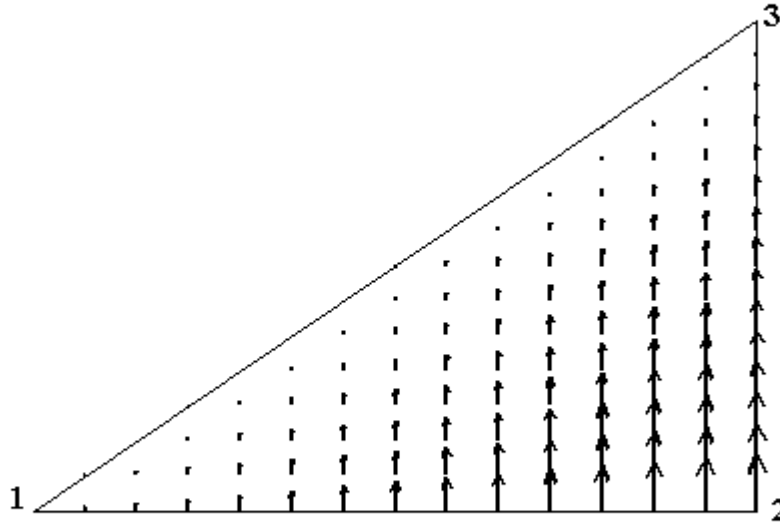
$$L_{n+1} \nabla L_n \quad (3.21)$$

$$L_3 (L_1 \nabla L_2 - L_2 \nabla L_1) \quad (3.22)$$

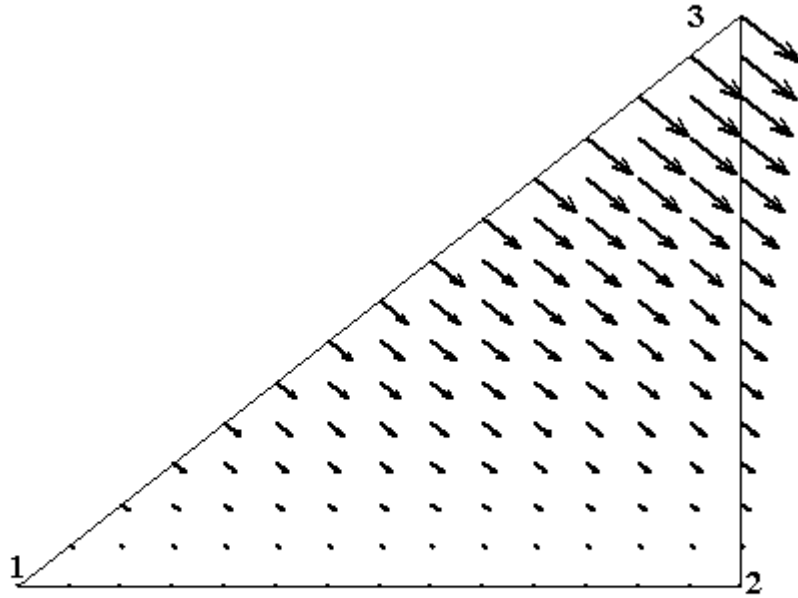
$$L_1 (L_2 \nabla L_3 - L_3 \nabla L_2) \quad (3.23)$$

where equations (3.20) to (3.21) are edge-based functions that provide nonzero tangential components along the cell edges, while equations (3.22) and (3.23) are face-based basis functions that do not contribute to a tangential component on the cell edges. The vector basis functions  $L_n \nabla L_{n+1}$  and  $L_{n+1} \nabla L_n$  have a linear tangential behavior on edge  $(n-1)$  with node  $n$  and node  $n+1$  as end points. Two functions related to edge 1 and one face basis function are shown in Figure 3.6. Figure 3.6 (a) and 3.6 (b) show the linear variation of the tangential component on first edge; on the other two edges, their tangential components vanish. These specific functions, when superimposed, have a linear varying normal component along all three edges.

The quadratic vector basis functions in equations (3.22) and (3.23) are added to the set to provide a complete linear representation of the curl of the field being expanded. By assigning two tangential field values at edge end points to each edge and two local unknowns per element, an LT/QN field along all edges and a quadratic variation within the element are obtained. The resulting representation is equivalent to the mixed-order Nedelec space of minimum polynomial degree 1 [11].

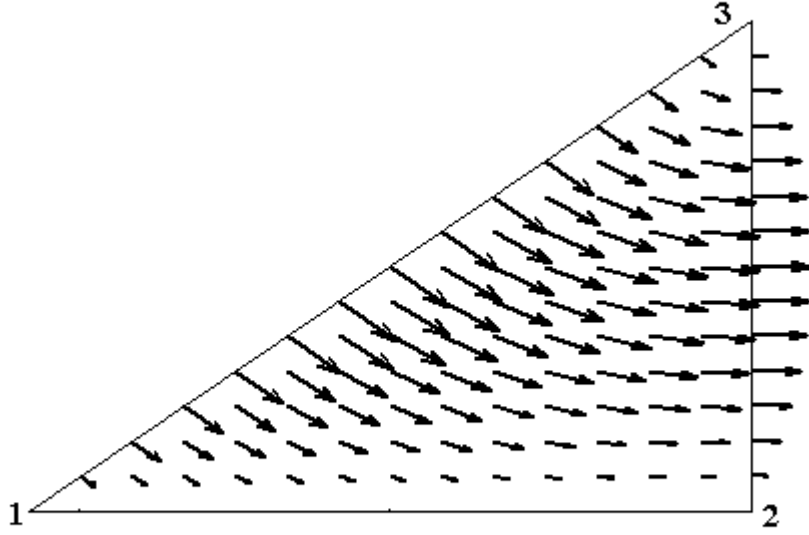


(a) First-order vector basis:  $\overline{\Omega}_1^1 = L_2 \nabla L_3$



(b) First-order vector basis:  $\overline{\Omega}_1^1 = L_3 \nabla L_2$

Figure 3.6 Non-hierarchical vector basis functions [17]



(c) Face vector basis:  $\bar{\Omega}_{1/2}^1 = L_3(L_1\nabla L_2 - L_2\nabla L_1)$

Figure 3.6 Continued

### **Mixed-order hierarchical vector basis functions**

A set of hierarchical vector basis functions proposed by Preissig and Peterson [28] is shown in Table 3.1. The lower-order basis functions are similar to the other sets proposed in the literature, such as the set proposed by Webb [24]. But for the higher-order basis functions, the linear independence is enhanced by a special polynomial construction.

For LT/QN vector basis functions, eight functions up to mixed-order 1/2 should be considered. Their edge-based functions and face-based functions are separated in Table 3.1.



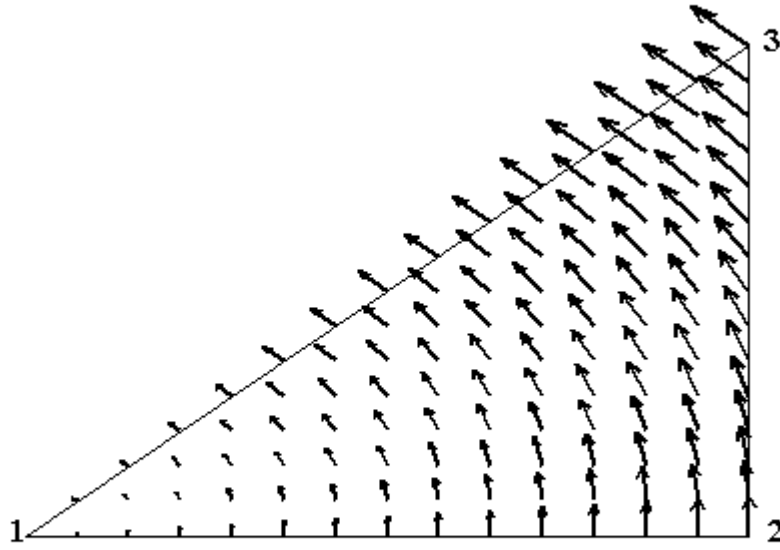
The shape of two edge-based functions related to edge 1 and one face-based function are illustrated in Figure 3.7.

Table 3.1 Hierarchical vector basis functions

Order	$\overline{\Omega}_{order}^{edge/face}(\vec{L}) = \Omega_{L_1}(\vec{L})\nabla L_1 + \Omega_{L_2}(\vec{L})\nabla L_2$	$\nabla \times \overline{\Omega} _{(L_1, L_2, L_3)}$
Mixed 0/1	$\overline{\Omega}_{0/1}^1(\vec{L}) = (-L_2)\nabla L_1 - (L_2 + L_3)\nabla L_2$	2
	$\overline{\Omega}_{0/1}^2(\vec{L}) = (L_1 + L_3)\nabla L_1 + (L_1)\nabla L_2$	2
	$\overline{\Omega}_{0/1}^3(\vec{L}) = (-L_2)\nabla L_1 + (L_1)\nabla L_2$	2
Complete 1	$\overline{\Omega}_1^1(\vec{L}) = (-L_2)\nabla L_1 + (L_3 - L_2)\nabla L_2$	0
	$\overline{\Omega}_1^2(\vec{L}) = (L_3 - L_1)\nabla L_1 + (-L_1)\nabla L_2$	0
	$\overline{\Omega}_1^3(\vec{L}) = (L_2)\nabla L_1 + (L_1)\nabla L_2$	0
Mixed $\frac{1}{2}$	$\overline{\Omega}_{1/2}^f(\vec{L}) = (-L_1 L_2)\nabla L_1 - (L_1 L_2 + L_1 L_3)\nabla L_2$	$[3L_1 - 1]$
	$\overline{\Omega}_{1/2}^f(\vec{L}) = (L_1 L_2 + L_2 L_3)\nabla L_1 + (L_1 L_2)\nabla L_2$	$[3L_2 - 1]$
Complete 2	$\overline{\Omega}_2^1(\vec{L}) = (2L_2 L_3 - L_2^2)\nabla L_1 - (L_2^2 + L_3^2 - 4L_2 L_3)\nabla L_2$	0
	$\overline{\Omega}_2^2(\vec{L}) = -(L_1^2 + L_3^2 - 4L_1 L_3)\nabla L_1 + (2L_1 L_3 - L_1^2)\nabla L_2$	0
	$\overline{\Omega}_2^3(\vec{L}) = (2L_1 L_2 - L_2^2)\nabla L_1 + (L_1^2 - 2L_1 L_2)\nabla L_2$	0
	$\overline{\Omega}_2^f(\vec{L}) = (L_2 L_3 - L_1 L_2)\nabla L_1 + (L_1 L_3 - L_1 L_2)\nabla L_2$	0
Mixed 2/3	$\overline{\Omega}_{2/3}^f(\vec{L}) = (-L_1 L_2^2)\nabla L_1 - L_1 L_2 (L_2 + L_3)\nabla L_2$	$[4L_1 L_2 - L_2]$
	$\overline{\Omega}_{2/3}^f(\vec{L}) = (-L_1 L_2 L_3)\nabla L_1 - L_1 L_3 (L_2 + L_3)\nabla L_2$	$[-L_3^2 + 3L_1 L_3 - L_2 L_3]$
	$\overline{\Omega}_{2/3}^f(\vec{L}) = L_2 L_3 (L_1 + L_3)\nabla L_1 + L_1 L_2 L_3 \nabla L_2$	$[-L_3^2 + 3L_2 L_3 - L_1 L_3]$

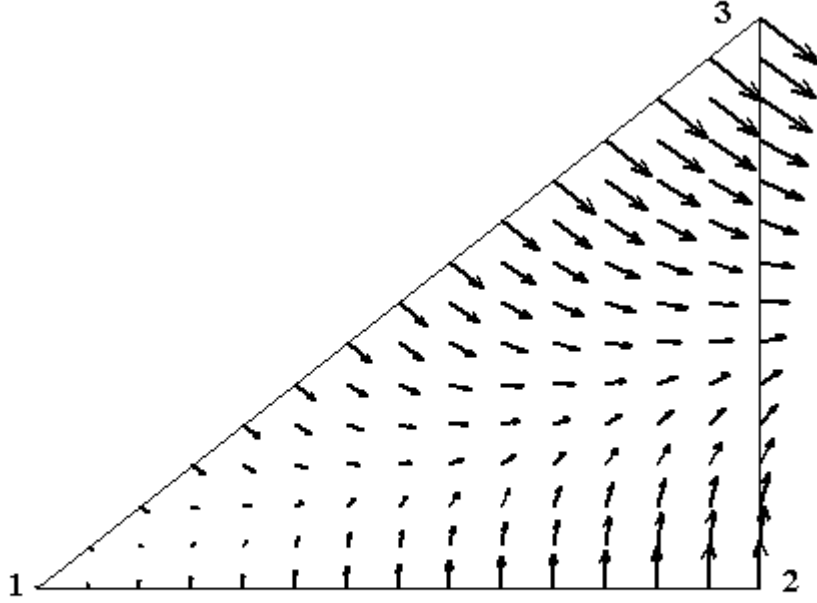
From Figure 3.7(a) and (b), these basis functions clearly provide a constant and a linearly varying tangential component along edge 1, respectively. They provide zero tangential components on the other two edges and a linear variation in normal component along all three edges. The face-based basis function,  $\overline{\Omega}_{1/2}^n = L_{n-1}(L_n \nabla L_{n+1} - L_{n+1} \nabla L_n)$ , has

no tangential component along any edges but has a quadratic variation in the normal component along edge  $n$  and edge  $n+1$ , but no normal component on edge  $n-1$ .

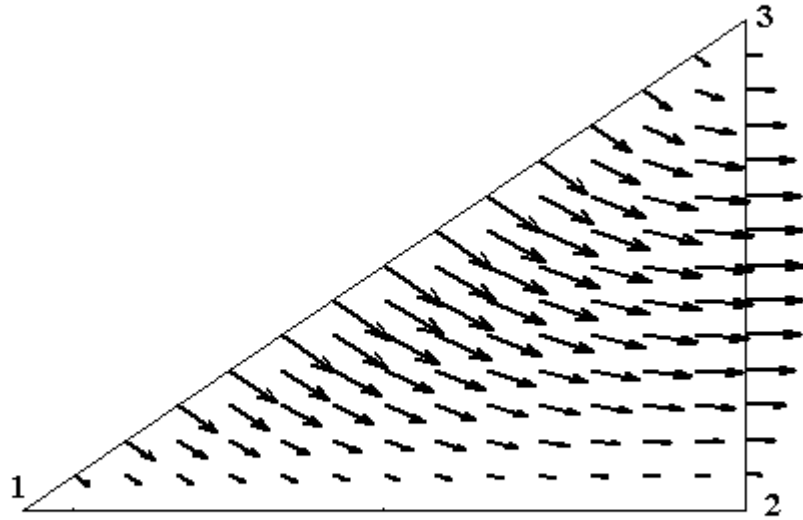


(a) First-order vector basis:  $\overline{\Omega}_0^1 = L_2 \nabla L_3 - L_3 \nabla L_2$

Figure 3.7 Hierarchical vector basis functions



(b) First-order vector basis:  $\overline{\Omega}_1^1 = L_2 \nabla L_3 + L_3 \nabla L_2$



(c) Face vector basis:  $\overline{\Omega}_{1/2}^1 = L_3 (L_1 \nabla L_2 - L_2 \nabla L_1)$

Figure 3.7 Continued

Two unknowns per edge of the mesh are assigned: the average of the tangential component of the field is assigned to the 0/1 mixed-order basis function and the derivative of the tangential component of the field is assigned to the complete 1 basis function. The edge-based functions can represent a linear tangential/linear normal (LT/LN) variation, while the face-based functions represent a quadratic variation of the field. Therefore, an overall LT/QN variation of the field is obtained by these hierarchical vector basis functions.

### **3.3. Summary**

This chapter has reviewed node-based and edge-based basis functions for representing electromagnetic fields. While node-based scalar functions have been successful for scalar equations, the literature suggests that edge-based vector functions provide a more robust formulation for the FEM solution of the vector Helmholtz equation.

Interpolatory and hierarchical functions have been described. Hierarchical functions offer some computational advantages when used with adaptive refinement procedures. The hierarchical functions of Table 3.1 will be implemented within a computer program that uses the FEM procedure to analyze the two-dimensional parallel-plate waveguide geometry introduced in Chapter 2. Chapter 4 provides some numerical results to illustrate the performance of the approach.

## CHAPTER 4: VERIFICATION OF HIERARCHICAL VECTOR FINITE ELEMENTS

In the previous chapters the basic mathematical background of the FEM and vector elements are expounded. Before error estimators are investigated, it is necessary to verify whether or not the vector FEM is correctly implemented. To this effect, the air-filled parallel plate waveguide will be analyzed using hierarchical vector elements. Two configurations, shown in Figure 4.1 and Figure 4.2, will be considered. The first is a section of unterminated waveguide that should support a pure traveling wave (T-PPWG). The second guide is short-circuited at  $z = z_2$  and should support a pure standing wave (S-PPWG). An exact analysis of T-PPWG and S-PPWG gives the fields, transmission coefficients and reflection coefficients. By comparison to this solution, the accuracy of the result obtained from the FEM analysis will be evaluated.

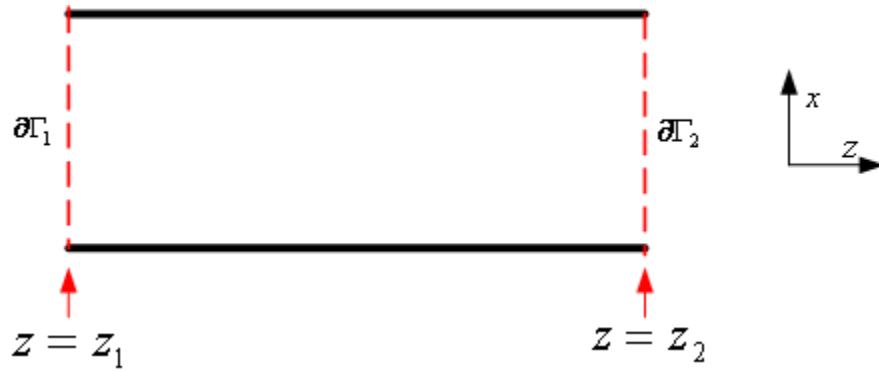


Figure 4.1 Unterminated parallel plate waveguide

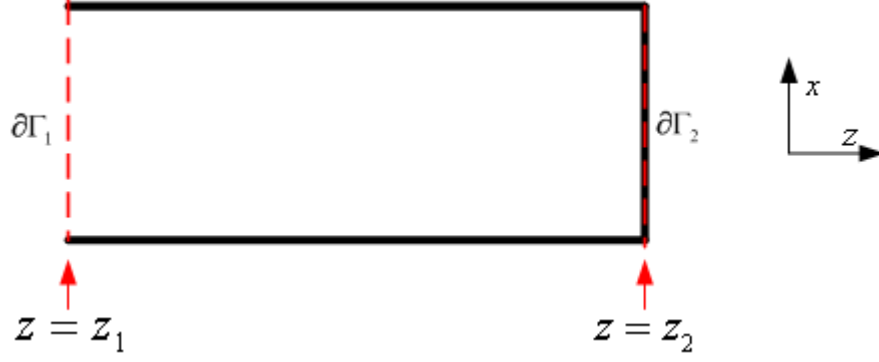


Figure 4.2 Parallel plate waveguide with short-circuited end

In the following sections the analytic solutions for the parallel plate waveguides will be derived and the simulation results for field propagation and scattering parameters will be compared to those derived from the analytic solution.

#### 4.1. Analytical Solution

Consider the test structures first. The computational domain of interest in the parallel plate waveguide is confined between the input port,  $\partial\Gamma_1$ , and the output port,  $\partial\Gamma_2$ . The incident wave is traveling from input to output ports. The output port can be changed to a short circuit, an open port, or a partial blocked septum. The short-ended PPWG (S-PPWG) and open-ended PPWG (T-PPWG) structures have analytical solutions and that permits a determination of the accuracy of a vector finite element result.

An incident wave,  $E_y^{inc}(x, z)$ , is generated from a source at  $z < z_1$  to the left of the domain shown in Figures 4.1 and 4.2. From the view point of the circuit analysis technique a reflected wave might be generated by any geometric or material discontinuities in a manner to satisfy the boundary conditions. Some fraction of the

incident wave propagates through to the output port. As in chapter II, the derivation of the analytic solution starts with a known incident electric field consisting of a single mode. The incident electric field is rewritten here.

$$E_y^{inc}(x, z) = e_1^{inc} \sin\left(\frac{\pi x}{d}\right) e^{-j\beta_1 z} = E_0^{inc} e^{-j\beta_1 z} \quad (4.1)$$

The field leaving the region ( $z > z_2$ ) has the form

$$E_y^t(x, z) = e_1^t \sin\left(\frac{\pi x}{d}\right) e^{-j\beta_1 z} = TE_0^{inc} e^{-j\beta_1 z} \quad (4.2)$$

where  $T$  is the transmission coefficient. To the left of the region, there is also a reflected field of the form

$$E_y^{ref}(x, z) = e_1^{ref} \sin\left(\frac{\pi x}{d}\right) e^{+j\beta_1 z} = RE_0^{inc} e^{-j\beta_1 z} \quad (4.3)$$

where  $R$  is a constant reflection coefficient. As mentioned above a portion of the incident wave reaches the output port and continues to propagate along the waveguide. Some energy carried by the incident wave will be reflected and propagates in the opposite direction. As a result the total wave in the computational domain is the superposition of the incident and the reflected wave from  $z_1$  to  $z_2$ :

$$\begin{aligned} E_y^{tot}(x, z) &= E_y^{inc}(x, z) + E_y^{ref}(x, z) = E_0^{inc} e^{-j\beta_1 z} + RE_0^{inc} e^{-j\beta_1 z} \\ &= \sin\left(\frac{\pi x}{d}\right) [e_1^{inc} e^{-j\beta_1 z} + e_1^{ref} e^{+j\beta_1 z}] \end{aligned} \quad (4.4)$$

The transmission coefficient and the reflection coefficient are defined as the ratio of the reflected wave to the incident wave and the transmitted wave to the incident wave, at some arbitrary position  $z$ , respectively.

$$T = S_{21} = \frac{E_y^t(x, z_2)}{E_y^{inc}(x, z_1)} = \frac{\sin\left(\frac{\pi x}{d}\right) e_1^t e^{-j\beta_1 z_2}}{\sin\left(\frac{\pi x}{d}\right) e_1^{inc} e^{-j\beta_1 z_1}} = \frac{e_1^t}{e_1^{inc}} e^{-j\beta_1 (z_2 - z_1)} \quad (4.5)$$

$$R = S_{11} = \frac{E_y^{ref}(x, z_1)}{E_y^{inc}(x, z_1)} = \frac{\sin\left(\frac{\pi x}{d}\right) e_1^{ref} e^{+j\beta_1 z_1}}{\sin\left(\frac{\pi x}{d}\right) e_1^{inc} e^{-j\beta_1 z_1}} = \frac{e_1^{ref}}{e_1^{inc}} e^{+j2\beta_1 z_1} \quad (4.6)$$

Consider the open-ended PPWG and short-ended PPWG with length equal to one-quarter of the guided wavelength,  $\lambda_g$  as shown in Figure 4.3 and Figure 4.4 below.

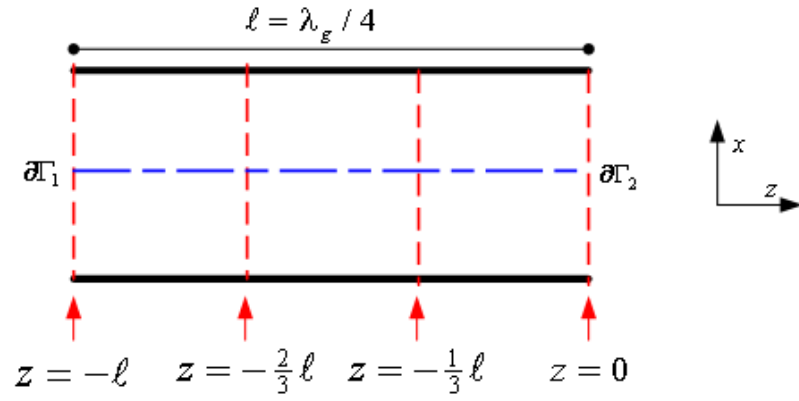


Figure 4.3 Unterminated parallel plate waveguide

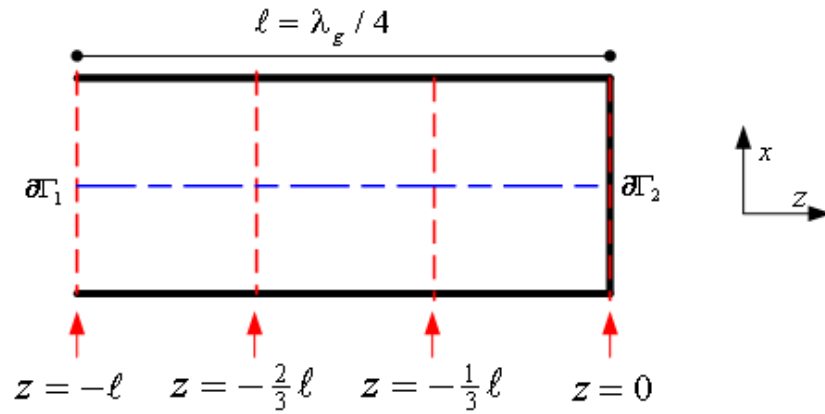


Figure 4.4 Parallel plate waveguide with short-circuited end



For the T-PPWG, the incident wave propagates through the computational domain without reflection. For the S-PPWG, a reflected wave is generated in order to satisfy the boundary condition that the tangential electric field vanishes at the PEC wall. Therefore, the relationship of amplitude of the incident, the transmitted and the reflected wave at position  $z = z_1$  are as follows,

$$e_1^t = e_1^{inc}, e_1^{ref} = 0 \quad \text{for T-PPWG} \quad (4.7)$$

$$e_1^t = 0, e_1^{ref} = -e_1^{inc} \quad \text{for S-PPWG.} \quad (4.8)$$

Substituting (4.7) and (4.8) into equations (4.5) and (4.6) for the transmission coefficient and the reflection coefficient at  $z = 0$  gives

$$\begin{cases} R_0 = 0, T_0 = 1 & \text{for T-PPWG} \end{cases} \quad (4.9)$$

$$\begin{cases} R_0 = -1, T_0 = 0 & \text{for S-PPWG.} \end{cases} \quad (4.10)$$

where the subscript means the reflection and transmission coefficients at  $z = 0$ . In general the phase of the reflection coefficient is varying according to measuring position as

$$R(x, z_1) = \frac{E_y^{ref}(x, z_1)}{E_y^{inc}(x, z_1)} = R_0 e^{-j2\beta_1 \ell} \quad (4.11)$$

where

$$\begin{cases} R(x, z_1) = 0 & \text{for T-PPWG} \end{cases} \quad (4.12)$$

$$\begin{cases} R(x, z_1) = R_0 e^{-j2\beta_1 \ell} = (-1)e^{-j\pi} = 1 & \text{for S-PPWG.} \end{cases} \quad (4.13)$$

Since the input port is located a quarter wavelength away from the output port, the phase of the reflection coefficient is  $-2\beta_1 \lambda_g / 4 = -\pi$  with  $\lambda_g = 2\pi / \beta_1$ , the guide wavelength. The transmission coefficient, however, is just dependent on the amplitude of

the transmitted wave. According to equation (4.5) with equations (4.9) and (4.10), the transmission coefficients for T-PPWG and S-PPWG at  $z = 0$  are

$$\left\{ \begin{array}{l} T(x, z_2) = \frac{e_1^t}{e_1^{inc}} e^{-j\beta_1 \ell} = e^{-j\frac{\pi}{2}} \text{ for T-PPWG} \end{array} \right. \quad (4.14)$$

$$\left\{ \begin{array}{l} T(x, z_2) = 0 \quad \text{for S-PPWG.} \end{array} \right. \quad (4.15)$$

Since the primary unknown in this study is the transverse magnetic field, the analytic magnetic field is required for comparison to the approximate magnetic field. Within the computational domain, the total magnetic field associated with equation (4.4) is of interest and can be derived from

$$\begin{aligned} \bar{H}^{tot} &= H_x^{tot} \hat{x} + H_z^{tot} \hat{z} = \frac{1}{j\omega\mu} \left[ \hat{x} \left( \frac{\partial E_y^{tot}}{\partial z} \right) - \hat{z} \left( \frac{\partial E_y^{tot}}{\partial x} \right) \right] \\ &= \left( \frac{-\beta_1}{\omega\mu} \right) \sin\left(\frac{\pi x}{d}\right) (e_1^{inc} e^{-j\beta_1 z} - e_1^{ref} e^{+j\beta_1 z}) \hat{x} \\ &\quad + \left( \frac{j\pi}{\omega\mu d} \right) \cos\left(\frac{\pi x}{d}\right) (e_1^{inc} e^{-j\beta_1 z} + e_1^{ref} e^{+j\beta_1 z}) \hat{z} \end{aligned} \quad (4.16)$$

As long as the tangential component of the field is known on some boundary, full knowledge of wave beyond that boundary can be guaranteed. The tangential component of magnetic field, the x-component in equation (4.16), is

$$\bar{H}_x^{tot} = \bar{H}_x^{inc} + \bar{H}_x^{ref} = \left( \frac{-\beta_1}{\omega\mu} \right) \sin\left(\frac{\pi x}{d}\right) (e_1^{inc} e^{-j\beta_1 z} - e_1^{ref} e^{+j\beta_1 z}) \quad (4.17)$$

The simpler form of this equation is

$$\bar{H}_x^{tot} = \left( \frac{-\beta_1}{\omega\mu} \right) \sin\left(\frac{\pi x}{d}\right) e_1^{inc} e^{-j\beta_1 z} \quad (4.18)$$

for the T-PPWG and

$$\overline{H}_x^{tot} = \left( \frac{-\beta_1}{\varpi\mu} \right) \sin\left(\frac{\pi x}{d}\right) e_1^{inc} \left( e^{-j\beta_1 z} + e^{+j\beta_1 z} \right) = \left( \frac{-2\beta_1 e_1^{inc}}{\varpi\mu} \right) \sin\left(\frac{\pi x}{d}\right) \cos(\beta_1 z) \quad (4.19)$$

for the S-PPWG. As with the total electric field, equation (4.18) has no variation with  $z$  in its amplitude but the magnetic wave in equation (4.19) is sinusoidal in  $z$ . It is similar to the standing wave made by a plane wave incident to an infinitely long PEC wall.

In this section, T-PPWG and S-PPWG are chosen as two testbeds for verifying the accuracy of the numerical vector finite element solution. The transmission/reflection coefficients in equations (4.13), (4.14) and the analytic solution of the magnetic field in equations (4.18) and (4.19) will be compared to the numerical solutions. Once the FEM solution for the magnetic field is found, the scattering parameters at the input and output ports and the tangential field component can be calculated. In the following section these quantities are calculated from the numerical solution.

## 4.2. Numerical Solutions

The FEM solution coefficients obtained with interpolatory vector elements represent the field values at the interpolation points. The coefficients obtained with hierarchical elements, however, do not carry a physical meaning. The FEM solution for the magnetic field value at an arbitrary position in the computational domain is the linear superposition of the product of basis functions, evaluated at that location and their appropriate coefficients.

In this section the magnetic field will be obtained with hierarchical vector basis functions. From the numerical results the transmission coefficient at the output port and the reflection coefficient at the input port will be computed. Simulation results show how close the approximate fields and scattering parameters are to the analytic solutions.

#### 4.2.1 Numerical Magnetic Field

The x-components of the magnetic field along the four dotted lines in Figures 4.3 and 4.4 are of interest. To get the x-component of the magnetic field at a specific  $z$  position all elements including the dotted lines,  $z = z_k$ , should be specified. For simplicity of explanation, consider a cell adjacent the first dotted line at  $z = z_k$ . The approximate magnetic field in that cell has following form

$$\tilde{H}(x, z) = \sum_{p=0}^N h_p \bar{B}_p(x, z) \quad (4.20)$$

where the parameters in (4.20) are

$\bar{B}_p$  : The hierarchical vector basis functions in a cell

$h_p$  : The coefficient of  $\bar{B}_p$

$N$  : The number of basis functions in a cell

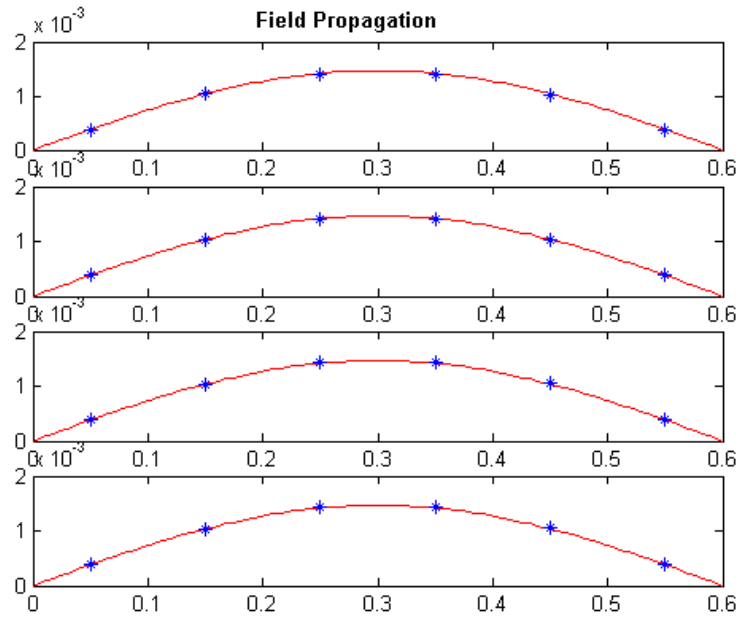
$\tilde{H}(x, z)$  is an approximation of the exact magnetic field  $H(x, z)$ .

Each vector basis functions,  $\bar{B}_p$ , is defined in the physical domain by transforming the basis function  $\bar{\Omega}_p$  from a reference cell defined by simplex coordinates. The geometrical transformation of domain is described in many basic FEM books [1-3].

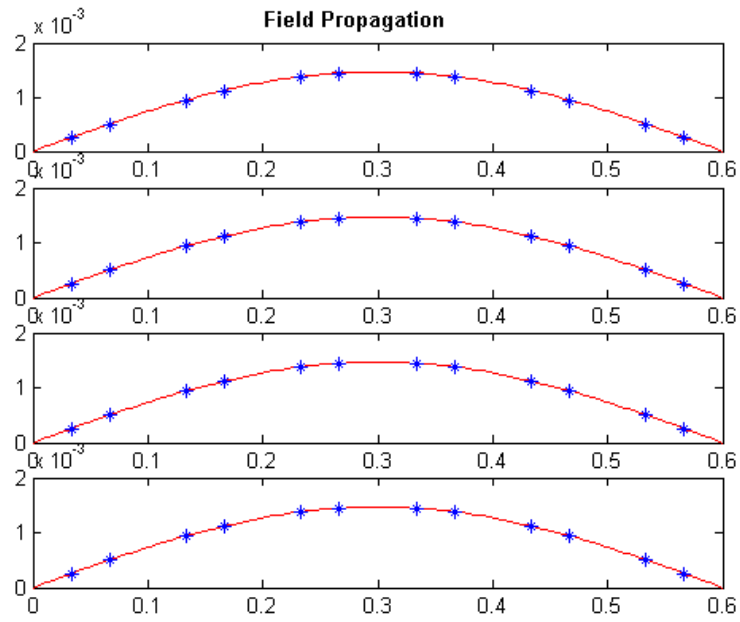
The characteristics of hierarchical vector basis functions are explained in detail in Chapter III. The x-component of  $\bar{H}(x, z)$  is the product of a unit vector in the x direction and the magnetic field:

$$\tilde{H}_x(x, z_k) = \hat{x} \cdot \tilde{H}(x, z_k) = \sum_{p=0}^N h_p \hat{x} \cdot \bar{B}_p(x, z_k). \quad (4.21)$$

The x-component field amplitude involves the superposition of every basis function with a nonzero x-component. For all other cells along the dotted line,  $z = z_k$ , the x-component of the approximate magnetic field can be calculated in the same way. Equation (4.21) is obtained from the FEM solution and compared to the analytic magnetic field values for the T-PPWG and S-PPWG structures. The simulation results are given below in Figures 4.5 and 4.6.

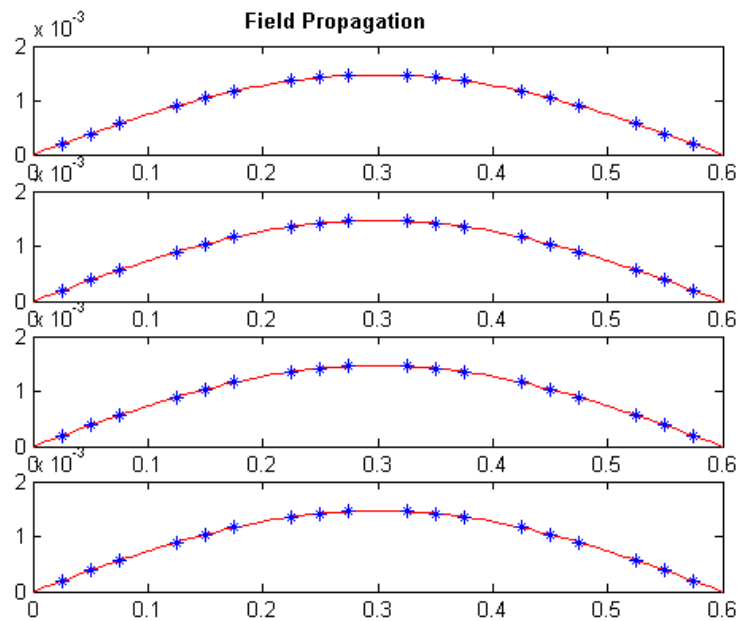


(a) Order = 0

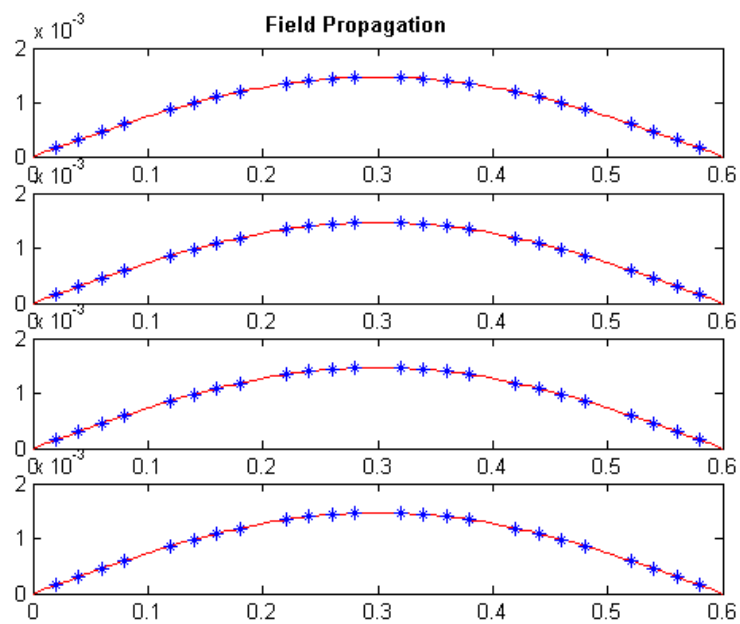


(b) Order = 1

Figure 4.5 Magnetic field for the open-ended parallel plate waveguide

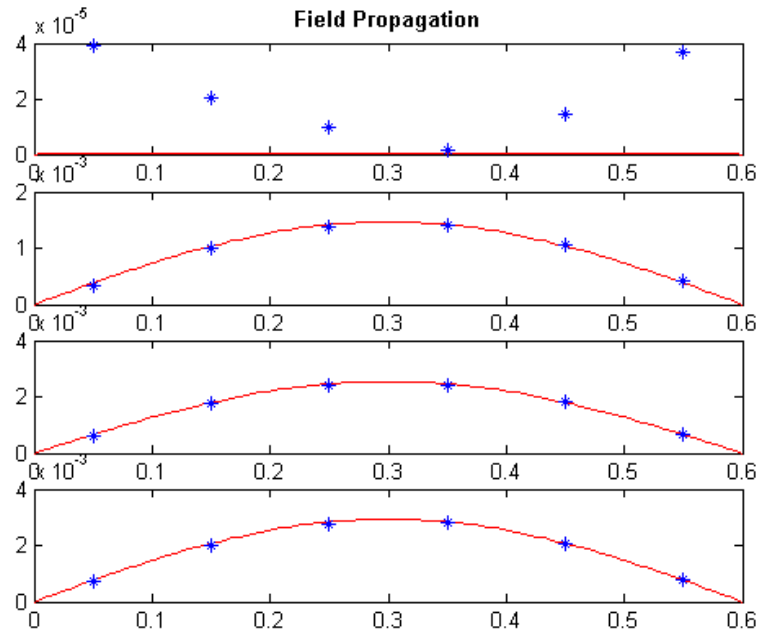


(c) Order = 2

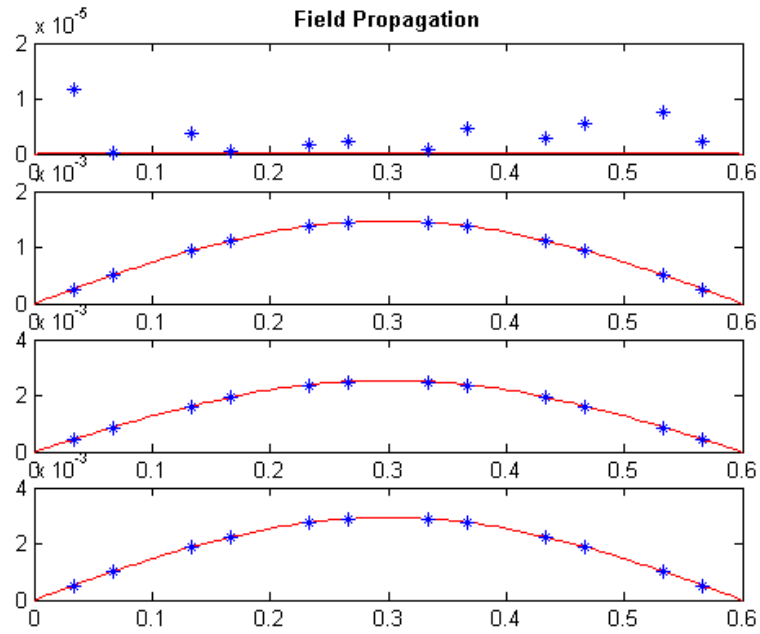


(d) Order = 3

Figure 4.5 Continued



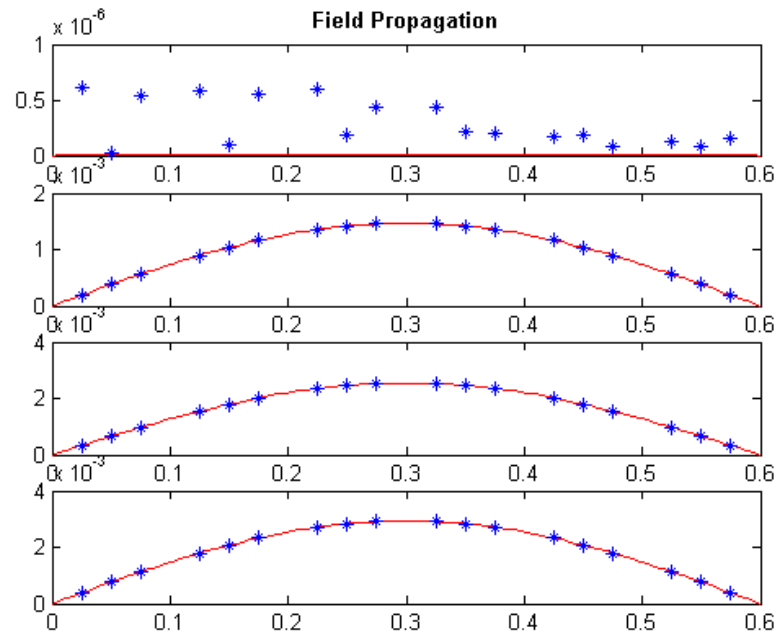
(a) Order = 0



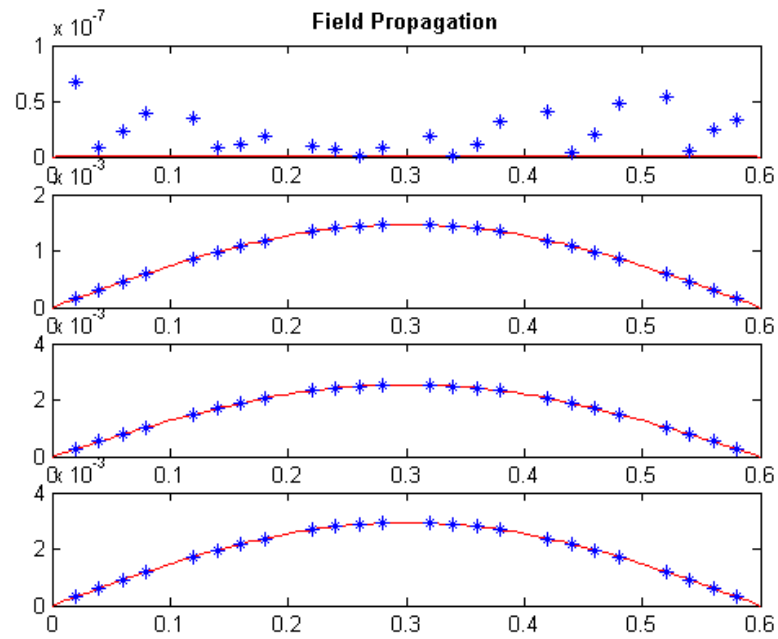
(b) Order = 1

Figure 4.6 Magnetic field for the short-circuited parallel plate waveguide





(c) Order = 2



(d) Order = 3

Figure 4.6 Continued

Figures 4.5 and 4.6 show a comparison of the numerical results and the analytic solutions for the x-component of magnetic field. The stars indicate the approximate magnetic field and the solid lines represent the analytic solutions. Results are presented for the four dotted lines in Figures 4.3 and 4.4, for T-PPWG and S-PPWG, respectively.

The simulation results indicate that the numerical solution obtained with vector hierarchical elements grows more accurate as the order of the basis function polynomial is increased. This provides some verification that the FEM code is functioning correctly.

#### ***4.2.2 The Numerical Transmission and Reflection Coefficients***

In this section scattering parameters are considered for evaluating the accuracy of the approximate solution obtained with vector hierarchical elements. Scattering parameters play an important role in reducing a complex field analysis in microwave engineering to a simple circuit analysis technique. Since most of microwave engineering applications require scattering parameters, no additional redundancy is necessary to calculate them. Therefore they provide a practical test as to whether or not the numerical FEM solutions reach the expected accuracy.

From the analytic scattering parameters in equation (4.9) for T-PPWG and in equation (4.13) for S-PPWG, the fact that no reflected wave and no transmitted wave exist is manifested. Therefore, the transmission coefficients for T-PPWG and the reflection coefficients for S-PPWG are of interest. Approximate transmission coefficients for T-PPWG and reflection coefficients for S-PPWG will be calculated from the

approximate solutions for the magnetic field in each case. Equations (4.5) and (4.6) relate the amplitude of the transmitted electric field and the amplitude of the reflected electric field to the numerical magnetic field coefficients.

The amplitude of the incident field,  $e_1^{inc}$ , is given. The coefficients of the total field are obtained from the FEM solution,  $\{h_i\}$ . For T-PPWG, the total magnetic field is the same as the transmitted field and the x-component of the magnetic field in equation (4.18) is given by

$$H_x^t = H_x^{tot} = \left( \frac{-\beta_1}{\varpi\mu} \right) e_1^t \sin\left(\frac{\pi x}{d}\right) e^{-j\beta_1 z_2}. \quad (4.22)$$

From (4.20) the amplitude of the first transmitted mode is

$$e_1^t = \left[ \left( \frac{-2\omega\mu}{\beta_m d} \right) e^{+j\beta_1 z_2} \right] \int_0^d H_x^{tot}(x, z_2) \sin\left(\frac{\pi x}{d}\right) dx. \quad (4.23)$$

Substituting  $\tilde{H}_x^{tot}$  in equation (4.21) into equation (4.23) gives the approximate amplitude of the transmitted wave:

$$\begin{aligned} \tilde{e}_1^t &= \left[ \left( \frac{-2\omega\mu}{\beta_m d} \right) \right] \int_0^d \sum_{p=0}^N h_p \hat{x} \cdot \bar{B}_p(x, z_2 = 0) \sin\left(\frac{\pi x}{d}\right) dx \\ &= \left[ \left( \frac{-2\omega\mu}{\beta_m d} \right) \right] \sum_{i=1}^M \sum_{p=0}^N \int_{\partial\Gamma_{i,O}} h_{i,p} \bar{B}_{i,x,p}(x, z_2 = 0) \sin\left(\frac{\pi x}{d}\right) dx \end{aligned} \quad (4.24)$$

where  $M$  is the number of cells contiguous to  $z = z_2 = 0$  and  $\bar{B}_{i,x,p}(x, z_2 = 0)$  is the x-component of a  $p$ -th order polynomial basis  $\bar{B}_p$  in an element  $i$  along the output port. The domain  $\partial\Gamma_{i,O}$  represents the cell boundary of an element  $i$  adjacent to the output port. The

line integration is calculated along  $\partial\Gamma_{i,o}$ . Consequently the approximate transmission coefficient is

$$\tilde{T}(x, z_2) = \frac{\tilde{e}_1^t}{e_1^{inc}} = \frac{\left[ \left( \frac{-2\omega\mu}{\beta_m d} \right) \right] \sum_{i=1}^M \sum_{p=0}^N \int_{\partial\Gamma_{i,o}} h_{i,p} \bar{B}_{i,x,p} \sin\left(\frac{\pi x}{d}\right) dx}{e_1^{inc}} \quad (4.25)$$

From equation (4.19) the incident wave and the reflected wave at input port,  $z = z_1$ , for S-PPWG are

$$H_x^{inc} = \left( \frac{-\beta_1}{\varpi\mu} \right) \sin\left(\frac{\pi x}{d}\right) e_1^{inc} e^{-j\beta_1 z_1} \quad (4.26)$$

and

$$H_x^{ref} = \left( \frac{\beta_1}{\varpi\mu} \right) \sin\left(\frac{\pi x}{d}\right) e_1^{ref} e^{+j\beta_1 z_1} \quad (4.27)$$

For S-PPWG the amplitude of the reflected wave can be obtained by subtracting the incident field from total field, to yield

$$H_x^{ref} = \left( \frac{\beta_1}{\varpi\mu} \right) \sin\left(\frac{\pi x}{d}\right) e_1^{ref} e^{+j\beta_1 z_1} = H_x^{tot} - H_x^{inc} \quad (4.28)$$

The reflection coefficient derived from equation (4.27) is obtained from

$$\int_0^d H_x^{ref} \sin\left(\frac{\pi x}{d}\right) dx = \left( \frac{\beta_1}{\varpi\mu} \right) e_1^{ref} e^{+j\beta_1 z_1} \int_0^d \sin\left(\frac{\pi x}{d}\right) \sin\left(\frac{\pi x}{d}\right) dx \quad (4.29)$$

By manipulating this equation into a form for  $e_1^{ref}$  we obtain

$$e_1^{ref} = \left( \frac{2\varpi\mu}{\beta_1 d} \right) e^{-j\beta_1 z_1} \int_0^d H_x^{ref} \sin\left(\frac{\pi x}{d}\right) dx$$

$$= \left( \frac{2\varpi\mu}{\beta_1 d} \right) e^{-j\beta_1 z_1} \int_0^d (H_x^{tot} - H_x^{inc}) \sin\left(\frac{\pi x}{d}\right) dx \quad (4.30)$$

Replacing  $H_x^{tot}$  with  $\tilde{H}_x^{tot}$  and  $H_x^{inc}$  with equation (4.26) gives  $e_1^{ref}$  in the form

$$\tilde{e}_1^{ref} = \left( \frac{2\varpi\mu}{\beta_1 d} \right) e^{-j\beta_1 z_1} \left[ \int_0^d \tilde{H}_x^{tot} \sin\left(\frac{\pi x}{d}\right) dx - \int_0^d H_x^{inc} \sin\left(\frac{\pi x}{d}\right) dx \right]$$

where

$$\begin{aligned} \int_0^d \tilde{H}_x^{tot} \sin\left(\frac{\pi x}{d}\right) dx &= \int_0^d \sum_{p=0}^N h_p \bar{B}_{p,x}(x, z_1) \sin\left(\frac{\pi x}{d}\right) dx \\ &= \sum_{i=1}^M \sum_{p=0}^N \int_{\partial\Gamma_{i,l}} h_p \bar{B}_{p,x}(x, z_1) \sin\left(\frac{\pi x}{d}\right) dx \end{aligned}$$

and

$$\int_0^d H_x^{inc} \sin\left(\frac{\pi x}{d}\right) dx = \int_0^d \left( \frac{-\beta_1}{\varpi\mu} \right) \sin\left(\frac{\pi x}{d}\right) e_1^{inc} e^{-j\beta_1 z_1} \sin\left(\frac{\pi x}{d}\right) dx = \left( \frac{-\beta_1 d}{2\varpi\mu} \right) e_1^{inc} e^{-j\beta_1 z_1}.$$

Therefore,

$$\tilde{e}_1^{ref} = \left( \frac{2\varpi\mu}{\beta_1 d} \right) e^{-j\beta_1 z_1} \sum_{i=1}^M \sum_{p=0}^N \int_{\partial\Gamma_{i,l}} h_p \bar{B}_{p,x}(x, z_1) \sin\left(\frac{\pi x}{d}\right) dx + e_1^{inc} e^{-j2\beta_1 z_1}. \quad (4.31)$$

Substituting equation (4.31) into equation (4.6) gives the reflection coefficient at the

input port,  $z = z_1$ :

$$\tilde{R}(x, z_1) = \frac{\tilde{e}_1^{ref}}{e_1^{inc}} e^{+j2\beta_1 z} = \frac{\left( \frac{2\varpi\mu}{\beta_1 d} \right) e^{+j\beta_1 z_1} \left[ \sum_{i=1}^M \sum_{p=0}^N \int_{\partial\Gamma_{i,l}} h_p \bar{B}_{p,x}(x, z_1) \sin\left(\frac{\pi x}{d}\right) dx \right] + e_1^{inc}}{e_1^{inc}}. \quad (4.32)$$

From equations (4.25) and (4.32), the transmission error and the reflection error are obtained as:

$$\begin{aligned}
e_T &= \left| \frac{T(x, z_2) - \tilde{T}(x, z_2)}{T(x, z_2)} \right| = \left| \frac{e_1^t - \tilde{e}_1^t}{e_1^t} \right| = \left| \frac{e_1^{inc} - \tilde{e}_1^t}{e_1^{inc}} \right| \\
&= \left| \frac{e_1^{inc} + \left[ \left( \frac{2\omega\mu}{\beta_m d} \right) \sum_{i=1}^M \sum_{p=0}^N \int_{\partial\Gamma_{i,0}} h_{i,p} \bar{B}_{i,x,p}(x, z_2 = 0) \sin\left(\frac{\pi x}{d}\right) dx \right]}{e_1^{inc}} \right| \quad (4.33)
\end{aligned}$$

and

$$\begin{aligned}
e_R &= \left| \frac{R(x, z_1) - \tilde{R}(x, z_1)}{R(x, z_1)} \right| = \left| \frac{e_1^{ref} - \tilde{e}_1^{ref}}{e_1^{ref}} \right| = \left| \frac{e_1^{inc} + \tilde{e}_1^{ref}}{e_1^{inc}} \right| \\
&= \left| \frac{e_1^{inc} (1 + e^{-j2\beta_1 z_1}) + \left( \frac{2\omega\mu}{\beta_1 d} \right) e^{-j\beta_1 z_1} \left[ \sum_{i=1}^M \sum_{p=0}^N \int_{\partial\Gamma_{i,l}} h_p \bar{B}_{p,x}(x, z_1) \sin\left(\frac{\pi x}{d}\right) dx \right]}{e_1^{inc}} \right|. \quad (4.34)
\end{aligned}$$

From the point of view of power conservation, a fraction of the incident power is reflected and some of the incident power is consumed while passing through the medium. The remaining power is delivered to the output port. Therefore if the material of the medium is lossless, then

$$T^2(x, z_2) + R^2(x, z_1) = 1. \quad (4.35)$$

By incorporating equations (4.25) and (4.32) into equation (4.35), another error measure in terms of power deliverance is derived as

$$e_P = \left| \frac{1 - \tilde{T}^2(x, z_2) - \tilde{R}^2(x, z_1)}{1} \right| \quad (4.36)$$

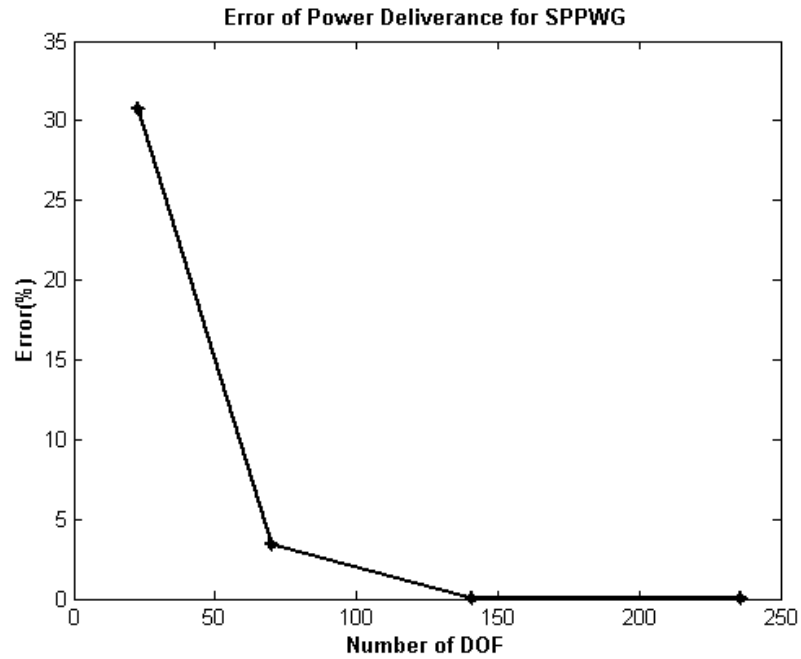
This error will be useful to check the accuracy of the numerical solution even if an analytic solution is not available. In addition, it can be used to stop the iteration of an adaptive FEM procedure when this measure reaches the desired accuracy.

The combination of equations (4.33) and (4.36) for T-PPWG and the combination of equations (4.34) and (4.36) for S-PPWG are presented in Figure 4.7 and 4.8. In these figures, the triangular-cell model is fixed and the polynomial degree of the basis is increased to obtain more degrees of freedom. For both S-PPWG and T-PPWG structures, the error in the reflection and transmission coefficients converge to zero as the number of degrees of freedom in the FEM solution is increased. Consequently the power conservation law of equation (4.35) is well satisfied by both configurations as the number of DoF increases.

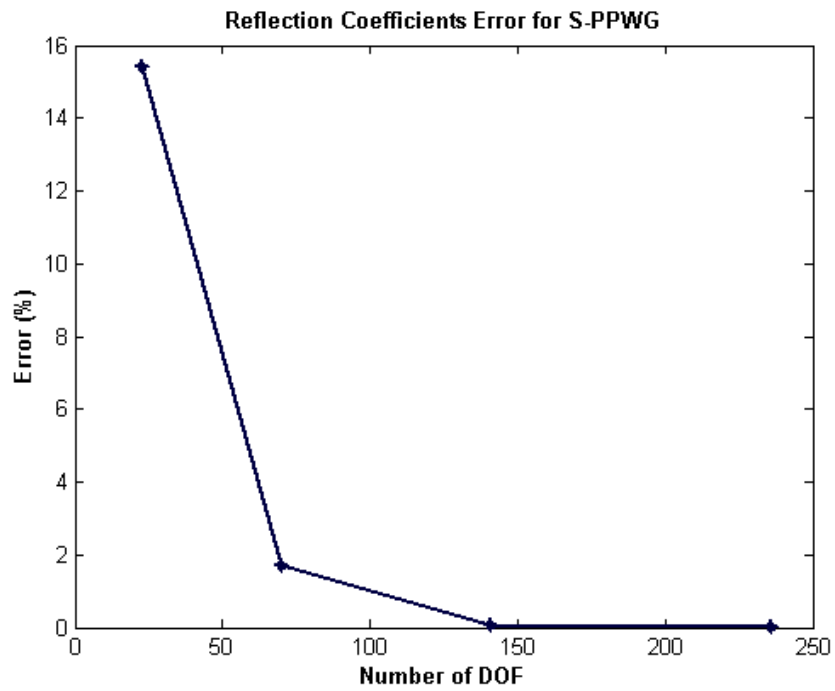
### 4.3 Summary

In this chapter, the fields within a parallel-plate waveguide and the associated reflection and transmission coefficients were used to evaluate the correctness of the FEM implementation. The numerical results for an open PPWG and a short-circuited PPWG are observed to improve in accuracy as the order  $p$  of the expansion is increased. These results suggest that the computer implementation is correctly programmed.

The FEM implementation incorporating hierarchical vector basis functions will be used to assess the performance of several error estimators in Chapter 5.



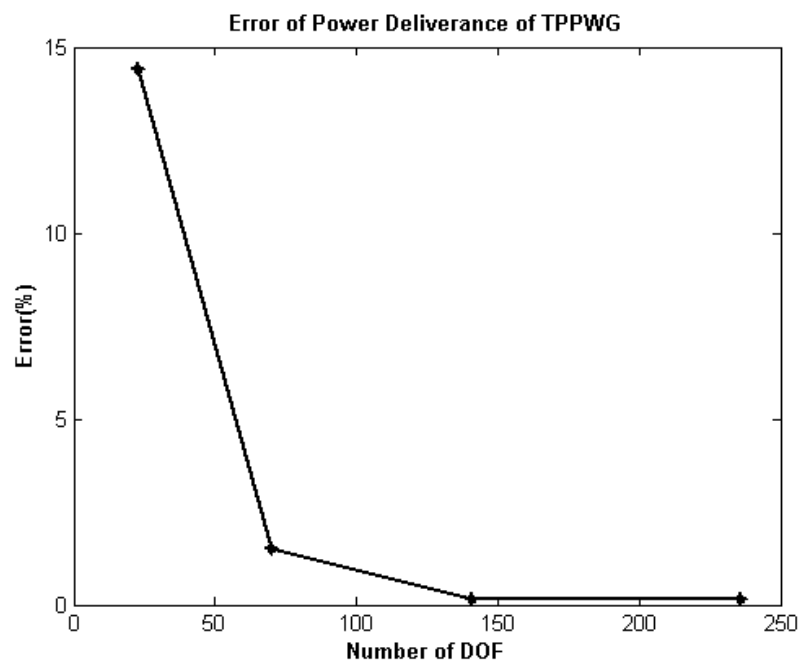
(a) Power Deliverance Error



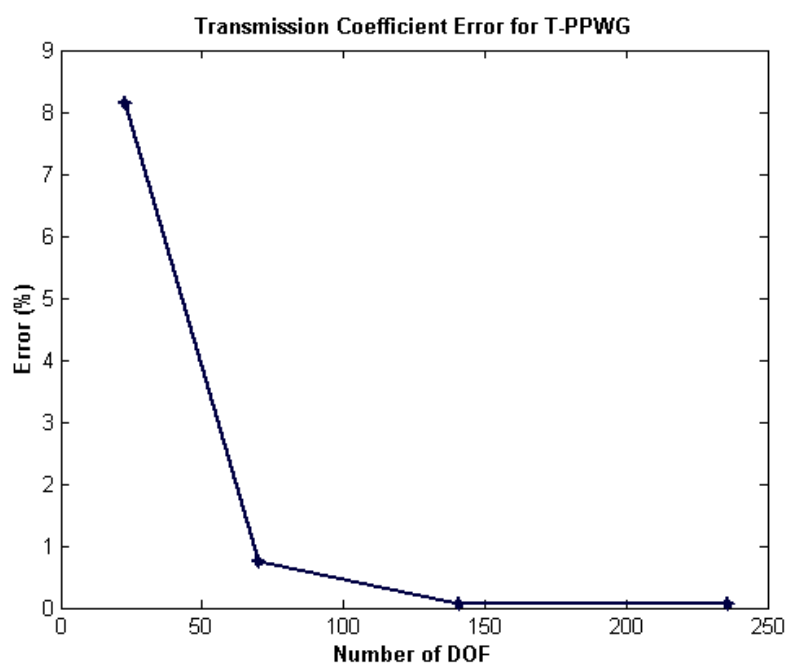
(b) Reflection Error

Figure 4.7 Scattering parameter error for the short-circuited parallel plate waveguide





(a) Power Deliverance Error



(b) Transmission Error

Figure 4.8 Scattering parameter error for the unterminated parallel plate waveguide

## CHAPTER 5: ERROR ESTIMATORS

Discretization error is intrinsically incurred when modeling a continuous solution with a finite number of expansion functions. It plays a crucial role in determining the accuracy of the final solution. *A posteriori* error estimators allow assessment of the quality of the computed solution by assigning an error value to a local element, to a local edge (for 2D) or a local face (for 3D). *A posteriori* error estimators can be used in connection with an adaptive refinement procedure to reduce the discretization error by distributing the degrees of freedom (DOF) in an optimal manner.

In this chapter four *a posteriori* error estimators considered in the current study will be explained in detail. These are the

- Normal Field Discontinuity (NFD) Error Norm
- Discontinuity of the Curl of Field (DCF) Error Norm
- Weak Form Residual (WFR) Error Norm
- Coefficient Sensitivity of the Highest-Order Polynomial (CSH) Error Norm.

To obtain an optimum DoF distribution, the local error norm should reflect the actual error in the numerical solution and allow a user to identify the area with relatively higher local error. However, in practice the actual solution is not known. Thus, this study will attempt to answer the following questions:

- Can the error estimator be implemented?
- Is the assigned error in proportion to the actual error?

- Does the assigned error decrease as the DoF increases and the solution improves?

The first is practical: it is easy to define an *a posteriori* error estimator that is not easy to compute. The second question is fundamental. The third one addresses the need for an error estimator that can be used as a termination criterion for an adaptive refinement procedure. A related issue is the validity of a global error estimate derived from local error estimator.

The first question will be explained in the following sections describing the definition of each error estimator. The second and third question will be answered by presenting simulation results that compare actual error patterns with those of the numerical error estimators. In this chapter simulations will be used to demonstrate two aspects of the error estimators: the first is the local error performance and the second is the global error performance.

Before the error estimators are discussed, we describe the manner in which the actual error in a numerical solution is determined. Subsequent sections will address how well each of the error estimators approximate the actual error.

## 5.1 Exact Solution for the T-PPWG and S-PPWG Structures

For problems with an exact analytical solution, the exact solution is a convenient reference to test the performance of each error estimator. The T-PPWG and S-PPWG structures shown in Figure 4.1 and Figure 4.2 will be used to analyze four error estimators. For these structures the analytic solution was presented in Chapter IV.

The x-component of the magnetic field for the T-PPWG and S-PPWG structures is derived in equations (4.18) and (4.19) and rewritten in equations (5.1) and (5.2) for convenience.

$$\bar{H}_x = \left( \frac{-\beta_1}{\varpi\mu} \right) \sin\left( \frac{\pi x}{d} \right) e_1^{inc} e^{-j\beta_1 z} \quad (5.1)$$

$$\bar{H}_x = \left( \frac{-\beta_1}{\varpi\mu} \right) \sin\left( \frac{\pi x}{d} \right) e_1^{inc} (e^{-j\beta_1 z} + e^{+j\beta_1 z}) = \left( \frac{-2\beta_1 e_1^{inc}}{\varpi\mu} \right) \sin\left( \frac{\pi x}{d} \right) \cos(\beta_1 z) \quad (5.2)$$

The z-component derived by substituting equations (4.7) and (4.8) into the second term in the right-hand side in equation (4.16) is given by each of the following:

$$\bar{H}_z = \left( \frac{j\pi}{\varpi\mu d} \right) \cos\left( \frac{\pi x}{d} \right) e_1^{inc} e^{-j\beta_1 z} \quad (5.3)$$

$$\bar{H}_z = \left( \frac{j\pi}{\varpi\mu d} \right) \cos\left( \frac{\pi x}{d} \right) (e_1^{inc} e^{-j\beta_1 z} - e_1^{inc} e^{+j\beta_1 z}) = \left( \frac{2\pi e_1^{inc}}{\varpi\mu d} \right) \cos\left( \frac{\pi x}{d} \right) \sin(\beta_1 z) \quad (5.4)$$

Equations (5.1) and (5.3) are for T-PPWG and Equations (5.2) and (5.4) are for S-PPWG. The magnetic field at an arbitrary point in the computational domain is easily obtained and can be compared to the numerical FEM solution. The details of the error norm computation will be considered in the next section.

### 5.1.1 Error Norm Calculation

The numerical magnetic field is computed as:

$$\tilde{H}(x, z) = \sum_{i=1}^N h_i \bar{B}_i(x, z) \quad (5.5)$$

where the coefficient set  $\{h_i\}$  represents the approximate solution found by the FEM,  $N$  is the number of the degrees of freedom used, and the tilda sign over the magnetic field means it is approximate. The vector basis functions have been detailed in Chapter III. Once the FEM solution is found, the numeric value of the field can be calculated by equation (5.5).

The error in the FEM result is defined by the  $L^2$  norm as

$$e = \frac{\iint |\bar{H} - \tilde{H}|_{L^2}^2 dx dz}{\iint |\bar{H}^{inc}|_{L^2}^2 dx dz}. \quad (5.6)$$

Equation (5.6) can be manipulated for easy implementation into the form

$$e = \frac{\sum_{p=1}^M |H(p) - \tilde{H}(p)|_{L_2}}{M |H_{x,peak}^{inc}|} = \frac{\sum_{p=1}^M E_p}{N |H_{x,peak}^{inc}|} \quad (5.7)$$

where  $H_{peak}^{inc}$  is the peak value of the x-component of the incident magnetic field at the input port,  $M$  represents the number of sample points per cell and  $E_p$  is the error in  $\tilde{H}$  at a point. The  $L^2$  norm of a vector quantity is defined as

$$|\tilde{A}_x + \tilde{A}_z|_{L_2} = \sqrt{|A_x|^2 + |A_z|^2}. \quad (5.8)$$

When the point  $p$  is on the cell boundary, the numerical magnetic field is not unique. The tangential component is uniquely determined due to the curl-conforming vector basis. For the normal component, however, two cells abutting an edge may have two different values. A new definition of error for points on edge is given by the average

$$E_p = \frac{E_{p,1} + E_{p,2}}{2}. \quad (5.9)$$

The subscript represents the two cells sharing the edge on which the point  $p$  is located.

### 5.1.2 Simulation Results

In this section the basic mesh for T-PPWG and S-PPWG is explained and simulation results will be presented. The simple PPWG has no rapid variation and the FEM results are reasonably accurate as the DoF reaches a certain level. Consequently a coarse mesh (Figure 5.1) is used to be able to show the variation of the local error norm and global error norm as a function of the DoF.

The mesh is a basic frame in x-z plane for the homogeneous air-filled T-PPWG and S-PPWG structures. The PEC walls are not denoted. The number on the dotted line represents the global edge number. The incident wave propagates from the input port to the output port. The top edges (8, 16, and 23) and the bottom edges (1, 10 and 17) are PEC walls. The S-PPWG has additional PEC walls at the output port edges (18 and 21). The field values along the two solid lines, one along the propagation direction, at  $x = 0.3$ , and the other along the x-axis, at  $z = -0.15$  will be used for the local error investigation.

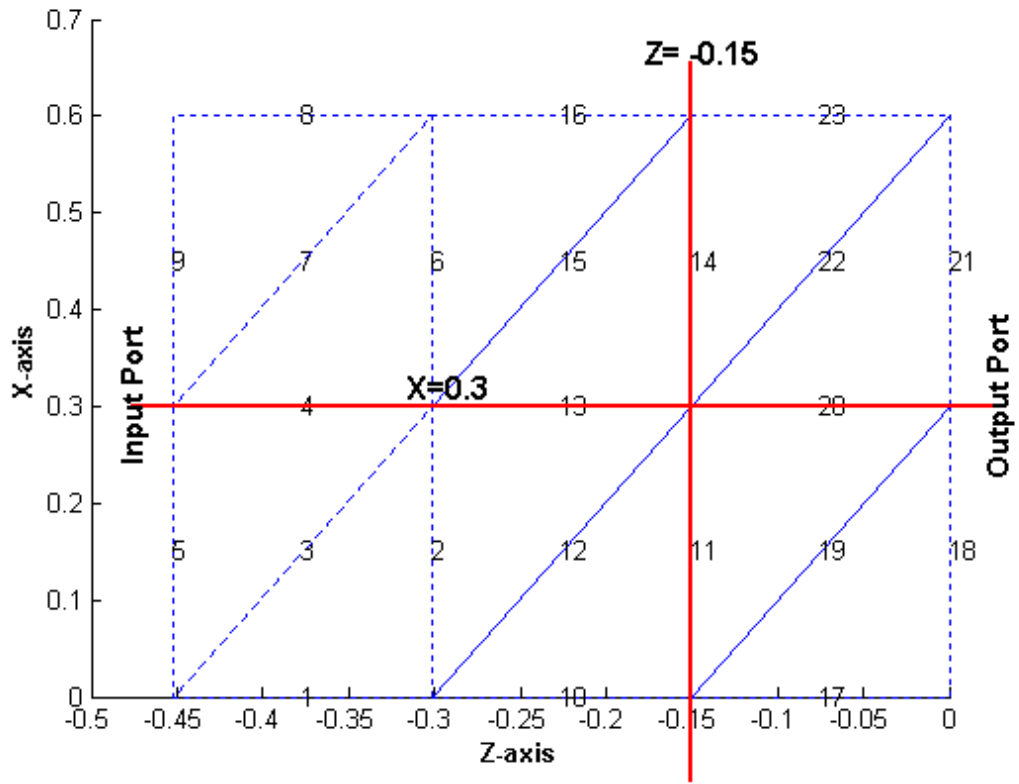
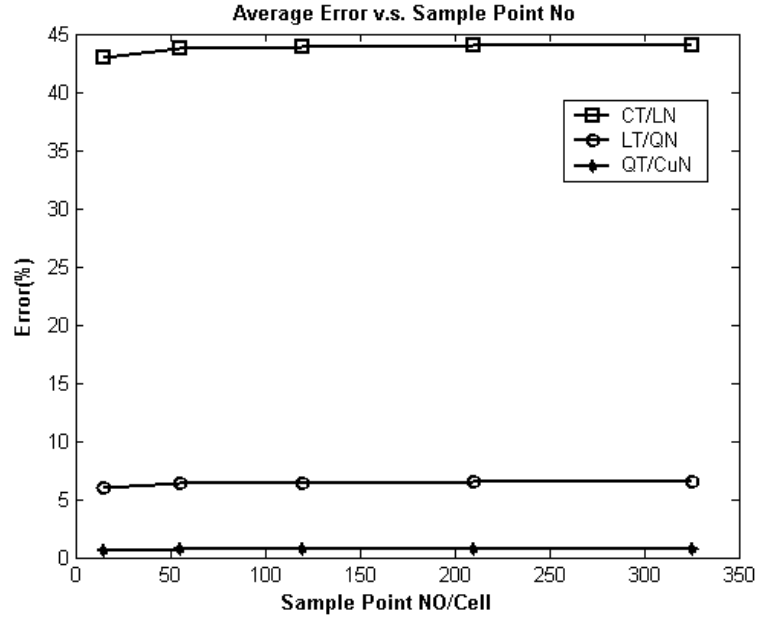
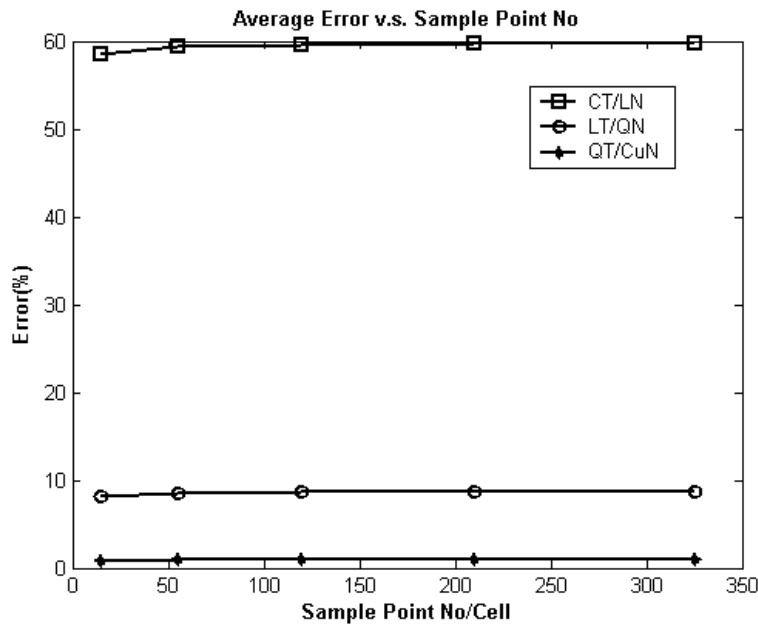


Figure 5.1 Coarse mesh for the parallel plate waveguide

Consider first the global error defined by equation (5.7). It is calculated by numerical quadrature with several sample points in each cell not on a boundary. To investigate the number of quadrature points required, Figure 5.2 plots the value of (5.7). Figure 5.2 shows that as the number of sample points in a cell increases the global error converges to some value for each polynomial order. When over 300 sample points per cell are employed, the convergent value may be taken as the exact evaluation of the error norm.



(a) T-PPWG



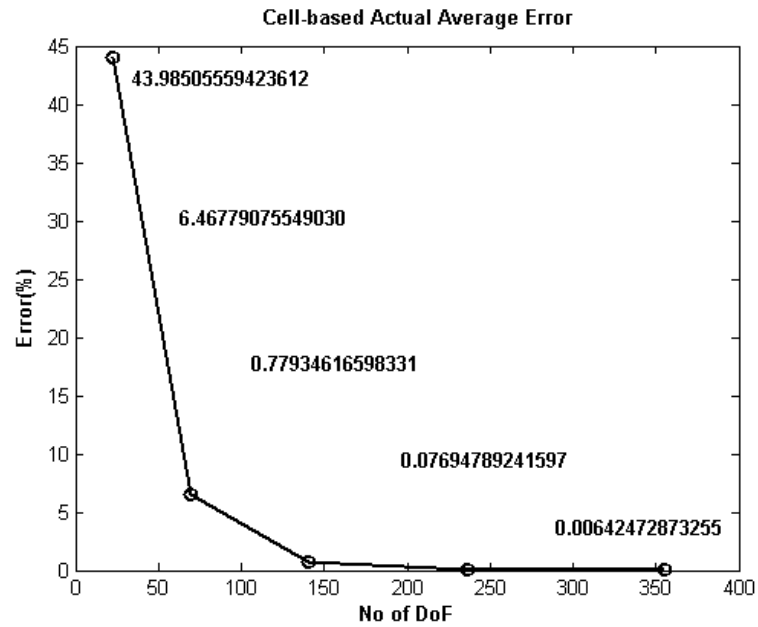
(b) S-PPWG

Figure 5.2 Global error computed as a function of the number of quadrature points used for three orders of vector basis functions

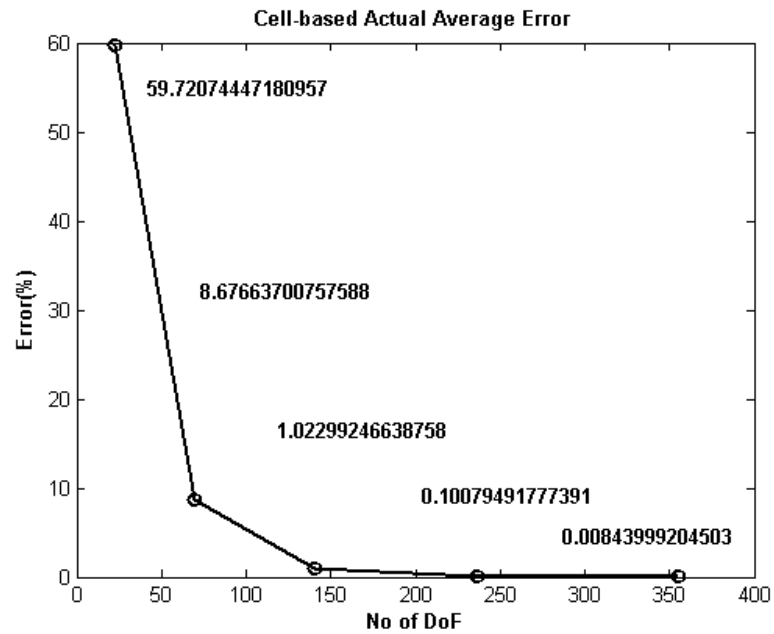
Figure 5.3 shows the behavior of the global error computed from (5.7) for the T-PPWG and S-PPWG structures, obtained with 325 sample points per cell with 5



different basis polynomial orders: CT/LN, LT/QN, QT/CuN, etc. The percentage error is indicated on each figure.



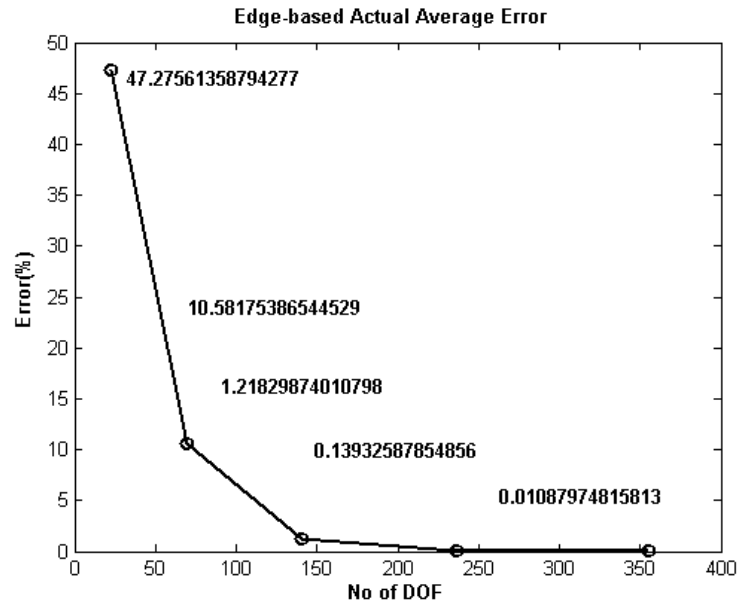
(a) T-PPWG



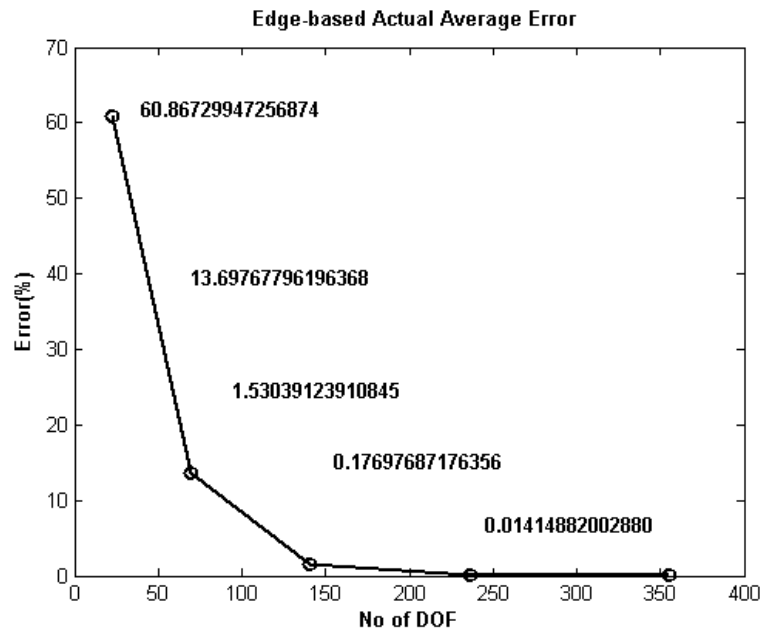
(b) S-PPWG

Figure 5.3 Global error defined from (5.7) as a function of the basis function order

Figure (5.4) shows the behavior of the global error computed from (5.9) for T-PPWG and S-PPWG structures, obtained at the midpoint of each edge with 5 different basis polynomial orders as in Figure (5.3). The percentage error is indicated on each figure.



(a) T-PPWG

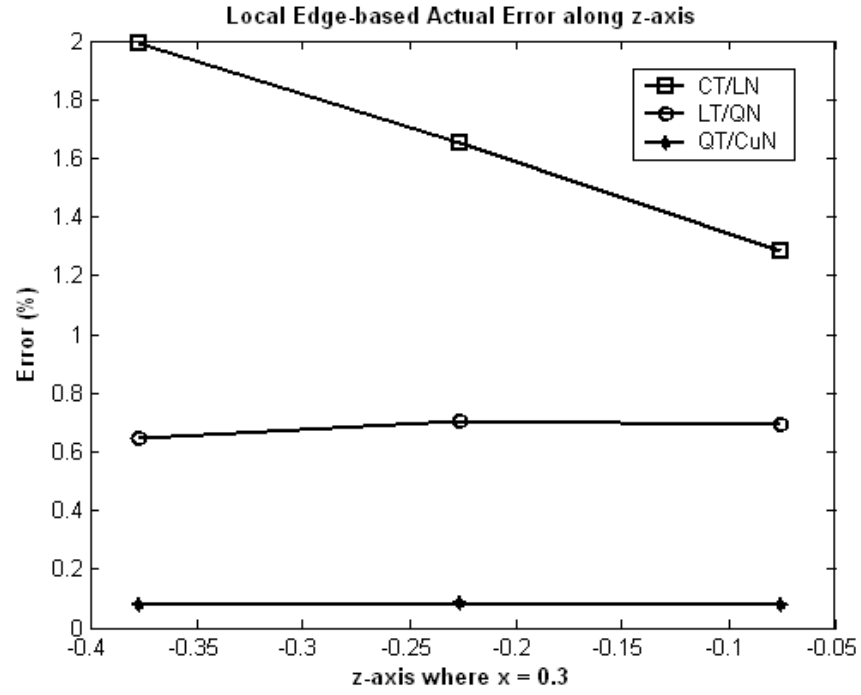


(b) S-PPWG

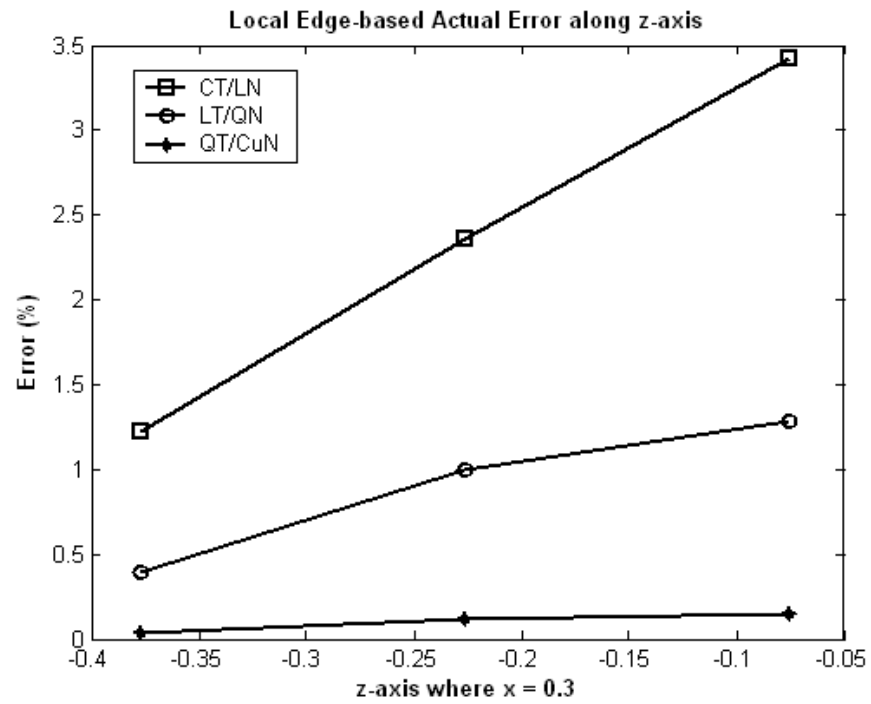
Figure 5. 4 Global error defined from (5.9) as a function of the basis function order

These global error levels will be used as reference value for comparison with the numerical error estimators in order to judge the validity of the four error estimators.

Figures 5.5 through 5.8 show the variation of the local error at points along the x- and z-lines shown in Figure 5.1. Figures 5.5 and 5.6 represent edge-based local error and Figures 5.7 and 5.8 represent cell-based local error. Figures 5.5 through 5.8 support the conclusion that the global and local error decreases as the basis polynomial order increases. These results further collaborate the conclusion that the FEM approach is correctly implemented. In the following sections, these results will be compared with those of the error estimators (obtained without use of the exact solution).

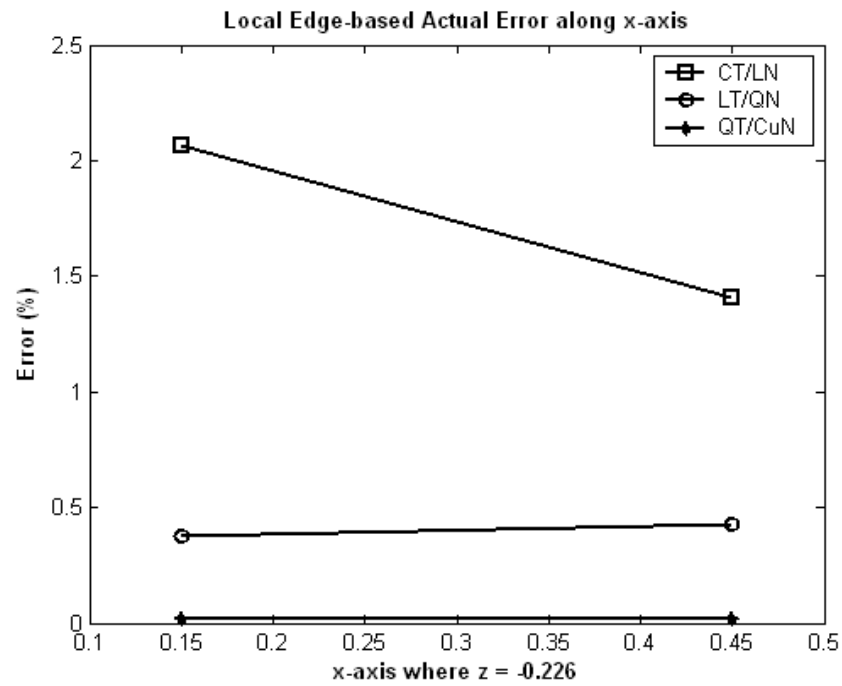


(a) T-PPWG

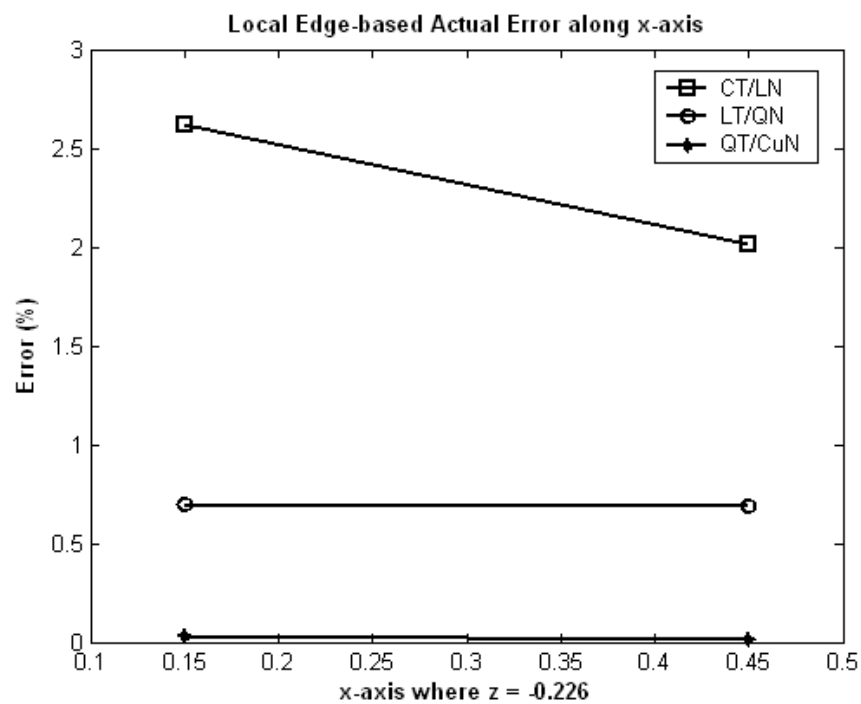


(b) S-PPWG

Figure 5.5 Local edge-based actual error along the z-axis where  $x = 0.3$

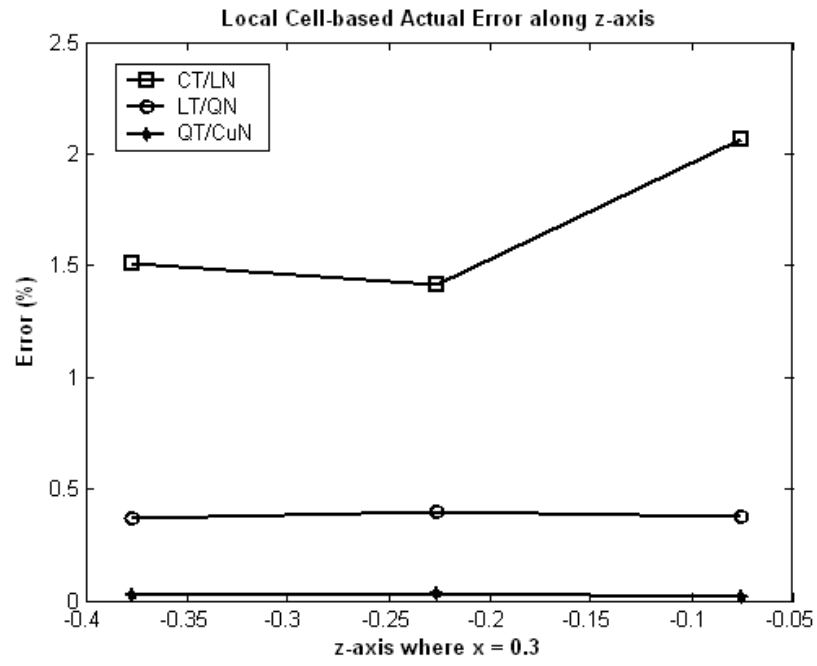


(a) T-PPWG

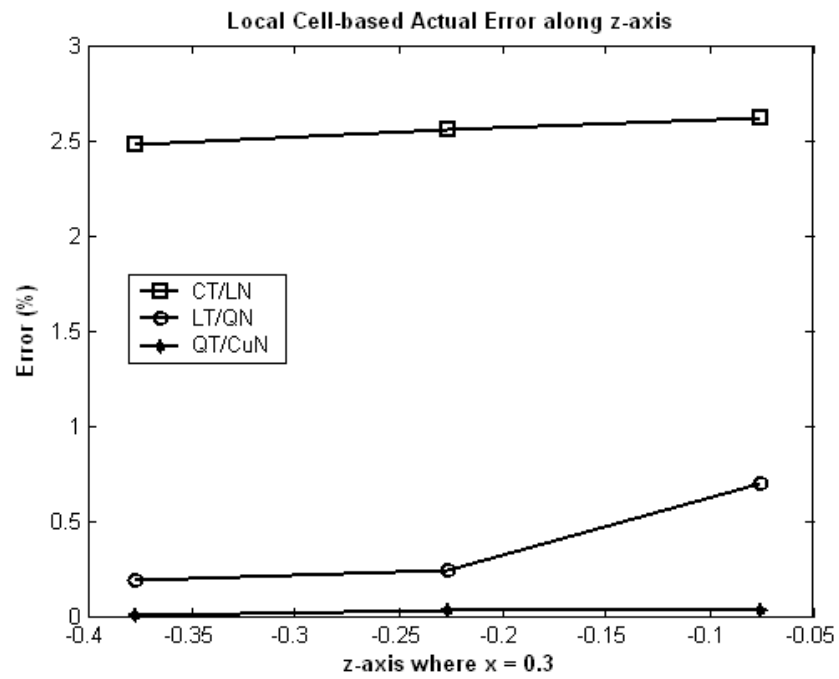


(b) S-PPWG

Figure 5.6 Local edge-based actual error along the x-axis where  $z = -0.226$

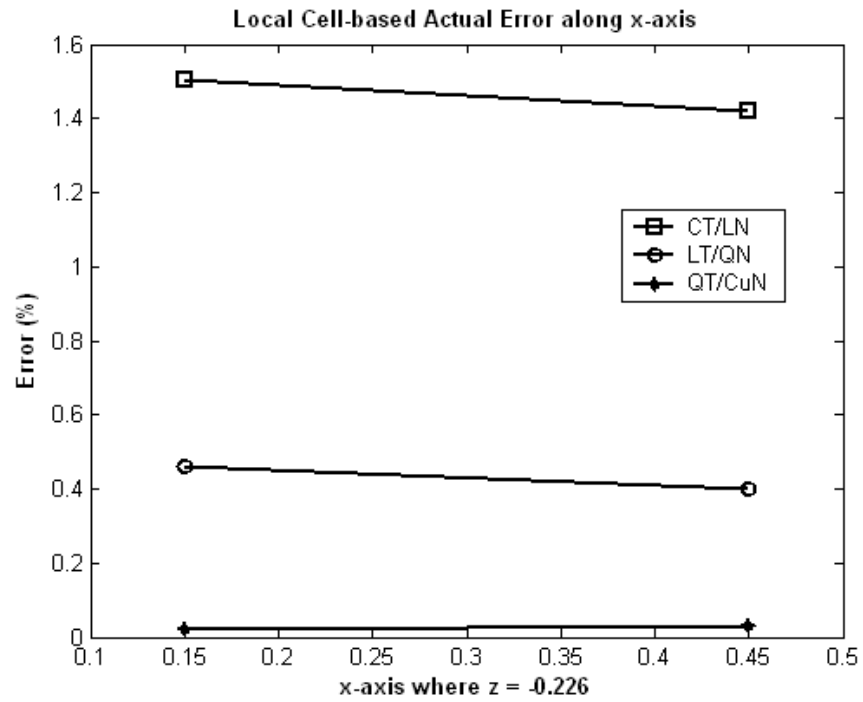


(a) T-PPWG

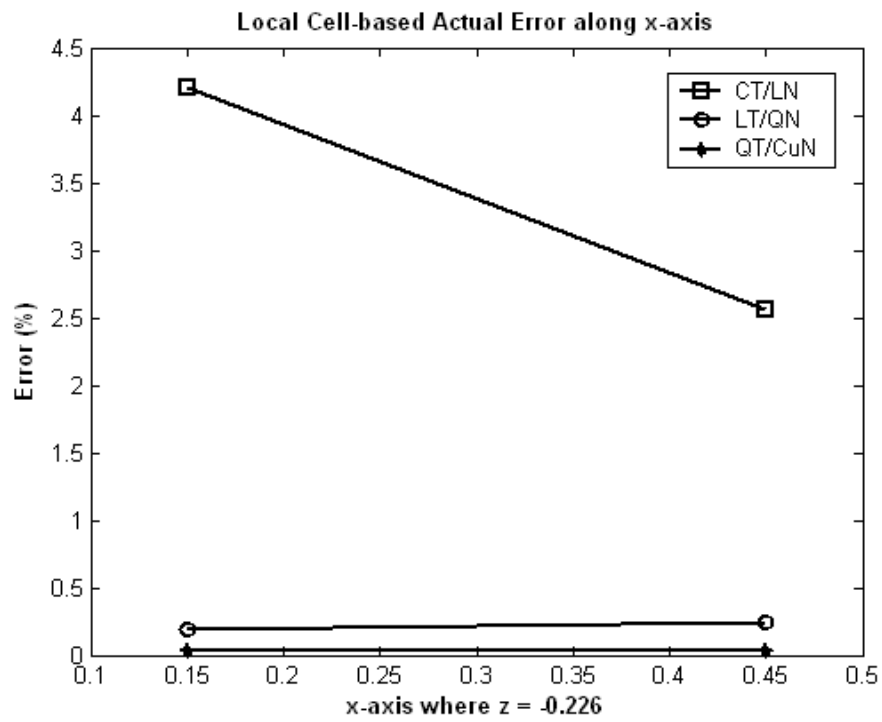


(b) S-PPWG

Figure 5.7 Local cell-based actual error along the z-axis where  $x = 0.3$



(a) T-PPWG



(b) S-PPWG

Figure 5.8 Local cell-based actual error along the x-axis where  $z = -0.226$

## 5.2 Normal Field Discontinuity (NFD) Error Estimator

The discontinuity of the field or its constitutive flux at the cell boundary can be taken as an error estimator since the physical unknown quantities only violate the continuity conditions due to the discretization error [29-36]. The true magnetic field and flux density satisfy the following [35]:

- $\hat{n} \cdot \bar{B} = 0$  at the surface of a perfect electric conductor (PEC).
- the normal components of  $\bar{B}$  are continuous at the interface of two elements.
- $\hat{n} \times \bar{H} = \bar{J}$  at the surface of a PEC.
- the tangential components of magnetic field,  $\bar{H}$ , at the interface of two elements are continuous.

In the approximate solution being considered, however, the flux density or the field may not be continuous due to the coarse mesh. So the larger this discontinuity is, the more erroneous the computed solution is. Thus the normal component discontinuity of  $\bar{B}$  and the tangential component discontinuity of  $\bar{H}$  can be taken as measures of the discretization error.

Using the local Gauss' law as applied in Figure 5.9, an error estimator can be derived and used for testing the accuracy of the solution at each element [35,37,38]. From the local Gauss' law we obtain

$$e = \int_S B_n dS \neq 0 \quad (5.10)$$

or



$$e = \int_{S_1} B_{n1} dS_1 + \int_{S_2} B_{n2} dS_2 + \int_{S_3} B_{n3} dS_3 \quad (5.11)$$

where  $B_n$  is the normal component of the magnetic flux on the surrounding surface  $S$  (in 3D problem). In a 2D problem, the integral reduces to the cell boundaries surrounding cell  $i$  in Figure 5.9. The surface integration with respect to variable  $dS_i$  corresponds to a line integration in 2D. The normal direction at the surface  $S$  is denoted  $ds_i$ , which also corresponds to the normal direction of the cell boundary in 2D.

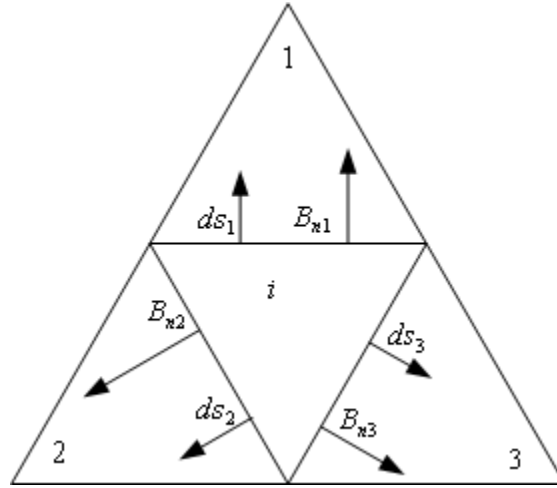


Figure 5.9 Gauss' law

The discontinuity error associated with an edge  $\ell$  shared by element  $i$  and element  $j$  is derived directly from the discontinuity of  $B_n$  [35,38,39] in Figure 5.10, resulting in

$$e = \text{Max} \left| \int_{S_1} \frac{(B_{ni} - B_{nj}) dS_1}{\sum B_i} \right| \quad (5.12)$$

where the index  $j=1, 2$ , and  $3$  representing the three elements abutting element  $i$ .

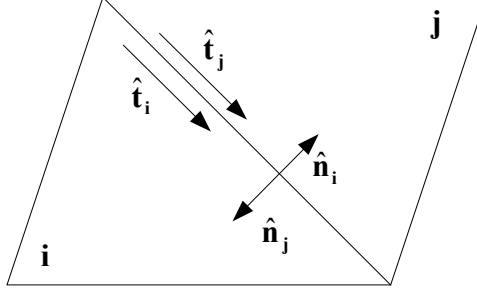


Figure 5.10 Boundary conditions.

This error estimator is easily adapted to the nature of the edge-based basis functions [33,34, 40], since the edge-based basis may have discontinuous normal components.

In the next two sections the normal field discontinuity (NFD) error estimator will be defined for the 2D problem and simulation results will be presented to illustrate its performance.

### 5.2.1 Definition of Normal Field Discontinuity Error Estimator

The system of equations for the FEM formulation is expressed in terms of the magnetic field. The error at edge  $k$  is

$$E_k = \frac{1}{\ell_k} \int \left| (\bar{B}_{i,k} - \bar{B}_{j,k}) \cdot \hat{n}_i \right| d\ell_k = \frac{1}{\ell_k} \int \left| (\mu_i \bar{H}_{i,k} - \mu_j \bar{H}_{j,k}) \cdot \hat{n}_i \right| d\ell_k \quad (5.13)$$

where  $\ell_k$  is the dimension of edge  $k$  at the boundary of two elements  $i$  and  $j$ ,  $\hat{n}_i$  is the outward normal unit vector to element  $i$ , and  $\mu_i$  represents the permeability of the medium consisting of cell  $i$ . For problems that have the electric field as the primary unknown, the electric flux density and permittivity can replace the magnetic flux density and permeability in (5.13). For a 3D problem, the boundary increment  $d\ell$  will be replaced

by  $ds$ , the interface surface between two elements. The local error at the edge  $k$  will be normalized by the peak value of the incident magnetic field  $H_{peak}^{inc}$  and total number of the interfacing edges:

$$e_k = E_k / (H_{peak}^{inc} \times N_{edge}) \quad (5.14)$$

In this study the evaluation of the integration in (5.13) is approximated by the value at the midpoint of the edge. The global average error norm will be defined by

$$e_a = \frac{1}{H_{peak}^{inc} \times N_{edge}} \sum_{k=1}^{N_{edge}} E_k = \sum_{k=1}^{N_{edge}} e_k . \quad (5.15)$$

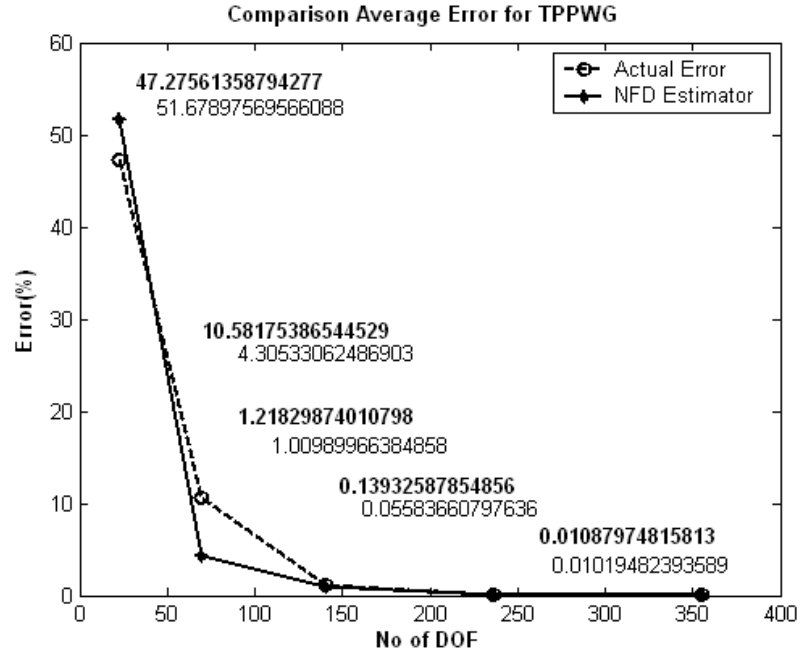
To see how closely the error norms follow the actual error, along the  $x$ - and  $z$ - paths in Figure 5.1, several simulation results will be presented for the global and local error norms versus the total number of degrees of freedom.

### 5.2.2 Evaluation of the NFD estimator

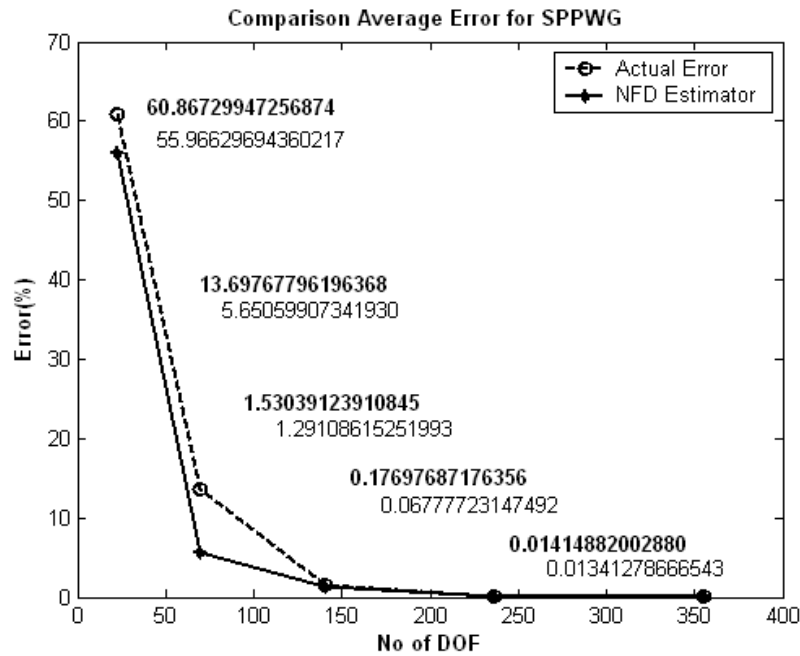
The global NFD error is compared with the actual global error reported in Figure 5.11. The local error estimate is evaluated in Figures 5.12 and 5.13. These estimators are applied with the same FEM solutions used for the actual error. In this case, the FEM solutions are obtained with a uniform order for the basis functions, where the order corresponds to the Nedelec mixed-order spaces described in Chapter III.

The global error estimator decreases as the order of the basis increases. The lowest number of DoF occurs for CT/LN polynomials, the next one occurs for LT/QN functions, and so on until five different representations are included. The global NFD estimator is within 31% of the actual error at all three discretization levels. By comparing

Figures 5.12 and 5.13 with Figure 5.5 and 5.6, it appears that the local error NFD estimator is within in the range of 40%-150% of the actual local error levels.

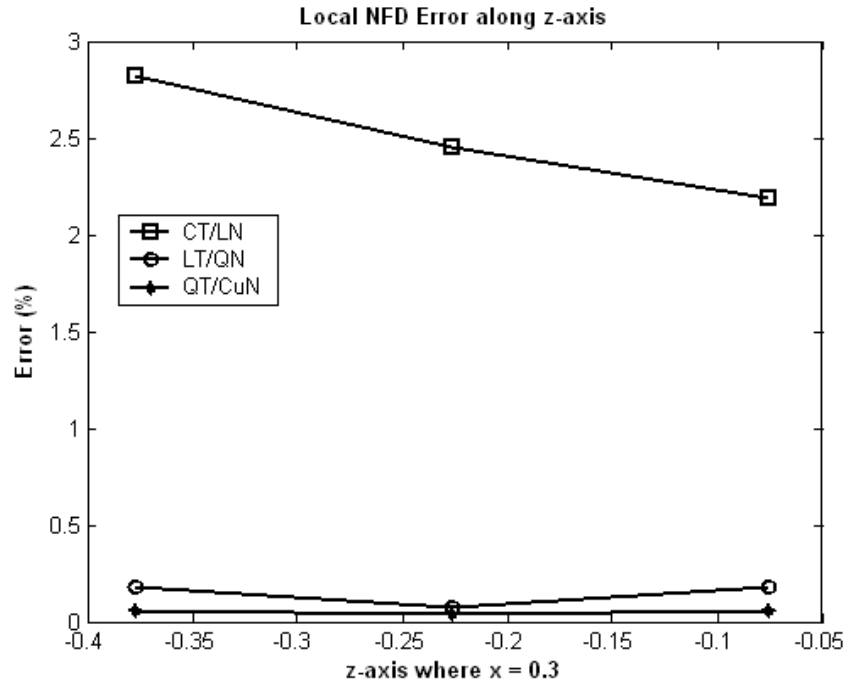


(a) Error Norm for T-PPWG  
(b)

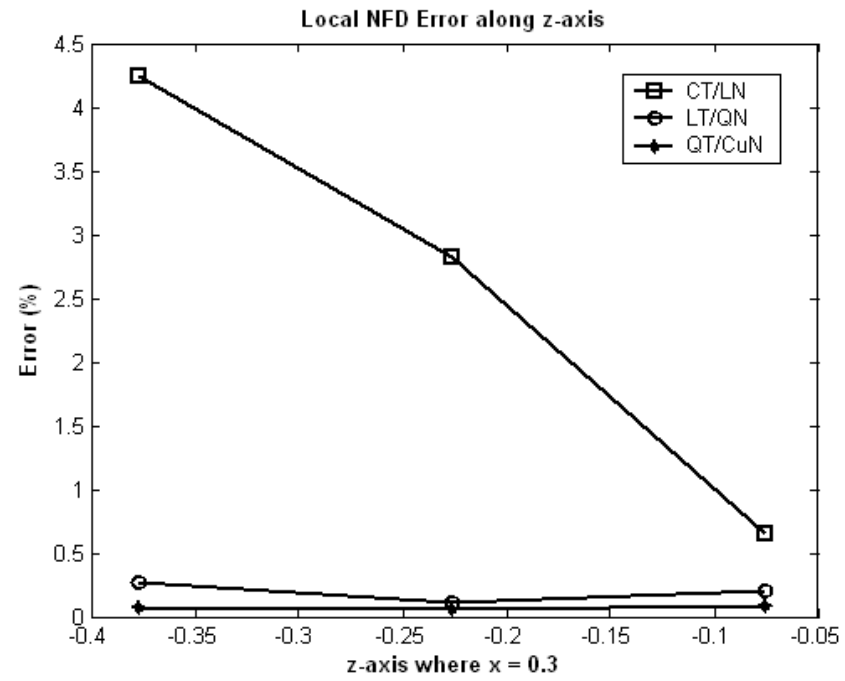


(c) Error Norm for S-PPWG

Figure 5.11 Global error comparison of NFD error estimator with the actual error

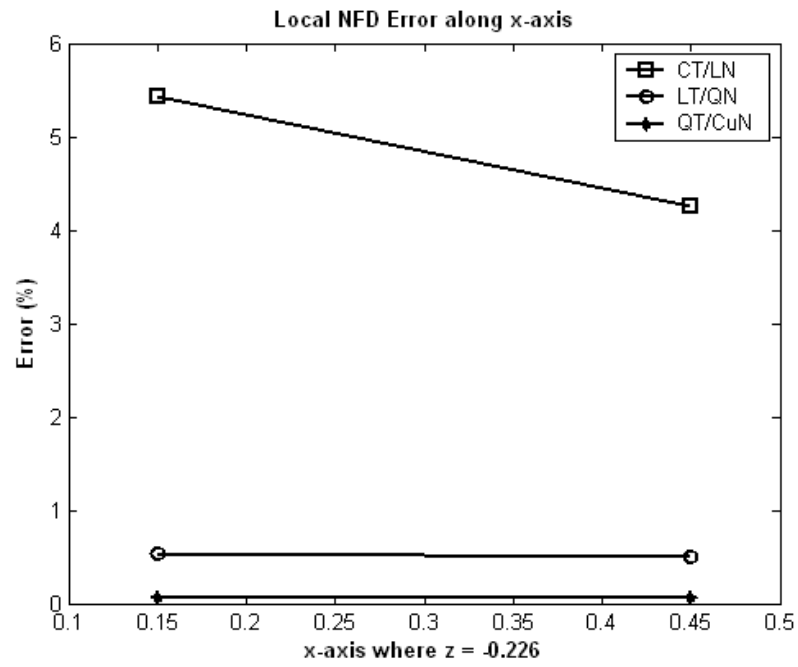


(a) T-PPWG

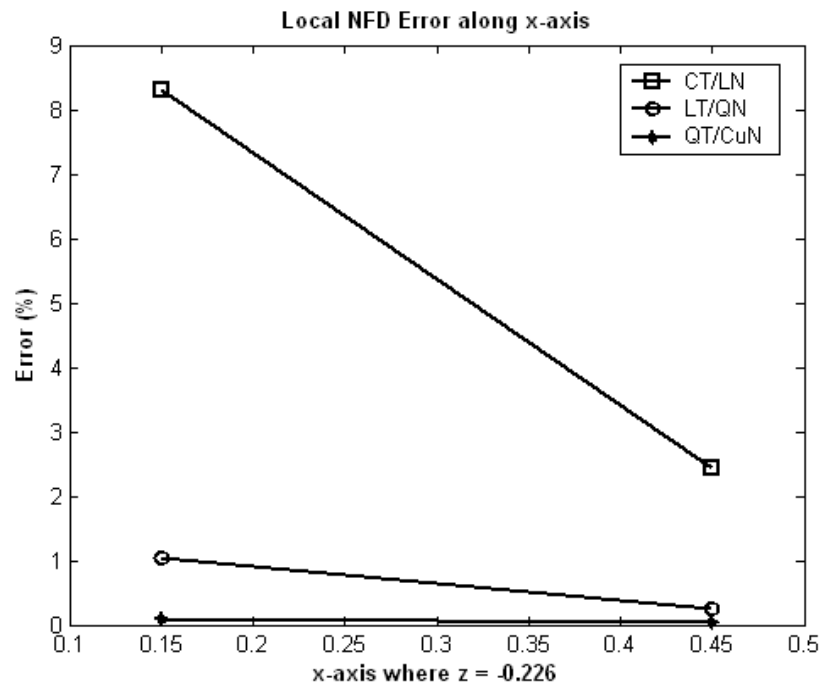


(b) S-PPWG

Figure 5.12 Local NFD error along the z-axis where  $x = 0.3$



(a) T-PPWG



(b) S-PPWG

Figure 5.13 Local NFD error along the x-axis where  $z = -0.226$

### 5.3 Discontinuity of the Curl of Field (DCF) Error Estimator

In this section, an error estimator based on the electric field will be derived from the primary unknown variable, the magnetic field. It is called “the discontinuity of the curl of field” (DCF) error estimator. The estimator measures the discontinuity in the tangential electric field at cell boundaries. The electric field must be obtained from the magnetic field by differentiation.

In this study, the 2D magnetic field transverse to  $y$  is the primary variable and its complementary electric field is directed out of the plane with only a  $y$  component. The electric field should be same in magnitude and phase at both sides of the cell boundaries. The degree of discrepancy in  $E_y$  at the interfacing edges will be used as an error estimator.

#### 5.3.1 Definition of DCF Error Estimator

The DCF error norm is based on the error

$$\bar{E}_k = \hat{n}^{(12)} \times \left[ \frac{1}{\epsilon_r^{(1)}} \nabla \times \bar{\mathbf{H}}_1 - \frac{1}{\epsilon_r^{(2)}} \nabla \times \bar{\mathbf{H}}_2 \right] \quad [A/m^2] \quad (5.16)$$

where edge  $k$  is the interfacing edge between element 1 and element 2, and  $\hat{n}^{(12)}$  is the normal unit vector at the interface of two contiguous cells, 1 and 2. The quantity inside of the bracket is the electric field discontinuity. The expression in (5.16) is evaluated at the center of edge  $k$ .

The curl of the magnetic field is

$$\nabla \times \bar{\mathbf{H}} = \sum_{i=1}^{N_e} h_i \nabla \times \bar{B}_i = h_0^1 \nabla \times \bar{B}_0^1 + h_0^2 \nabla \times \bar{B}_0^2 + h_0^3 \nabla \times \bar{B}_0^3 + \sum_{i=1}^{N_f} h_i^f \nabla \times \bar{B}_i^f \quad (5.17)$$

where  $N_e$  is number of degrees of freedom in the element  $e$  and  $N_f$  is the number of face DoF associated with the element. The edge DoF with non-zero order polynomial degrees belongs to the gradient subspace of the solution space. Therefore their curl values are zero. The discontinuity is determined by two zeroth-order basis functions on other edges that are not the interfacing edge, and by face basis functions that reside inside of the cell. As the order of the basis polynomial increases and the zeroth-order representation is improved, the main contribution to the discontinuity is from the face basis functions. The DCF error estimator essentially ignores discretization error due to basis functions in the gradient subspace.

Coming back to the main subject of this section,  $\bar{E}_k$  represents the tangential discontinuity of the electric field at the interelement edges. Equation (5.16) is normalized as follows

$$e_k = |\bar{E}_k| / N \quad (5.18)$$

where

$$N = |\nabla \times \bar{H}^{inc, peak}| \times N_{edge} = |j\omega \epsilon \bar{E}^{inc, peak}| \times N_{edge} = \omega \epsilon_0 \times N_{edge} [A / m^2]$$

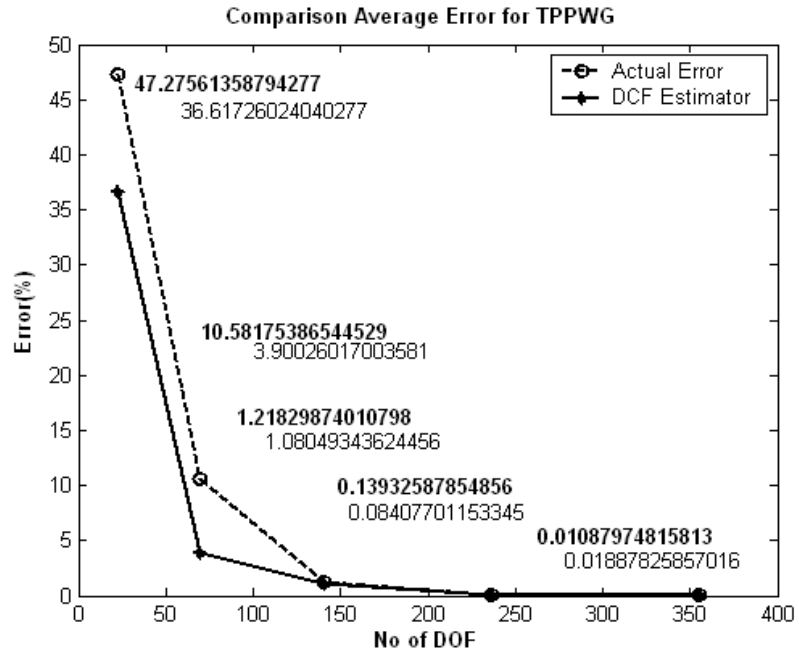
and  $N_{edge}$  is the number of interior edges in the mesh. For all interfacing edges,  $e_k$  represents the relative error norm associated the local edge  $k$ . The global average error



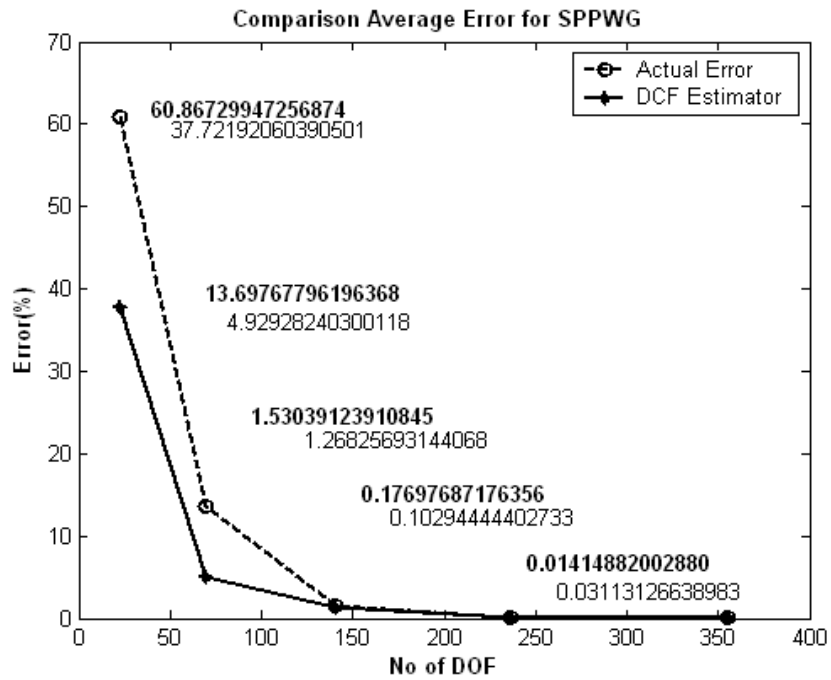
norm,  $e_a$ , of the same numerical solution is defined by averaging the sum of all error norms in the same way as in equation (5.15).

### ***5.3.2 Evaluation of DCF Estimator***

Figure 5.14 compares the global DCF estimator with the actual global error for the PPWG examples. Each marker on the plots corresponds to a different order of basis function, following Nedelec's mixed-order spaces. While five different orders, CT/LN, LT/QN, QT/CuN, etc., are employed for the global error, only the lower three orders are reported for the local error plots. The error estimator and the actual error exhibit agreement to approximately 56%. The comparison of Figures 5.5 and 5.6 with Figures 5.15 and 5.16 conclude that the local error of DCF is in agreement with the actual local error within in the range over 1250% - 6500% depending on the structure.

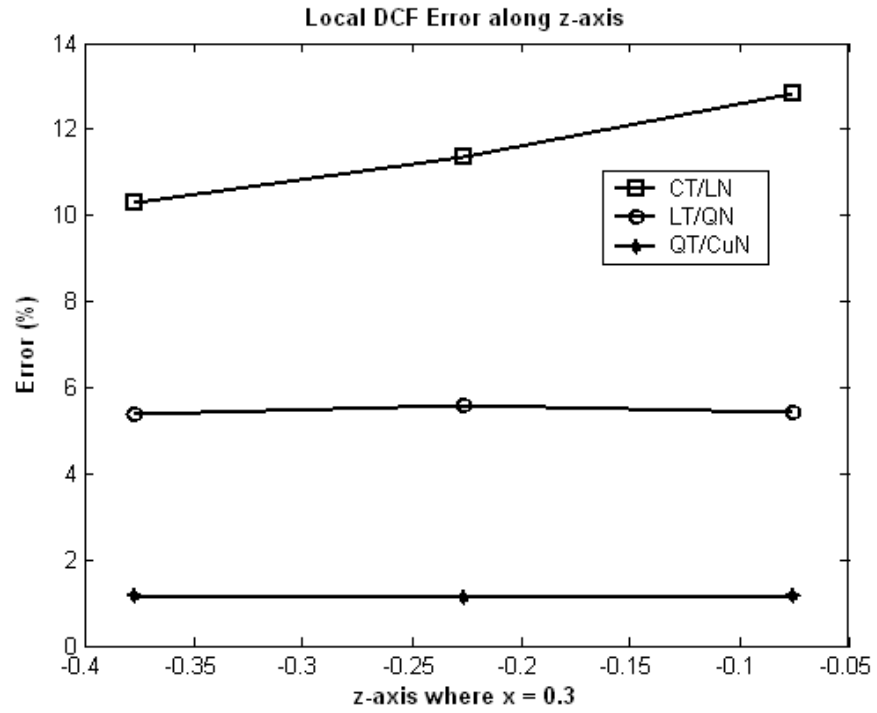


(a) T-PPWG

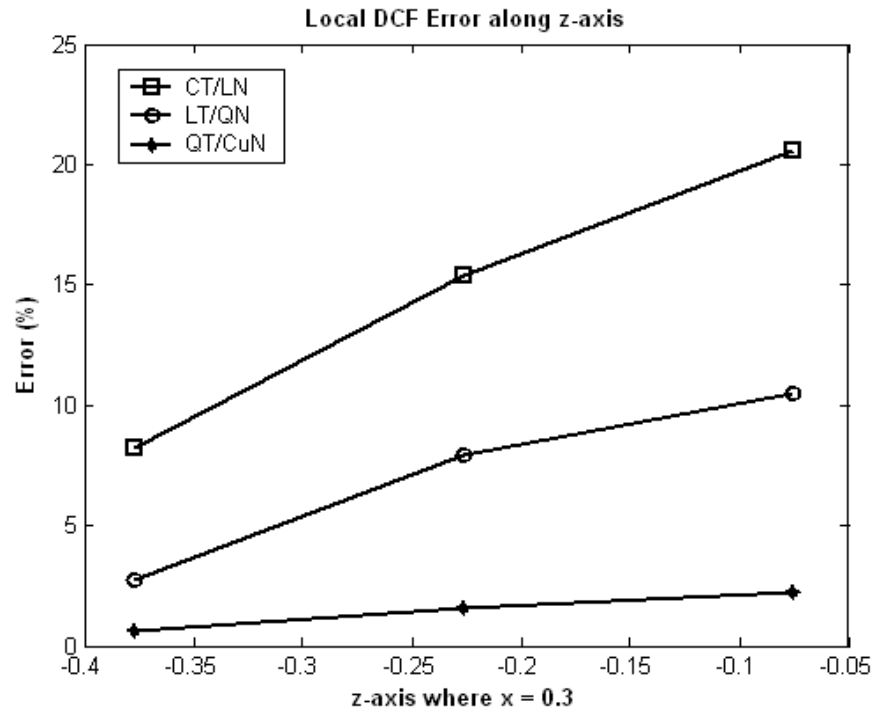


(b) S-PPWG

Figure 5.14 Global error comparison of the DCF error estimator and the actual error in the FEM solution

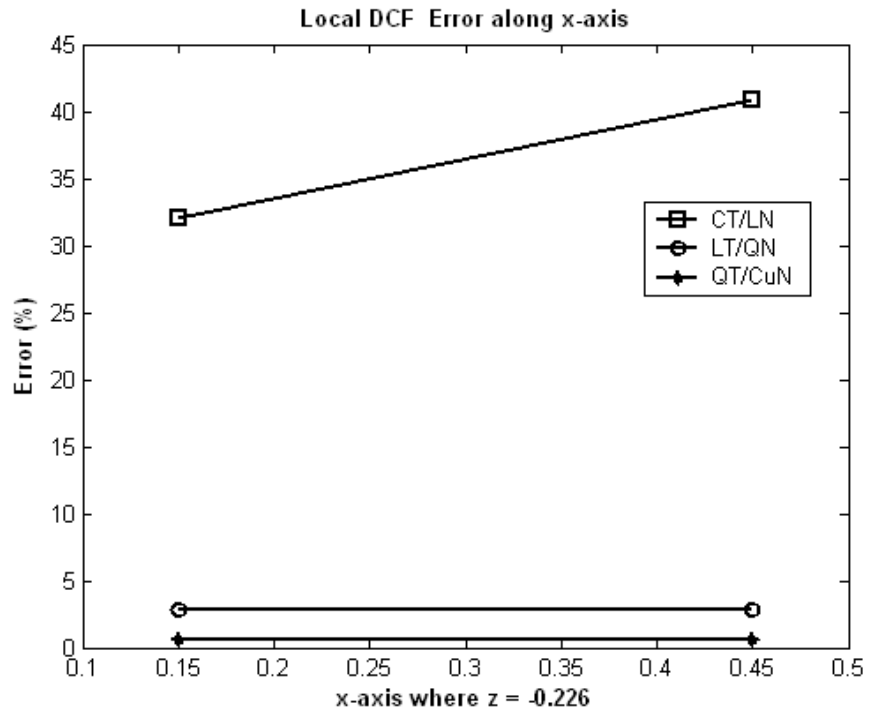


(a) T-PPWG

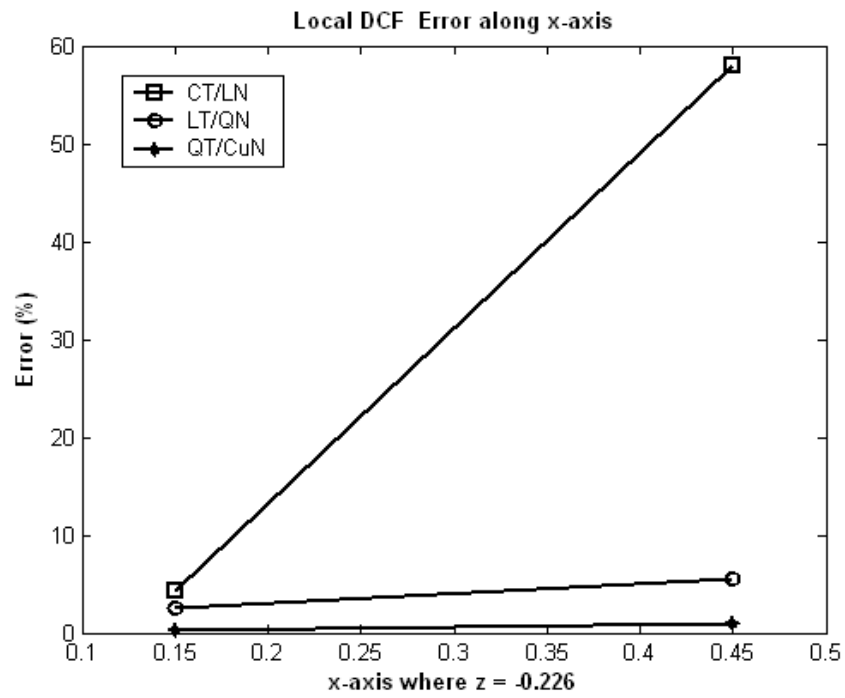


(b) S-PPWG

Figure 5.15 Local DCF error along the z-axis where  $x = 0.3$



(a) T-PPWG



(b) S-PPWG

Figure 5.16 Local DCF error along the x-axis where  $z = -0.226$

#### **5.4. Weak Form Residual (WFR) Error Estimator**

The finite element formulation is based on the solution of a weak form of the residual equation. Since that residual equation is exactly satisfied by the numerical solution, that residual cannot be used directly to estimate the solution error. A closely related estimate can be obtained from the normal derivative discontinuity at interelement cell boundaries. Most residual error estimators in the literature contain a residual error term and the normal derivative discontinuity term as well. The gradient of the field and the normal discontinuity of the field derivative can't measure the errors in the FEM solution but only its steepness and curvature [46,47]. These error estimators can efficiently detect where the field variation is very rapid, such as near the singularities. They fail, however, when higher-order elements are employed [46]. Therefore, better approaches to estimate the residual and normal discontinuity have been proposed, known as the local Dirichlet analysis and local Neumann analysis [47-54].

Fernandes et. al proposed several error estimators and compared their performance [48-52]. One method known as the local error method calculates the local error by solving a differential equation defined by the Neumann problem on each element. A second simplified approach, called the incomplete residual method, is faster than the first approach since the error estimator is derived directly from the driving function of the error differential equation instead of solving it [48]. A third approach, named the complete residual error estimator, includes estimating the error of the gradient of the solution as well as the solution itself without deteriorating its speed and simplicity [50]. Residual errors are tested by separating the effect of the error estimate on the choice of

the element to be refined and that of the refinement termination [51]. The local error method shows better performance than the extended complete residual and incomplete residual methods [50,51]. The implementation of these proposed error estimators is explained in [49].

Even though these residual error estimators are used for electrostatic or magnetostatic problems with scalar basis functions, their extension to a vector formulation is not difficult [36,55-57]. Normal discontinuity as well as volumetric error estimators derived by O.C. Zienkiewicz et al. [58] and W. Daigang et al.[59] have been modified for the vector Helmholtz equation [55]. Validation is provided by showing that the global error estimate agrees with the exact error norm for a rectangular cavity problem. The h- and p- refinements were tested with the proposed error estimators [40,54,55] but p-refinement was not fully tested since these articles only used the first two orders of Webb's vector basis functions [56,57,60].

In this section two residual error estimators will be introduced. The residual error can be defined in two different ways, from the strong vector Helmholtz equation or the variational weak form of that equation:

- Residual from the Vector Helmholtz Equation:

$$\bar{r}_e = \nabla \times \frac{1}{\epsilon_r} \nabla \times \bar{\mathbf{H}} - k_0^2 \mu_r \bar{\mathbf{H}} \quad (5.19)$$

- Residual from the Weak Form:

$$\bar{r}_e = \int \left( \nabla \times \bar{\mathbf{T}} \cdot \frac{\mathbf{1}}{\varepsilon_r} \nabla \times \bar{\mathbf{H}} - k_0^2 \mu_r \bar{\mathbf{T}} \cdot \bar{\mathbf{H}} \right) ds \quad (5.20)$$

The quantity in (5.19) is called the strong form of the residual (SFR) while (5.20) is the weak form residual (WFR). The two residuals are not exactly zero because of insufficient meshes, provided that the function  $\bar{\mathbf{T}}$  in (5.20) is not one of the test functions used to construct the FEM system. Therefore they can be used to construct error estimators. These error estimators are often used in combination with error estimators that reflect the boundary discontinuity such as the DCF or NFD error estimators in previous sections [36,56,57].

The SFR involves two consecutive derivatives of the field. If used with CT/LN vector basis functions, the second derivative of the zeroth-order CT/LN basis function is zero. Since the zeroth-order basis function carries the average value of the tangential variation at the edge, its contribution to error norm should be very significant. Thus the SFR is not straightforward to implement and will not be practical until a way to estimate the second derivative of the basis function is developed. The SFR implementation remains for further study.

In this section the WFR in (5.20) will be considered. The manipulation of (5.20) yields two formulations, described previously in equation (2.38) and equation (2.52). From equation (2.52), a global error norm will be derived and it will be used to test the FEM solution along with the power conservation law when the problem has no analytical solution. A local error norm will be derived from (2.38) in the following sections.

#### 5.4.1 Definition of the Global Weak Form Residual Error Estimator

Equation (2.52) is given as

$$\begin{aligned}
& \iint_{\Gamma} \left( \frac{1}{\epsilon_r} \nabla \times \bar{T} \cdot \nabla \times \bar{H} - k^2 \mu_r \bar{T} \cdot \bar{H} \right) dx dz + \frac{2}{d} \int_{\partial \Gamma_1} \left( \frac{1}{\epsilon_r} \bar{T} \cdot \hat{x} \int_0^d H_x(x', z_1) G(x, x') dx' \right) dt \\
& + \frac{2}{d} \int_{\partial \Gamma_2} \left( \frac{1}{\epsilon_r} \bar{T} \cdot \hat{x} \int_0^d H_x(x', z_2) G(x, x') dx' \right) dt \\
& = \frac{4}{d} \int_{\partial \Gamma_1} \left( \frac{1}{\epsilon_r} \bar{T} \cdot \hat{x} \int_0^d H_x^{inc}(x', z_1) G(x, x') dx' \right) dt \tag{5.21}
\end{aligned}$$

From equations (2.54) and (2.56), a global system matrix is constructed of the form

$$[A] \{h\} = \{g\} \tag{5.22}$$

where the global matrix  $[A]$  is  $N$ -by- $N$  in size and is sparse. The  $N$  denotes the number of test functions and basis functions within the computational domain, which are usually the same. Most of the non-zero elements are gathered near the diagonal and form a band. However, the absorbing boundary condition terms position a number of non-zero entries outside that band. Two column matrices,  $\{h\}$  and  $\{g\}$ , are  $N$ -by-1 in size.  $\{h\}$  is the set of unknowns. For  $\{g\}$ , the non-zero elements represent the contributions of the global test functions on the input port. By solving (5.22) the FEM solution is obtained.

Different matrices  $[A']$  and  $\{g'\}$  can be formed by another set of test functions.

In FEM system, the set of test functions is the same as the set of basis functions. Suppose equations are obtained with one set of test functions substituted into (5.22) that are different from the specific basis functions. Since the FEM solution  $\{h\}$  is approximate, the residual matrix



$$\{r\} = [A']\{h\} - \{g'\} \neq \{0\}. \quad (5.23)$$

will not be zero, where  $\{r\}$  is a column matrix of dimension  $m'$ -by-1. The parameter  $m'$  is the number of alternative test functions employed for  $[A']$  and  $\{g'\}$ , which is usually different from the number of basis functions originally used to obtain the FEM system. To assign a global error to the FEM solution, the global WFR estimator is defined by

$$e_g = \frac{\sum_{i=1}^{m'} |r_i|_{L^2}}{N} \times 100. \quad (5.24)$$

where  $r_i$  is obtained using global test function  $i$ . The normalization factor is

$$N = N_e \sum_i^{m'} |g_i|_{L^2} \quad (5.25)$$

where  $N_e$  is the number of cells in the computational domain and

$$g_i = \frac{4}{d} \int_{\partial\Gamma_1} \left( \frac{1}{\varepsilon_r} \bar{T}_i \cdot \hat{x} \int_{x1}^{x2} H_x^{inc}(x', z_1) G(x, x') dx' \right) dt. \quad (5.26)$$

The limits  $x1$  and  $x2$  denote the integration range along the cell edge that is limited to the length of the edge along the input port.

If the FEM solution  $\{h\}$  is the exact solution, then the residual matrix  $\{r\}$  contains nothing but zero elements independent of the test function. The global WFR error norm in (5.24) can be used to evaluate the FEM solution accuracy even when no analytical solution is available. In this study, test functions of one order higher than the basis functions will be employed to compute the WFR estimator.

#### 5.4.2 Definition of Local Weak Form Residual Error Estimator

The manipulation of the weak form equation in (5.20) yields the local residual vector

$$[R]_k = \iint_{\Gamma_k} [(\nabla \times \bar{T}) \cdot \left( \frac{1}{\epsilon_r} \nabla \times \bar{H} \right) - \bar{T} \cdot k^2 \mu_r \bar{H}] dx dz + \int_{\partial \Gamma_k} (\bar{T} \cdot \hat{n} \times \frac{1}{\epsilon_r} \nabla \times \bar{H}) dt. \quad (5.27)$$

If imposed over a single element,  $\Gamma_k$  is the interior of the cell  $k$  and  $\partial \Gamma_k$  represent the cell boundary. A local element matrix can be obtained in the same form as equation (5.22) for element  $k$ , and it is given by

$$[A]_k \{h\}_k = \{g\}_k. \quad (5.28)$$

The subscript means that each matrix is defined by degrees of freedom in a local element  $k$  and the dimensions  $m$  and  $n$  represent the number of test and basis functions overlapping cell  $k$ . The right hand side vanishes unless the cell boundary is contiguous to the input or the output port. The local residual vector for cell  $k$  is defined by

$$\{r\}_k = [A]_k \{h\}_k - \{g\}_k. \quad (5.29)$$

Normally the test functions residing on the cell boundary are involved in local residuals for neighboring cells, and thus the residual is not localized cell-by-cell. A careful choice of test functions circumvents this problem. First, test functions should be independent of any other cell for the local residual purpose. In other words, the test functions should be tangentially confined to a single cell. They are the subset of test functions in Table 3.1 that have no nonzero tangential component on the cell boundary. Second, the test functions should be different from the basis functions used for the FEM solution,  $\{h\}_k$ . In this study hierarchical functions of one additional polynomial degree

will be employed for computing the error estimator. Using test functions satisfying these conditions, Equation (5.27) is manipulated into the form

$$[R]_k = \iint_{\Gamma_k} \left( \nabla \times \bar{T}_{a/b}^f \cdot \frac{1}{\epsilon_r} \nabla \times \bar{H} - k_0^2 \mu_r \bar{T}_{a/b}^f \cdot \bar{H} \right) dx dz \quad (5.30)$$

$\bar{T}_{a/b}^f$  represents a member of the next greater-degree mixed-order test function set defined in Table 3.1 that has no tangential component on the cell boundary. A new local residual vector is computed as follows

$$\{r'\}_k = [A']_k \{h\}_k - \{g'\}_k. \quad (5.31)$$

The residual  $\{r'\}_k$  is a column vector with the number of entries the same as the number of test functions used in cell  $k$ . Note that each entry may change depending on the normalization of the hierarchical vector test function. Therefore, the test functions should be scaled to unit-stored energy according to

$$\hat{T}_i = S_i \bar{T}_i \quad . \quad (5.32)$$

where

$$S_i = \sqrt{\frac{1}{\iint_e \bar{T}_i \cdot \bar{T}_i dx dz}} \quad (5.33)$$

The local WFR error estimator is defined for cell  $k$  as

$$E_k = \frac{\sum_{i=1}^{m'} |r'_i|_{L^2}}{N} \times 100 \quad (5.34)$$

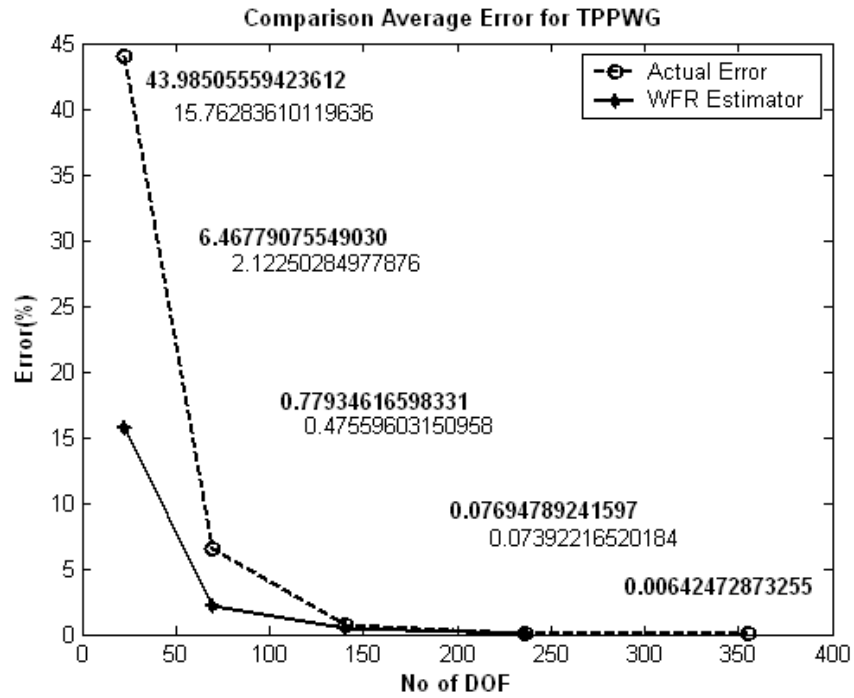
where  $m'$  is the number of test functions used in equation (5.30). The WFR norm is one way of estimating the residual over the cell. The normalization value is the same as in equation (5.25), but uses

$$\{g\} = \frac{4}{d} \int_{\partial\Gamma_1} \left( \frac{1}{\varepsilon_r} \hat{T}_{\max}^e \cdot \hat{x} \int_{x_1}^{x_2} H_x^{inc}(x', z_1) G(x, x') dx' \right) dt \quad . \quad (5.35)$$

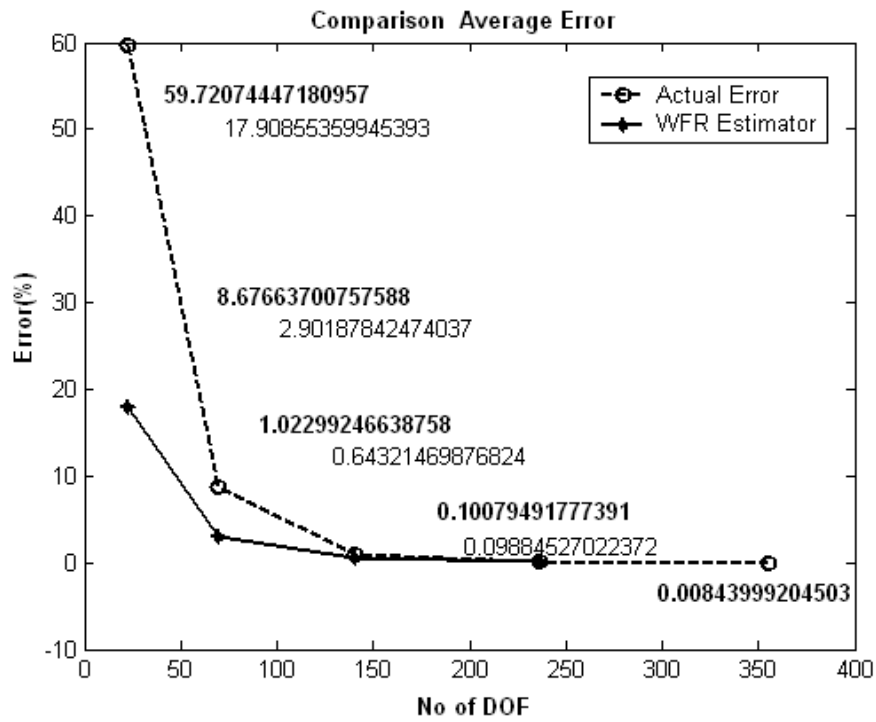
where  $\hat{T}_{\max}^e$  represents a normalized test function of the next higher degree abutting the input port. The average error is the sum of all local error estimates. Simulation results for the global WFR and the local WFR error estimates are presented in the next section.

#### ***5.4.3 Evaluation of WFR Error Estimator***

Figures 5.17 compares the global WFR error estimate to the actual FEM error from these results for the T-PPWG and S-PPWG examples. It appears that the WFR estimator is within 44% of the actual error based on five different basis orders. Figures 5.18 and 5.19 plot the local error estimates along the x- and z-axis and should be compared with cell-based actual local errors in Figures 5.7 and 5.8 for the lower three basis orders. The results are in agreement with the actual error to within 1400%.

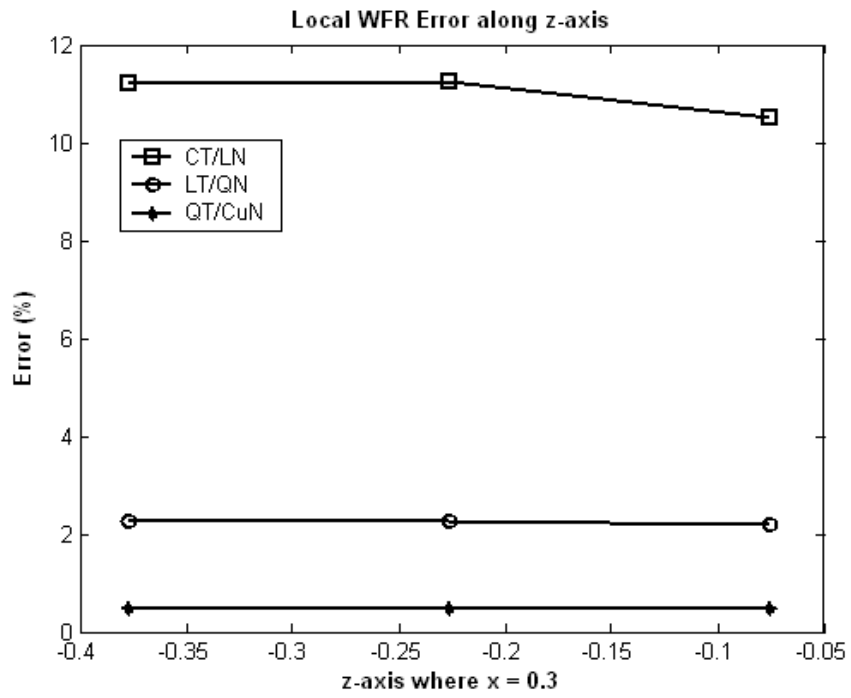


(a) T-PPWG

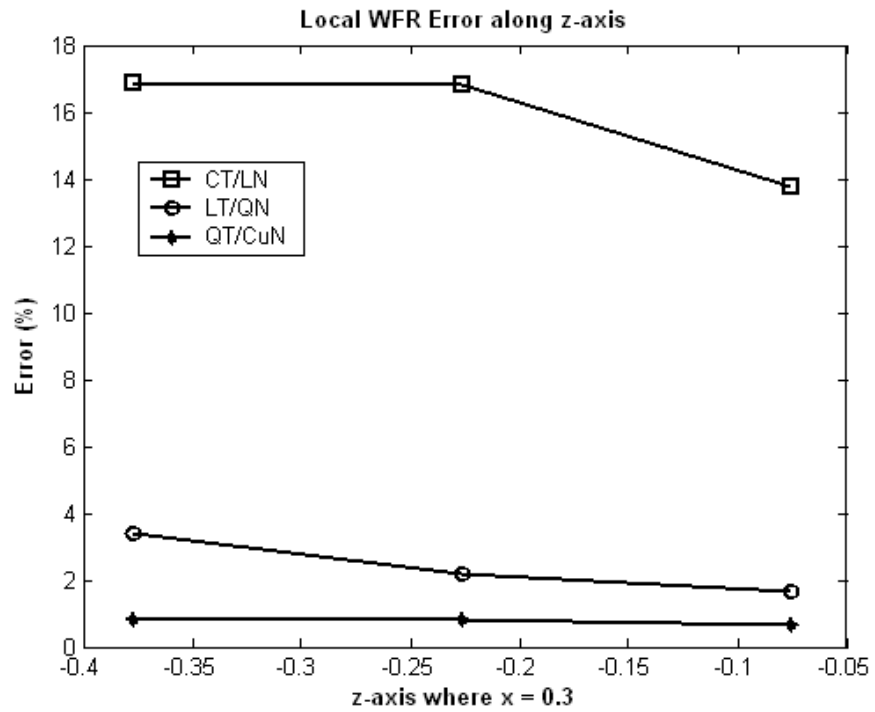


(b) S-PPWG

Figure 5.17 Global error comparison of WFR error estimator

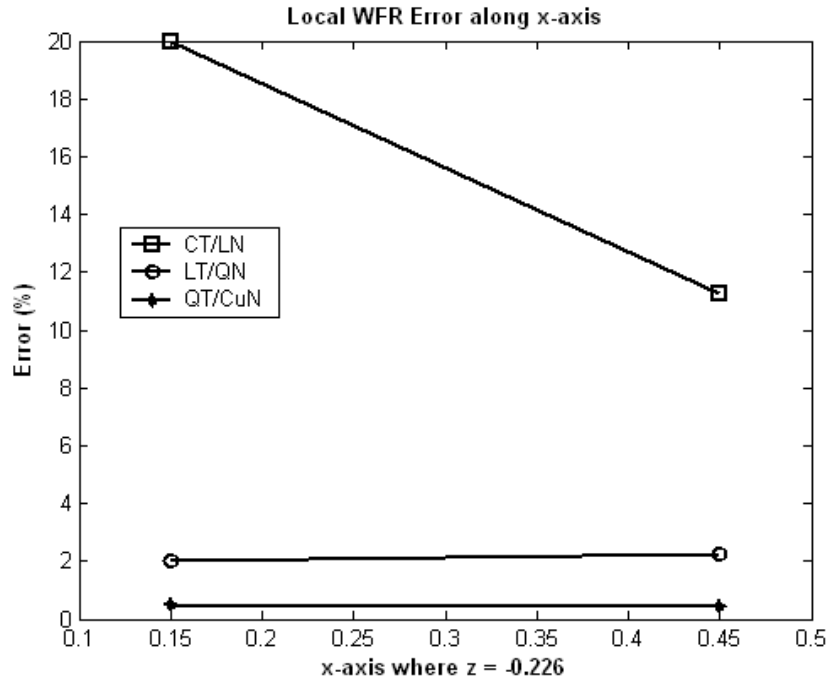


(a) T-PPWG

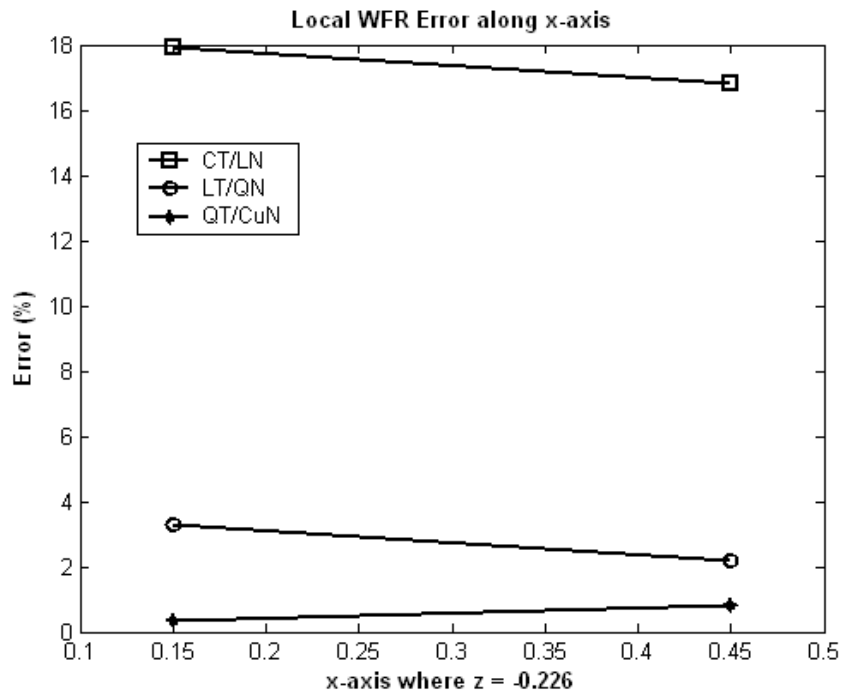


(b) S-PPWG

Figure 5.18 Local WFR error along the z-axis where  $x = 0.3$



(a) T-PPWG



(b) S-PPWG

Figure 5.19 Local WFR error along the x-axis where  $z = -0.226$

### **5.5. The Coefficient Sensitivity of the Highest-Order Polynomial (CSH) Error Estimator**

J. P. Webb suggested a new kind of error estimator. The sensitivity of a global quantity of interest to a new added DoF in a cell is taken as a targeted error estimator for that global quantity. Many FEM error estimators are focused on the field itself, but, in a specific application, users are more interested in secondary quantities such as inductance, capacitance, or scattering parameters. Webb classified the error estimators into two categories: a general error indicator (GEI) and a targeted error indicator (TEI). A GEI is used to estimate the accuracy of the field, the primary variable itself in an FEM formulation. However, the improvement of the field accuracy may be slow within an adaptive FEM procedure. It may be more efficient to base the adaptive process on the accuracy of a specific global quantity, say one of the scattering parameters. To speed up the adaptive refinement procedure to yield accurate scattering parameters, a TEI was proposed [61-63].

The ideal targeted error indicator (TEI) is very costly because the FEM has to resolve a problem having each element order increased by one in order to calculate the sensitivity of scattering parameters to the new DoFs. An approximate approach to this ideal TEI has been proposed to calculate the sensitivity to a new added DoF in an element without all new DoFs. It outperforms the ideal TEI in terms of cost and speed [62].

In this section, a new GEI error estimator is proposed that is motivated from the easy calculation of sensitivity and the characteristics of hierarchical vector elements. The estimator approximates the sensitivity of the stored energy that the highest degree



hierarchical polynomial contributes to an element, relative to that of all lower degree hierarchical polynomials in that element. The more energy that is stored in the highest degree polynomial, the more additional DoF should be assigned to that cell during the subsequent adaptive refinement step. The magnetic FEM formulation is used in this study and the stored magnetic energy can be easily calculated from

$$\begin{aligned}
 U_{\tilde{H}} &= \frac{1}{2} \iint_e \mu \tilde{H} \cdot \tilde{H} dx dz \\
 &= \frac{1}{2} \mu \sum_{p \in e} h_p^2 \iint_e \bar{B}_p \cdot \bar{B}_p dx dz
 \end{aligned} \tag{5.36}$$

where  $e$  represents the element of interest and  $p$  represents the polynomial order in that element. Since (5.36) depends on the normalization of each hierarchical vector basis function, they should be scaled to unit stored energy as explained in (5.33) and (5.34), using

$$S_i = \sqrt{\frac{1}{\iint_e \bar{B}_i \cdot \bar{B}_i dx dz}} . \tag{5.37}$$

In this calculation, Gauss-Quadrature numerical integration is employed. The normalized vector function is denoted by

$$\hat{B}_i = S_i \bar{B}_i . \tag{5.38}$$

Once the FEM solution is obtained with the normalized basis, equation (5.36) reduces to

$$U_{\hat{H}} = \frac{1}{2} \mu \sum_{p \in e} \hat{h}_p^2 \iint_e \hat{B}_p \cdot \hat{B}_p dx dz = \frac{1}{2} \sum_{p \in e} \hat{h}_p^2 . \tag{5.39}$$

The introduction of a normalization factor for the vector basis functions makes the problem much easier; the simple calculation of the square of the coefficient of interest gives the magnitude of the stored energy of that basis function.

The new error estimator is named the “coefficient sensitivity of the highest-order polynomial” (CSH) error estimator. If the sensitivity of the highest-order coefficients is large, the energy stored in the highest-order basis is still substantial and additional basis functions are required in that cell. Compared to the previous error estimators, the CSH error estimator begins with the LT/QN hierarchical vector basis functions in order to have two different orders, in this case, constant and linear variation in the tangential component, available. The CSH error norm can be associated with cell edges.

### 5.5.1 Definition of CSH Error Estimator

Consider first the numerical magnetic field given by the linear combination

$$\begin{aligned} \hat{H}_e = & \left[ \hat{h}_1 \hat{B}_1 + \hat{h}_2 \hat{B}_2 + \hat{h}_3 \hat{B}_3 \right]_{0/1} + \left[ \hat{h}_4 \hat{B}_4 + \hat{h}_5 \hat{B}_5 + \hat{h}_6 \hat{B}_6 + \hat{h}_7 \hat{B}_7 + \hat{h}_8 \hat{B}_8 \right]_{1/2} \\ & + \left[ \hat{h}_9 \hat{B}_9 + \hat{h}_{10} \hat{B}_{10} + \hat{h}_{11} \hat{B}_{11} + \hat{h}_{12} \hat{B}_{12} + \hat{h}_{13} \hat{B}_{13} + \hat{h}_{14} \hat{B}_{14} + \hat{h}_{15} \hat{B}_{15} \right]_{2/3} \end{aligned} \quad (5.40)$$

where the vector basis/test functions are normalized as in (5.38) over a physical element. The bracket classifies the basis function order according to Table 3.1. All the basis functions in a bracket are used together when uniformly increasing the polynomial order. With the CSH error estimator, a minimum of CT/LN and LT/QN basis functions should be used to obtain meaningful results. The error estimator requires the calculation of the ratio of the energy of the LT/QN functions to that of the combination of the CT/LN and LT/QN functions.

The CSH error estimator is defined by

$$E_k = \frac{\sum_{i \in S_{2/3}} \left| \hat{h}_{k,i} \right|_{L^2}^2}{\sum_{i \in S_T} \left| \hat{h}_{k,i} \right|_{L^2}^2} \quad (5.41)$$

where  $S_{a/b}$  is the set of basis function with a/b order in Table 3.1. The denominator is the total energy stored by all basis functions used in a cell. The numerator sums the energy kept in the highest basis functions. A local error could be assigned to an edge or a cell, either of index  $k$ . Two CSH local error estimators, are given by

$$e_{edge,k} = \frac{E_{1,k} + E_{2,k}}{2N_{edge}} \times 100 \quad (5.42)$$

for an edge-based error norm where subscript 1 and 2 represent two cells sharing edge  $k$ . and

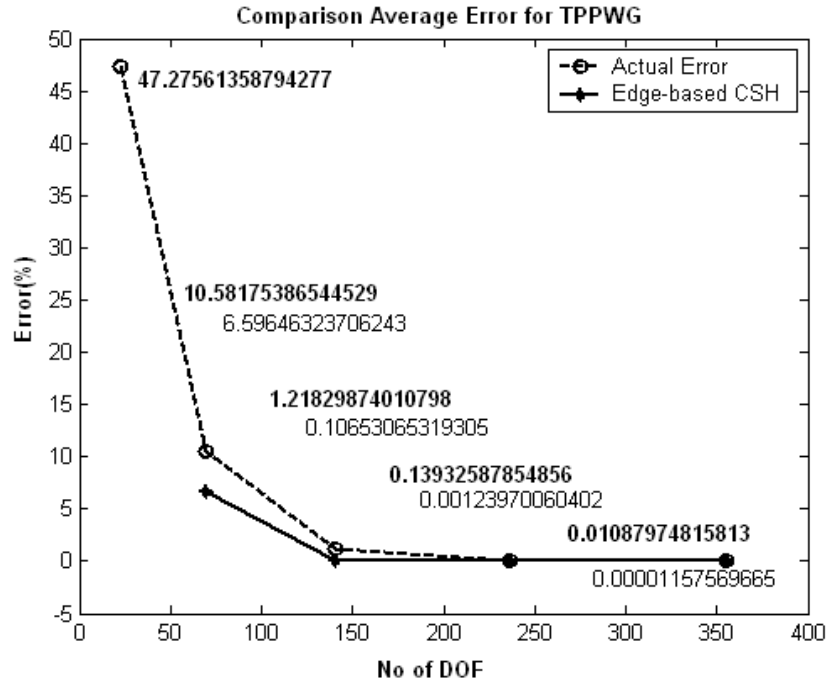
$$e_{cell,k} = \sum_{i=1}^3 \frac{E_{edge,i}}{N_{edge}} \times 100 \quad (5.43)$$

for a cell-based error norm. The edge-based error norm is averaged by two contiguous cells when the edge is shared. In equation (5.43), the subscript  $i$  represents the three local edges on cell  $k$ . The global average error estimate is defined by the sum of all local error estimates.

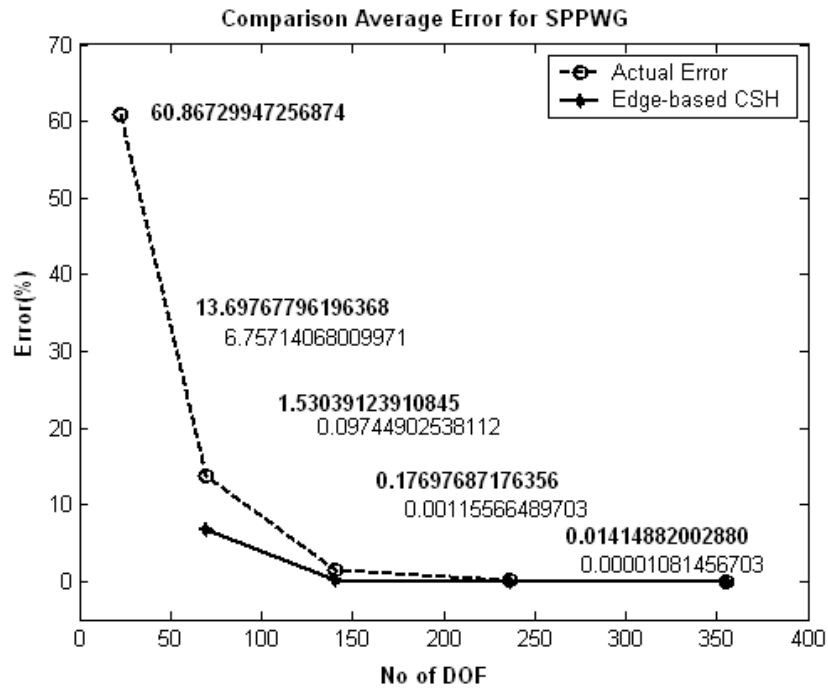
### 5.5.2 Evaluation of CSH Error Estimator

Figure 5.20 reports the edge-based global error from equation (5.42) while Figure 5.21 reports the cell-based global error of equation (5.43). The simulation results in Figures 5.20 and 5.21 confirm that the global CHS error estimator decreases as the basis

polynomial order increases, but they only agree within 85% for edge-based and 120 % for cell-based errors. Figures 5.22 through 5.25 depict the local error estimator for edge-based and cell-based errors as well. They are to be compared to the actual local error in Figures 5.5 through 5.8. The edge-based local estimator agrees within 100% within the actual local error while the cell-based estimator is in agreement within 260% of the actual error. Even though these CSH estimators appear to be poor at estimating the true error, they could be used within a p-adaptive technique to systematically improve the numerical solution.

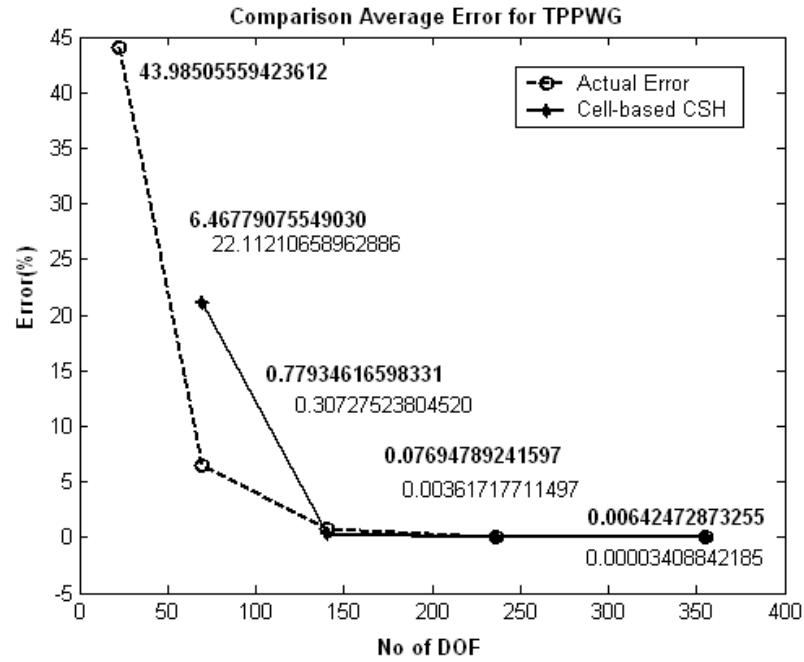


(a) T-PPWG

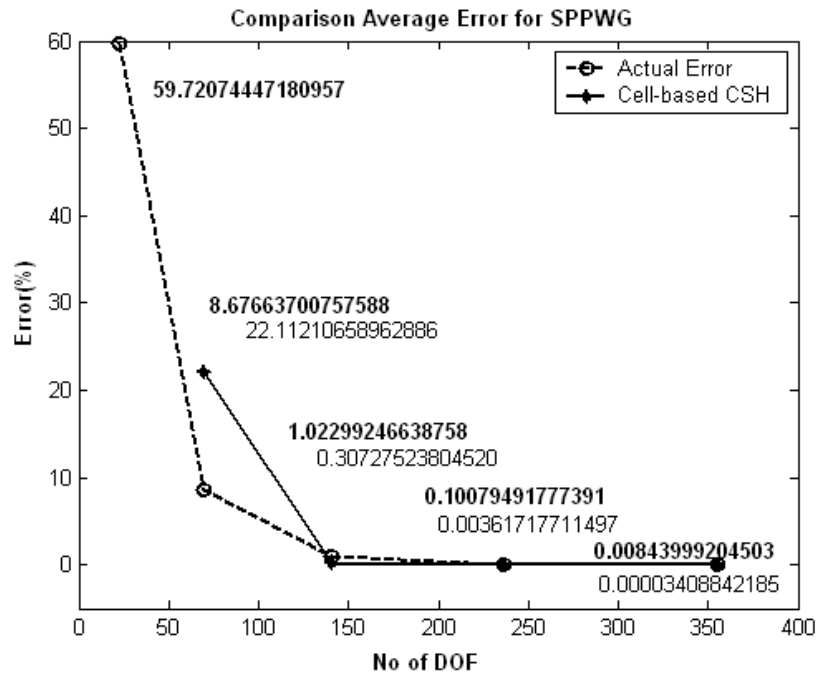


(b) S-PPWG

Figure 5.20 Global error comparison of the edge-based CSH error estimator

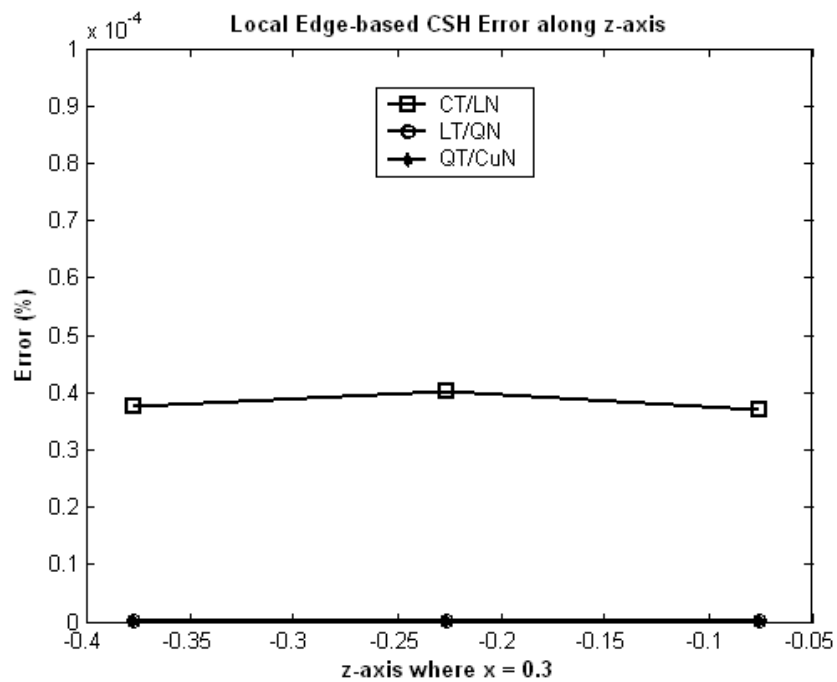


(a) T-PPWG

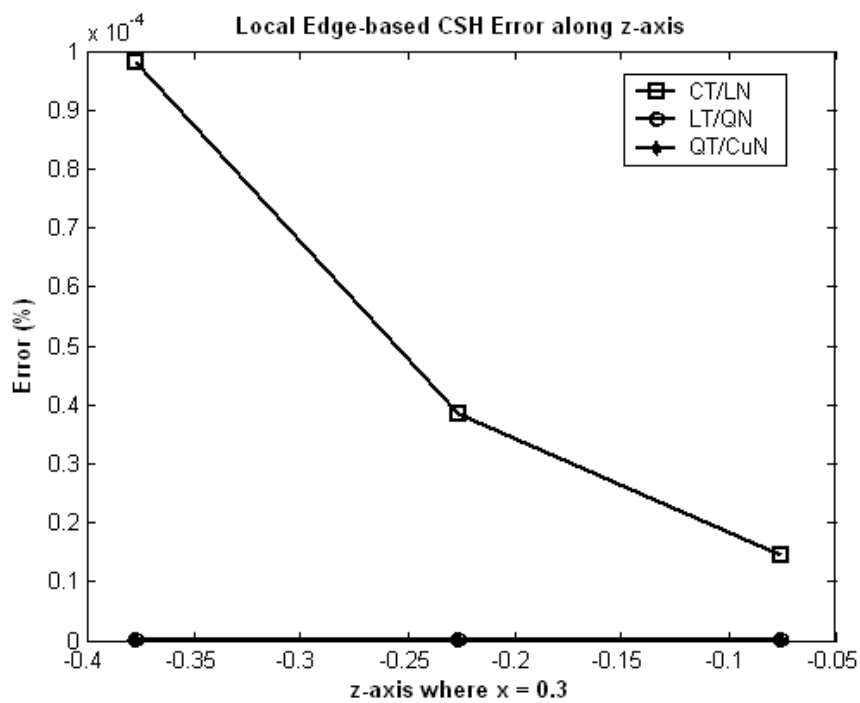


(b) S-PPWG

Figure 5.21 Global error comparison of the cell-based CSH error estimator

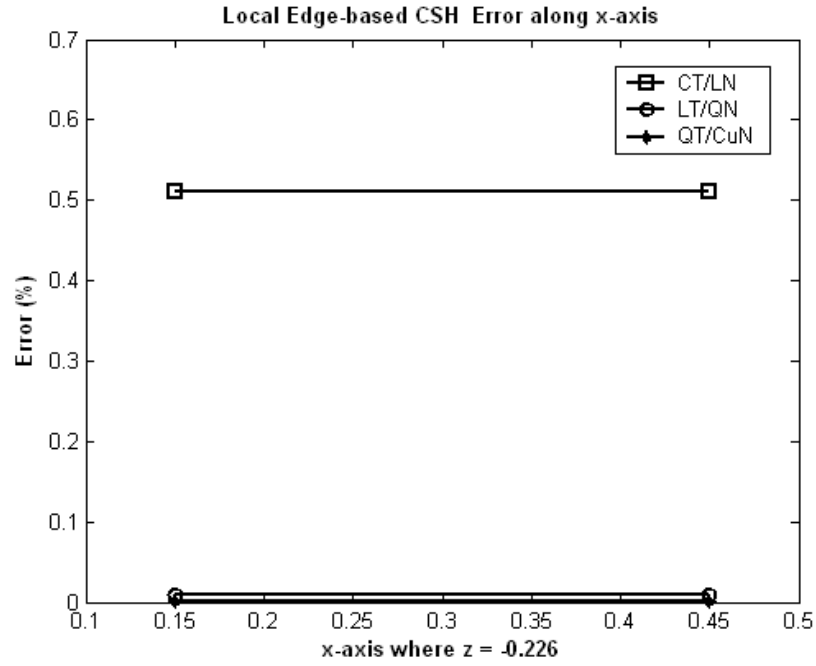


(a) T-PPWG

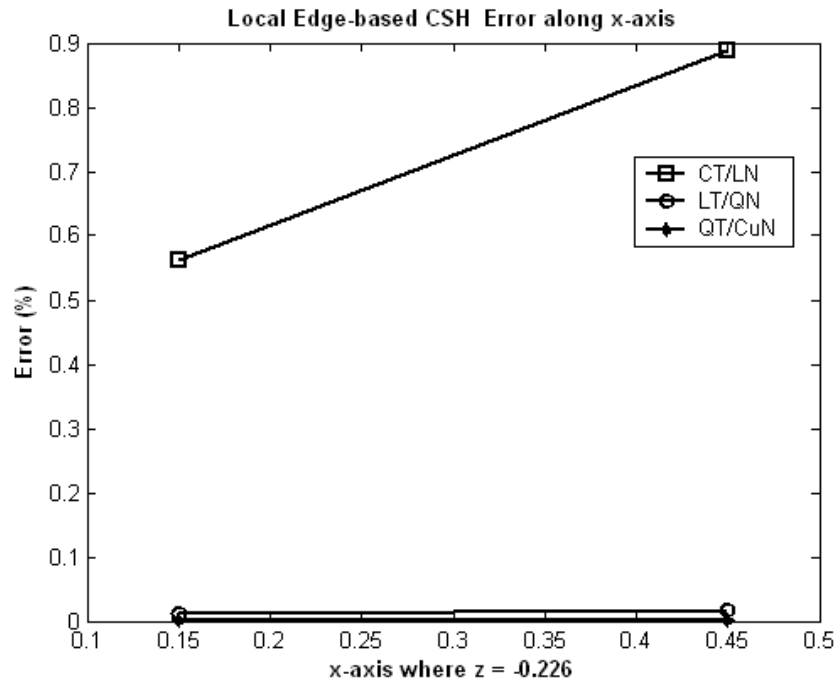


(b) S-PPWG

Figure 5.22 Local edge-based CSH error along the z-axis where  $x = 0.3$



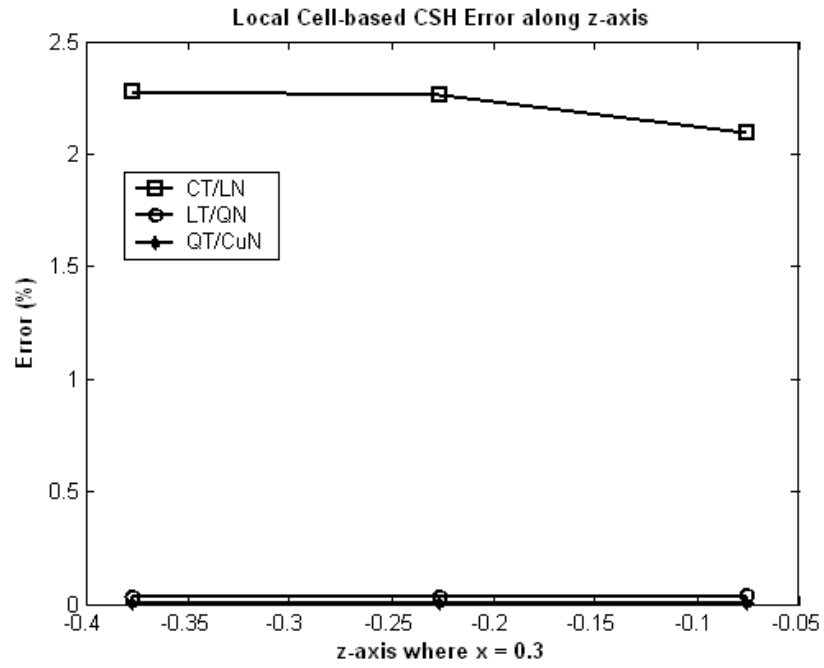
(a) T-PPWG



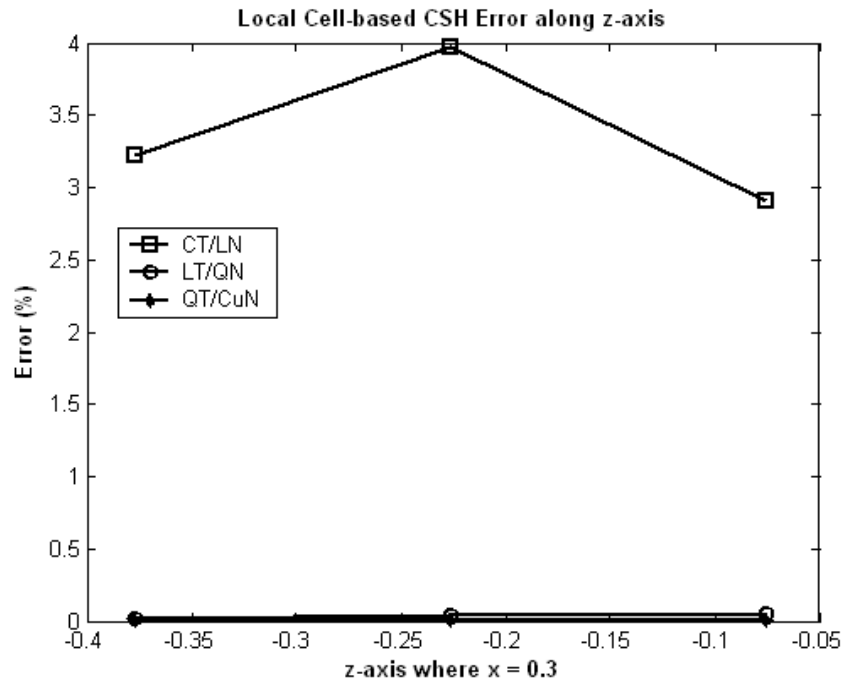
(b) S-PPWG

Figure 5.23 Local edge-based CSH error along the x-axis where  $z = -0.226$



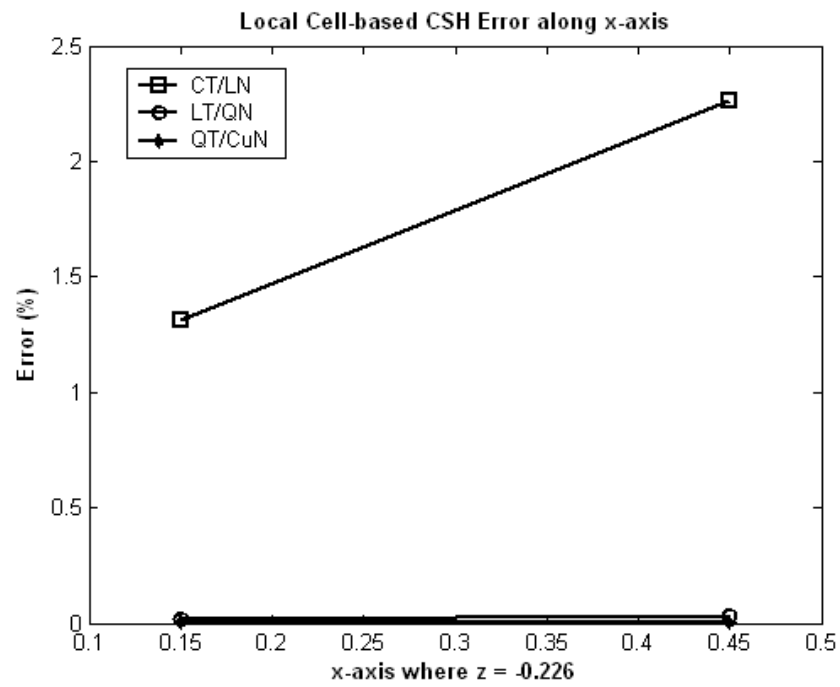


(a) T-PPWG

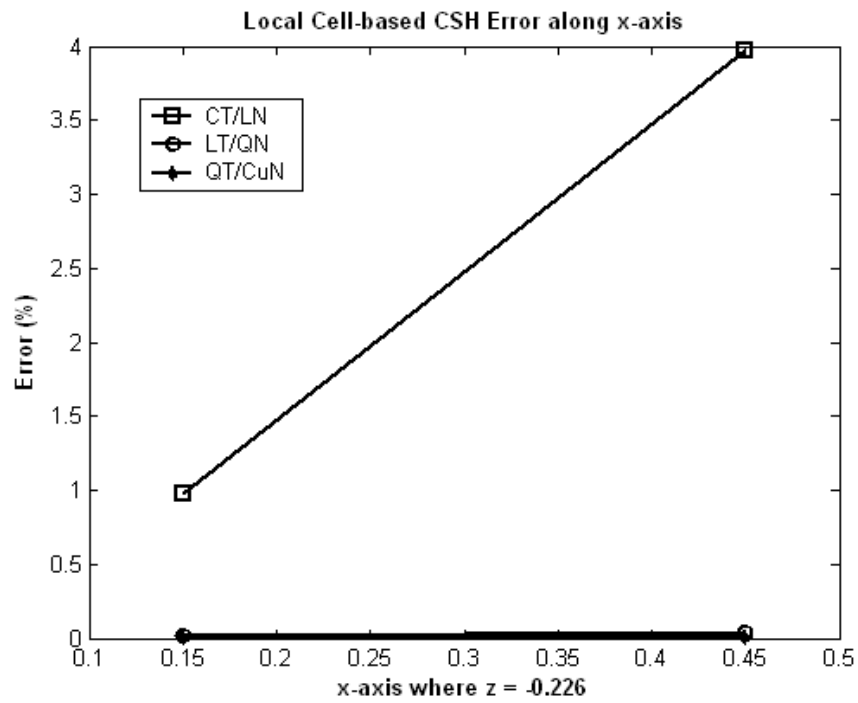


(b) S-PPWG

Figure 5.24 Local cell-based CSH error along the z-axis where  $x = 0.3$



(a) T-PPWG



(b) S-PPWG

Figure 5.25 Local cell-based CSH error along the x-axis where  $z = -0.226$

## **5.6 Evaluation of Error Estimators by Comparing Global Errors and Local Errors with Actual Errors**

In the previous sections, simulation results for global and local errors obtained from four error estimators are compared with the actual errors. The same FEM solution is used for comparison. For the T-PPWG and S-PPWG examples, the actual error is easily calculated.

In this section, the four error estimators previously introduced will be evaluated in terms of their accuracy in estimating the global error and local error. The previous functions will be used as the source of the prediction accuracy. The percentage errors in the estimates are tabulated in Table 5.1 and 5.2 for T-PPWG and S-PPWG, respectively. Each percentage error is based on the difference of the two values specified on the plots of the global error. Tables 5.3 through 5.6 represent the percentage difference between the local estimates and the actual local error. At the bottom of each table, the average values of the global or local errors are presented for comparison. In these tables, a percentage error less than 100% implies that the estimate is within a factor of 2 of the actual error. Such an estimate is likely to be quite useful in an adaptive refinement procedure.

The estimate from the cell-based and edge-based CSH estimators approaches 100 %. For these structures, the CSH estimator significantly under-estimates the actual error as the order of the basis polynomial increases. Thus, the CSH estimator produces error estimates that are essentially zero and lead to a percentage error of 100%. For the DCF and WFR estimators, the local error estimates are much larger than 100%. These

estimators over-estimate the actual error as the order increases. However, the average local error estimates decrease as the order of the basis functions increases, and provide some guidance to an adaptive refinement process.

For the global error, the NFD error estimator appears to offer the best performance and the cell-based CSH estimator seems the worst. The NFD estimator also appears best at estimating local error. Although the error range of the DCF and WFR estimators is very broad, the local estimates decrease in proportion to the actual errors.

It is not possible to draw a conclusion as to which estimator is the best in overall performance. To further explore the utility of these estimators for local error presentation, a numerical solution is corrupted with a known error and used to test each estimator in the following section.

Table 5.1 Percentage error in the global error estimates for T-PPWG

<b>EST order</b>	<b>NFD</b>	<b>DCF</b>	<b>WFR</b>	<b>Cell-based CSH</b>	<b>Edge-based CSH</b>
<b>0</b>	9.31	22.55	64.16		
<b>1</b>	59.31	63.14	67.18	225.27	37.66
<b>2</b>	17.11	11.31	38.98	58.27	91.26
<b>3</b>	59.92	39.65	3.932	95.10	99.11
<b>4</b>	6.30	73.52		99.45	99.89
<b>Average</b>	<b>30.40</b>	<b>42.03</b>	<b>43.56</b>	<b>119.53</b>	<b>81.98</b>

Table 5.2 Percentage error in the global error estimates for S-PPWG

<b>EST</b> <b>order</b>	<b>NFD</b>	<b>DCF</b>	<b>WFR</b>	<b>Cell-based</b> <b>CSH</b>	<b>Edge-based</b> <b>CSH</b>
<b>0</b>	8.05	38.03	70.01		
<b>1</b>	58.75	64.01	66.56	154.85	50.67
<b>2</b>	15.64	17.13	37.12	69.96	93.63
<b>3</b>	61.70	41.83	1.93	96.41	99.35
<b>4</b>	5.20	120.03		99.60	99.92
<b>Average</b>	<b>29.87</b>	<b>56.21</b>	<b>43.91</b>	<b>105.20</b>	<b>85.90</b>

Table 5.3 Percentage error in the local error estimates along the x-axis for T-PPWG

<b>EST</b> <b>order</b>	<b>NFD</b>	<b>DCF</b>	<b>WFR</b>	<b>Cell-based</b> <b>CSH</b>	<b>Edge-based</b> <b>CSH</b>
<b>0</b>	178.75	1997.56	969.23		
<b>1</b>	28.56	604.24	392.73	315.39	27.60
<b>2</b>	232.63	299.12	1773.46	5.43	48.59
<b>3</b>	77.97	133.79	1968.64	91.15	96.65
<b>4</b>	251.80	15634.79		98.59	99.37
<b>Average</b>	<b>153.94</b>	<b>4272.32</b>	<b>1276.02</b>	<b>127.63</b>	<b>68.05</b>

Table 5.4 Percentage error in the local error estimates along the x-axis for S-PPWG

<b>EST</b> <b>order</b>	<b>NFD</b>	<b>DCF</b>	<b>WFR</b>	<b>Cell-based</b> <b>CSH</b>	<b>Edge-based</b> <b>CSH</b>
<b>0</b>	132.22	1245.12	414.17		
<b>1</b>	6.15	492.76	1155.76	176.52	4.68
<b>2</b>	220.75	287.80	1661.28	66.32	27.13
<b>3</b>	90.64	30.14	2364.85	96.90	97.25
<b>4</b>	247.25	27591.66		99.61	99.05
<b>Average</b>	<b>139.40</b>	<b>6447.54</b>	<b>1399.01</b>	<b>109.84</b>	<b>57.03</b>

Table 5.5 Percentage error in the local error estimates along the z-axis for T-PPWG

<b>EST</b> <b>order</b>	<b>NFD</b>	<b>DCF</b>	<b>WFR</b>	<b>Cell-based</b> <b>CSH</b>	<b>Edge-based</b> <b>CSH</b>
<b>0</b>	51.53	600.68	559.68		
<b>1</b>	78.61	701.70	486.66	479.27	99.99
<b>2</b>	37.53	1329.73	1671.92	32.50	100.00
<b>3</b>	18.46	1568.53	1900.03	89.39	100.00
<b>4</b>	56.68	2033.88		98.37	100.00
<b>Average</b>	<b>48.56</b>	<b>1246.90</b>	<b>1154.58</b>	<b>174.88</b>	<b>100.00</b>

Table 5.6 Percentage error in the local error estimates along the z-axis for S-PPWG

<b>EST order</b>	<b>NFD</b>	<b>DCF</b>	<b>WFR</b>	<b>Cell-based CSH</b>	<b>Edge-based CSH</b>
<b>0</b>	10.32	530.19	519.85		
<b>1</b>	78.28	689.53	539.12	791.97	99.99
<b>2</b>	27.00	1365.52	3555.63	85.89	100.00
<b>3</b>	12.25	1616.05	1032.17	91.52	100.00
<b>4</b>	66.95	2057.34		98.23	100.00
<b>Average</b>	<b>38.96</b>	<b>1251.73</b>	<b>1411.69</b>	<b>266.90</b>	<b>100.00</b>

## 5.7 Error Estimators Applied to Structures with a Cell Corrupted with a Known Error

In this section, the four error estimators previously introduced are tested to see if each estimator can identify a cell with higher error relative to neighboring cells. To this effect, a cell in the test structures, T-PPWG and S-PPWG, is corrupted with a known error. This study can provide insight into which error estimator is best in actual local error presentation, which was missed in the previous section.

Consider the triangular-cell mesh for the PPWG structure shown in Figure 5.26. A known error is added to one cell located near the center of the mesh (the cell highlighted with bold dashed lines in Figure 5.26).

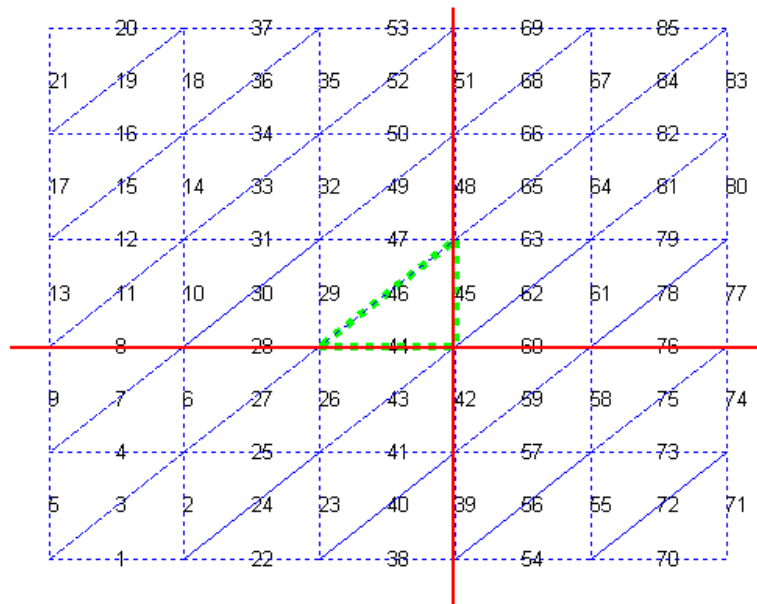


Figure 5.26 Mesh with a cell corrupted with a known error



The specific process of constructing the known error is as follows. First, the error is obtained by selecting values for the coefficients of an expansion in interpolatory vector basis functions. This representation of the error can be expressed as

$$\bar{E}_k(x, z) = \sum_{i=1}^N c_i \bar{I}_i(x, z) \quad (5.42)$$

where  $\bar{I}_i(x, z)$  denotes an interpolatory vector basis function, and the coefficients  $\{c_i\}$  are chosen to produce the derived error function. The function in (5.42) can be projected onto the set of hierarchical basis functions  $\{\bar{B}_i\}$  to yield

$$\bar{E}_k(x, z) = \sum_{i=1}^N e_{k,i} \bar{B}_i(x, z) \quad (5.43)$$

The error coefficients,  $e_{k,i}$ , are calculated using

$$\begin{aligned} e_j &= \iint_{\text{cell } k} \bar{E}(x, z) \cdot \bar{B}_j(x, z) dx dz = \sum_{i=1}^N \iint_{\text{cell } k} c_i \bar{I}_i(x, z) \cdot \bar{B}_j(x, z) dx dz \\ &= \sum_{i=1}^N c_i \iint_{\text{cell } k} I_i(x, z) \cdot B_j(x, z) dx dz . \end{aligned} \quad (5.44)$$

Although this projection process is only correct if the basis functions are orthogonal, it is adequate for constructing an error function to test the estimators. The un-corrupted FEM solution obtained with hierarchical functions has the form

$$\bar{H}_k(x, z) = \sum_{i=1}^N h_{k,i} \bar{B}_i(x, z) \quad (5.45)$$

Therefore, the corrupted FEM solution can be expressed by superposition as

$$\bar{H}'_k(x, z) = \sum_{i=1}^N (h_{k,i} + e_i) \bar{B}_i(x, z) = \sum_{i=1}^N h'_{k,i} \bar{B}_i(x, z) \quad (5.46)$$

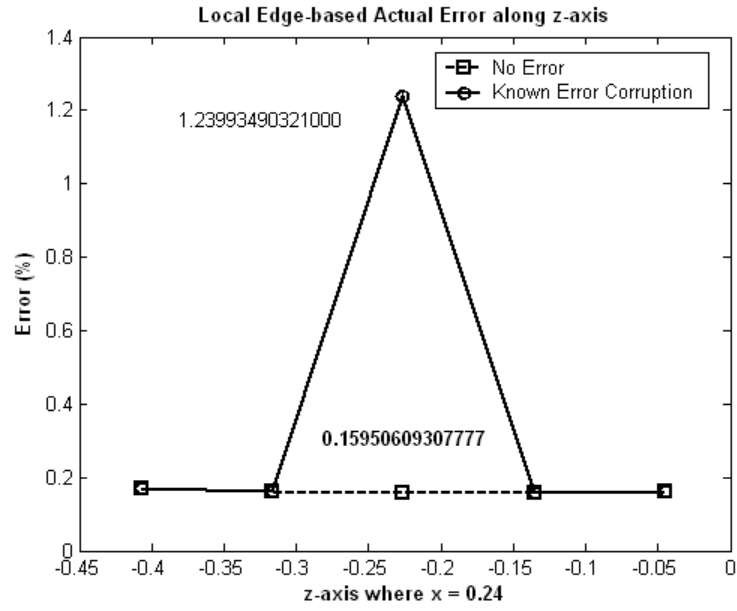
Each error estimator will be tested using this corrupted FEM solution. The local error estimates for the un-corrupted and corrupted structures are presented below.

### **5.7.1 Simulation Results**

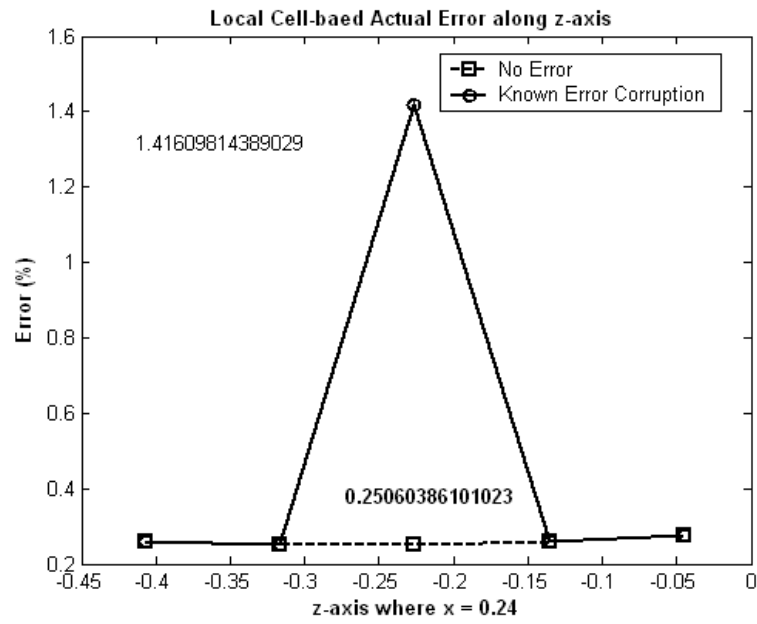
Figure 5.26 shows a mesh used for the local error estimates. Additional cells are used compared to the mesh in Figure 5.1 to better judge the sensitivity of the error estimators. A cell with edges 41, 45, and 46 is corrupted and depicted as bold dashed lines. Local errors are calculated along two vertical and horizontal lines.

Figures 5.27 and 5.29 show the actual local error behavior for the T-PPWG results (after being corrupted with a known error) along the z-axis and x-axis, respectively. Figures 5.31 and 5.33 show similar behavior for the S-PPWG. Figures 5.28, 5.30, 5.32, and 5.34 show the local errors as estimated by the four estimators for the same structures. The dashed line with square markers represents the local errors for the un-corrupted structures, while the bold line with circle markers represents the corrupted cases. The estimated local error functions are plotted for comparison.

Figures 5.28-5.34 were obtained using CT/LN basis functions for the NFD, DCF, and WFR estimators and LT/QN basis functions for the edge-based and cell-based CSH estimators. Even though the error corruption is confined to a cell, the error function calculated by each error estimator predicts additional error into the neighboring cells or edges (except for the cell-based CSH error estimator). The results show that each estimator detects the error in the corrupted cell.

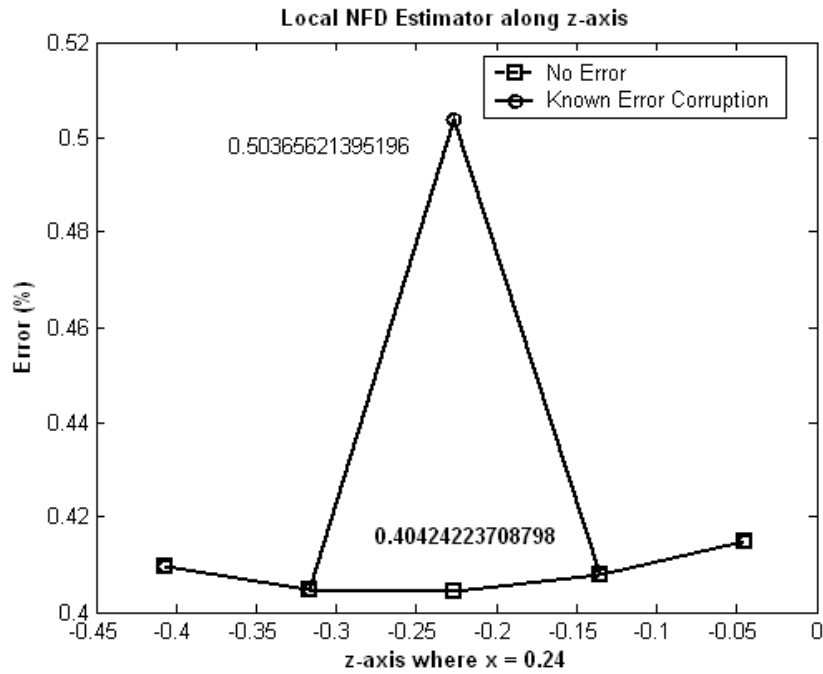


(a) Actual edge-based error

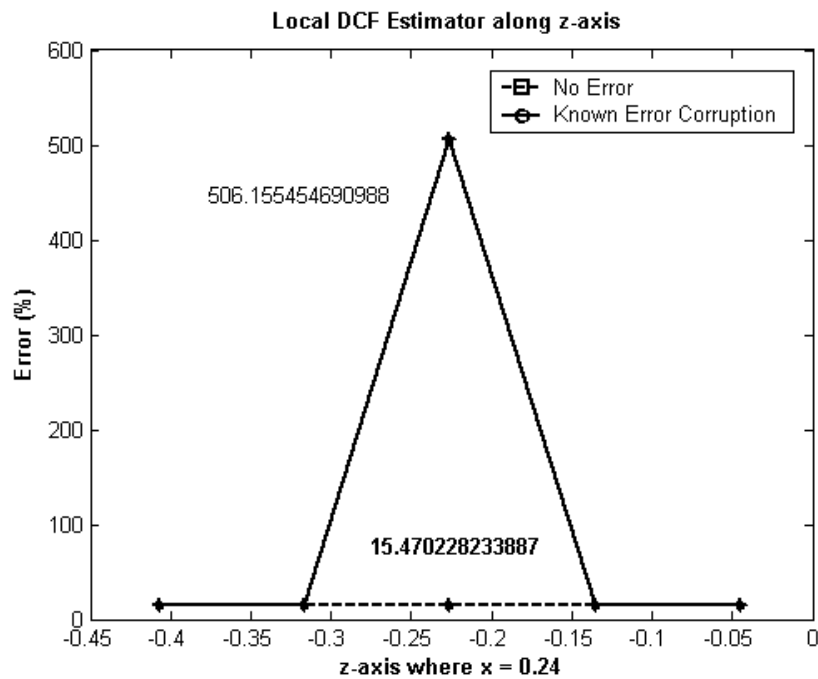


(b) Actual cell-based error

Figure 5.27 The actual local error with and without the additional corruption, as plotted along the z-axis at  $x = 0.24$  for the T-PPWG structure

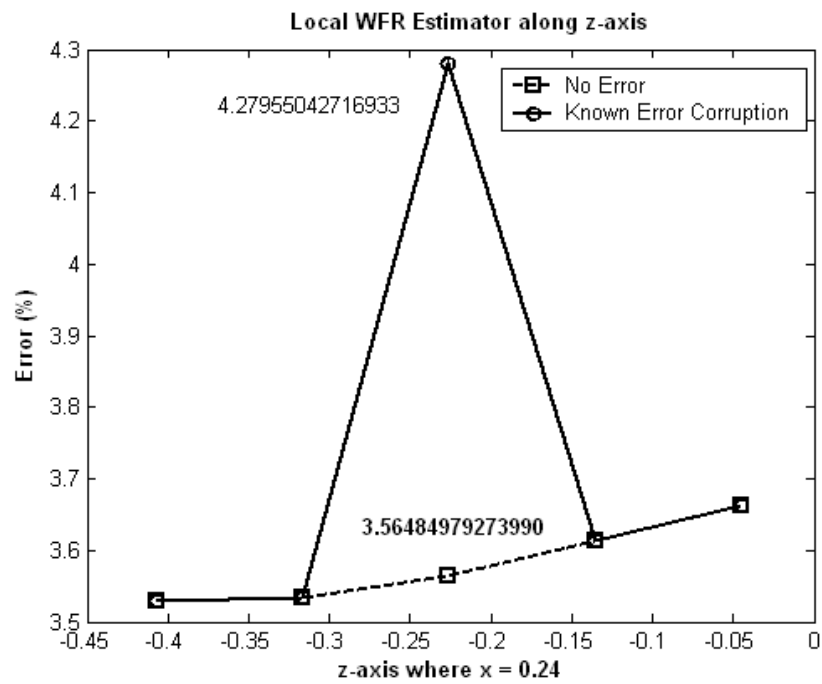


(a) NFD estimator

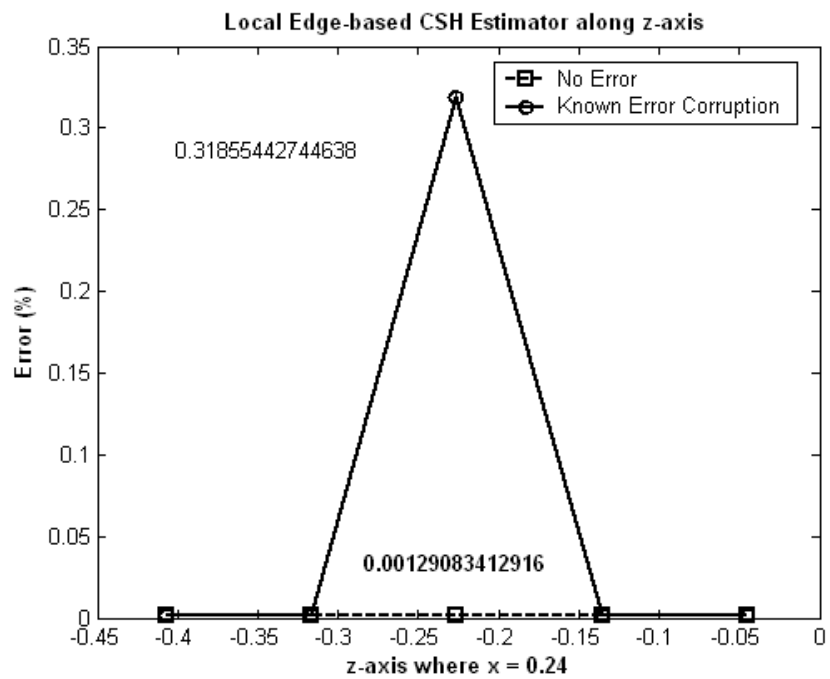


(b) DCF estimator

Figure 5.28 The error functions produced by the estimators for the corrupted and un-corrupted results. The error is plotted along the z-axis at  $x = 0.24$  for the T-PPWG structure

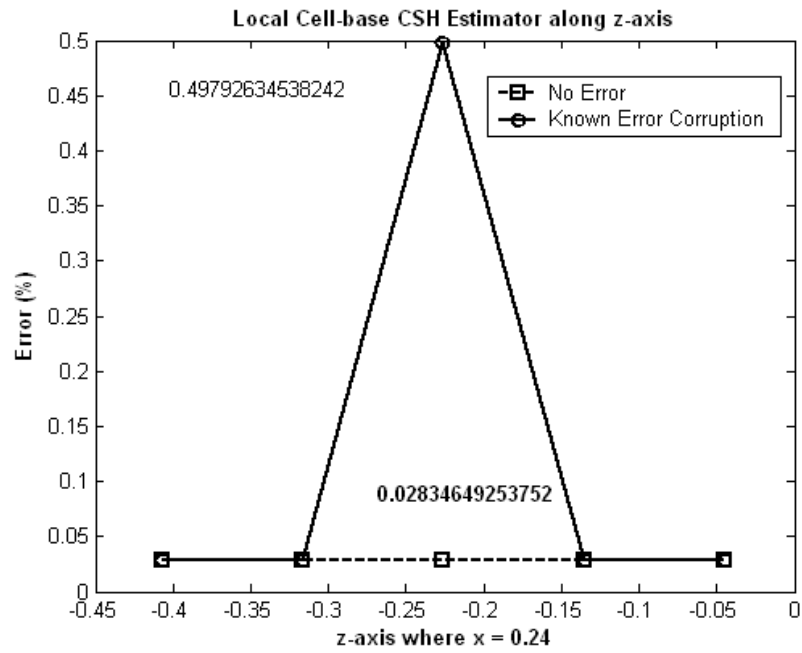


(c) WFR estimator



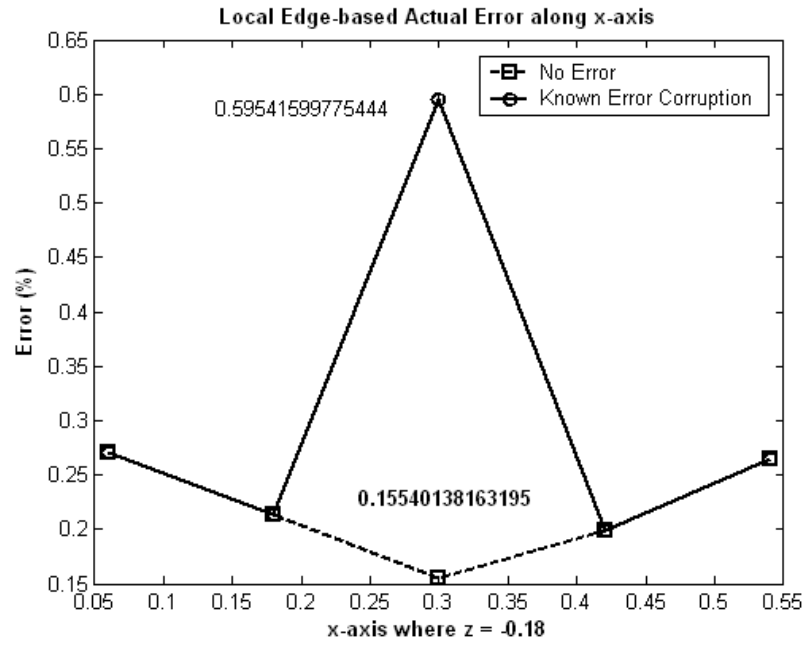
(d) Edge-based CSH estimator

Figure 5.28 Continued

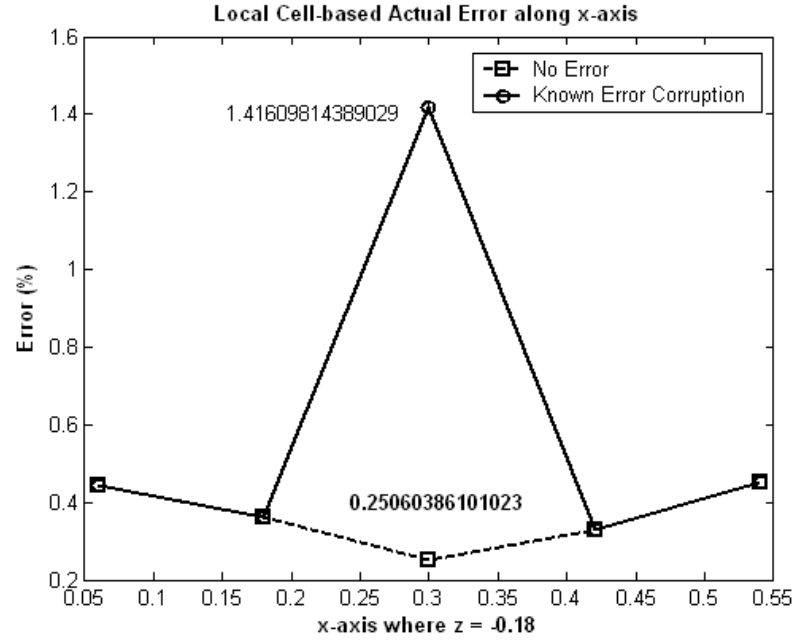


(e) Cell-based CSH estimator

Figure 5.28 Continued

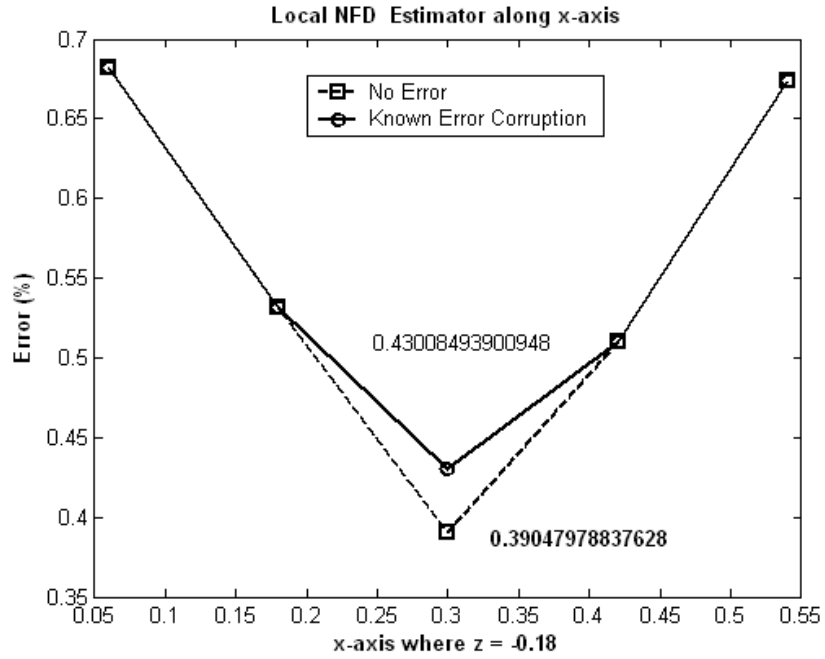


(a) Actual edge-based error

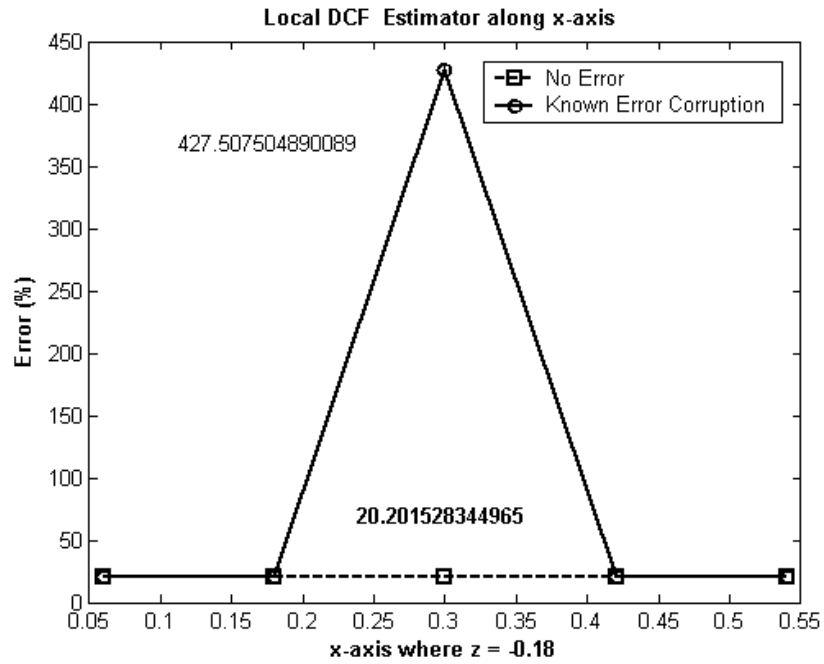


(b) Actual cell-based error

Figure 5.29 The actual local error with and without the additional corruption, as plotted along the x-axis at  $z = -0.18$  for the T-PPWG structure



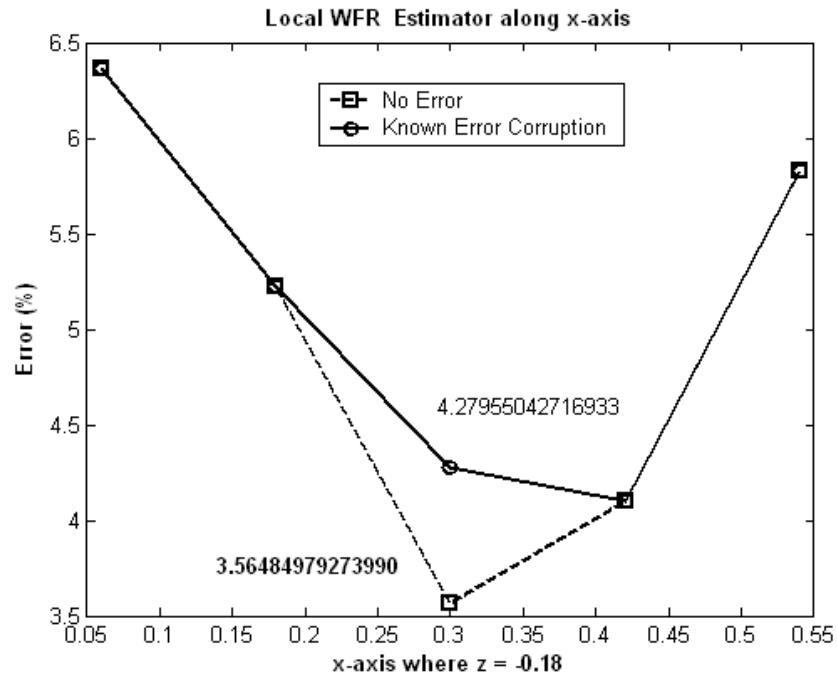
(a) NFD estimator



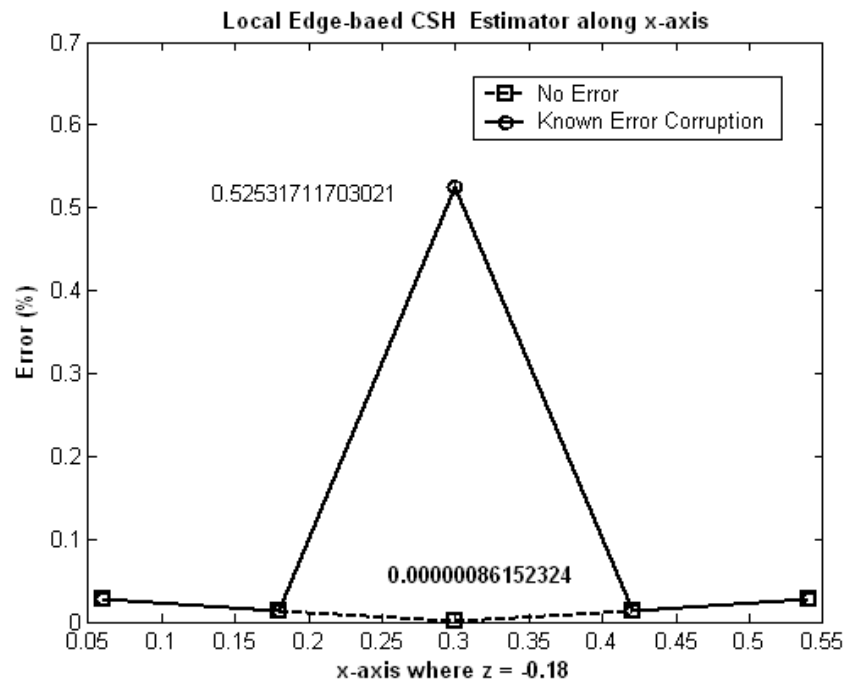
(b) DCF estimator

Figure 5.30 The error functions produced by the estimators for the corrupted and uncorrupted results. The error is plotted along the x-axis at  $z = -0.18$  for the T-PPWG structure



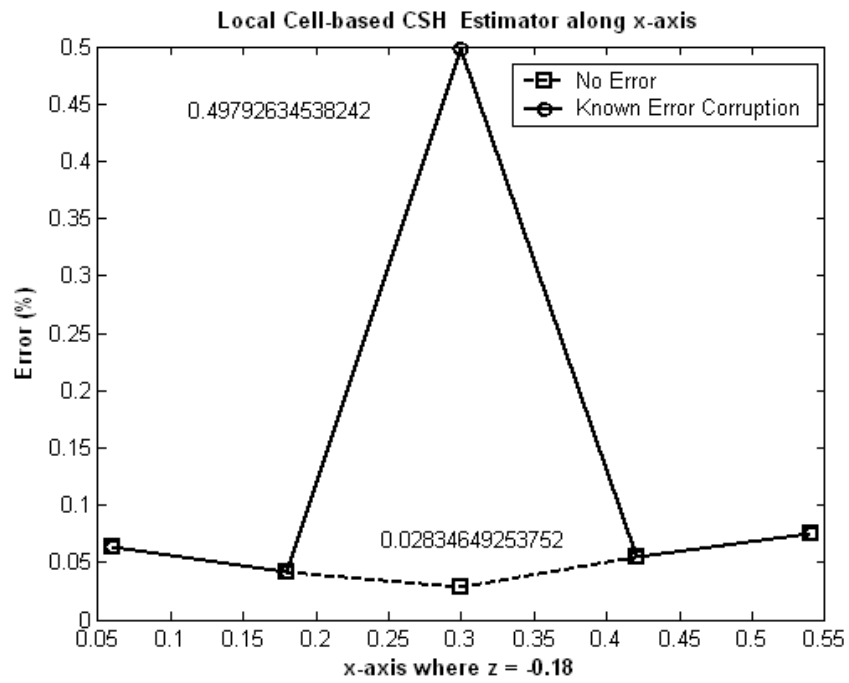


(c) WFR estimator



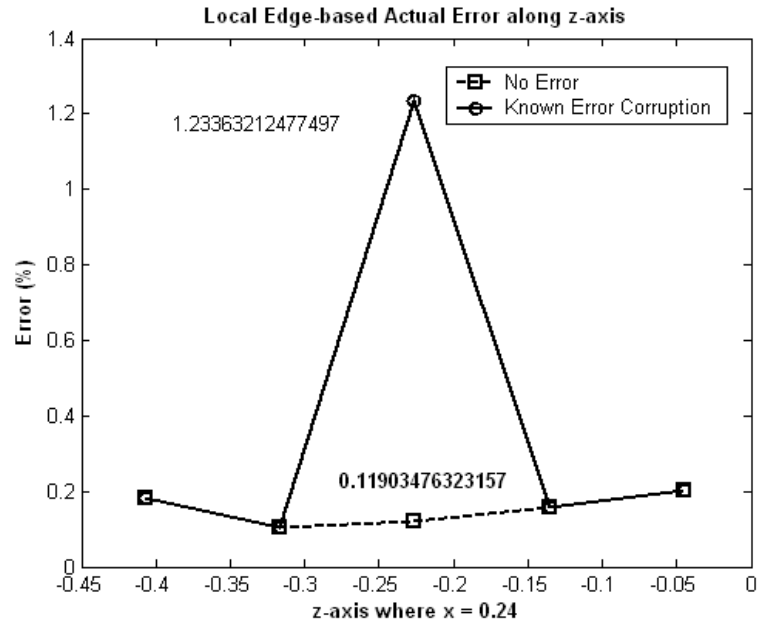
(d) Edge-based CSH estimator

Figure 5.30 Continued

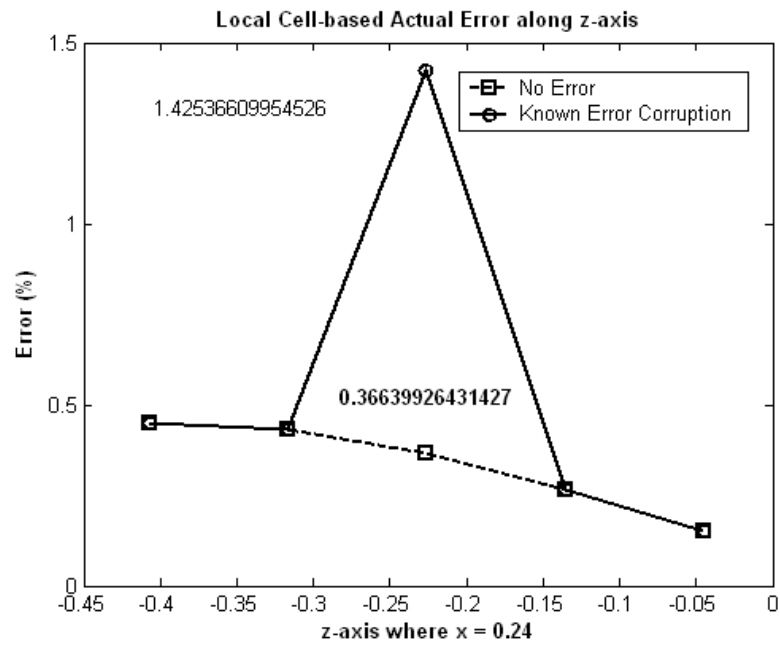


(e) Cell-based CSH estimator

Figure 5.30 Continued

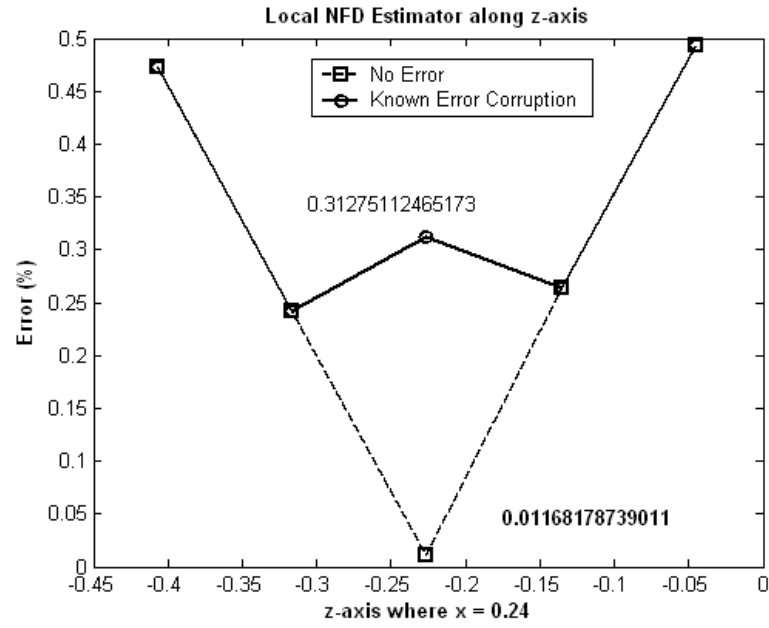


(a) Actual edge-based error

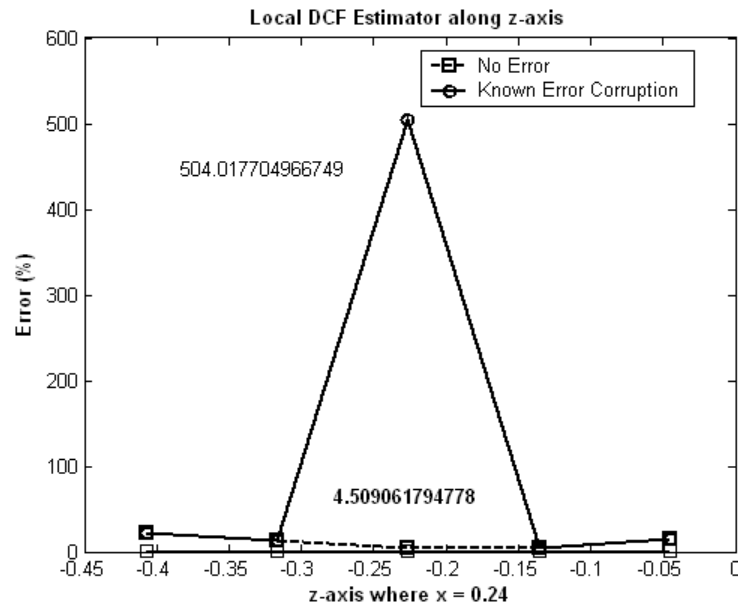


(b) Actual cell-based error

Figure 5.31 The actual local error with and without the additional corruption, as plotted along the z-axis at  $x = 0.24$  for the S-PPWG structure

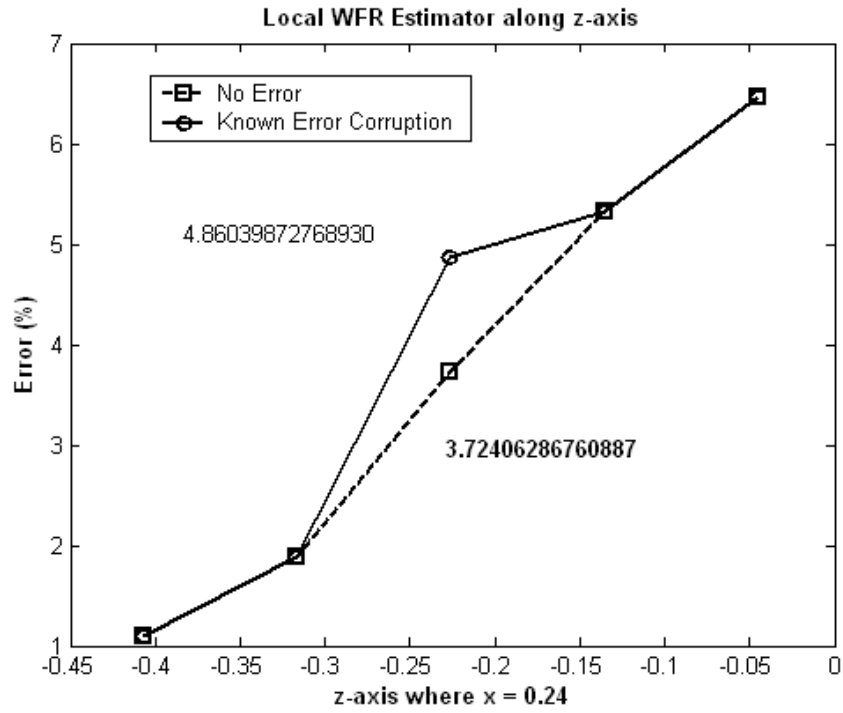


(a) NFD estimator

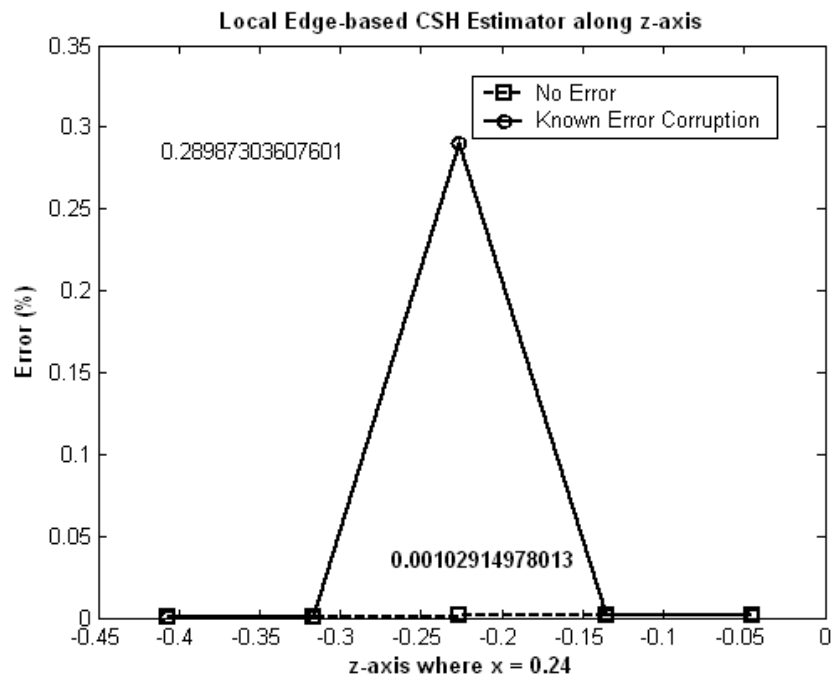


(b) DCF estimator

Figure 5.32 The error functions produced by the estimators for the corrupted and uncorrupted results. The error is plotted along the z-axis at  $x = 0.24$  for the S-PPWG structure

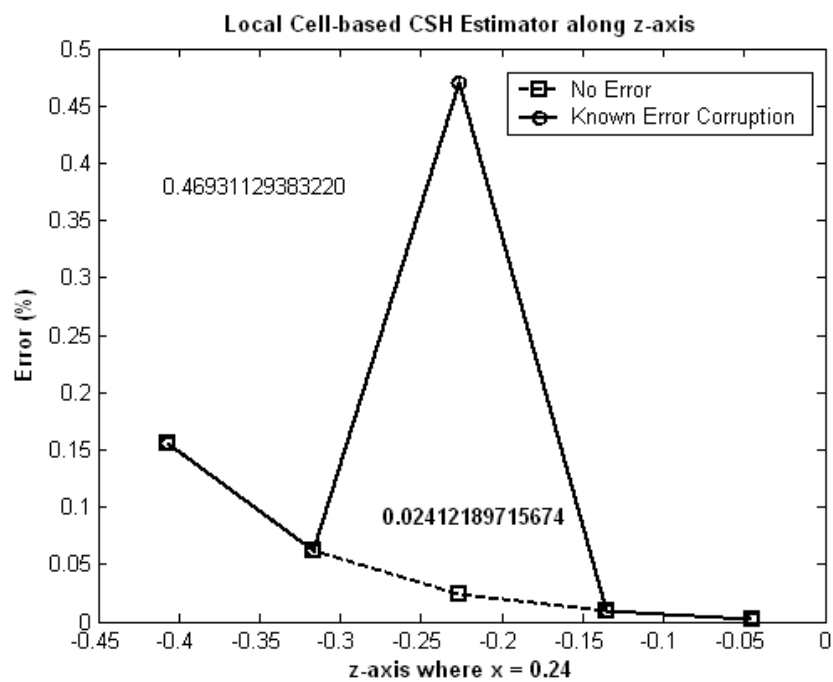


(c) WFR estimator



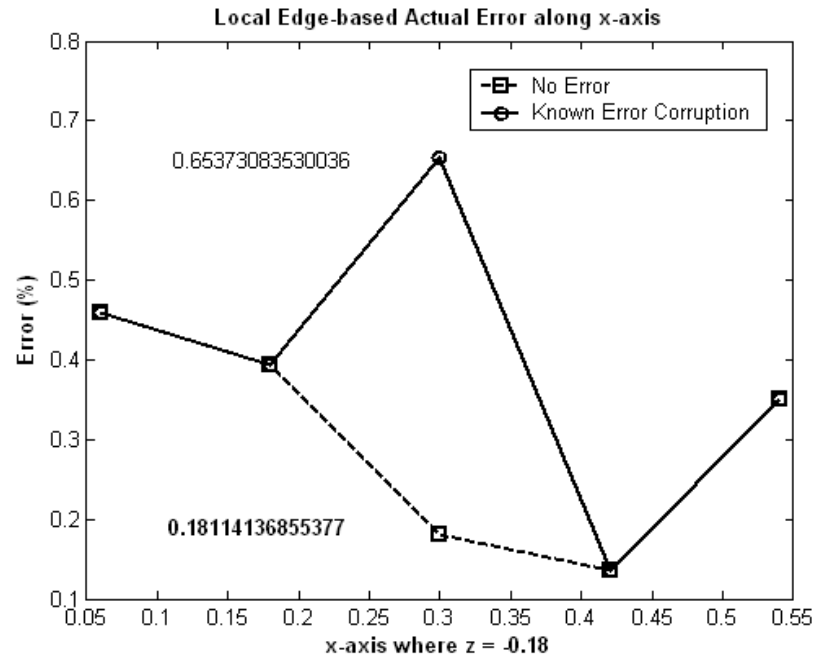
(d) Edge-based CSH estimator

Figure 5.32 Continued

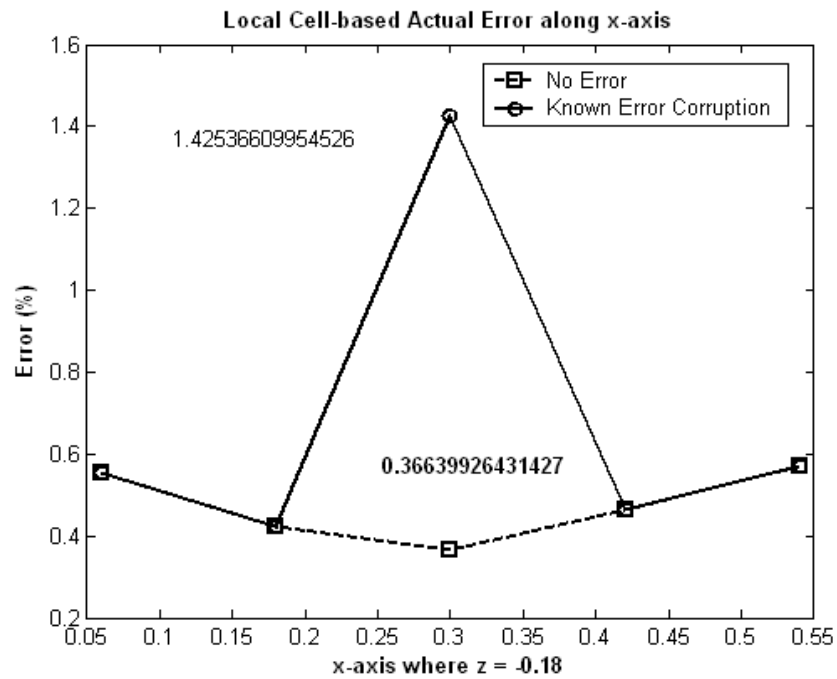


(e) Cell-based CSH estimator

Figure 5.32 Continued

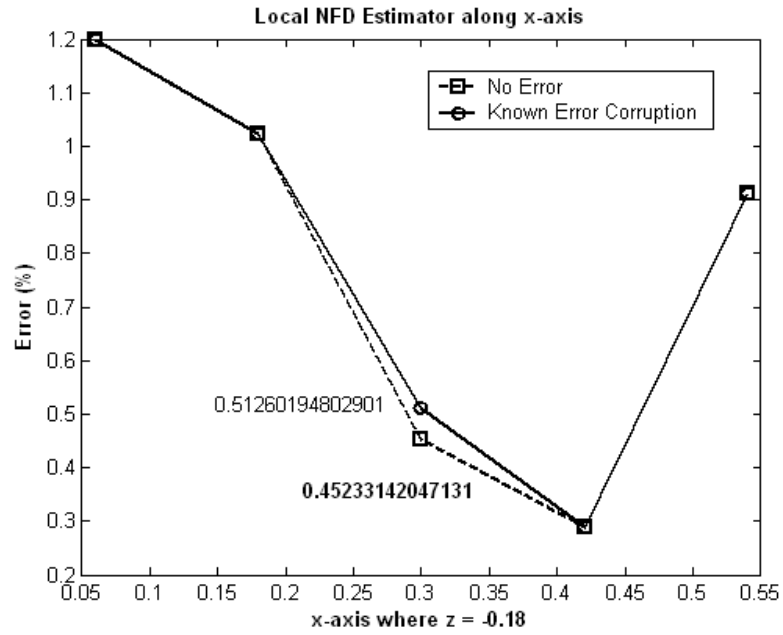


(a) Actual edge-based error

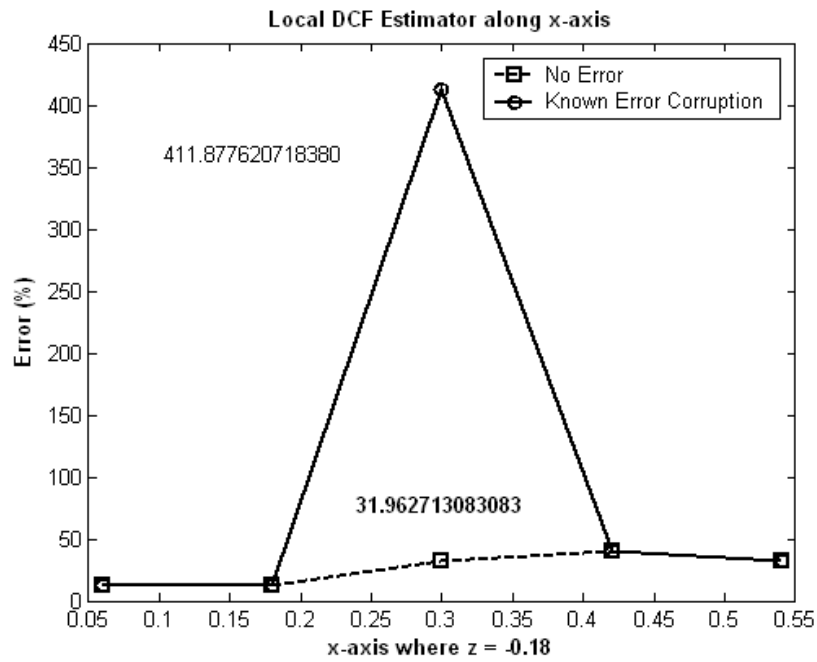


(b) Actual cell-based error

Figure 5.33 The actual local error with and without the additional corruption, as plotted along the x-axis at  $z = -0.18$  for the S-PPWG structure



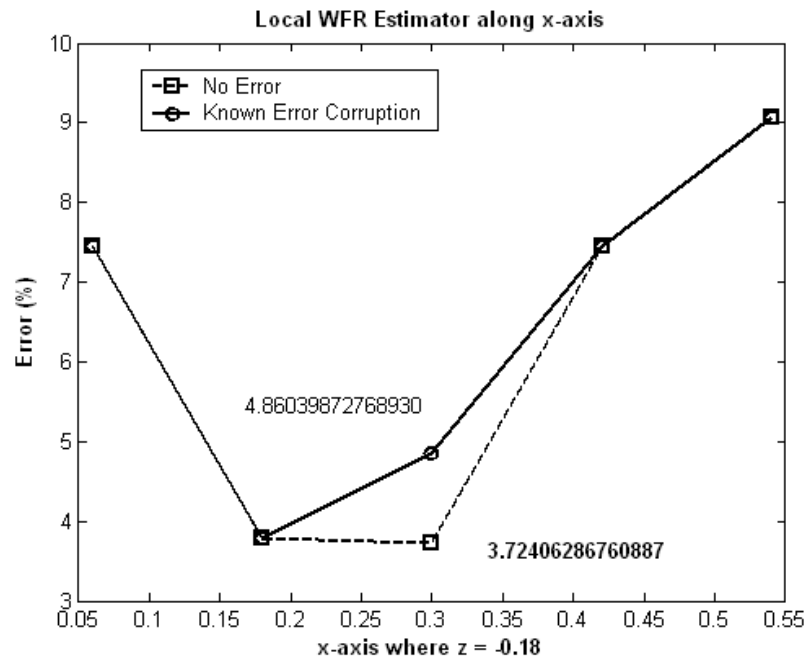
(a) NFD estimator



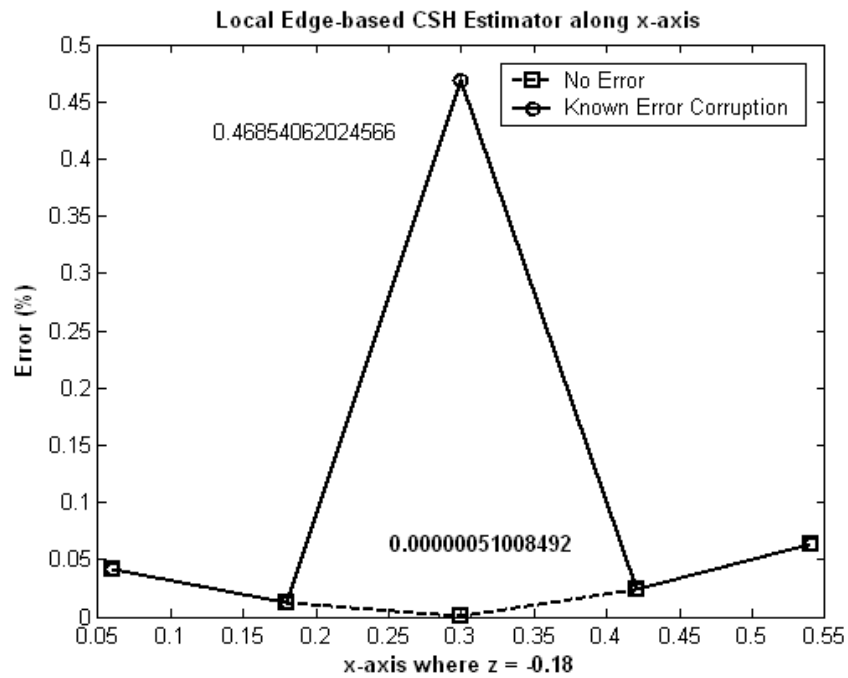
(b) DCF estimator

Figure 5.34 The error functions produced by the estimators for the corrupted and un-corrupted results. The error is plotted along the x-axis at  $z = -0.18$  for the S-PPWG structure



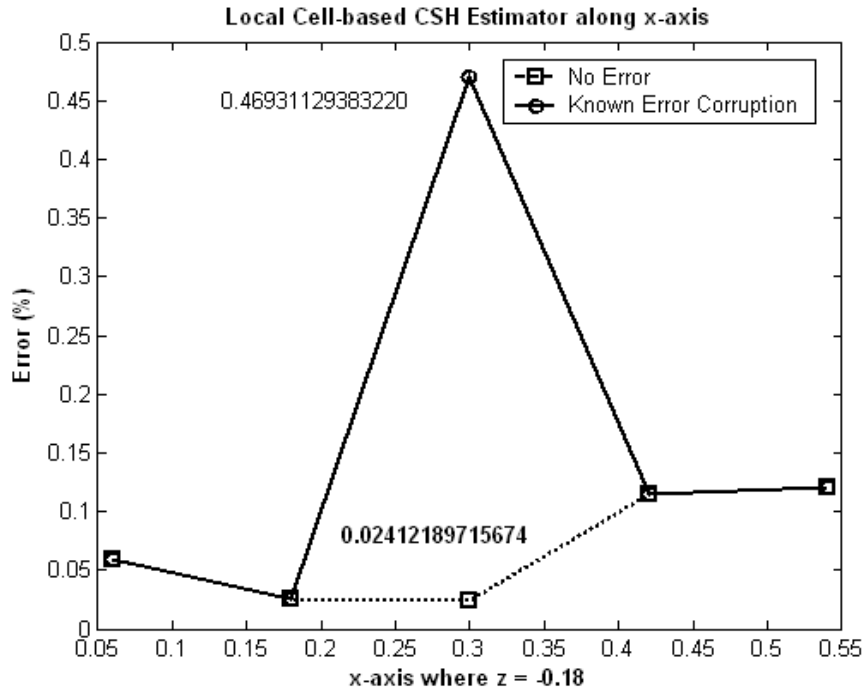


(c) WFR estimator



(d) Edge-based CSH estimator

Figure 5.34 Continued



(e) Cell-based CSH estimator

Figure 5.34 Continued

### 5.7.2 Evaluation of Error Estimators

The errors in the various estimates obtained from the corrupted data are tabulated in Tables 5.7 through 5.10. In this calculation, the actual local error with corruption is taken as a reference. The percentage error in the local estimates is much larger than previous values (which were obtained for structures with no known error corruption) shown in Tables 5.3 through 5.6. From the plots, all error estimators can identify the corrupted cell or edge.

Points on the tables represent cells abutting the vertical or horizontal lines for cell-based estimators such as WFR and CSH. For edge-based estimators such as NFD, DCF, and CSH, points represent edges along the vertical and horizontal lines in the mesh. For the NFD, DCF, and WFR estimators, CT/LN basis functions are employed and for the CSH estimator, LT/QN basis function is used in the following tables 5.7 through 5.13.

Table 5.7 Percentage errors in the local error estimates for points along the z-axis for T-PPWG

<b>Point EST</b>	<b>1</b>	<b>2</b>	<b>3</b>	<b>4</b>	<b>5</b>	<b>Average</b>
<b>NFD</b>	143.46	148.63	59.38	155.59	154.87	<b>132.39</b>
<b>DCF</b>	9274.84	9473.87	40721.18	9605.53	9519.27	<b>15718.93</b>
<b>WFR</b>	1265.36	1299.71	202.21	1302.35	1237.42	<b>1061.41</b>
<b>Cell-based CSH</b>	143.46	148.63	59.38	155.59	154.87	<b>132.39</b>
<b>Edge-based CSH</b>	99.21	99.21	74.31	99.19	99.22	<b>94.23</b>

Table 5.8 Percentage errors in the local error estimates for points along x-axis  
for T-PPWG

<b>Point</b> <b>EST</b>	<b>1</b>	<b>2</b>	<b>3</b>	<b>4</b>	<b>5</b>	<b>Average</b>
<b>NFD</b>	151.41	148.24	27.77	156.71	154.68	<b>127.77</b>
<b>DCF</b>	7256.03	9140.89	71699.80	10265.30	7641.80	<b>21200.76</b>
<b>WFR</b>	1335.60	1339.90	202.20	1146.10	1194.82	<b>1043.73</b>
<b>Cell-based CSH</b>	85.80	88.60	64.84	83.44	83.29	<b>81.19</b>
<b>Edge-based CSH</b>	90.16	94.12	11.77	93.67	89.91	<b>75.93</b>

Table 5.9 Percentage errors in the local error estimates for points along z-axis  
for S-PPWG

<b>Point</b> <b>EST</b>	<b>1</b>	<b>2</b>	<b>3</b>	<b>4</b>	<b>5</b>	<b>Average</b>
<b>NFD</b>	157.37	136.33	74.65	67.91	144.61	<b>116.18</b>
<b>DCF</b>	11486.38	13192.98	40756.40	3143.07	7006.58	<b>15117.08</b>
<b>WFR</b>	141.94	338.35	1226.53	1900.00	4119.26	<b>1545.22</b>
<b>Cell-based CSH</b>	65.45	85.73	28.09	96.69	98.18	<b>74.83</b>
<b>Edge-based CSH</b>	99.93	99.40	76.50	99.15	99.24	<b>94.84</b>

Table 5.10 Percentage errors in the local error estimates for points along x-axis  
for S-PPWG

<b>EST \ Point</b>	<b>1</b>	<b>2</b>	<b>3</b>	<b>4</b>	<b>5</b>	<b>Average</b>
<b>NFD</b>	160.19	150.00	21.59	113.90	160.40	<b>123.01</b>
<b>DCF</b>	2509.03	3010.19	62904.16	29106.01	9074.14	<b>21320.71</b>
<b>WFR</b>	1238.60	795.31	241.00	1498.87	1495.65	<b>1053.89</b>
<b>Cell-based CSH</b>	89.39	93.94	67.07	75.48	78.78	<b>80.93</b>
<b>Edge-based CSH</b>	90.82	97.00	28.33	82.55	81.83	<b>76.11</b>

Table 5.11 Percentage error of the error at point 3 to sum of errors at all points

<b>EST \ Cases</b>	<b>NFD</b>	<b>DCF</b>	<b>WFR</b>	<b>Cell_based CSH</b>	<b>Edge_based CSH</b>
<b>Along z-axis for T-PPWG</b>	8.97	51.81	3.81	8.97	15.77
<b>Along x-axis for T-PPWG</b>	4.35	67.64	3.87	15.97	3.10
<b>Along z-axis for S-PPWG</b>	12.85	53.92	15.88	7.51	16.13
<b>Along x-axis for S-PPWG</b>	3.51	59.01	4.57	16.5	7.44
<b>Average of percentage error</b>	<b>7.42</b>	<b>58.10</b>	<b>7.03</b>	<b>12.24</b>	<b>10.61</b>

Table 5.11 shows the ratio of the error at point 3 to the sum of the errors at all five points for the preceding tables. These results suggest the sensitivity of each error estimator to detecting an area with high local relative error. The smaller the value in Table 5.11, the more sensitive the estimator is.

Even though the WFR estimator is not very accurate in predicting the actual error levels, it is very good at detecting cells with high local error. The best error estimators at identifying high local errors are the WFR and NFD estimators, which according to Table 5.11 predict the error within an average of 7%. The DCF is not very accurate in predicting the actual error levels. The CSH estimator shows reasonable performance, too, in this regard.

Table 5.12 Ratio of edge-based actual local error to local error estimates at point 3

<b>EST</b> <b>Cases</b>	<b>Actual</b>	<b>NFD</b>	<b>DCF</b>	<b>Edge_based</b> <b>CSH</b>
<b>Along z-axis for T-PPWG</b>	<b>7.7737</b>	1.2459	32.7180	246.7818
<b>Along x-axis for T-PPWG</b>	<b>3.8314</b>	1.1014	21.1621	6.0975e+005
<b>Along z-axis for S-PPWG</b>	<b>10.3664</b>	26.7725	111.7788	281.6626
<b>Along x-axis for S-PPWG</b>	<b>3.8314</b>	1.1332	12.8862	9.1855e+005
<b>Average</b>	<b>6.4507</b>	7.5633	44.6363	3.8221e+005
<b>Error of Average (%)</b>	<b>0</b>	<b>17.2477</b>	<b>591.9602</b>	<b>5.9250e+006</b>

Table 5.13 Ratio of cell-based actual local error to local error estimates at point 3

<b>EST</b> <b>Cases</b>	<b>Actual</b>	<b>WFR</b>	<b>Cell_based</b> <b>CSH</b>
<b>Along z-axis for T-PPWG</b>	<b>5.6508</b>	1.2005	17.5657
<b>Along x-axis for T-PPWG</b>	<b>5.6508</b>	1.2005	17.5657
<b>Along z-axis for S-PPWG</b>	<b>3.8903</b>	1.3051	19.4558
<b>Along x-axis for S-PPWG</b>	<b>3.8903</b>	1.3051	19.4558
<b>Average</b>	<b>4.7706</b>	1.2528	18.5107
<b>Error of Average (%)</b>	<b>0</b>	<b>73.7392</b>	<b>288.0162</b>

Tables 5.12 and 5.13 show the ratio of the local error when corrupted to the un-corrupted local error at point 3. As shown in Figures 5.27 through 5.34, the actual corrupted error exists only at point 3. The ratio is calculated from the local errors indicated at points on the plots.

To summarize the performance of the error estimators, the NFD estimator is able to detect the relative variation caused by the corruption error within 18% of the actual local error. The WFR estimator shows reasonable performance (within 70% of the actual error) in detecting the relative variation of local error. The DCF estimator is bad at detecting areas with high error. For the CSH estimators, the edge-based CSH estimator cannot detect the relative variation of the local error, while the cell-based CSH estimator is a little better in performance. The best at detecting the relative variation of the local error are the NFD and WFR estimators.

From these tables, we conclude that the NFD and WFR estimators are best at detecting the relative local error variation and areas with high local error.



## 5.8 Summary

Four error estimators are introduced for the purpose of guiding an adaptive FEM procedure. The assessment of the accuracy of the same FEM solution by each error estimator in terms of local and global error is carried out and simulation results are presented.

Figures 5.35 and 5.36 compare the performance of all error estimators for structures with no known error corruption in terms of global error performance. The predictions of the NFD, DCF, and WFR estimators are confined below 100% of the actual error and the WFR estimator improves as the order of basis increases. CSH underestimates the actual error levels and therefore appears to stagnate near 100% as the order of basis increases. As mentioned in the previous section, the NFD and WFR estimators show good performance in detecting a cell with high local error.

By comparing these with the actual errors, we conclude that all four error estimators are poor at predicting the actual errors. However, all error estimators except the edge-based CSH and DCF estimators can detect the relative variation of the actual local error. The local error norms and the global average error norms decrease as the order of hierarchical basis increases. Furthermore, they all are practical from the point of view of ease of implementation.

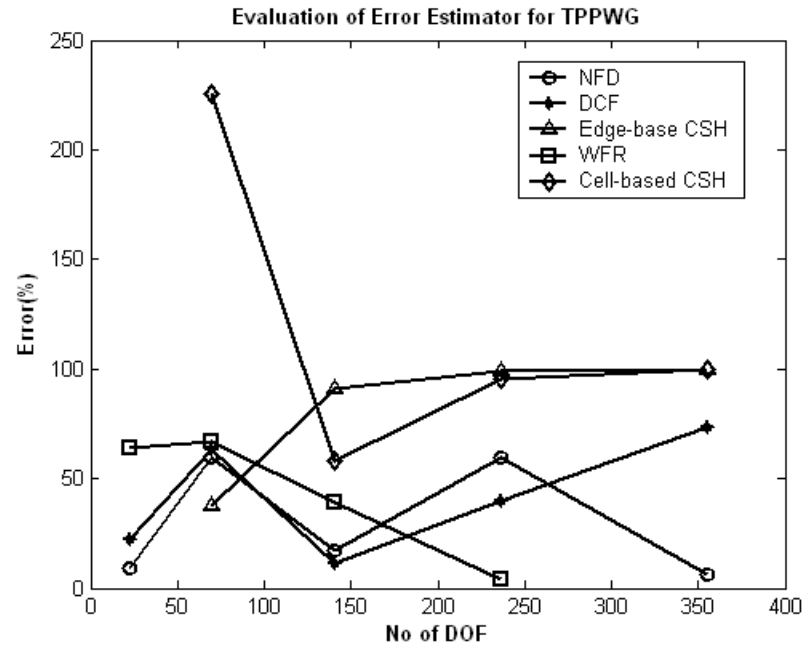


Figure 5.35 Comparison of error estimators for T-PPWG (un-corrupted)

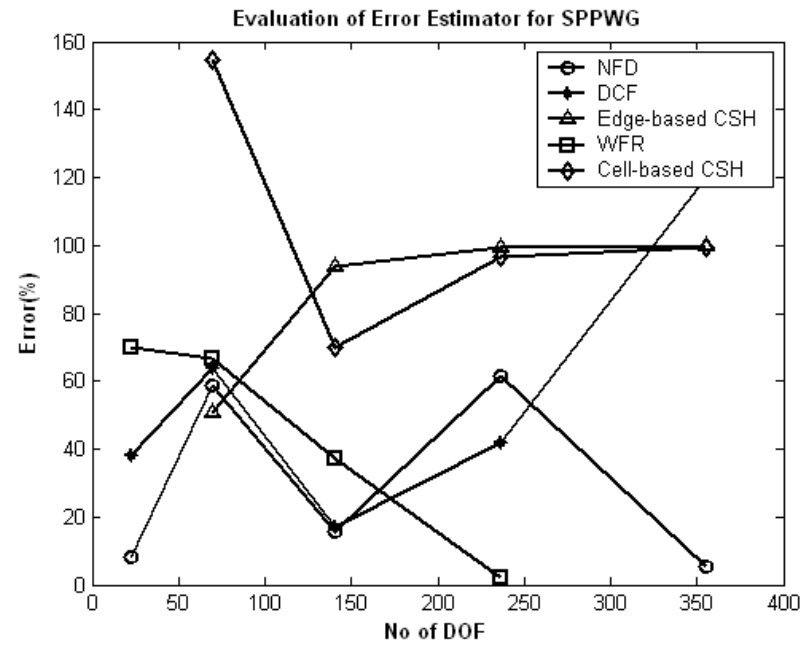


Figure 5.36 Comparison of error estimators for S-PPWG (un-corrupted)

The NFD and WFR estimators can detect the relative variation of the actual error and the regions of a mesh with high local error. They also show good performance with respect to global error in Figures 5.35 and 5.36. Thus, they appear superior to the other estimators for use in an adaptive refinement code.

In the next chapter, the NFD and WFR error estimators will be used within adaptive refinement algorithms applied to structures containing one or more septums, which have no analytical solution.

## CHAPTER 6: ADAPTIVE P-REFINEMENT FEM

The primary purpose of the *a posteriori* error estimators evaluated in Chapter 5 is to guide an adaptive refinement process. The adaptive process is hoped to provide a result of sufficient accuracy far more efficiently (with fewer degrees of freedom and smaller computer time and memory) than would be the case if a uniform polynomial order was used throughout the mesh. In this chapter, two simple p-adaptive algorithms are implemented and used for illustration. The structures considered are PPWG geometries containing septums to provide rapid field variation in localized regions. Since these problems do not yield analytical solutions, numerical results obtained with high order interpolatory basis functions (Nedelec mixed-order 7/8) are used as a reference solution.

The two error estimators identified in Chapter 5 as the better performers (the normal-field discontinuity (NFD) estimator and the weak form residual (WFR) estimator) will be used and their results compared. The NDF estimator is edge-based, while the WFR estimator is cell-based.

The adaptive refinement algorithm requires a control strategy for guiding the process. Two different approaches will be considered. Initially, with either approach, a result is generated using the lowest-order basis functions (those of Nedelec mixed-order 0/1, or the CT/LN type). The error estimator is applied to this result to yield a map of the local error within the mesh. In the first refinement implementation, the basis polynomial

order in those cells or along those edges with the top 25% of the reported error levels is increased by one degree. Hierarchical functions are used, so that various orders may overlap a given cell. At this point, the basis functions orders are adjusted so that the maximum difference in order within any cell is limited to 2 degrees. This ensures reasonably continuous representations throughout the mesh. Then the procedure repeats iteratively: a new FEM analysis based on the updated distribution of basis functions is carried out, the error estimator is applied to the new result to generate an error map, and a new distribution of degrees of freedom is determined. Once cells or edges reach the maximum available degree (Nedelec mixed-order 4/5 in the present implementation) the equivalent number of degrees of freedom will instead be assigned to the cells/edges with the highest predicted error that have not yet reached the maximum available degree. This approach is denoted the *single-step* adaptive refinement algorithm.

The single-step algorithm suffers from the drawback that it must gradually iterate toward having some regions of the mesh with high-order basis functions, regardless of the initial error map. Therefore, a second algorithm (the *multi-step* adaptive refinement algorithm) will also be considered. The steps involved in the multi-step algorithm are the same as those of the single-step algorithm, except that in addition to incrementing the polynomial orders of the basis functions in regions with the highest 25% error by one degree, the process also increments the orders of the basis functions in regions with the highest 10% error by a second degree. In this manner, the multi-step algorithm more rapidly increases the polynomial orders in regions where the estimated error is the highest.

Figure 6.1 shows the two PPWG test structures that will be used for illustration. In order to provide regions within the FEM mesh where relatively rapid field variation might occur and benefit from greater polynomial orders, septums are introduced into the waveguides. Although these structures act as filters, and their performance as a function of frequency makes an interesting application, for the purpose of the present investigation they will only be considered as testbeds for the various p-refinement algorithms.

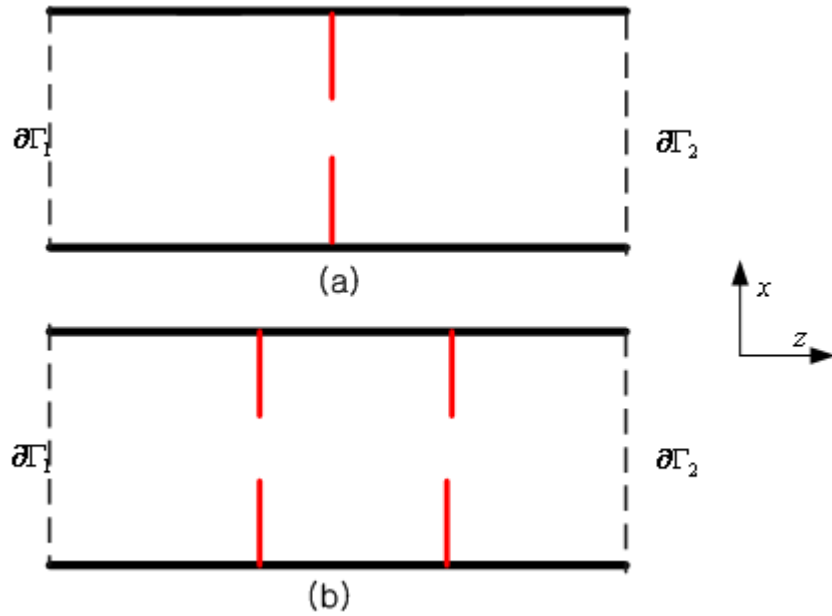


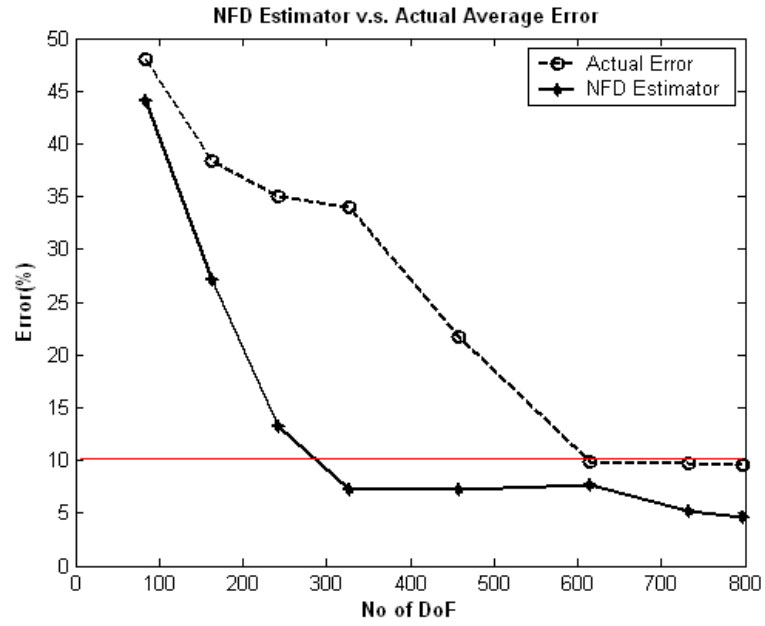
Figure 6.1 (a) One-septum T-PPWG structure  
(b) Two-septum T-PPWG structure

## 6.1 Simulation Results

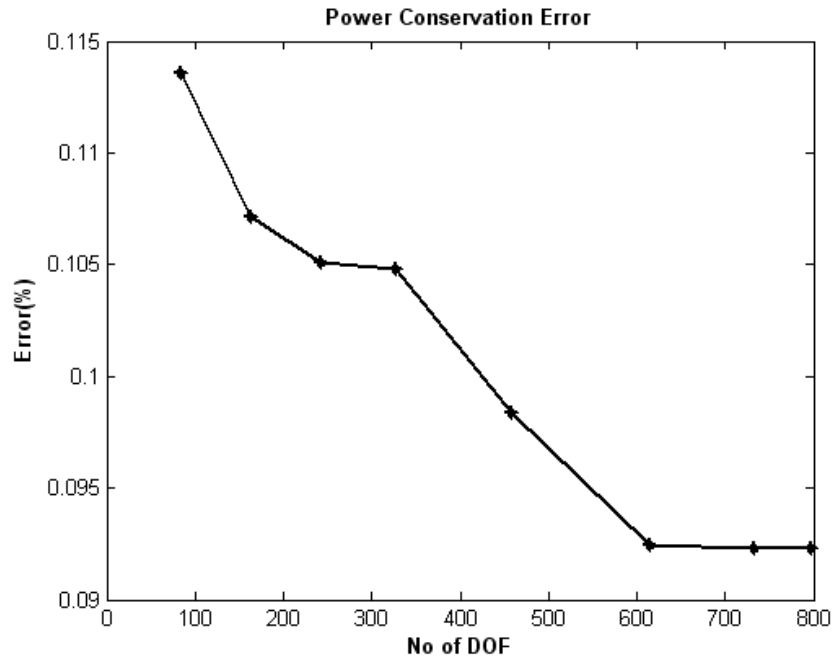
Simulation results are presented below for the single-step and multi-step adaptive refinement algorithms, based on the NFD and WFR estimators. Figure 6.2 shows the

performance of the single-step algorithm used in conjunction with the NFD estimator, for the PPWG structure in Figure 6.1a. Figure 6.2a reports the actual and estimated error levels as the adaptive refinement process is carried out. The horizontal line at 10% error is provided to aid the reader in comparing the results of the various simulations. Figure 6.2b reports the percent error in the power conservation check discussed in Section 4.2.2. We note that the power check is within 0.1% when the number of degrees of freedom exceeds 400. Figures 6.2c and 6.2d report the error in the transmission coefficient and reflection coefficient, respectively, as the adaptive process is carried out. The reference solution in all cases is that obtained using order 7/8 interpolatory basis functions throughout the mesh.

Figure 6.3 shows similar plots for the multi-step refinement algorithm with the NFD estimator, for the PPWG structure in Figure 6.1a. The improvement in power conservation, and the error in transmission and reflection coefficients, is generally about the same with respect to the number of degrees of freedom as with the single-step algorithm.



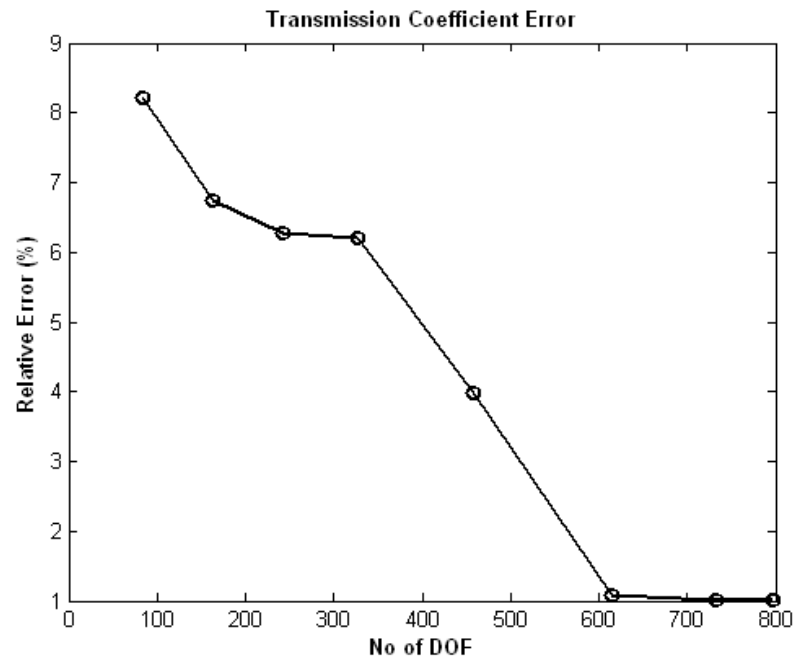
(a) Comparison of numerical estimates to the actual error



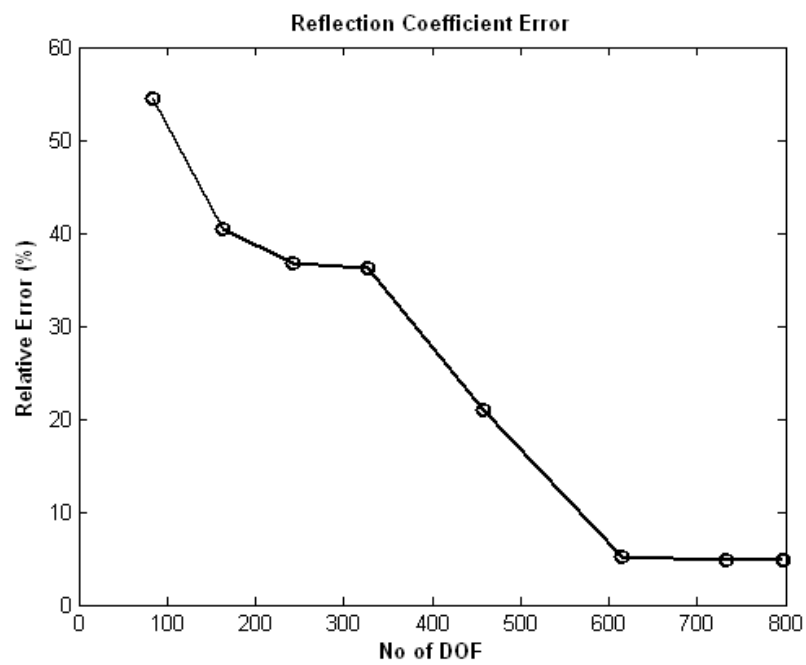
(b) Power conservation error

Figure 6.2 The NFD estimator with 25% single-step iteration technique for the structure in (a) of Figure 6.1



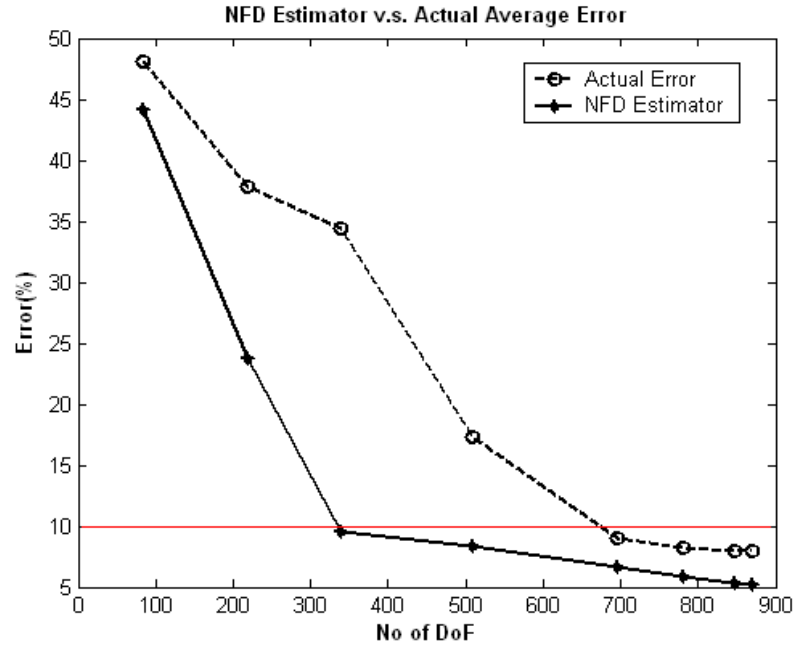


(c) Transmission coefficients error

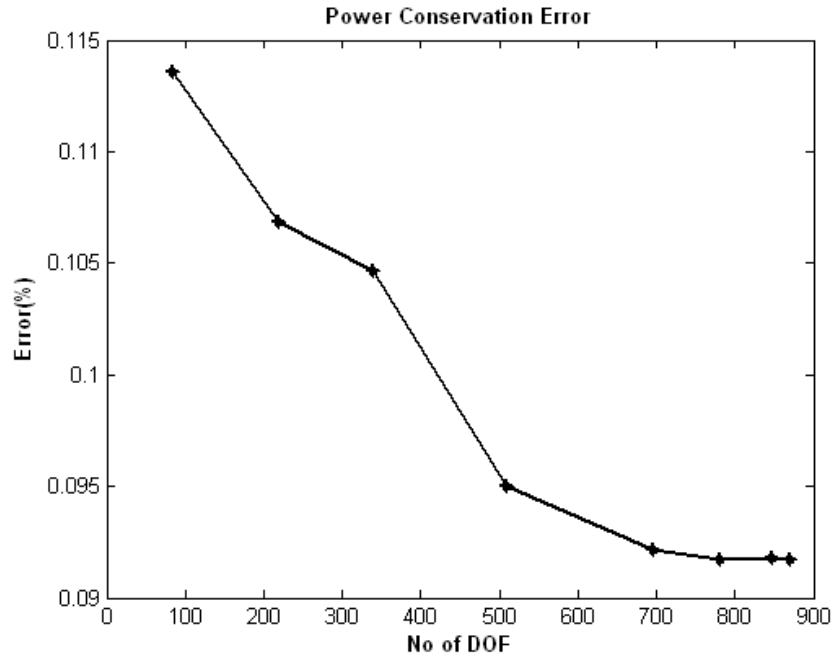


(d) Reflection coefficients error

Figure 6.2 Continued

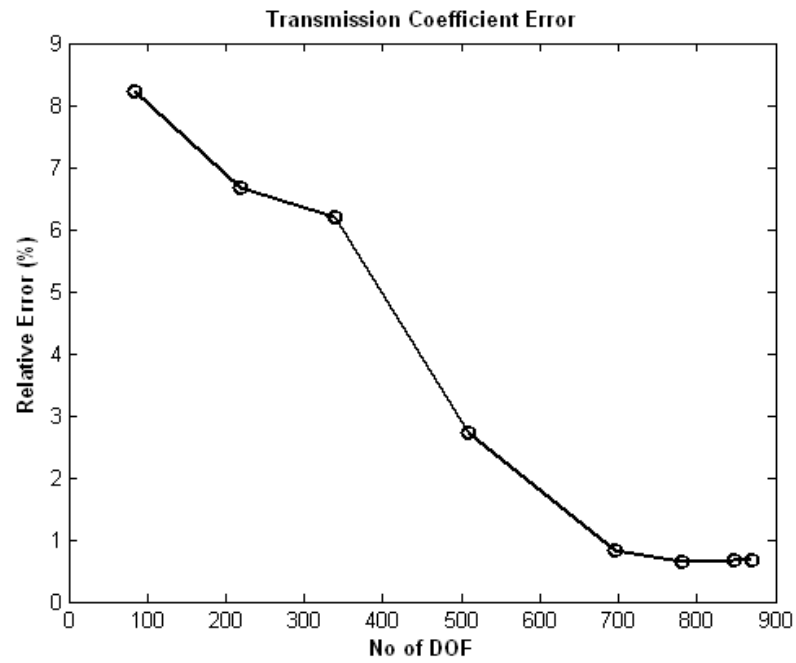


(a) Comparison of numerical estimates to the actual error

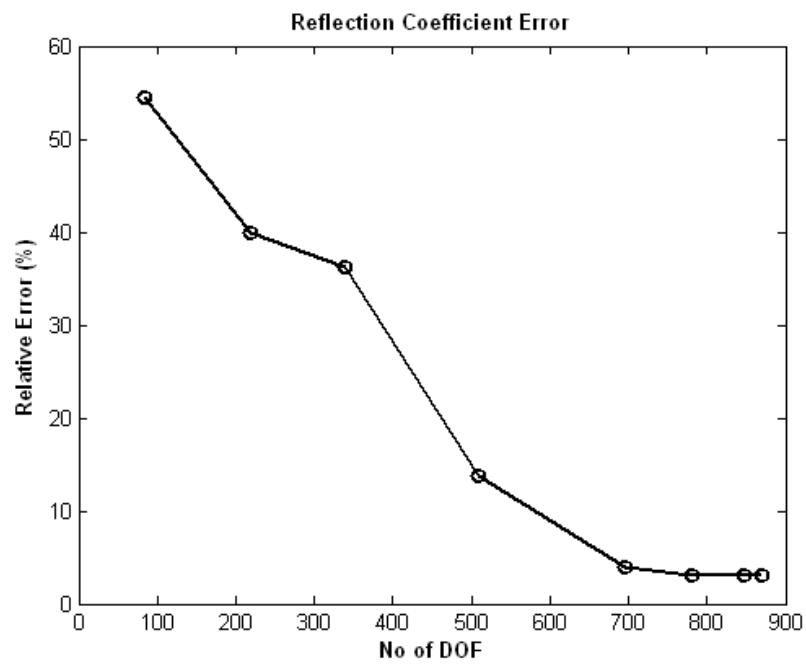


(b) Power conservation error

Figure 6.3 The NFD estimator with 25%+10% multi-step iteration technique for the structure in (a) of Figure 6.1



(c) Transmission coefficients error

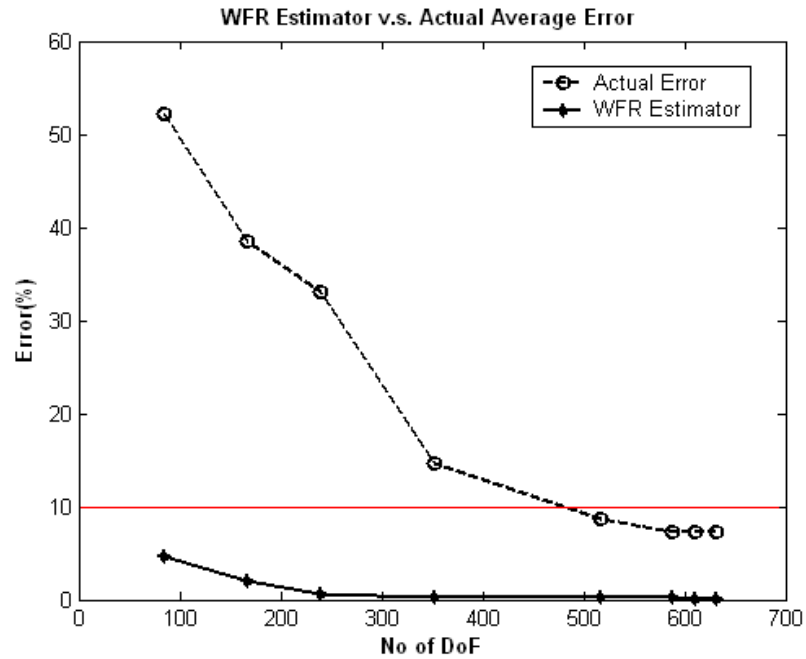


(d) Reflection coefficients error

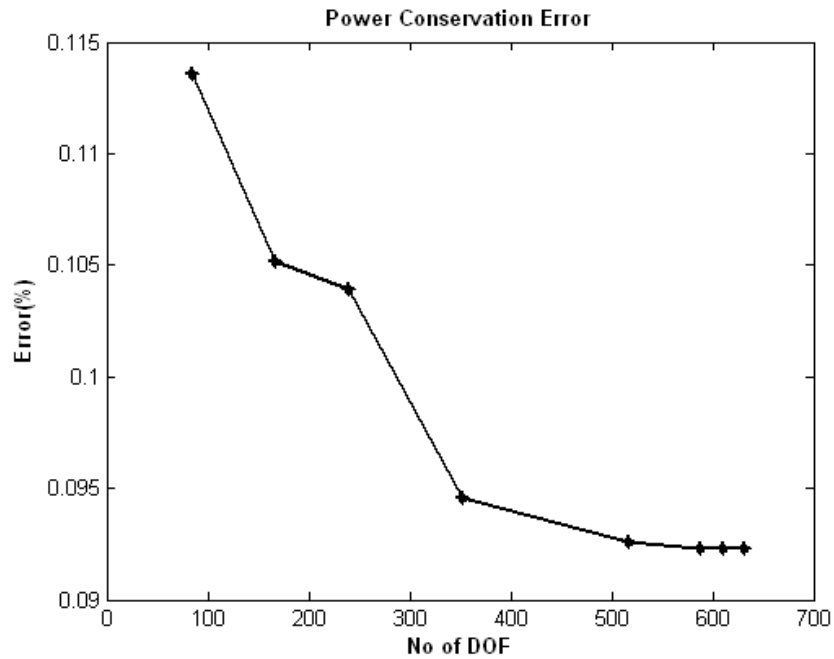
Figure 6.3 Continued

Figure 6.4 shows the performance of the single-step algorithm used in conjunction with the WFR estimator, for the PPWG structure in Figure 6.1a. In these simulations, the WFR consistently underestimates the error in the solution. However, the actual solution error converges faster than it did with the NFD estimator. The power conservation is within 0.1% at less than 300 degrees of freedom, and there is a similar improvement in the accuracy of the transmission and reflection coefficients. The improvement in power conservation, and the error in transmission and reflection coefficients, is generally about the same with respect to the number of degrees of freedom as with the single-step algorithm.

Figure 6.5 shows similar plots for the multi-step algorithm used in conjunction with the WFR estimator. The rate of convergence with the multi-step algorithm does not appear as fast as that of the single-step approach.

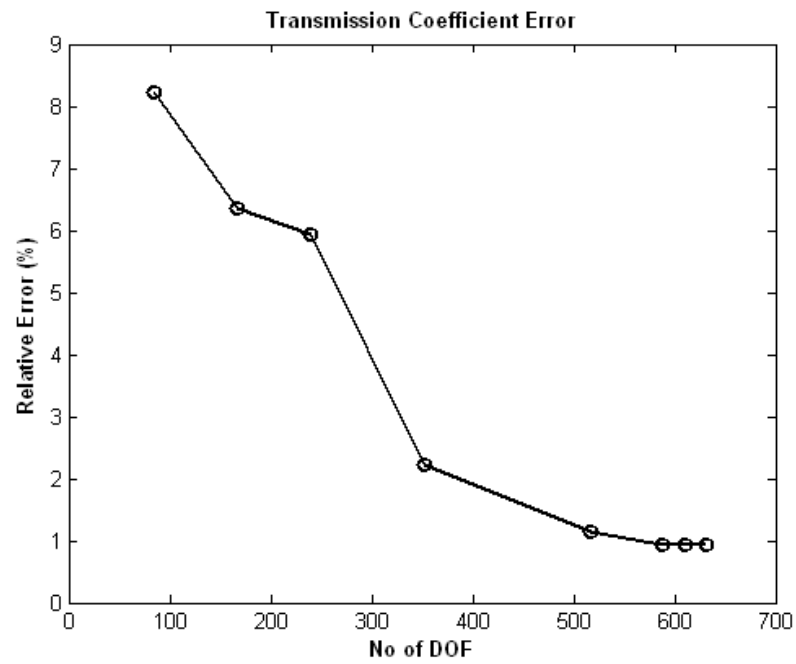


(a) Comparison of numerical estimates to the actual error

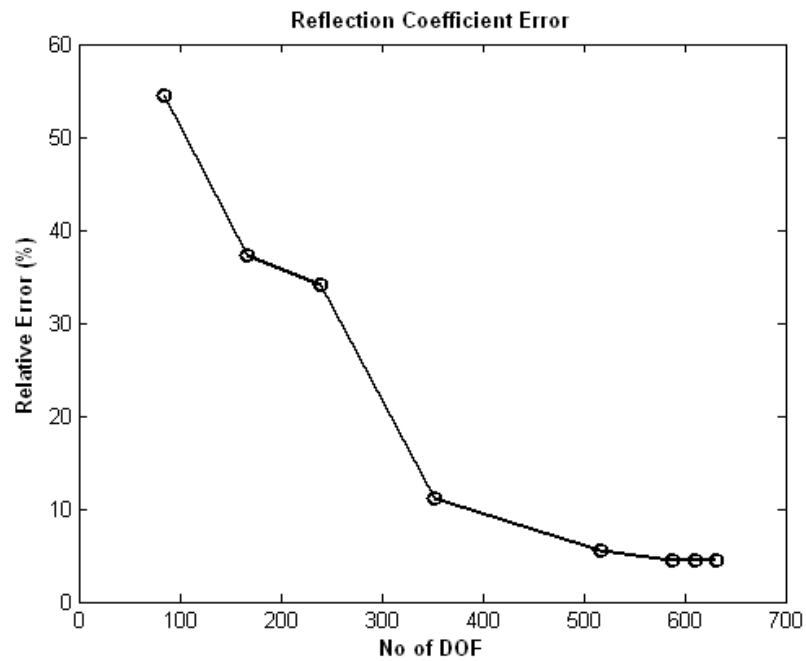


(b) Power conservation error

Figure 6.4 The WFR estimator with 25% single-step iteration technique for the structure in (a) of Figure 6.1

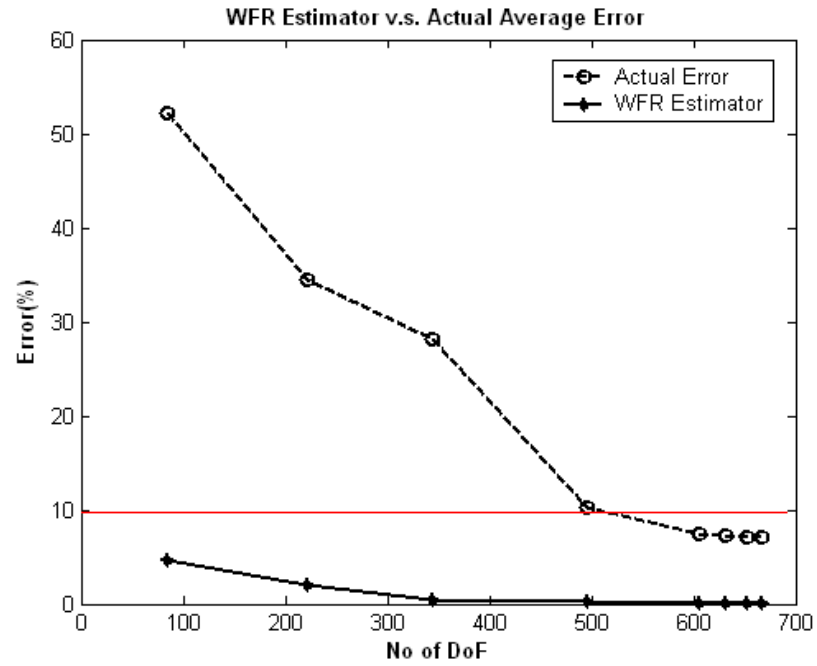


(c) Transmission coefficients error

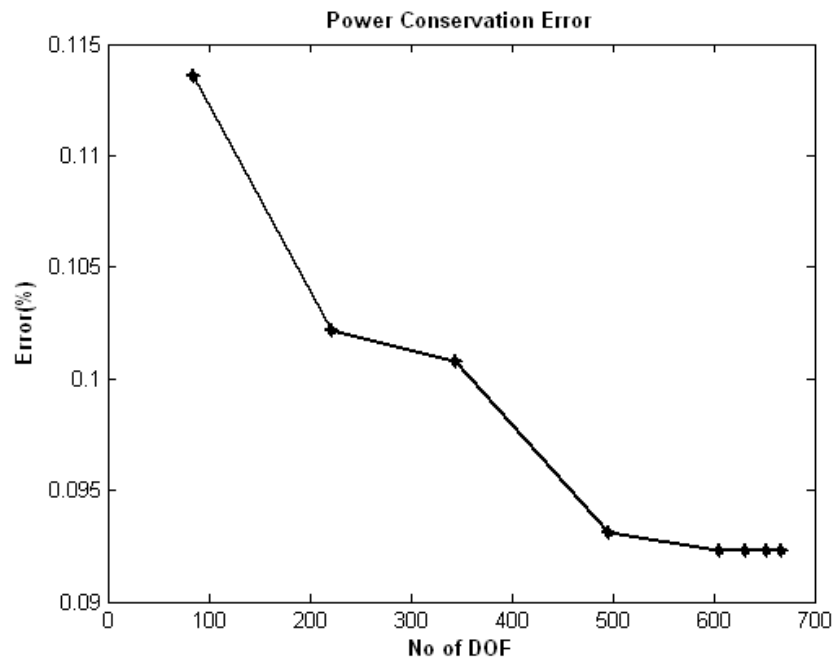


(d) Reflection coefficients error

Figure 6.4 Continued

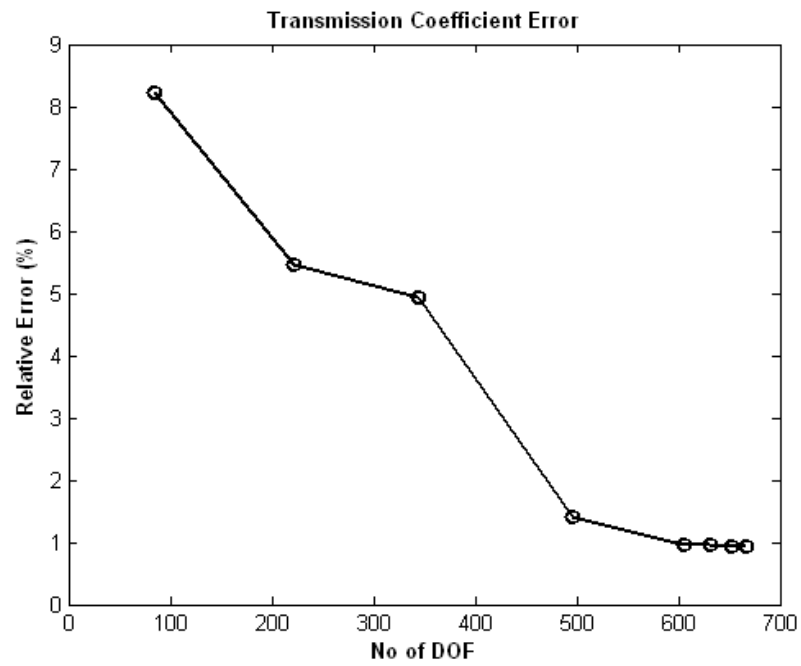


(a) Comparison of numerical estimates to the actual error

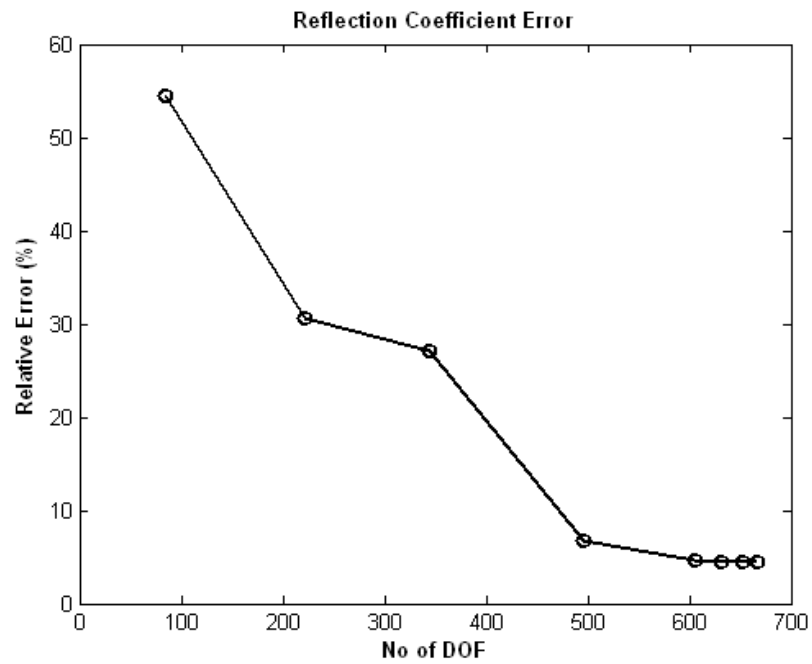


(b) Power conservation error

Figure 6.5 The WFR estimator with 25%+10% multi-step iteration technique for the structure in (a) of Figure 6.1



(c) Transmission coefficients error



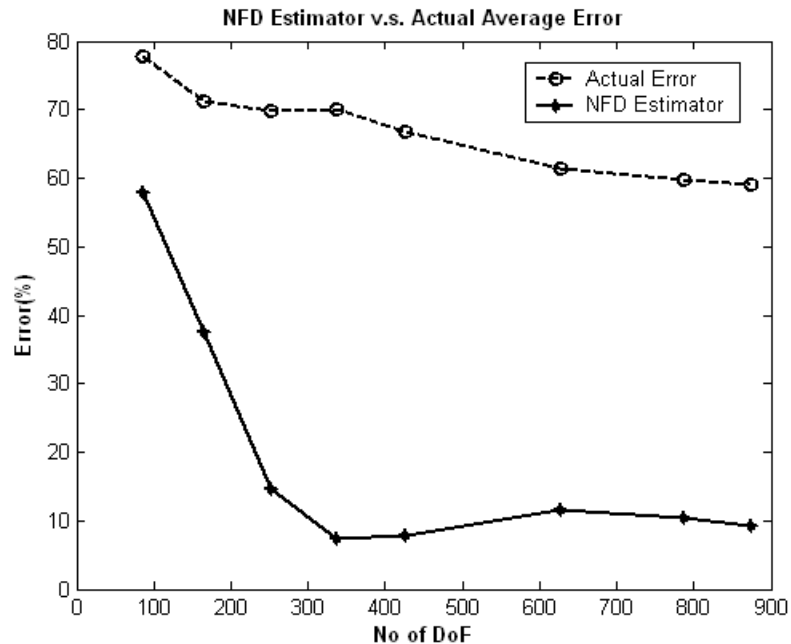
(d) Reflection coefficients error

Figure 6.5 Continued



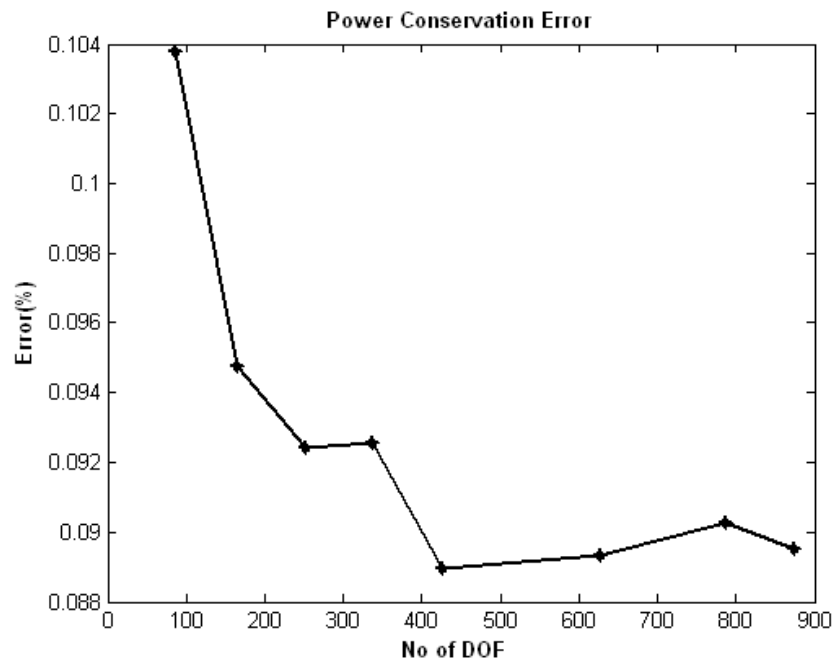
Figure 6.6 shows the performance of the single-step algorithm used in conjunction with the NFD estimator for the PPWG structure in Figure 6.1b. As measured by the actual error in the field (Figure 6.6a), the rate of convergence is much slower for the structure with additional septums. While the power conservation check is within 0.1% at less than 200 degrees of freedom, the convergence rate of the transmission and reflection coefficients is also somewhat slower than the corresponding rates for the one-septum structure.

Figure 6.7 shows similar plots for the multi-step algorithm used in conjunction with the NFD estimator on the structure of Figure 6.1b. The rate of convergence with the multi-step algorithm is slightly slower than that of the single-step approach.

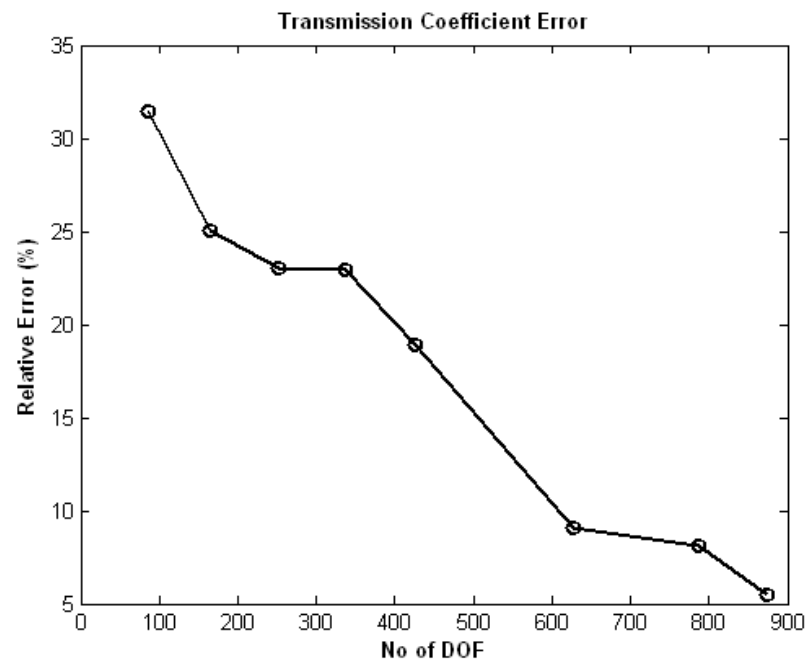


(a) Comparison of numerical estimates to the actual error

Figure 6.6 The NFD estimator with 25% single step iteration technique for the structure in (b) of Figure 6.1

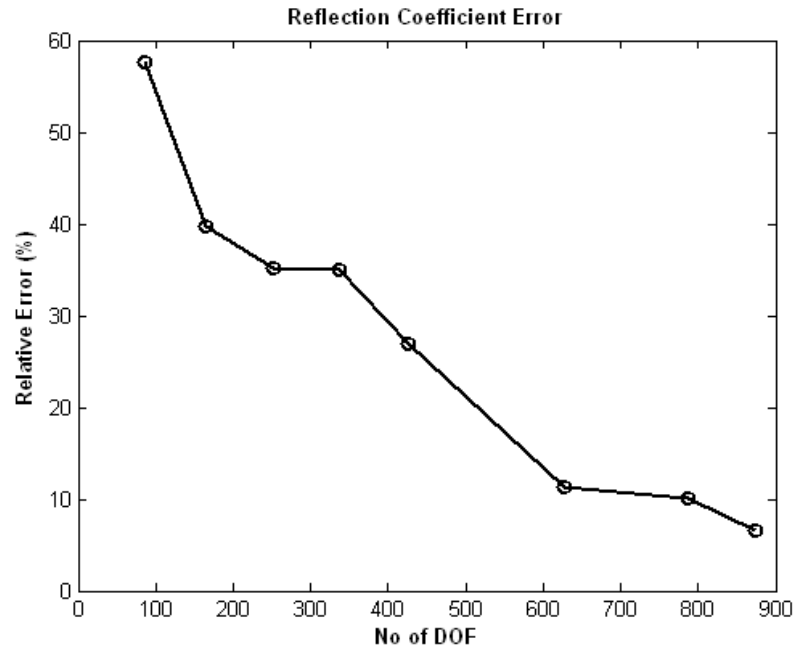


(b) Power conservation error



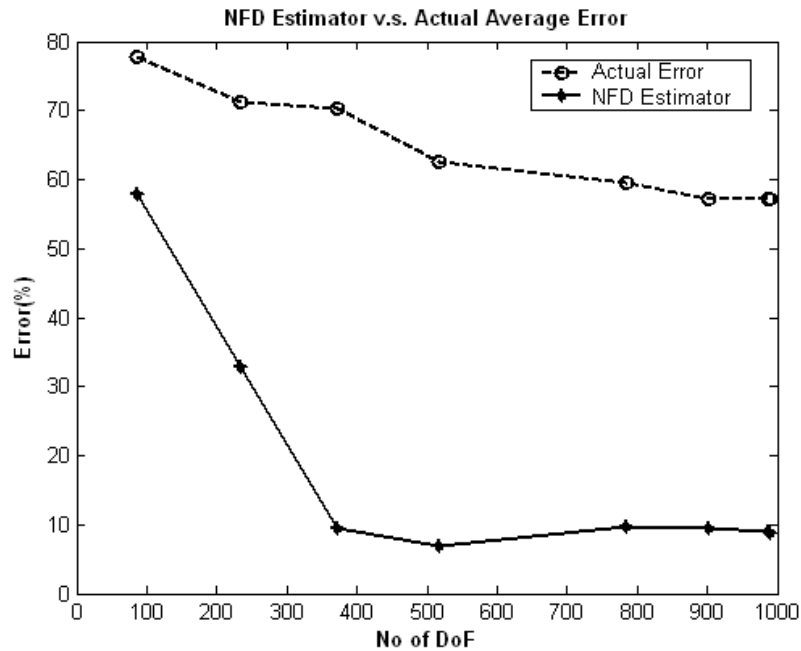
(c) Transmission coefficients error

Figure 6.6 Continued



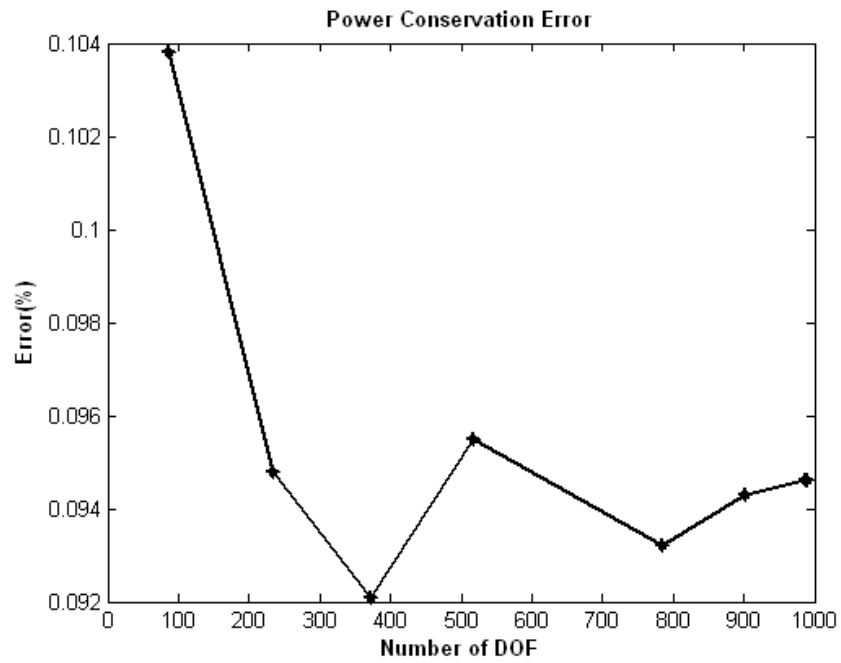
(d) Reflection coefficients error

Figure 6.6 Continued

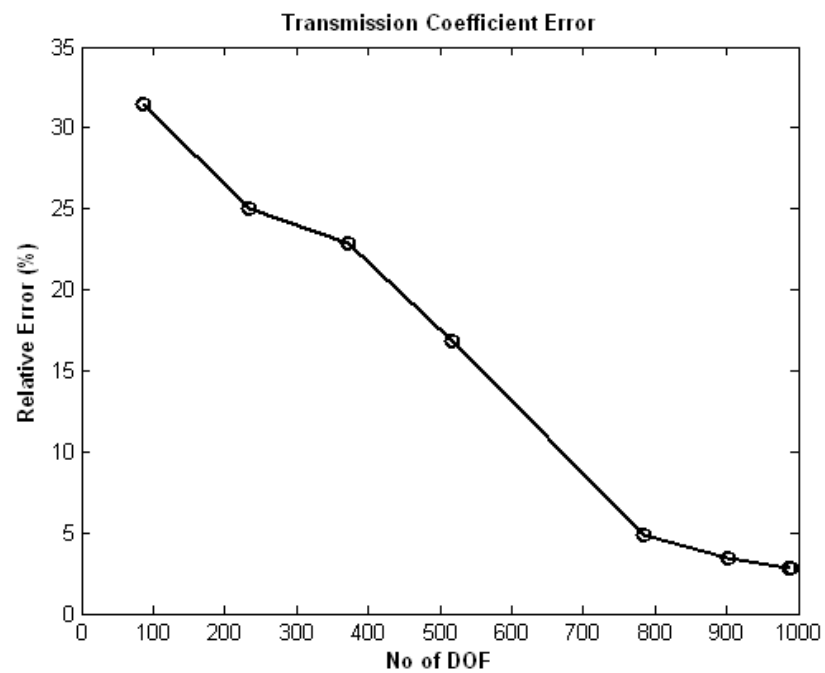


(a) Comparison of numerical estimates to the actual error

Figure 6.7 The NFD estimator with 25% +10% multi-step iteration technique for the structure in (b) of Figure 6.1

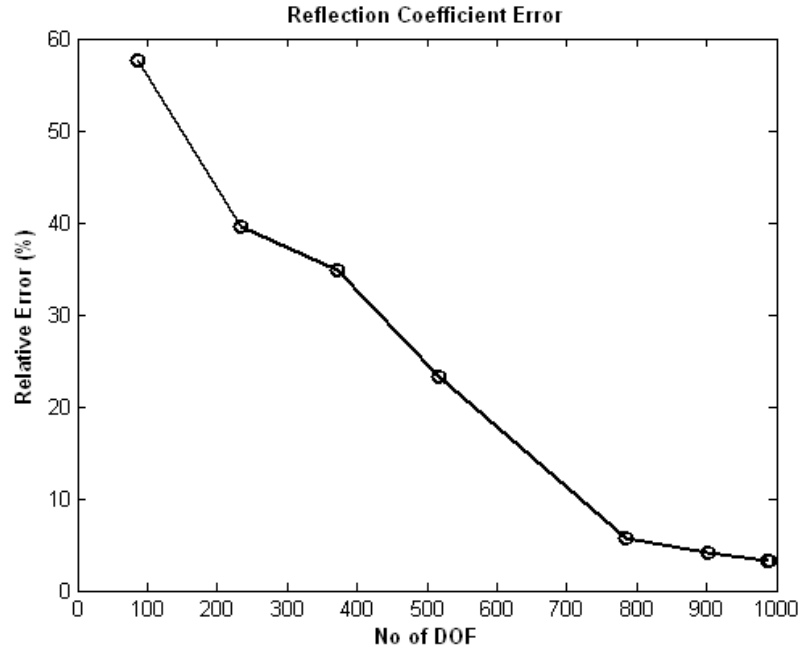


(b) Power conservation error



(c) Transmission coefficients error

Figure 6.7 Continued

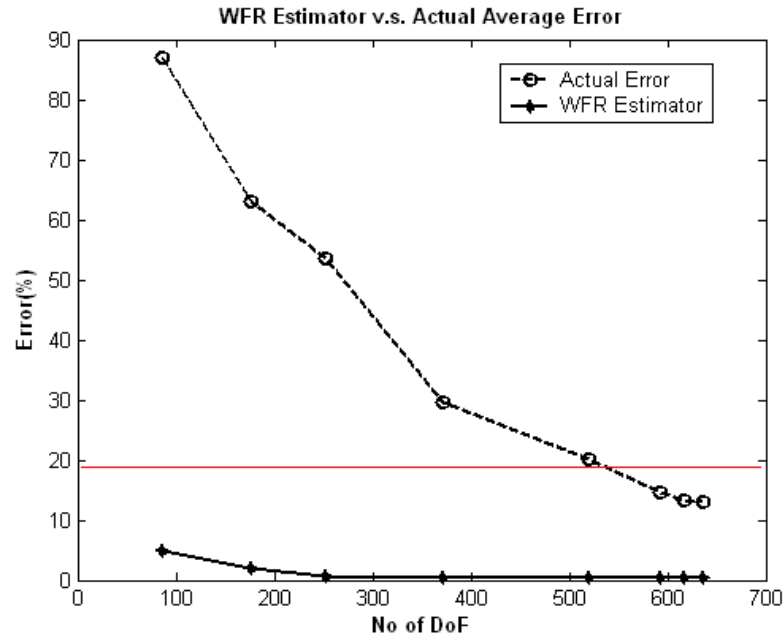


(d) Reflection coefficients error

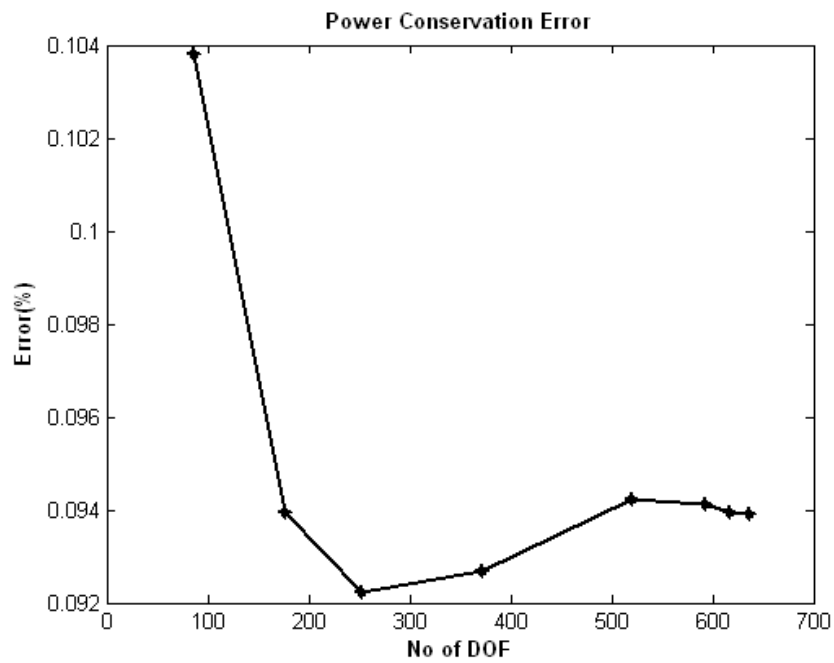
Figure 6.7 Continued

Figure 6.8 shows the performance of the single-step algorithm used in conjunction with the WFR estimator, for the PPWG structure in Figure 6.1b. As indicated previously, the WFR estimator significantly underestimates the actual error in the field. However, the rate of convergence is substantially faster than that of the adaptive refinement algorithms based on the NFD estimators.

Figure 6.9 shows similar plots for the multi-step algorithm used in conjunction with the WFR estimator on the structure of Figure 6.1b. The rate of convergence with the multi-step algorithm is slightly slower than that of the single-step approach.

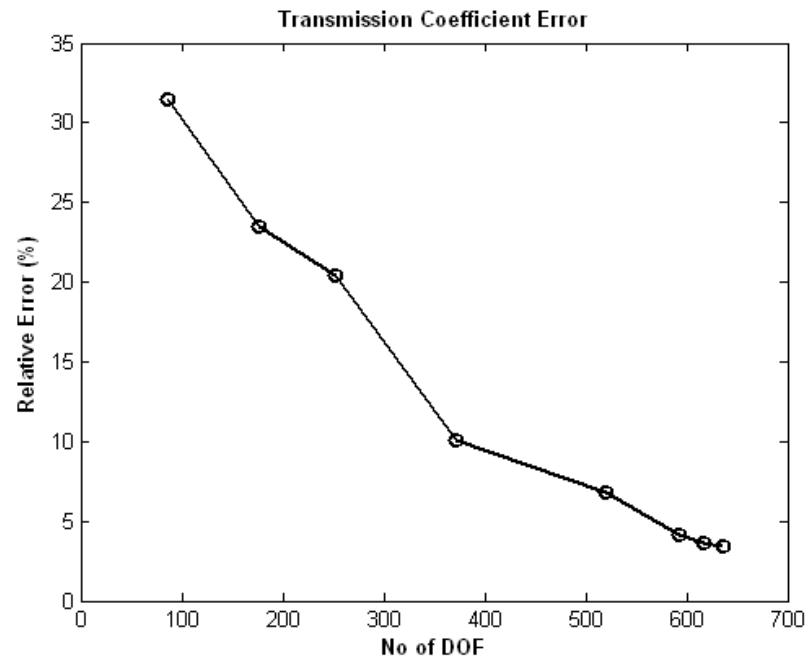


(a) Comparison of numerical estimates to the actual error

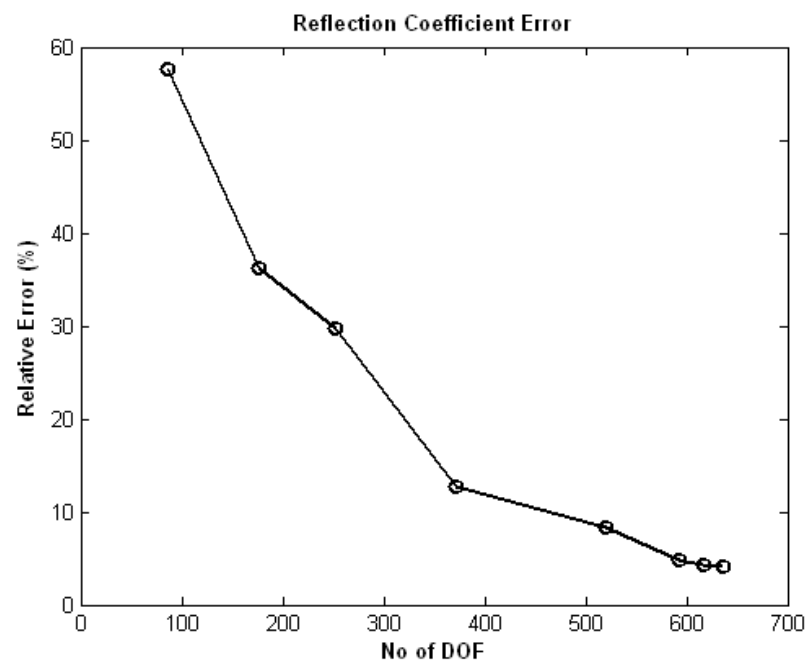


(b) Power conservation error

Figure 6.8 The WFR estimator with 25% single step iteration technique for the structure in (b) of Figure 6.1

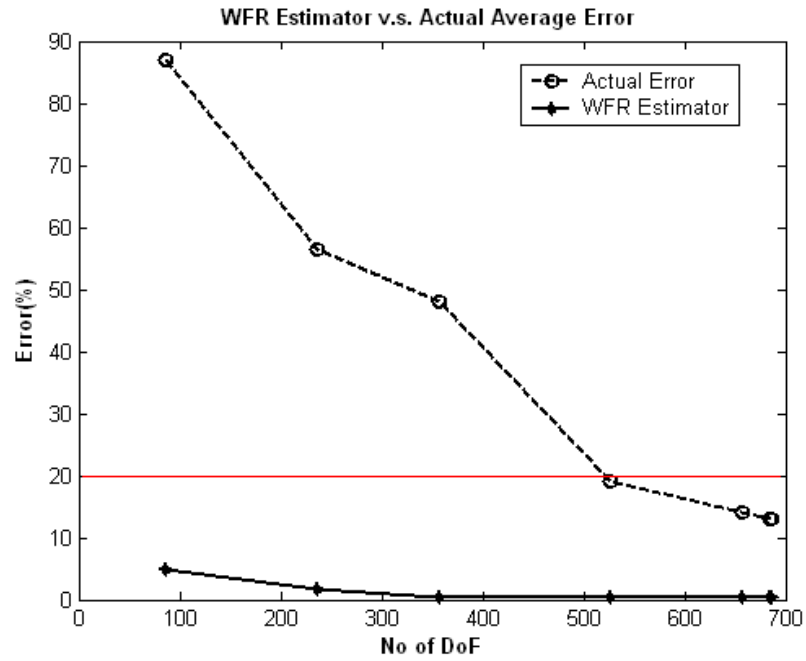


(c) Transmission coefficients error

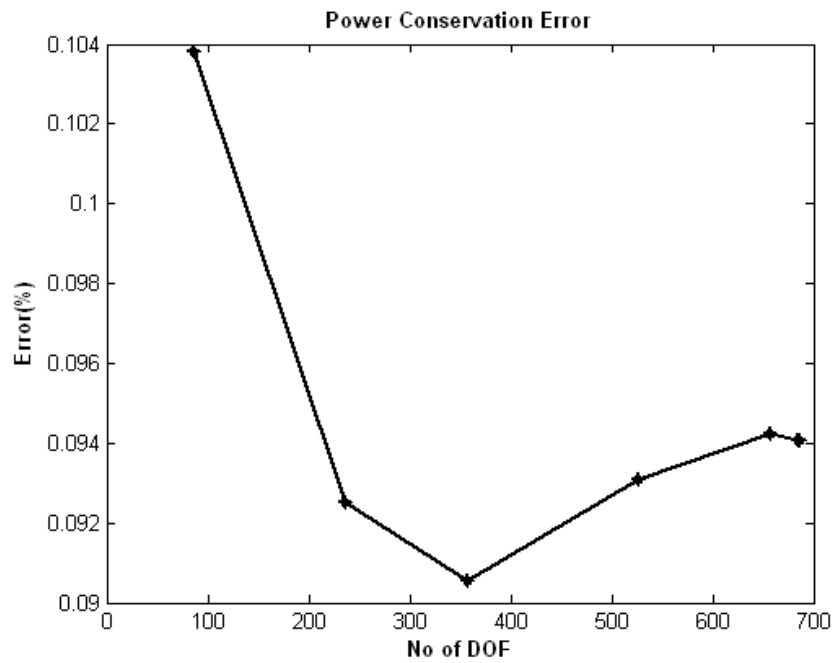


(d) Reflection coefficients error

Figure 6.8 Continued



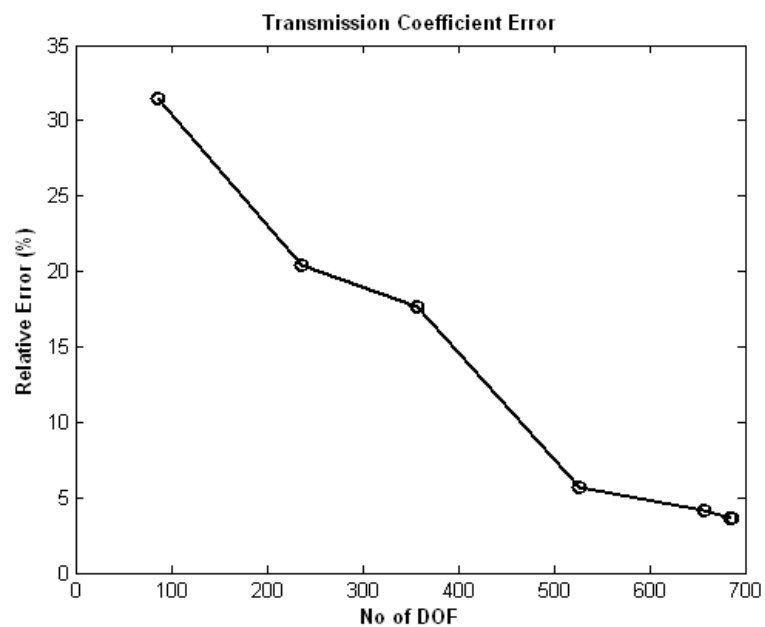
(a) Comparison of numerical estimates to the actual error



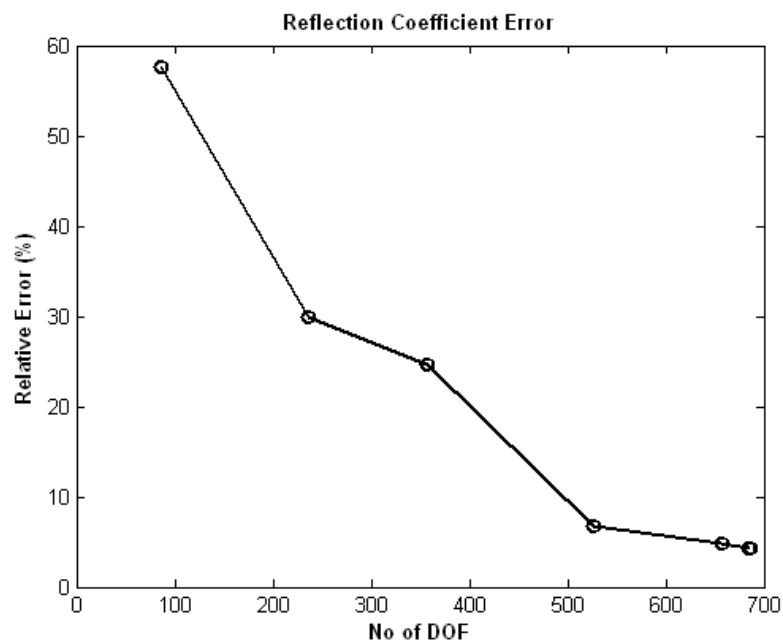
(b) Power conservation error

Figure 6.9 The WFR estimator with 25% +10% multi-step iteration technique for the structure in (b) of Figure 6.1





(c) Transmission coefficients error



(d) Reflection coefficients error

Figure 6.9 Continued

The following tables present numerical data corresponding to the previous plots of this chapter. Table 6.1 provides the reference solutions for the structure of Figure 6.1a obtained with uniform-order interpolatory basis functions. (The “actual” error is zero at the highest level since that is the reference solution.) Tables 6.2 through 6.5 summarize the results of the simulations for the structure of Figure 6.1a. Table 6.6 provides the reference solution for the structure in Figure 6.1b, while Tables 6.7 through 6.10 provide results of the simulations for that structure.

In Tables 6.1 to 6.5, the row in bold font represents the point in the simulation where the actual solution error is within 10% of the reference solution, for the PPWG structure in Figure 6.1a. Tables 6.6, 6.9, and 6.10 similarly indicate where the actual error is within 20% of the reference solution. (Tables 6.7 and 6.8, based on the NFD estimator for the structure of Figure 6.1b, report results that always exceed that error level.) By comparing the number of degrees of freedom required to reach that error level in each case, we can make several observations about the relative performance of the algorithms.

First, we observe that there is not much difference between the single-step and multi-step algorithms in the overall number of degrees of freedom required to reach a comparable error level. (These results do not show the relative computer time, which may be somewhat smaller for the multi-step algorithm since there are fewer intermediate iterative steps required for that approach.)

Second, we observe that the level of error in the transmission coefficient and reflection coefficient is comparable to that of the actual error in the field, as one might expect. The error in the power conservation check is much smaller, and is not as simply related to the other errors. As pointed out in Chapter 5, the error levels reported by the two estimators do not track the actual error very well, either.

These results clearly show, however, that the adaptive refinement algorithm based on the WFR estimator outperforms the algorithm based on the NFD estimator for both structures. There may be a reason for the relatively poor performance of the NFD estimator. For these PPWG structures, the presence of the septums is expected to create rapid field fluctuations in the vicinity of the septum tips. The basis functions used to represent the fields cannot exactly model the field singularity at those tips. The NFD estimator, which samples the normal fields at the center of cell edges, might be expected to be more sensitive to nearby field singularities than the WFR estimator, which works with fields within the cells. Therefore an adaptive refinement algorithm based on the NFD estimator might have a greater tendency to report large errors near field singularities, forcing the refinement process to direct most of the available degrees of freedom to those regions, to the detriment of the overall distribution of actual error in the result.

Table 6.1 Uniform p-refinement with interpolatory vector basis  
for one-septum structure

Order	DoF No	Actual Average Error	Relative Power	Reflection Coefficients	Transmission Coefficients
0/1	84	52.16525	0.99886	0.19157	0.98090
1/2	264	20.72738	0.99902	0.33890	0.94030
<b>2/3</b>	<b>540</b>	<b>10.88942</b>	<b>0.99906</b>	<b>0.38445</b>	<b>0.92264</b>
3/4	912	6.474662	0.99908	0.40200	0.91513
4/5	1380	4.098341	0.99908	0.41093	0.91116
5/6	1944	3.44189	0.99909	0.41606	0.90883
6/7	2604	2.01325	0.99909	0.41928	0.90736
7/8	3360	0	0.99909	0.42142	0.90636

Table 6.2 Adaptive p-refinement with single-step of 25% using NFD estimator  
for one-septum structure

DoF No	Actual Average Error	Relative Power	Reflection Coefficients	Transmission Coefficients
84	48.09234	0.99886	0.19156	0.98090
163	38.33930	0.99892	0.25077	0.96749
242	35.01174	0.99894	0.26634	0.96333
327	33.97659	0.99895	0.26896	0.96260
458	21.77441	0.99901	0.33272	0.94250
<b>615</b>	<b>9.94083</b>	<b>0.99907</b>	<b>0.39949</b>	<b>0.91623</b>
732	9.67399	0.99907	0.40106	0.91554
797	9.53427	0.99907	0.40121	0.91548

Table 6.3 Adaptive p-refinement with multi-steps of 25%+10% using NFD estimator for one-septum structure

DoF No	Actual Average Error	Relative Power	Reflection Coefficients	Transmission Coefficients
84	48.0923	0.99886	0.191566	0.98090
219	37.8507	0.99893	0.253112	0.96688
339	34.4163	0.99895	0.269019	0.96259
509	17.2677	0.99905	0.363292	0.93116
<b>696</b>	<b>8.99107</b>	<b>0.99907</b>	<b>0.405000</b>	<b>0.91381</b>
780	8.27354	0.99908	0.408481	0.91226
848	8.01221	0.99908	0.408141	0.91241
870	7.93597	0.99908	0.408336	0.91232

Table 6.4 Adaptive p-refinement with single-step of 25% using WFR estimator for one-septum structure

DoF No	Actual Average Error	Relative Power	Reflection Coefficients	Transmission Coefficients
84	52.16525	0.99886	0.19157	0.98090
167	38.53593	0.99895	0.26399	0.96398
239	33.11426	0.99896	0.27743	0.96021
353	14.67843	0.99905	0.37481	0.92659
<b>517</b>	<b>8.624254</b>	<b>0.99907</b>	<b>0.39822</b>	<b>0.91679</b>
588	7.364189	0.99908	0.40258	0.91488
610	7.270222	0.99908	0.40261	0.91487
632	7.194764	0.99908	0.40261	0.91487

Table 6.5 Adaptive p-refinement with multi-steps of 25%+10% using WFR estimator for one-septum structure

DoF No	Actual Average Error	Relative Power	Reflection Coefficients	Transmission Coefficients
84	52.1652	0.99886	0.19157	0.98090
222	34.4557	0.99898	0.29214	0.95584
345	28.2070	0.99899	0.30720	0.95112
<b>496</b>	<b>10.2028</b>	<b>0.99907</b>	<b>0.39305</b>	<b>0.91901</b>
605	7.51394	0.99908	0.40204	0.91512
632	7.28962	0.99908	0.40238	0.91497
653	7.06954	0.99908	0.40264	0.91485
667	7.06790	0.99908	0.40264	0.91485

Table 6.6 Uniform p-refinement with Interpolatory vector basis for two-septum structure

Order	DoF No	Actual Average Error	Relative Power	Reflection Coefficients	Transmission Coefficients
0/1	86	86.99498	0.99896	0.28981	0.95654
1/2	268	35.97367	0.99901	0.56689	0.82324
<b>2/3</b>	<b>546</b>	<b>19.18278</b>	<b>0.99907</b>	<b>0.63448</b>	<b>0.77234</b>
3/4	920	11.42511	0.99906	0.65900	0.75152
4/5	1390	7.376884	0.99905	0.67113	0.74070
5/6	1956	6.306470	0.99905	0.67798	0.73443
6/7	2618	3.749598	0.99904	0.68223	0.73049
7/8	3376	0	0.99904	0.68504	0.72784

Table 6.7 Adaptive p-refinement with single-step of 25% using NFD estimator for two-septum structure

<b>DoF No</b>	<b>Actual Average Error</b>	<b>Relative Power</b>	<b>Reflection Coefficients</b>	<b>Transmission Coefficients</b>
86	77.76464	0.99896	0.28981	0.95654
165	71.18441	0.99905	0.41316	0.91014
252	69.86788	0.99907	0.44419	0.89542
337	69.95831	0.99907	0.44565	0.89469
427	66.87464	0.99911	0.50021	0.86539
628	61.46841	0.99910	0.60757	0.79370
788	59.84874	0.99910	0.61649	0.78679
874	59.01051	0.99910	0.63982	0.76794

Table 6.8 Adaptive p-refinement with multi-steps of 25%+10% using NFD estimator for two-septum structure

<b>DoF No</b>	<b>Actual Average Error</b>	<b>Relative Power</b>	<b>Reflection Coefficients</b>	<b>Transmission Coefficients</b>
86	77.76464	0.99896	0.28980	0.95654
233	71.24195	0.99905	0.41435	0.90959
372	70.20905	0.99907	0.44597	0.89453
518	62.60296	0.99904	0.52553	0.85020
785	59.41848	0.99906	0.64554	0.76311
902	57.17812	0.99905	0.65712	0.75315
988	57.22235	0.99905	0.66277	0.74818
990	57.18941	0.99905	0.66271	0.74823

Table 6.9 Adaptive p-refinement with single-step of 25% using WFR estimator for two-septum structure

DoF No	Actual Average Error	Relative Power	Reflection Coefficients	Transmission Coefficients
86	86.99498	0.99896	0.28981	0.95654
176	63.09614	0.99906	0.43666	0.89910
253	53.59824	0.99908	0.48077	0.87632
371	29.71183	0.99907	0.59755	0.80125
<b>520</b>	<b>20.14653</b>	<b>0.99906</b>	<b>0.62822</b>	<b>0.77743</b>
592	14.60024	0.99906	0.65176	0.75781
617	13.38243	0.99906	0.65617	0.75399
636	13.00406	0.99906	0.65715	0.75314

Table 6.10 Adaptive p-refinement with multi-steps of 25%+10% using WFR estimator for two-septum structure

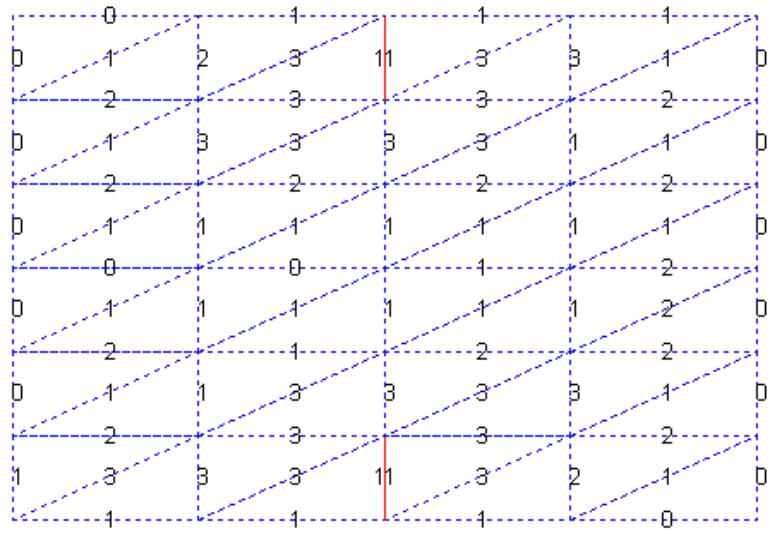
DoF No	Actual Average Error	Relative Power	Reflection Coefficients	Transmission Coefficients
86	86.99498	0.99896	0.28980	0.95654
236	56.33796	0.99907	0.47992	0.87678
358	47.99359	0.99909	0.51588	0.85613
<b>527</b>	<b>19.12508</b>	<b>0.99906</b>	<b>0.63871</b>	<b>0.76884</b>
658	14.20549	0.99905	0.65188	0.75769
685	13.05426	0.99905	0.65612	0.75403
686	13.05552	0.99905	0.65612	0.75403
86	86.99498	0.99896	0.28980	0.95654



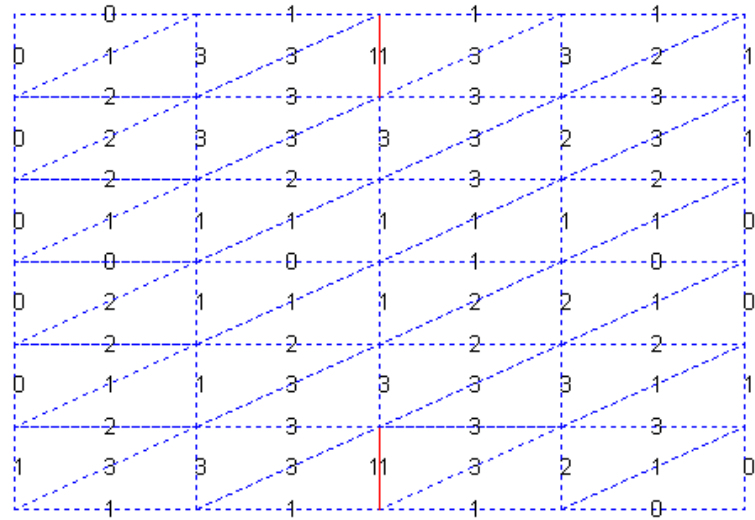
## 6.2 Summary

The WFR and NFD error estimators identified in the preceding chapter as the most promising were implemented within adaptive refinement algorithms. Two variations on the adaptive refinement algorithm were employed, and applied to the analysis of PPWG structures containing septums. Results were presented in the form of plots and tables.

Figure 6.10 through 6.12 plot the DoF distribution captured after the final iteration with the NFD and WFR error estimators. The NFD estimator is carried out for a one-septum structure while the WFR estimator is carried for one-septum and two-septum structures. The highest order basis functions are assigned to cells or edges near the septum in which the rapid variation of field is expected. We can conclude that the WFR estimators are good at detecting the rapid fluctuation of the field of the given structures while the NFD estimator is not suitable for the complicated structure.

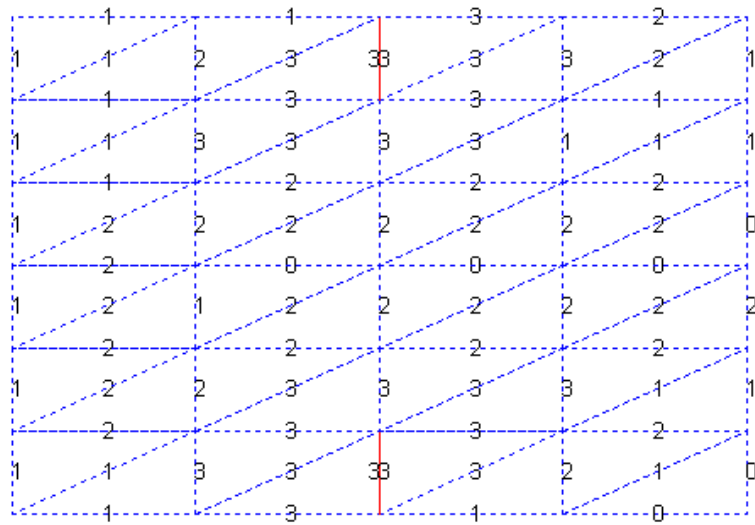


(a) The single-step NFD estimator DoF distribution

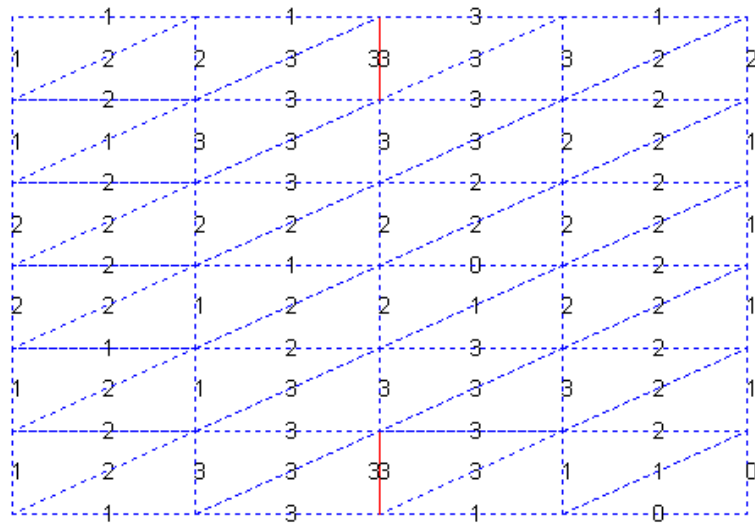


(b) The multi-step NFD estimator DoF distribution

Figure 6.10 DoF distribution of the NFD error estimator

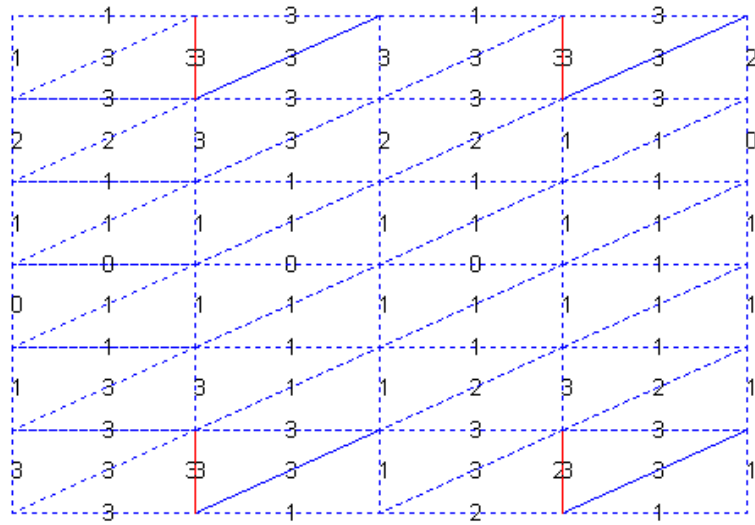


(a) The single-step WFR estimator DoF distribution

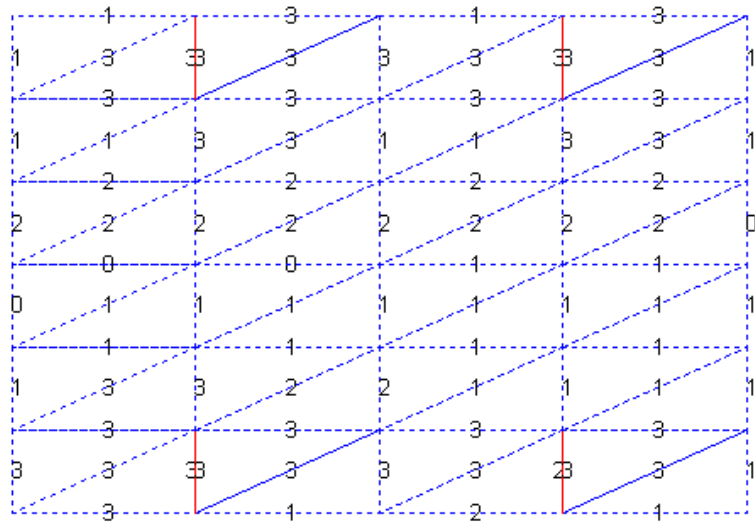


(b) The multi-step WFR estimator DoF distribution

Figure 6.11 DoF distribution of the WFR error estimator for one-septum structure



(a) The single-step WFR estimator DoF distribution



(b) The multi-step WFR estimator DoF distribution

Figure 6.12 DoF distribution of the WFR error estimator for two-septum structure

Table 6.11 summarizes the simulations carried out for p-adaptive FEM schemes of this chapter. The smaller simulation time of the NFD is due to the fact that only one sample point is used for error norm calculation, while the WFR estimator takes a longer computational time since it employed over 300 sample points for the cell-based error norm. The WFR error estimator shows better performance than the NFD in general since the NFD can not reach the expected accuracy for the two-septum structure.

Considering the two-septum structure with the WFR estimator, the multi-step iteration technique requires fewer iterations number to reach around 20% in solution accuracy. The multi-step technique gives better performance in terms of total simulation time despite of the greater numbers of DoF at the final iteration.

Table 6.11 Comparison of two iteration techniques for one-septum and two-septum T-PPWG structures

	<b>Septum 1</b>				<b>Septum 2</b>	
	<b>NFD Single- Step IT</b>	<b>NFD Multi- Step IT</b>	<b>WFR Single- Step IT</b>	<b>WFR Multi- Step IT</b>	<b>WFR Single- Step IT</b>	<b>WFR Multi- Step IT</b>
<b>Global Average Error at Termination</b>	<b>9.94083</b>	<b>8.99107</b>	<b>8.624254</b>	<b>10.2028</b>	<b>20.14653</b>	<b>19.12508</b>
<b>Iteration No</b>	<b>6</b>	<b>5</b>	<b>5</b>	<b>4</b>	<b>5</b>	<b>4</b>
<b>DoF No</b>	<b>615</b>	<b>696</b>	<b>517</b>	<b>496</b>	<b>520</b>	<b>527</b>
<b>Operation Time (Sec)</b>	<b>70.656</b>	<b>117.547</b>	<b>344.187</b>	<b>287.234</b>	<b>351.656</b>	<b>305.813</b>

Although the WFR estimator was not very accurate at predicting the actual error levels, the adaptive refinement algorithms based on the WFR estimator outperformed the algorithms incorporating the NFD estimator.

## CHAPTER 7: CONCLUSIONS

There are compelling reasons to suggest that computational methods for electromagnetic analysis be adaptive. Adaptive methods reduce the dependence on user expertise, provide a more robust self-correcting process of analysis, and can increase user confidence in the results. In the general engineering and applied mathematics communities, h-refinement and p-refinement procedures have been explored for more than two decades. H-refinement techniques have been used with vector finite elements; the commercial High-Frequency Structure Simulator (HFSS) tool by the Ansoft Corporation employs h-refinement. To date, however, little attention has been directed at the use of p-refinement with vector finite elements for electromagnetics.

The present investigation implemented a two-dimensional vector finite element testbed that employed both interpolatory and hierarchical vector bases of the Nedelec mixed-order types. Interpolatory elements with mixed-order degrees ranging from 0/1 to 7/8 and hierarchical elements with orders from 0/1 to 4/5 were incorporated. At the outset of this study, no other investigation had reported the implementation of such a wide range of polynomial degrees. Background information and results to support the verification of the finite element testbed were summarized in Chapters 2, 3, and 4.

A key aspect of adaptive refinement algorithms is the error estimator used to drive the process. No systematic study of error estimators has been reported for vector finite element problems. In the present investigation, four distinct error estimators were

implemented and evaluated. Chapter 5 presented the details of their implementation and the results of this comparison. Surprisingly, none of the error estimators was particularly good at predicting the actual local or global error levels in a specific solution. All were adequate at identifying regions of the problem domain with relatively high local error, although there was a wide variation in their accuracy.

Comparisons with actual error levels in Chapter 5 led to the conclusion that two estimators, the normal-field discontinuity (NFD) estimator and the weak form residual (WFR) estimator, were superior in overall performance to the others. These two estimators were used in additional simulations in Chapter 6, to illustrate the process of adaptive p-refinement.

Although the present investigation was limited to the two-dimensional case, it is hoped that because it dealt with vector equations and basis functions, the results have applicability to the full three-dimensional situation. It is expected that future work will be directed toward the three-dimensional problem.



## REFERENCES

- [1] J. Jin, The finite element method in electromagnetics, John Wiley & Sons, 1993
- [2] M. Salazar-Palma et. al., Iterative and self-adaptive finite-elements in electromagnetic modeling, Boston, Artech House, 1998
- [3] A.F. Peterson, S.L. Ray ,R. Mittra, Computational methods for electromagnetics, IEEE Press, New York, 1998
- [4] I.S. Duff, J.K. Reid, "The multifrontal solution of indefinite sparse symmetric linear equations," ACM Trans. Math. Softw., vol. 9, pp. 302-325, 1983
- [5] G. Karypis, V. Kumar. METIS 4.0: Unstructured graph partitioning and sparse matrix ordering system. Technical report, Dept. of Computer Science, university of Minnesota, 1998. Available on the WWW at URL <http://www.cs.umn.edu/~metis>.
- [6] J.M. Jin, J.L. Volakis, "A finite element-boundary integral method for scattering by three-dimensional cavity-backed apertures," IEEE Trans. Antennas Propagation, vol. 39, pp. 97-104, Jan. 1991
- [7] J.P. Berenger, "A perfectly matched layer for the absorption of electromagnetic waves," J. Computational Physics, vol. 114, pp. 185-200, 1994
- [8] S. Alfonzetti, G. Borzi, N. Salerno, "Iteratively-improved Robin boundary conditions for the finite element solution of scattering problems in unbounded domains," Int. J. Number. Meth. Eng., vol. 42, pp. 601-629, June 1998
- [9] W. Kinsner, E.D. Torre, "An iterative approach to the finite element method in field problems," IEEE Trans. Microwave Theory Tech., vol. 20, pp. 221-228, Mar. 1974
- [10] H. Whitney, Geometric Integration Theory, Princeton, NJ: Princeton University Press, 1957

- [11] J.C. Nedelec, "Mixed finite elements in  $R^3$ ," Num. Math., vol. 35, pp. 315-341, 1980
- [12] J.C. Nedelec, "A new family of mixed finite elements in  $R^3$ ," Num. Math., vol.50, pp.57-81,1986
- [13] J.F. Lee, D.K. Sun, Z. J. Cendes, "Full-wave analysis of dielectric waveguides using tangential vector finite elements," IEEE Transactions on Microwave Theory and Technology, vol. 39, pp. 1262-1271, Aug., 1991
- [14] Z.J. Cendes, "Vector finite elements for electromagnetic field computation," IEEE Transactions on Magnetics, vol. 27, pp. 3959-3966, Sep. 1991
- [15] J.P. Webb, "Edge Elements and What They can do for you," IEEE Transactions on Magnetics, vol. 29, no.2, pp. 1460-1465, March 1993
- [16] J.P. Webb, B. Forghani, "Hierarchal scalar and vector tetrahedral," IEEE Transactions on Magnetics, vol. 29, pp. 1495-1498, Mar. 1993
- [17] A.F. Peterson, "Vector finite element formulation for scattering from two-dimensional heterogeneous bodies," IEEE Trans. on Antennas and Propagation, vol. 42, pp. 357-365, Mar. 1994
- [18] J.S. Savage, A.F. Peterson, "Higher-order vector finite elements for tetrahedral cells," IEEE Transactions on Microwave Theory and Technology, vol. 44, pp. 874-879, June, 1996
- [19] R.D. Graglia, D.R. Wilton, A.F. Peterson, "Higher order interpolatory vector bases for computational electromagnetics," IEEE Transactions on Antennas Propagation, vol. 45, pp. 329-342, Mar. 1997
- [20] T.V. Vioultis, T.D. Tsiboukis, "Development and implementation of second and third order vector finite elements in various 3-D electromagnetics field problems," IEEE Transactions on Magnetics, vol. 33, pp. 1812-1815, Mar. 1997

- [21] L.S. Andersen, J.L. Volakis, "Mixed-order tangential vector finite elements for triangular elements," IEEE Trans. on Antennas and Propagation, vol. 40, pp. 104-108, Feb. 1998
  
- [22] L.S. Andersen, J.L. Volakis, "Development and Application of a Novel Class of Hierarchical Tangential Vector Finite Elements for Electromagnetics," IEEE Transactions on Antennas Propagation, vol. 47, pp. 112-120, Jan. 1999
  
- [23] J.L. Volakis, A. Chatterjee, L.C. Kempel, Finite element method for electromagnetics, IEEE Press, 1998
  
- [24] J.P. Webb, "Hierarchical Vector Basis Functions of Arbitrary Order for Triangular and Tetrahedral Finite Elements," IEEE Transactions on Antennas Propagation, vol. 47, pp.1244-1253, Aug. 1999
  
- [25] M.M. Ilic, M. Notaros, "Higher Order Hierarchical Curved Hexahedral Vector Finite Elements for Electromagnetic Modeling," IEEE Transactions on Microwave Theory and Techniques, vol. 51, no. 3, pp. 1026-1033, March 2003
  
- [26] M. Ainsworth, J.T. Oden, Posteriori Error Estimation in Finite Element Analysis, New York, John Wiley, 2000
  
- [27] A Bossavit, "Solving Maxwell's equations in a closed cavity, and the question of spurious modes," IEEE Trans. Magnetics, vol. 26, no. 2, pp. 1819-1824, Dec. 1988
  
- [28] Pressig, R.S, Peterson A.F., "A rationale for p-refinement with the Vector Helmholtz equation and two dimensional vector finite elements," Applied Computational Electromagnetics Society Journal, v 19, n 2, July 2004, p 65-75
  
- [29] S.Y Hahn, C. calmels, G. Meunier, J.L. Coulomb, "A posteriori error estimator for adaptive finite element mesh generation," IEEE Trans. Magn. vol. 24, no. 1, pp.315-317, 1988
  
- [30] H.Kim, S. Hong, K. Choi, H. Jng, S. Hahn, "A three dimensional adaptive finite element method for magnetostatic problems," IEEE Trans. Magn. vol. 27, pp. 4081-4084, 1991

- [31] N.A. Golias, T.D. Tsiboukis, "Three dimensional automatic adaptive mesh generation," IEEE Trans. Magn., vol. 28, pp. 1700-1703, Mar.,1992
- [32] N.A. Golias, T.D. Tsiboukis, "Adaptive refinement strategies in three dimensions," IEEE Transactions on Microwave Theory and Techniques, vol. 29, no. 2, pp. 1886-1889, Mar., 1993
- [33] N.A. Golias, A.G. Papagiannakis, T.D. Tsiboukis, "Efficient mode analysis with edge elements and 3-D adaptive refinement," IEEE Transactions on Microwave Theory and Techniques, vol. 42, no. 1, pp. 99-106, Jan., 1994
- [34] N.A. Golias, T.D. Tsiboukis, "3-D eddy-current computation with a self-adaptive refinement technique," IEEE Trans. on. Magn., vol. 31, no. 3, pp. 2261-2268, May, 1994
- [35] M.G. Vanti, A. Raizer, "A magnetostatic 2D comparison of local error estimators in FEM," IEEE Transaction on Magnetics, vol. 29, no. 2, pp. 1902-1905, Mar. 1993
- [36] D.K. Sun, Z. Cendes, J.F. Lee, "Adaptive mesh refinement, h-version, for solving multiport microwave devices in three dimensions," IEEE Trans. Magn., vol. 36, no. 4, pp. 1596-1599, July, 2000
- [37] A.Raizer, G. Meunier, J.L. Coulomb, "An approach for automatic adaptive mesh refinement in finite element computation of magnetic fields," IEEE Trans. Magn., vol. 25, no. 4, pp. 2965-2967,1989
- [38] A. Raizer, S.H. Hoole, G. Meunier, J.L. Coulomb, "P- and h- type adaptive mesh generation," Journal of Applied Physics, vol. 67, no. 9, pp. 5803-5805, 1990
- [39] S.R.H. Hoole, S. Yoganathan, S. Jayakumaran, "Implementing the smoothness criterion in adaptive meshes," IEEE Trans. Magn. vol. 22, pp. 808-810, September, 1986
- [40] D. Giannacopoulos, "Field Discontinuity Refinement Criteria and Optimal Discretizations in Adaptive Finite-Element Electromagnetic Analysis for Microelectronic System Interconnections," IEEE Transactions on Magnetics, vol. 39, no.3, pp.1658-1661, May 2003

- [41] I. Babuska, W.C. Rheinboldt, "Error estimates for adaptive finite element computations," SIAM J. Num. Anal., vol. 15, pp. 736-754, 1978
- [42] I. Babuska, W.C. Rheinboldt, "A-posteriori error estimates for the finite element method," Int. J. Num. Meth. Eng., vol. 12, pp. 1597-1615, 1978
- [43] I. Babuska, R.B. Kellogg, J. Pitkaranta, "Direct and inverse error estimates for finite elements with mesh refinements" Num. Meth., vol. 33, pp. 447-471, 1979
- [44] W.C. Rheinboldt, "On a theory of mesh-refinement processes," SIAM J. Num. Anal. vol. 17, pp. 766-778, 1980
- [45] W.C. Rheinboldt, "Adaptive mesh refinement processes for finite element solutions," Int. J. Num. Meth. Eng. vol. 17, pp. 649-662, 1981
- [46] I. Babuska, W.C. Rheinboldt, "A posteriori error analysis of finite element solutions for one-dimensional problems," SIAM J. Num. Anal. vol. 18, pp. 565-589, 1981
- [47] Z.J. Cendes, D.N. Shenton, "Adaptive mesh refinement in the finite element computation of magnetic field," IEEE Trans. Magn., vol.21, no. 5, pp. 1811-1816, Sep.,1985
- [48] P. Fernandes, P. Girdinio, P. Molfino, M. Repetto, "Local error estimates for adaptive mesh refinement," IEEE Trans. Magn. vol. 24, no. 1, pp. 299-302, Jan., 1988
- [49] P. Fernandes, P. Girdinio, P. Molfino, M. Repetto, "A comparison of adaptive strategies for mesh refinement based on a posteriori local error estimation procedures," IEEE Trans. Magn. vol. 26, no. 2, pp. 795-798, Mar., 1990
- [50] P. Fernandes, P. Girdinio, P. Molfino, M. Repetto, "An enhanced error estimator procedure for finite element field computation with adaptive mesh refinement," IEEE Trans. Magn. vol. 26, no. 6, pp. 2187-2189, Sep., 1990
- [51] P. Fernandes, P. Girdinio, P. Molfino, M. Repetto, "Local error estimation procedures as refinement indicators in adaptive meshing," IEEE Trans. Magn. vol. 27, no. 5, pp. 4189-4192, Sep., 1991

- [52] P. Fernandes, P. Girdinio, M. Repetto, G. Secondo, "Refinement strategies in adaptive meshing," IEEE Trans. Magn., vol. 28, no. 2, pp. 1739-1742, Mar., 1992
- [53] M.G. Vanti, A. Raizer, "Optimal meshes and h-p refinement," IEEE Trans. Magn., vol. 33, no. 2, pp. 1752-1755, Mar., 1997
- [54] M.G. Vanti, A. Raizer, "h-p Adaptivity with Hierarchic Hexahedral Element," IEEE Trans. Magn., vol. 34, no. 5, pp. 3272-3275, Sep. 1998
- [55] T. Ezzedine, B. Kouki, A. Bouallegue, "A 3D posteriori Error Estimator for FEM Solution of Electromagnetic Problems," Microwave and Optical Technology Letters, vol. 36, no. 4, pp.300-302, Feb. 2003
- [56] M.M Botha, D.B. Davidson, "A Posteriori Error Estimation Results for The FEM Analysis of a Waveguide Filter," IEEE Africon, pp. 541-544, 2002
- [57]M.M. Botha, D.B. Davidson, "P-adaptive FE-BI analysis of homogenous, lossy regions for SAR-and far-field calculation," IEEE Antennas and Propagation Society International Symposium, vol. 1, 22-27, pp.684 – 687, June 2003
- [58] O.C. Zienkiewicz, D.W. Kelly, J. Gago, I. Babuska, The Mathematics of Finite Elements and Applications, Ed. J.R. Whiteman, Academic Press, 1982, pp313-346
- [59] W. Daigang, J. Kexun, "P-version Adaptive Computation of FEM," IEEE Trans. Magn., vol. 30, no. 5, pp. 3515-3518, Sep. 1994
- [60] L.S. Andersen, J.L. Volakis, "Adaptive multiresolution antenna modeling using hierarchical mixed-order tangential vector finite elements," IEEE Trans. on Antennas Propagation, vol. 49, pp. 211-222, Feb. 2001
- [61] M.M. Gavrilovic, J.P. Webb, "An error indicator for the calculation of global quantities by the p-adaptive finite element method," IEEE Trans. Magn., vol. 33, no. 5, pp. 4128-4130, September 1997
- [62] M.M. Gavrilovic and J.P. Webb, "Targeted error indicators for use in finite-element p-adaption," IEEE Trans. Magn., vol.34, pp. 3280-3283, Sept. 1998

[63] D. Nair and J.P. Webb, "P-Adaptive Computation of the Scattering Parameters of 3-D Microwave Devices," IEEE Trans. Magn., vol.40, No.2, March 2004